



City Research Online

City, University of London Institutional Repository

Citation: Ho, Y. S. (1993). Modelling of the conical entrance orifice plate flow sensor. (Unpublished Doctoral thesis, City, University of London)

This is the accepted version of the paper.

This version of the publication may differ from the final published version.

Permanent repository link: <https://openaccess.city.ac.uk/id/eprint/29941/>

Link to published version:

Copyright: City Research Online aims to make research outputs of City, University of London available to a wider audience. Copyright and Moral Rights remain with the author(s) and/or copyright holders. URLs from City Research Online may be freely distributed and linked to.

Reuse: Copies of full items can be used for personal research or study, educational, or not-for-profit purposes without prior permission or charge. Provided that the authors, title and full bibliographic details are credited, a hyperlink and/or URL is given for the original metadata page and the content is not changed in any way.

MODELLING OF THE
CONICAL ENTRANCE ORIFICE PLATE FLOW SENSOR

BY

YICK SING HO

THESIS SUBMITTED FOR THE DEGREE OF
DOCTOR OF PHILOSOPHY

CITY UNIVERSITY, LONDON
DEPARTMENT OF ELECTRICAL, ELECTRONIC
AND INFORMATION ENGINEERING

MARCH 1993

CONTENTS

	<u>page number</u>
TABLE OF CONTENTS	2
ACKNOWLEDGEMENT	6
DECLARATION	7
ABSTRACT	8
NOMENCLATURE	9
1 INTRODUCTION	
1.1 The use of orifice in flowmetering	11
1.2 Basic principle of operation	11
1.3 Square edge orifice	12
1.3.1 Experimental studies	13
1.3.2 Theoretical studies	14
1.4 Conical entrance orifice plates	18
1.4.1 Review of literature	18
1.5 Objectives of the study	22
2 OUTLINE OF THEORY	
2.1 The basic equations	25
2.1.1 Time-averaged Navier-Stokes equation	26
2.2 Turbulence models	28
2.2.1 The standard k- ϵ turbulence model	28
2.3 Low Reynolds number k- ϵ model	30
2.3.1 The Lam and Bremhorst's k- ϵ model	32
2.4 Selection of the model used in the investigation	34 (a)

	<u>page</u> <u>number</u>
3 SOLUTION PROCEDURE	
3.1 Introduction	
3.1.1 The general conservation equation	35
3.1.2 The "PHOENICS" computer code	37
3.2 The finite-domain equations	39
3.2.1 The finite-domain grid	39
3.2.2 Derivation of the finite-domain equation	41
3.2.3 General form of the finite-domain equation	44
3.2.4 Momentum equations	45
3.2.5 Pressure and velocity correction equations	45
3.3 Solution procedure	49
4 DEVELOPMENT OF A MODEL FOR CONICAL ENTRANCE ORIFICE PLATE FLOW SENSOR	
4.1 Introduction	51
4.2 Incorporating the Lam-Bremhorst $k-\epsilon$ model into the computer program	52
4.2.1 Modification to subroutine 'GROUND'	52
4.3 Modelling of flow through a conical entrance orifice plate	58
4.3.1 Geometry	58
4.3.2 Grid distribution	62
4.3.3 Boundary conditions	64
4.3.4 Auxiliary information	66
4.4 Tests on the conical entrance orifice plates	69
4.4.1 General information on the test cases	70
4.4.2 Tests on the $\beta = 0.1$ conical entrance orifice plates	74

	<u>page</u> <u>number</u>
4.4.3 Tests on the $\beta = 0.2$ conical entrance orifice plates	81
4.4.4 Tests on the $\beta = 0.3$ conical entrance orifice plates	88
4.4.5 Concluding remarks on the tests	95
5 APPLICATIONS OF THE MODEL	
5.1 Introduction	98
5.2 Effect of Reynolds number on the dis- charge coefficient	
5.2.1 Computed discharge coefficients	98
5.2.2 Comparison with experimental re- sults	104
5.2.3 Comparison with values given in British Standard	109
5.3 Pressure profile and flow pattern through the conical entrance orifice plate	
5.3.1 Variation of wall pressure along pipe	112
5.3.2 Flow pattern through the orifice	141
5.3.3 Recirculation zone downstream of the conical entrance orifice plate	154
5.4 Effect of turbulence intensity and length scale factor	169
5.5 Effects of geometric tolerances on conical entrance orifice plate	171
5.5.1 Effect of variation in the thick- ness of the conical entrance	175
5.5.2 Effect of variation in the axial length of the parallel bore	180
5.5.3 Effect of variation in the angle of the conical entrance	185

	<u>page</u> <u>number</u>
5.5.4 Concluding remarks	190
6 CONCLUSIONS	
6.1 Introductory remarks	193
6.2 Achievements of the present study	193
6.3 Suggestions for future work	195
REFERENCES	197
APPENDIX A - Modification of subroutine 'GROUND'	210
APPENDIX B - Q1 input file	217

ACKNOWLEDGEMENT

The author wishes to express his sincere thanks to his supervisor Dr. F. Abdullah for his many valuable opinions and assistance during the course of this investigation, and to Professor T.P. Leung for placing the facilities of the Department of Mechanical and Marine Engineering of Hong Kong Polytechnic at his disposal for this investigation.

DECLARATION

I grant powers of discretion to the University Librarian to allow this thesis to be copied in whole or in part without further reference to me. This permission covers only single copies made for study purposes, subject to normal conditions of acknowledgement.

ABSTRACT

This thesis presents a model for conical entrance orifice plate flow sensor and the results of the application of the model.

The model for the conical entrance orifice plate flow sensor was developed using a low Reynolds number $k-\epsilon$ model of turbulence - the Lam and Bremhorst $k-\epsilon$ model, and the 'PHOENICS' computer code. The flow fields modelled were axisymmetric and the geometry of the conical entrance orifice plate is in accordance with that given in BS 1042 : Section 1.2.

A pipe 100 mm in diameter and with water as the working fluid was used in the simulation. Numerical results were obtained with diameter ratios β equal to 0.1, 0.2 and 0.3, and for pipe Reynolds numbers between 80 and 60,000. The model predicted the discharge coefficient to within $\pm 3\%$ of the value stated in the British Standard for the range of β ratios and Reynolds numbers investigated, which suggest that the conical entrance orifice plate can be used at Reynolds numbers higher than that specified in BS 1042 : Section 1.2 : 1989 for the smaller β ratios.

The model also suggested that the discharge coefficient is a function of β ; that pressure tappings other than corner tappings can be used and the conical entrance orifice was relatively insensitive to turbulence level upstream at the pipe inlet. The effects of geometric tolerances were explored and the results indicated that some latitude on the geometric tolerances as specified in the Standard may be allowed.

NOMENCLATURE

A	Area of a control volume face
a	Discretization coefficient
A_μ, A_t, A_{c1}	Turbulence model constants
C_D	Discharge coefficient
C_1, C_2, C_μ	Turbulence model constants
d	Diameter of orifice
D	Diameter of pipe
f_1, f_2, f_μ	Turbulence model functions
k	Kinetic energy of turbulence
p	Pressure
Re_D	Reynolds number in pipe flow based on bulk velocity and pipe diameter
R_k, R_t	Turbulence Reynolds number
S_ϕ	Source term for variable ϕ
u_i, u_j, u_k	Tensor notation for velocities in the i, j and k directions respectively
u, v	Velocity component in x and y direction
V_r	Radial velocity
V_z	Axial velocity
x_i, x_j, x_k	Tensor notation for space coordinates

Greek symbols

β	Orifice to pipe diameter ratio $(\beta = \frac{d}{D})$
---------	---

Γ_ϕ	Exchange coefficient for variable ϕ
ϵ	Rate of dissipation of turbulence energy
μ	Viscosity
ν	Kinematic viscosity
ρ	Density of fluid
ϕ	A generalised dependent variable
σ_k	Diffusion Prandtl number for turbulence energy k
σ_ϵ	Diffusion Prandtl number for dissipation rate ϵ

Subscripts

t	Turbulent
l	Laminar
E, N, P, S, W	Grid points
e, n, s, w	Control volume faces
nb	Neighbouring grid point

(other notations are dealt with as they arise)

CHAPTER 1

INTRODUCTION

1.1 The use of orifice in flowmetering

For many years, differential pressure meters were available for measuring flowrate of fluids in a pipe with reasonable accuracy at a reasonable cost. In spite of technological progress and innovation over the last few decades, many requirements for flow metering are still adequately met by differential pressure meters. It has been estimated that differential pressure devices still hold 50% of the market (1), and will continue to contribute to the major share of flowmeter sales. Of the pressure differential devices, the orifice plate is the most popular. The wide popularity of the orifice plate is due to the ease of construction, absence of need for calibration unless high precision is required, installation simplicity and its ability to handle some of the difficult applications.

1.2 Basic principle of operation

The basic principle of operation of the meter depends upon the fact that when a fluid flows through a contraction, it must accelerate; this causes its kinetic energy to increase, and consequently, its pressure must fall by a corresponding amount in accordance with the principle of the conservation of energy. The ideal flowrate may be related to the pressure drop by applying

the Continuity and Bernoulli equations (2). Then empirical correction factors may be applied to obtain the actual flowrate.

For an incompressible fluid, the mass rate of flow Q_m is given by

$$Q_m = C_D \frac{A_{ori}}{\sqrt{1 - \left(\frac{A_{ori}}{A_{pipe}}\right)^2}} \sqrt{2 \rho \Delta p} \quad (1.1)$$

where A_{pipe} is the cross sectional area of the pipe, A_{ori} is the orifice hole area, ρ is the density of fluid, Δp is the pressure difference across the orifice and C_D is called the discharge coefficient.

1.3 Square edge orifice

Although the orifice has achieved widespread popularity only in the last 100 years or so, records indicate that it was used by the Romans for regulating the flow of water to householders. Just when and where a thin plate orifice was first used in the measurement of fluids, particularly for sales purposes, has not been definitely determined, but it was probably before 1890 (3). It was after this period that the importance of orifice as a means of measuring volumes of gas and liquids for sale, and for the control of flow rates in continuous industrial processes, has become better known

and exploited.

1.3.1 Experimental studies

In 1903, Weymouth (4) started experimenting with a thin-plate sharp-edged concentric orifice, using Flange Taps for measuring the differential pressure. In 1915, Hickstein (5) published data similar to Weymouth's but based on the use of pressure connections at 2.5 pipe diameters upstream and 8 pipe diameters downstream of the orifice. In 1916, Judd (6) proposed the use of vena contracta taps, and also referred, for the first time, to the design of eccentric and segmental orifices. Meanwhile, Hodgson (7,8) developed many types of orifices over the period 1909-1924 and established a whole range of coefficient curves for various values of diameter ratio and for a wide range of Reynolds numbers.

First attempt at collecting and organizing the available data into a commercially usable form was begun in 1915 by the then newly formed American Society of Mechanical Engineers (ASME) Flow Meters Committee. Until 1931, the ASME and the American Gas Association (AGA) accumulated and assimilated data for orifice meters independently. In December of that year, the Joint AGA-ASME Orifice Coefficient Committee was formed. The eventual outcome of this effort was a 1928-1932 Joint ASME-AGA Program at Ohio State University to determine the absolute values of orifice discharge coefficients.

Following these tests, a long series of similar projects was undertaken, and the results appeared in a series of releases and revisions that continues to the present time.

1.3.2 Theoretical studies

With the advent of computers, efforts to model orifice flow begun. Mills (9) obtained numerical solutions of the Navier-Stokes equations for axi-symmetric, viscous, incompressible flow through a square edged orifice in a circular pipe for Reynolds numbers (based on orifice diameter) up to 50, and fixed diameter ratio $\beta = 0.5$. The discharge coefficients calculated showed good agreement with the values obtained experimentally by Johansen (10) even though there was not a complete similarity in regard to orifice geometry and location of pressure tappings. Keith (11,12) extended the work of Mills to other β ratio (0.3, 0.5 and 0.7). Mattingly and Davis (13) obtained numerical results for laminar flow through square edged orifice for Reynolds numbers (based on pipe radius) of 10 and 25, and β ratio from 0.3 to 0.7. The effects of orifice plate thickness on the discharge coefficient was also investigated. The discharge coefficients calculated were compared with the experimental values presented by Johansen (10) and Tuve and Sprenkle (14), and Mills' result, and close agreement was noted. Nigro et al. (15) considered three geometries of orifice plate, namely that of the square edge orifice

plate, the "thin" orifice plate and the bevelled edge orifice plate. Solutions were presented for Reynolds numbers (based on orifice diameter) up to 1,000 for a range of orifice to pipe diameter ratios from 0.2 to 0.8. They concluded that orifice geometry played a significant role in the flow structure in the vicinity of the orifice and as such would affect the calculated discharge coefficient. The numerical results were also compared with the experimental results compiled by Tuve and Sprenkle for a half-bevelled orifice plate.

With the development of the $k-\epsilon$ two-equation model of turbulence at Imperial College, London, various workers (16,17,18) used the model to study turbulent flow through orifice, as the model is in wide use and has been successfully tested against recirculating flows similar to those encountered downstream of an orifice plate.

Davis and Mattingly (16) modeled the flow through infinitely thin orifice plates with β ratios from 0.4 to 0.7. Reynolds numbers (based on pipe radius) studied were in the approximate range $10^4 - 10^6$. The numerical results were obtained using 13 grids in the radial direction and up to 68 grids in the axial direction. The results were compared with available experimental data, and the agreement between computed and experimental discharge coefficient was within 4%.

Hafiz (17) used the same model to investigate flow through square-edged orifice plates with β ratios from 0.3 to 0.7 and for Reynolds numbers (based on orifice diameter) of 10^5 , 2.5×10^5 and 10^6 . The numerical results were obtained using a 32×22 (axial and radial) grid. The results for the lower Reynolds numbers showed that the discharge coefficients were predicted to within $\pm 3\%$ of experiment; while for a Reynolds number of 10^6 , the difference was about $+5\%$ for the discharge coefficient corresponding to the flange tapping. The variation of discharge coefficient with orifice plate thickness was also investigated, and the results showed an increase of discharge coefficient with plate thickness. When the plate became thinner, the discharge coefficient became asymptotically constant.

Patel and Sheikholeslami (18) simulated an orifice plate with a β ratio of 0.4 at an orifice-diameter Reynolds number of 10^6 . The grids used were 80×60 (axial and radial). The numerical results enabled the computation of the discharge coefficient to within 1.5% of standard values. Computations of the discharge coefficient at different Reynolds numbers showed that the coefficient decreases with increasing Reynolds numbers.

The $k-\epsilon$ two-equation model of turbulence had also been used by various workers in investigating the influence of geometric effects (upstream step, plate

buckling, pipe roughness), and the effect of rough pipework on the discharge coefficients of orifice plates.

Langsholt and Thomassen (19) modelled the flow through a square edged orifice meter with artificially introduced geometric effects (upstream step, plate buckling, pipe roughness). Depending on the geometric effects introduced, the β ratios of the orifice plates used in the modelling were 0.3, 0.5 and 0.6, and the Reynolds numbers used were 1.7×10^5 and 2.0×10^6 . The grids used were 48×19 (axial and radial) for the majority of the results presented. The results were compared with available experimental data, and the conclusion was that relative changes in the flow coefficient due to a geometrical alteration was simulated in an apparently correct manner, although there was a lack in absolute accuracy in the simulated flow coefficient.

Reader-Harris (20) examined the effect of rough pipework on the discharge coefficients of orifice plates. An orifice plate of zero thickness was specified, and the β ratios ranged from 0.5 to 0.8. The computational test section contained 40 grid points in the axial direction and 25 in the radial direction. In all cases the Reynolds number based on pipe diameter and mean velocity was 4×10^5 . The change in discharge coefficient due to roughness was shown to be approximately proportional to β^4 .

1.4 Conical entrance orifice plates

The square edged or standard orifice plate has been extensively studied. At high Reynolds numbers, the coefficient of discharge is well-established to be nearly constant. However, at low Reynolds numbers, appreciable variation in the value of this coefficient has been observed (10,14). Therefore, the use of the standard forms of orifice plates for the metering of high viscosity fluids such as oil are unsatisfactory. In view of the industrial importance of metering such liquids, there is a considerable interest among differential pressure flowmeter users in any device which has a constant discharge coefficient in the low Reynolds number region. Special forms of orifices have been developed. The conical entrance orifice plates and quarter circle orifice plates are given in BS 1042 as having a constant discharge coefficient down to a low Reynolds number, thus making it suitable for the measurement of flowrate of viscous fluids such as oil. Conical entrance orifice plates have the further property that their discharge coefficient is the same at any diameter ratio (within the limits specified by the standard). The conical entrance orifice plate is illustrated in Figure (1.1).

1.4.1 Review of literature

The conical entrance orifice plate was first developed in 1930 by H.E. Dall of George Kent Ltd. as the Kent P.L. orifice. Some data on the P.L. orifice is

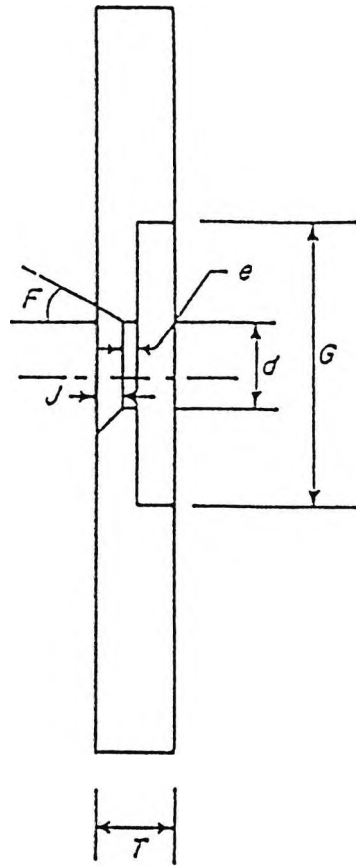


Fig. 1.1 Conical Entrance Orifice Plate

available from its U.S. patent specifications (21), and Linford (22) based on Dall's work, gave characteristic curves showing the variations of discharge coefficient with change of Reynolds number. The data on the conical entrance orifice plate given in BS 1042: Part 1: 1964 is based on information from George Kent Ltd.

Since the publication of BS 1042: Part 1: 1964, the characteristics of conical entrance orifice plates have been explored by a number of investigators. Kastner and McVeigh (23) investigated orifice plate profiles for low Reynolds numbers. They conducted tests on a number of orifice plates and eight of these are of the conical entrance type. The eight plates were tested using a 50 mm (2 inches) internal diameter brass pipe with β value ranges from 0.063 to 0.3. Stoll and Zientara (24) reported work by three fluid metering companies using a 50 mm (2 inches) diameter pipe and 5 conical entrance orifice plates having β values of 0.1 to 0.5. They described the testing program and listed all of the data accumulated.

The effect of installation conditions on the discharge coefficient of the conical entrance orifice plates was investigated by McVeigh (25). He conducted tests using a 38.1mm (1.5 inches) diameter copper pipe and orifice plates having a diameter ratio of 0.267, 0.4 and 0.5. The upstream straight pipe length was varied,

and 90° bends were placed before the orifice.

Turton (26) also published results on tests carried out on conical entrance orifice plates having diameter ratios of 0.1 to 0.5, using a 50 mm diameter copper pipe.

Additional information on the performance characteristics of conical entrance orifice plates are provided by Ho and Leung (27). They tested plates with diameter ratios of 0.247, 0.360 and 0.448 using a 25 mm diameter pipe. The orifices were tested both in the concentric and eccentric position.

The British Standard (28) for conical entrance orifice plates specifies a constant conic entrance angle of 45° and a constant value of 0.084 for the ratio J/d (fig. 1.1). It is limited to $0.1 \leq \beta \leq 0.316$. For the Kent P.L. plates, both the conic entrance angle and depth of bevel J vary with β . At low values of β , the Kent P.L. plate is similar to that specified by BS 1042. The differences between the two plates increase with β . At $\beta = 0.3$, the difference in conical entrance angle is about 6% and the difference in J/d is about 12%.

The work reported by Stoll and Zientara (24) and McVeigh (25) was on plates similar to the Kent P.L. plates. Only the work by Kastner and McVeigh (23), Turton (26) and Ho and Leung (27) was based on plates as

specified in BS 1042. Kastner and McVeigh conducted tests for pipe Reynolds numbers below 1,200 for six of the plates and below 4,000 for the remaining two plates. Turton performed tests over a range of pipe Reynolds numbers of 800 to 23,000 while Ho and Leung tested the orifices for the pipe Reynolds numbers in the region of 100 to about 1,000.

In the above investigations, the differential pressure across the orifices was measured by means of corner tapings or are not reported. The investigators were of the opinion that observance of the dimensional tolerance associated with the conical entrance orifice plate was time consuming and difficult especially for the smaller diameter plates (23,24,26,27). Many of the results reported were on plates that do not meet the dimensional tolerances specified in the Standard.

1.5 Objectives of the study

As can be seen from the literature review, relatively few experimental results were available in the performance characteristics of conical entrance orifice plates. No information is available on the use of pressure tapings other than corner tapings. BS 1042 specifies dimensional tolerances which were found difficult to satisfy especially for the smaller diameter plates. Thus, there is a need to further explore the characteristics of conical entrance orifice plates.

The performance of flowmeters are affected by a number of parameters, and for each of the parameters, there is a wide range of values encountered in practice. Therefore, laboratory experiments for all situations are practically impossible. However, widely ranging parameters can be introduced and evaluated using computer methods, and, for selected cases, validation experiments would demonstrate credibility. Thus, the number of experimental investigations can be reduced.

In the last two decades, significant progress has been made in the development of computational fluid dynamics (CFD) techniques. These developments, and continually increasing ease and economy of digital computers, are now making numerical flow simulation a valuable tool in the development of various engineering equipment. The progress of CFD has also aided the developments of models of turbulence. Various turbulence models have been developed and tested in details, and some have been found satisfactory for engineering analysis purposes. As a result, computer simulation using a suitable turbulence model can be extremely useful in conjunction with experiments in the investigations of the performance of various types of flowmeters.

Hence, the performance characteristics of conical entrance orifice plates are investigated using existing turbulence models. The effects of the Reynolds number and

the variation in dimensional tolerance on the discharge coefficient are studied. Computations were performed with the aid of a general - purpose, flow - analysis computer code, "PHOENICS". It is hoped that this investigation will provide more information on the performance characteristics of conical entrance orifice plates and to identify areas where further experimental investigations might be needed. This will ultimately lead to the better utilization of the conical entrance orifice plates as a low Reynolds number flow measuring device.

CHAPTER 2

OUTLINE OF THEORY

2.1 The basic equations

In order to model fluid flow processes, it is necessary to consider the general physical laws that describe the fluid dynamics of the flow. These physical laws include the conservation of mass and momentum.

The equations of motion, in the absence of external forces, can be written in the following tensorial form for Newtonian fluids.

Continuity

$$\frac{\partial \rho}{\partial t} + \frac{\partial \rho u_i}{\partial x_i} = 0 \quad (2.1)$$

Momentum

$$\rho \left(\frac{\partial u_i}{\partial t} + u_j \frac{\partial u_i}{\partial x_j} \right) = - \frac{\partial p}{\partial x_i} + \frac{\partial}{\partial x_j} \left\{ \mu \left(\frac{\partial u_i}{\partial x_j} + \frac{\partial u_j}{\partial x_i} \right) - \frac{2}{3} \mu \delta_{ij} \frac{\partial u_k}{\partial x_k} \right\} \quad (2.2)$$

where the Kronecker delta $\delta_{ij} = 0$ for $i \neq j$ and $\delta_{ij} = 1$ for $i = j$.

Equation (2.2) is usually called the Navier-Stokes equation of motion. The derivation of equations (2.1) and (2.2) can be found in a variety of books on fluid dynamics (29,30).

2.1.1 Time - averaged Navier-Stokes equation

The Navier-Stokes equations apply equally to turbulent or laminar flows if actual velocities, etc., are used. Because of the complexity and apparently random nature of the velocity fluctuations in turbulent flow, overwhelming difficulties are involved in undertaking a complete analysis involving the instantaneous turbulent fluctuations. As it is futile to deal with actual velocities and other fluctuating quantities in turbulent flow, the development of equations to describe turbulent flows for applied problems is accomplished by time averaging the turbulent fluctuations about a mean flow field (31).

Thus, assuming that all the flow variables can be expanded in the form $f = \bar{f} + f'$ where \bar{f} is a mean value of f and f' is a fluctuation about the mean, the instantaneous velocity U_i and pressure p_i can be written as

$$u_i = \bar{u}_i + u_i' \quad (2.3)$$

$$\bar{u}_i = \frac{1}{t_1} \int_{t_0}^{t_0+t_1} u_i dt \quad (2.4)$$

$$\frac{1}{t_1} \int_{t_0}^{t_0+t_1} u_i' dt = \bar{u}_i' = 0 \quad (2.5)$$

$$p_i = \bar{p}_i + p_i' \quad (2.6)$$

$$\bar{p}_i = \frac{1}{t_1} \int_{t_0}^{t_0+t_1} p_i dt \quad (2.7)$$

$$\frac{1}{t_1} \int_{t_0}^{t_0+t_1} p_i' dt = \overline{p_i'} = 0 \quad (2.8)$$

The mean values are taken over a sufficiently long interval of time, t_1 , for them to be completely independent of time.

By introducing these mean and fluctuating components into equations (2.1) and (2.2), the following equations are obtained for steady incompressible flow with body forces neglected.

Continuity

$$\frac{\partial \bar{u}_i}{\partial x_j} = 0 \quad (2.9)$$

Momentum

$$\frac{\partial}{\partial x_j} (\rho \bar{u}_i \bar{u}_j) = -\frac{\partial \bar{p}}{\partial x_i} + \frac{\partial}{\partial x_j} \left[\mu \left(\frac{\partial \bar{u}_i}{\partial x_j} + \frac{\partial \bar{u}_j}{\partial x_i} \right) - \rho \overline{u_i' u_j'} \right] \quad (2.10)$$

Equation (2.10) is the time-averaged Navier-Stokes equation or the Reynolds equation. The quantity $-\rho \overline{u_i' u_j'}$ is commonly called the Reynolds stresses of turbulent flow, and represents the transfer of momentum by the turbulent motion.

The Reynolds equations cannot be solved in the form given because the new apparent turbulent stresses or Reynolds stresses must be regarded as new unknowns. To proceed further, it is necessary to find additional equations involving the new unknowns or make assumptions regarding the relationship between the new apparent turbulent quantities and the time-mean flow variables. This is known as the closure problem and is most commonly tackled through turbulence modelling.

2.2 Turbulence models

The turbulence models can be classified in several ways. The one most often used is that in accordance with the number of differential equations solved in addition to the mean flow equations. The turbulence model which appears to be most widely used for engineering calculations are the two equations k - ϵ model.

2.2.1 The standard k - ϵ turbulence model

The k - ϵ model of turbulence was first put forward by Harlow and Nakayama (32) in 1968, and has appeared in the papers of Jones and Launder (33,34) and Launder et al. (35). A full account of the model is given by Launder and Spalding (36).

In this model, the Reynolds stresses are calculated using the Boussinesq eddy viscosity hypothesis and may be written as :

$$-\rho \overline{u'_i u'_j} = \mu_t \left(\frac{\partial \bar{u}_i}{\partial x_j} + \frac{\partial \bar{u}_j}{\partial x_i} \right) - \frac{2}{3} \rho \delta_{ij} k$$

where μ_t is a turbulent viscosity, k is the turbulent kinetic energy $\frac{1}{2} \overline{u'_i u'_i}$, and δ_{ij} is the Kronecker delta. The turbulent viscosity μ_t is specified by

$$\begin{aligned} \mu_t &= C_\mu \rho k^{1/2} L_\epsilon \\ &= C_\mu \rho k^2 / \epsilon \end{aligned} \quad (2.12)$$

where C_μ is a constant, k is the turbulent kinetic energy, and L_ϵ is the length scale related to ϵ , the rate of energy dissipation by viscosity. L_ϵ is typical of the size of the eddies in the energy transfer range.

Thus, two unknowns, k and ϵ are introduced which require two equations for closure. Exact equations expressing transport of k and ϵ can be derived from the Navier-Stokes equations and modelled forms of these may be expressed as follows (36):

a) Kinetic energy equation

$$\begin{aligned} \frac{Dk}{Dt} &= \frac{1}{\rho} \frac{\partial}{\partial x_k} \left[(\mu + \frac{\mu_t}{\sigma_k}) \frac{\partial k}{\partial x_k} \right] + \frac{\mu_t}{\rho} \frac{\partial \bar{u}_i}{\partial x_k} \left[\frac{\partial \bar{u}_i}{\partial x_k} + \frac{\partial \bar{u}_k}{\partial x_i} \right] \\ &\quad - \epsilon \end{aligned} \quad (2.13)$$

b) Kinetic energy dissipation rate equation

$$\begin{aligned} \frac{D\varepsilon}{Dt} = & \frac{1}{\rho} \frac{\partial}{\partial x_k} \left[\left(\mu + \frac{\mu_t}{\sigma_\varepsilon} \right) \frac{\partial \varepsilon}{\partial x_k} \right] \\ & + \frac{C_1 \mu_t}{\rho} \frac{\varepsilon}{K} \frac{\partial \bar{u}_i}{\partial x_k} \left[\frac{\partial \bar{u}_i}{\partial x_k} + \frac{\partial \bar{u}_k}{\partial x_i} \right] - C_2 \frac{\varepsilon^2}{K} \end{aligned} \quad (2.14)$$

In equation (2.12), (2.13) and (2.14), it is assumed that C_1 , C_2 , C_μ , σ_ε , σ_k are constants, and have the following values as given by Launder et al. (35) and Launder and Spalding (36):

$$C_\mu = 0.09 \quad C_1 = 1.44 \quad C_2 = 1.92 \quad \sigma_k = 1.0 \quad \sigma_\varepsilon = 1.3$$

The closed set of equations with this set of parameters has come to be known as the standard k - ε model for high Reynolds number flows.

The standard k - ε model has been applied in the studies of such diverse flow situations as flow over a backward facing step (37), flow in a sudden pipe expansion (38), flow in diffusers (39), and flow over a square obstacle (40). In general, the comparisons between calculations and experiments is considered to be satisfactory. Thus, the standard k - ε model is widely used in engineering calculations.

2.3 Low Reynolds number k - ε model

The standard k - ε model is derived by assuming high Reynolds number condition (41). During the past few years, many attempts were made for extending the turbu-

lence closure models to enable them to be used at low Reynolds numbers condition.

Most of the low Reynolds number models proposed make use of either a wall damping effect and/or a direct effect of molecular viscosity on the constants and functions of the turbulence-transport equations originally used for high Reynolds number condition. As there is a lack of reliable turbulence data at low Reynolds numbers, these modifications were largely based on numerical experiments and comparisons between calculations and experiments in terms of global parameters.

Patel et al. (42) evaluated in detail eight low Reynolds number turbulence models, namely those of Chien (43), Dutoya and Michard (44), Hassid and Poreh (45), Hoffmann (46), Lam and Bremhorst (47), Launder and Sharma (48), Reynolds (49), and Wilcox and Rubesin (50). The first seven models are based on the standard $k-\epsilon$ model. The different models were evaluated in the light of available physical and experimental evidence. Patel et al. showed that most modifications to the basic high Reynolds number model do not have a sound physical basis. The models of Hassid-Poreh, Hoffmann, Dutoya-Michard, and Reynolds failed to reproduce results of even the simplest test case, that of the flat-plate boundary layer.

After an overall evaluation of the results obtained

for all the test cases, Patel et al concluded that the models of Launder and Sharma, Chien, and Lam and Bremhorst, which are based on the modification of the standard k- ϵ model, and that of Wilcox and Rubesin produce comparable results and their performance are considerably better than other models.

Of these models, only the one by Lam and Bremhorst is of a form similar to the standard k- ϵ model of Launder and Spalding. The other models require the introduction of extra terms in the transport equations for k and ϵ , and are thus more complicated than the Lam and Bremhorst model.

2.3.1 The Lam and Bremhorst's k- ϵ model

Lam and Bremhorst (47) proposed that the turbulence kinetic energy k and the dissipation rate of turbulence energy ϵ can be determined from the following transport equations:

$$\frac{Dk}{Dt} = \frac{\partial}{\partial x_j} \left[\left(\frac{\nu_t}{\sigma_k} + \nu_l \right) \frac{\partial k}{\partial x_j} \right] + \nu_t \left[\frac{\partial u_i}{\partial x_j} + \frac{\partial u_j}{\partial x_i} \right] \frac{\partial u_i}{\partial x_j} - \epsilon \quad (2.15)$$

$$\begin{aligned} \frac{D\epsilon}{Dt} = \frac{\partial}{\partial x_j} \left[\left(\frac{\nu_t}{\sigma_\epsilon} + \nu_l \right) \frac{\partial \epsilon}{\partial x_j} \right] + C_1 f_1 \nu_t \frac{\epsilon}{k} \left(\frac{\partial u_i}{\partial x_j} + \frac{\partial u_j}{\partial x_i} \right) \frac{\partial u_i}{\partial x_j} \\ - C_2 f_2 \frac{\epsilon^2}{k} \end{aligned} \quad (2.16)$$

and the turbulent viscosity given by

$$\nu_t = c_\mu f_\mu k^2 / \epsilon \quad (2.17)$$

where $\sigma_k = 1.0$, $\sigma_\epsilon = 1.3$, $c_1 = 1.44$, $c_2 = 1.92$ and $c_\mu = 0.09$, same as that given by Launder and Spalding.

In the above equations, the functions f_μ , f_1 and f_2 are introduced to account for the low Reynolds number and wall-proximity effects. When the f 's are all assumed to be equal to one, the above equations are similar in form to the standard $k-\epsilon$ model of Launder and Spalding.

i) the function f_μ

Function f_μ in equation (2.17) is introduced to account for the effect of molecular viscosity on the shear stress (42). In regions near a wall where viscous effects become important, f_μ will differ considerably from unity. Jones and Launder (33, 34) proposed a formula for f_μ that made it a unique function of the turbulence Reynolds number R_t ($R_t = \frac{k^2}{\nu \epsilon}$). In this formulation, f_μ is affected only indirectly by the presence of a wall through R_t .

Lam and Bremhorst argued that the presence of a wall should have a direct influence, and they postulated that

$$f_{\mu} = (1 - e^{-A_{\mu} R_k})^2 \left(1 + \frac{A_t}{R_t}\right) \quad (2.18)$$

where $R_k = \frac{k^2 y}{\nu_t}$ is a turbulence Reynolds number, and A_{μ} and A_t are constants; the y in R_k is the normal distance from the nearest wall. This renders f_{μ} a function of both R_k and R_t . Also, ν_t is proportional to y^4 near the wall, in agreement with the mixing length formula of Van Driest. The presence of a wall now has a direct and indirect influence on f_{μ} . The values of the constants A_{μ} and A_t , determined by trial and error, have the following values:

$$A_{\mu} = 0.0165 \quad A_t = 20.5$$

ii) the function f_1

The function f_1 is introduced to increase the ϵ -production near the wall. Remote from a wall, f_1 is approximately unity. In the near wall region, it is found that f_1 has to assume larger values. This has the effect of increasing the dissipation rate, and results in a lower peak of k to match available experimental data. Lam and Bremhorst proposed that

$$f_1 = 1 + \left(\frac{A_{c1}}{f_{\mu}}\right)^3 \quad (2.19)$$

The constant A_{c1} is given a small value so that remote from a wall and when the turbulence level is high, f_{μ} and hence f_1 will be approximately unity. Close to a wall, f_{μ} will be small and f_1 will become large. The value of the

constant A_{c1} is taken to be 0.05, and is determined by trial and error.

iii) the function f_2

Function f_2 is introduced to simulate the change in the decay rate of homogeneous turbulence as the Reynolds number R_t becomes small. It was chosen so that the model, when applied to the calculation of the decay of isotropic grid turbulence, accorded with experiment for both high and low turbulence intensities. Lam and Bremhorst assumed that

$$f_2 = 1 - e^{-R_t^2} \quad (2.20)$$

2.4 Selection of the model used in the investigation

Lam and Bremhorst (47) tested their model by application to fully developed turbulent pipe flow. Satisfactory predictions have been obtained with the model and agreement with available experimental data is found to be good. Patel et al. (42) evaluated eight low Reynolds number turbulence models, and concluded that the Lam and Bremhorst model, along with the models of Launder and Sharma, Chien, and Wilcox and Rubesin produce comparable results in the test cases chosen and their performance are considerably better than other models.

The Lam and Bremhorst model is also simpler than

other models. It is similar in form to the standard k- ϵ model of Launder and Spalding. Thus, existing computer codes that use the standard k- ϵ model can be easily modified to implement the Lam and Bremhorst model. Therefore, this model is selected in the investigation of the performance of conical entrance orifice plate, which is essentially used at low Reynolds number condition.

CHAPTER 3

SOLUTION PROCEDURE

3.1 Introduction

3.1.1 The general conservation equation

The differential equations which describe turbulent flows were presented in chapter 2. For steady axisymmetric flow through a pipe, the general form of these conservation equations governing the transport of mass, momentum, turbulence kinetic energy and its dissipation rate can be written in cylindrical coordinates (z, r) as

$$\frac{1}{r} \frac{\partial}{\partial r} (\rho r V_r \phi) + \frac{\partial}{\partial z} (\rho V_z \phi) = \frac{1}{r} \frac{\partial}{\partial r} (\Gamma_\phi r \frac{\partial \phi}{\partial r}) + \frac{\partial}{\partial z} (\Gamma_\phi \frac{\partial \phi}{\partial z}) + S_\phi \quad (3.1)$$

In the above equation, ϕ stands for a general variable, namely, V_r the radial velocity, V_z the axial velocity, k the turbulent kinetic energy, and ϵ , its dissipation rate. The equation for $\phi = 1$ is the conservation of mass equation. The corresponding values of Γ_ϕ and S_ϕ are given in table 3.1.

The differential equations represented by equation (3.1) and table (3.1) were solved by means of the "PHOENICS" computer code. The version of "PHOENICS" used is version 1.3. This computer code embodies a finite-domain formulation of the differential equations and a procedure for solving them.

Conservation of	ϕ	Γ_ϕ	S_ϕ
mass	1	0	0
axial momentum	V_z	μ_{eff}	$\frac{\partial}{\partial z}(\mu_{\text{eff}} \frac{\partial V_z}{\partial z}) + \frac{1}{r} \frac{\partial}{\partial r}(\mu_{\text{eff}} r \frac{\partial V_r}{\partial z}) - \frac{\partial p}{\partial z}$
radial momentum	V_r	μ_{eff}	$\frac{\partial}{\partial z}(\mu_{\text{eff}} \frac{\partial V_z}{\partial r}) + \frac{1}{r} \frac{\partial}{\partial r}(\mu_{\text{eff}} r \frac{\partial V_r}{\partial r}) - \frac{2 \mu_{\text{eff}} V_r}{r^2} - \frac{\partial p}{\partial r}$
kinetic energy	K	$\mu + \frac{\mu_t}{\sigma_K}$	$G_K - \rho \epsilon$
dissipation rate	ϵ	$\mu + \frac{\mu_t}{\sigma_\epsilon}$	$\frac{\epsilon}{K} (f_1 C_1 G_K - f_2 C_2 \rho \epsilon)$

$$G_K = \mu_t \left\{ 2 \left[\left(\frac{\partial V_r}{\partial r} \right)^2 + \left(\frac{\partial V_z}{\partial z} \right)^2 + \left(\frac{V_r}{r} \right)^2 \right] + \left(\frac{\partial V_r}{\partial z} + \frac{\partial V_z}{\partial r} \right)^2 \right\}$$

$$= \mu_t G$$

$$\mu_{\text{eff}} = \mu + \mu_t$$

Table 3.1 Exchange coefficients Γ_ϕ and source terms S_ϕ for any general property ϕ

The calculation procedure was derived from the work of Patankar and Spalding (51), and has also been reported by Caretto et al. (52) and Patankar (53,54,55). The "PHOENICS" computer code has been described by Spalding (56). Information were also given in technical reports published by CHAM Limited of London (57,58). Thus, the "PHOENICS" computer code will only be briefly described here.

3.1.2 The "PHOENICS" computer code

"PHOENICS" is a general purpose computer code for the simulation of fluid flow, heat transfer, chemical reaction and related phenomena, and was developed by CHAM Limited of London.

It comprises of two distinct computer programs. The smaller one is called the 'SATELLITE', and the larger one 'EARTH'. The 'SATELLITE' is a data-preparation program. In order to simulate a physical phenomenon, the problem-specific information is expressed in 'PHOENICS Input Language' and turned into commands which are contained in a 'quick-input' file, Q1. The 'SATELLITE' reads the Q1 file and converts the problem-specific information into a data file for transmission to 'EARTH'. All information as to what is to be simulated is supplied to 'EARTH' through the use of the Q1 file.

The 'EARTH' program is the code that actually

performs the simulation. It can be regarded as a general purpose partial-differential-equation solver. It contains sequences for computer memory storage allocation, formulation and solution of the finite domain equations, output of results etc. 'EARTH' contains a subroutine 'GREX1' which has been created to provide fluid property, boundary condition and other commonly required features for 'EARTH' to carry out its flow simulating function.

As the variety of actual fluid flow, heat transfer and chemical reaction phenomena that 'EARTH' may be called upon to simulate is virtually unlimited, there is a need to be able to extend the capabilities of 'EARTH' as the case may be. 'EARTH' contains a Fortran subroutine called 'GROUND'. 'GROUND' is a mere empty shell which user may access to insert his own special coding sequences as necessary to suit his own particular need. 'GROUND' is called by 'EARTH' at pre-set points of the solution cycle, and if the user inserts appropriate Fortran statements in the appropriate location of the 'GROUND' subroutine, 'EARTH' absorbs these into the solution process. Thus, the subroutine 'GROUND' may be problem-specific. 'GREX1' can be regarded as an exemplary 'GROUND'.

Besides 'SATELLITE' and 'EARTH', an interactive graphics program, 'PHOTON', is supplied as part of the "PHOENICS" package. 'PHOTON' serves as a post-processor

to display the results of 'EARTH' calculations and can be used to display the grid, the velocity vectors, and contour levels of scalar variables.

3.2 The finite-domain equations

"PHOENICS" employs a finite-domain formulation of the differential equations represented by equation (3.1) and table (3.1). The formulation and the associated solution procedure has been reported by Patankar and Spalding (51), Caretto et al. (52) and Patankar (53,54, 55), and will only be briefly described here.

3.2.1 The finite-domain grid

The whole domain under study is divided into small, discrete regions (called cells) by a set of orthogonally intersecting grid lines. The grid spacing may be non-uniform. Figure (3.1) shows a typical control cell.

Within each cell is a typical point P (called a grid node) formed by the intersection of the grid lines. The other grid points E, W, N, S are the east, west, north and south neighbours of P. The corresponding faces of the control cell are denoted by e, w, n and s, and are located midway between the nodes.

With the exception of the velocities, all the variables are calculated at the grid nodes. The velocity components are calculated at the faces of the control

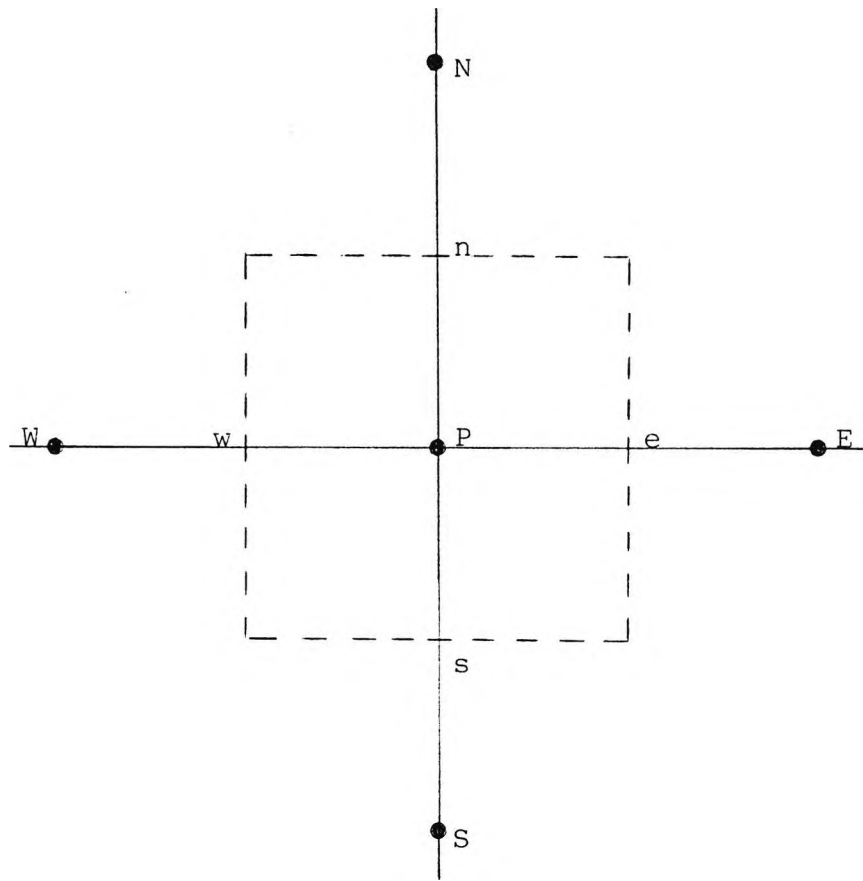


Fig. 3.1 A typical two dimensional cell

cell. This is known as the staggered-grid system. Figure (3.2) shows a staggered grid arrangement. The advantages of the staggered grid arrangement are that the normal velocity components are directly available for the calculation of mass flow rate at the control volume faces, and that the pressure gradients driving the velocities can be calculated conveniently.

3.2.2 Derivation of the finite-domain equation

The finite-domain equations are obtained by integrating the differential equations over the control cells. The treatment for the convection terms, diffusion terms and the source terms will be briefly described.

i) the radial direction convection term

Integration of the convection term in the radial direction over a control volume (with unit angular distance, i.e. one radian) gives

$$\begin{aligned} \bar{I}_{rc} &= \iint_{vol} \frac{1}{r} \frac{\partial}{\partial r} (\rho v_r \phi) r dr dz \\ &= (\rho v_r A)_n \phi_n - (\rho v_r A)_s \phi_s \end{aligned}$$

In the above expression, all fluid properties are assumed to be uniform over cell faces. $(\rho v_r A)_n$ and $(\rho v_r A)_s$ denotes the mass fluxes through the north and south cell faces respectively. ϕ_n and ϕ_s are the values of the variable at the north and south cell faces. A is the area

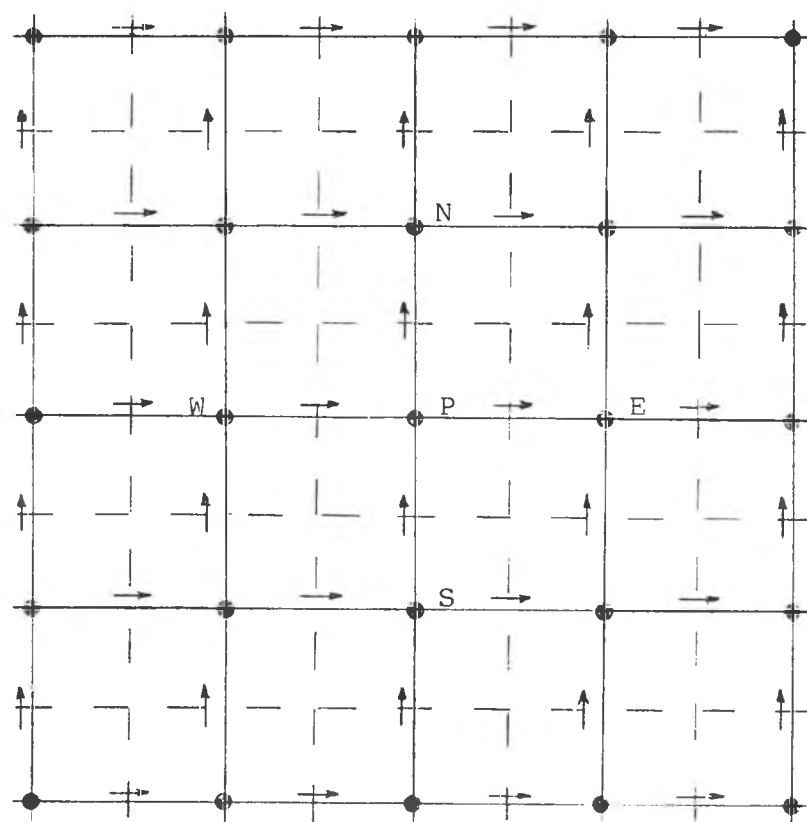


Fig. 3.2 Staggered grid system

of the cell face. With the exception of V_r , the values prevailing at the cell face are those at the nearest grid node on the 'upwind' side of the face.

ii) the axial direction convection term

Similarly, integration of the convection term in the axial direction gives

$$\begin{aligned} I_{zc} &= \iint_{vol} \frac{\partial}{\partial z} (\rho V_z \phi) r dr dz \\ &= (\rho V_z A)_e \phi_e - (\rho V_z A)_w \phi_w \end{aligned}$$

where the subscript e and w stands for the east and west cell faces.

iii) the diffusion terms

The diffusion terms are integrated, similar to the convection terms, over a given control volume. The property gradients $\frac{\partial \phi}{\partial r}$, $\frac{\partial \phi}{\partial z}$ and exchange coefficients Γ_ϕ are taken to be uniform over cell faces. The properties ϕ are assumed to vary linearly, and that the value of the exchange coefficient Γ_ϕ on the cell face is taken to be the arithmetic mean of those on either side of the cell faces in the present study.

Thus the diffusion flux of ϕ across the east face of the control cell is given by

$$\left(\Gamma A \frac{\partial \phi}{\partial z} \right)_e = \left(\frac{\Gamma_E + \Gamma_P}{2} \right) A_e \frac{\phi_E - \phi_P}{\Delta PE}$$

where Δ_{PE} is the distance from grid node P to grid node E.

iv) the source term

The source term S_p is integrated over the control volume and is expressed as a linear function of ϕ_p . Thus,

$$\begin{aligned} I_s &= \iiint_{\text{vol}} S_p r dr dz \\ &= S_1 + S_2 \phi_p \end{aligned}$$

where S_2 is the coefficient of ϕ_p , and S_1 is the part of I_s that does not explicitly depend on ϕ_p .

3.2.3 General form of the finite-domain equation

The combination of the convection, diffusion and source terms leads to the finite-domain equation, which can be written as :

$$a_p \phi_p = a_N \phi_N + a_S \phi_S + a_E \phi_E + a_W \phi_W + S_1 \quad (3.2)$$

where a_N , a_S , a_E , and a_W are coefficients expressing convection and diffusion, and

$$a_p = a_N + a_S + a_E + a_W - S_2$$

Equation (3.2) can be written in a generalized form

$$a_p \phi_p = \sum a_{nb} \phi_{nb} + S_1 \quad (3.3)$$

where the subscript nb denotes the neighbouring grid

nodes of P, and the summation is to be taken over all the neighbouring grid points. For two dimensional cases, there are four neighbouring points, and for three dimensional cases, there are six neighbouring points. A typical three-dimensional control cell is shown in figure (3.3)

3.2.4 Momentum equations

The treatment of the momentum equations is the same as above, with the control volume staggered in relation to the normal control volume around the main grid point P. The momentum control volumes is shown in figure (3.4). Thus, the resulting discretization equation for the velocity component u_e can be written as

$$\begin{aligned} a_e u_e &= \sum a_{nb} u_{nb} + S_1 + (p_p - p_E) A_e \\ &= \sum a_{nb} u_{nb} + S \end{aligned} \quad (3.4)$$

The term S_1 includes the source terms other than the pressure gradient. The term $(p_p - p_E) A_e$ is the pressure force acting on the control volume, A_e being the area on which the pressure differences acts. The coefficients a_e and a_{nb} are similar to those given in equation (3.3). Expressions similar to equation (3.4) can be written for each of the velocity components.

3.2.5 Pressure and velocity correction equations

The momentum equations can only be solved when the

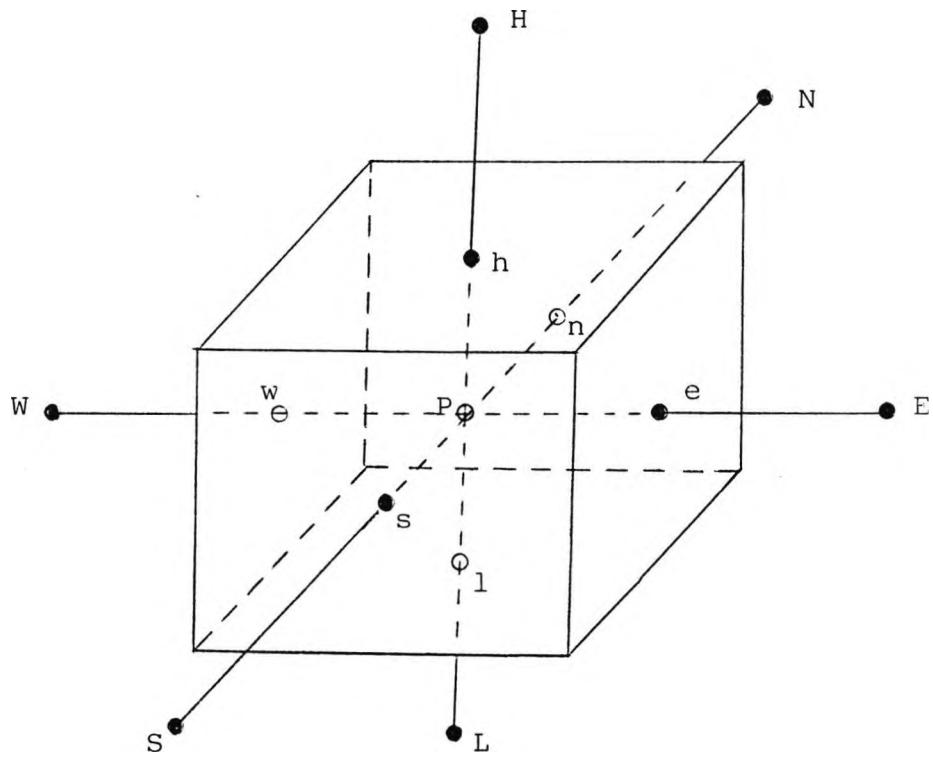
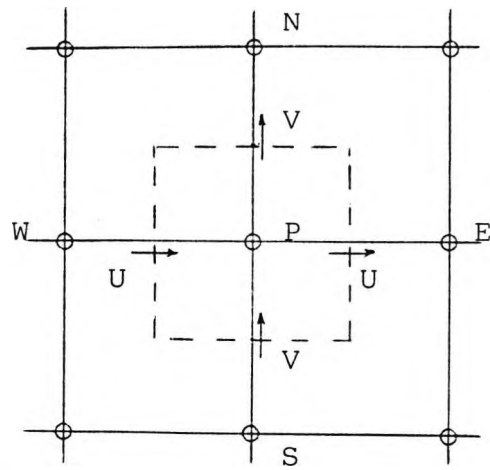
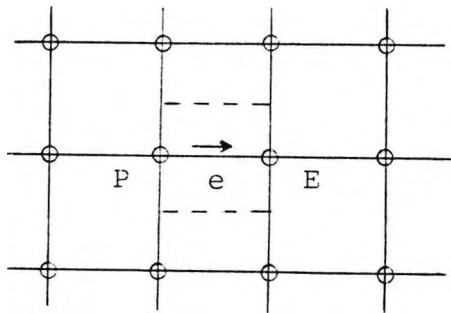
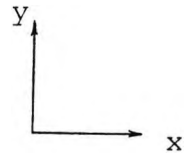


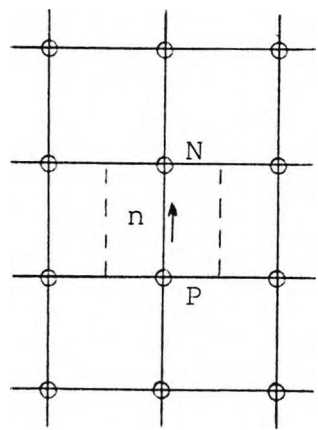
Fig. 3.3 A typical 3 dimensional control cell



normal control volume



control volume for U



control volume for V

Fig. 3.4 Momentum Control Volume

pressure field is given. Let u^* denotes the velocity field based on an estimated pressure field p^* . u^* will, in general, not satisfy the continuity equation and must be corrected by an amount of u' as a consequence of a pressure correction p' applied to the estimated pressure p^* . Thus,

$$p = p^* + p' \quad (3.5)$$

and

$$u = u^* + u' \quad (3.6)$$

A discretization equation for the pressure correction p' can be obtained (54,55,57), and for two dimensional cases, is of the form

$$a_p p'_p = a_n p'_n + a_s p'_s + a_e p'_e + a_w p'_w + b \quad (3.7)$$

where $b = (\rho u^* A)_w - (\rho u^* A)_e + (\rho v^* A)_s - (\rho v^* A)_n$

and is the continuity error of the cell. The a 's are influence coefficients of the form $\frac{\partial}{\partial P_i} (\rho_i A_i u_i)$.

Velocity - correction formula can be obtained by manipulating equations like equation (3.4) and (3.6), and is of the form

$$a_e u'_e = (p'_p - p'_e) A_e \quad (3.8)$$

A velocity - correction equation can be obtained for each velocity component.

3.3 Solution procedure

The finite-domain equations like equations (3.3) and (3.4) are only nominally linear. The coefficients in these equations are themselves dependent on the value of the physical quantity ϕ . Also, the coefficients for one physical quantity may be influenced by the values of other physical quantities. Because of these interlinkages and nonlinearities, the final solution has to be obtained by iteration.

A solution procedure called 'SIMPLE' has been developed for the calculation of the flow field. The procedure has been described by Patankar and Spalding (51), Caretto et al (52) and Patankar (53, 54, 55). The important operations of the 'SIMPLE' algorithm are :

1. Guess the pressure field p^* .
2. Solve the momentum equations such as equation (3.4) to obtain the velocity components.
3. Solve the pressure-correction equations such as equation (3.7) to obtain p' .
4. Calculate the pressure p from equation (3.5), and the corrected velocity components from equation (3.6).
5. Solve the finite-domain equations for all other

variables.

6. Use the newly obtained values of the variables as improved estimates, return to step 2, and repeat the whole procedure until convergence.

"PHOENICS" use the 'SIMPLEST' solution algorithm (59), which is a variant of the 'SIMPLE' algorithm. In 'SIMPLEST', the coefficients a_{nb} of the momentum equations (equation (3.4)) contain only the diffusion contributions; the convection terms are added in to S.

CHAPTER 4

DEVELOPMENT OF A MODEL FOR CONICAL ENTRANCE

ORIFICE PLATE FLOW SENSOR

4.1 Introduction

The conical entrance orifice plate is essentially used as a low Reynolds number flow measuring device, and, as discussed in chapter 2, the Lam and Bremhorst $k-\epsilon$ model is selected in the investigation of its performance characteristics. However, the "PHOENICS" computer code, which is used in the present study, is only equipped with the standard $k-\epsilon$ model. Therefore, to develop a model for the conical entrance orifice flow sensor, it is necessary, first of all, to incorporate the Lam and Bremhorst $k-\epsilon$ model into the "PHOENICS" computer code, making use of the facilities provided by "PHOENICS".

An instruction file called Q1 must also be created to transmit to the 'EARTH' program of "PHOENICS" all the necessary information for the simulation. These include the orifice plate geometry, upstream and downstream lengths, the number and distribution of the grid points and relevant properties of medium such as viscosity and density of fluid used in the simulation. The number of grid points must also be determined for the final solution to be 'grid-independent'.

4.2 Incorporating the Lam-Bremhorst k- ϵ model into the computer program

The Lam and Bremhorst k- ϵ model differs from the standard k- ϵ model embodied in "PHOENICS" in the expression for the source terms and viscosity. Therefore, these have to be incorporated into the computer program through the use of the subroutine 'GROUND'.

4.2.1 Modification to subroutine 'GROUND'

'GROUND' is merely an empty shell provided by "PHOENICS" for the user to insert his own coding sequences for his own special purposes. The listings of the coding sequences required to be inserted in subroutine 'GROUND' for the implementation of the Lam and Bremhorst k- ϵ model are given in Appendix A and is described here.

i) Calculation of the length scale of turbulence

The length scale $l = C_0 k^{3/2} / \epsilon$ (36) is first calculated from existing values of k and ϵ and stored in the 'EARTH' array AUX(LEN1) for later use. It is required in the evaluation of the source terms for the k and ϵ equations. The required coding is inserted in section 12 of group 9 of subroutine 'GROUND'.

ii) Calculation of the turbulent kinematic viscosity

The turbulent kinematic viscosity in the Lam and Bremhorst model is given by $\nu_t = C_\mu f_\mu k^2 / \epsilon$ (equation 2.17). The function f_μ (equation 2.18) depends on the turbulence

Reynolds number $R_k = k^{1/2} y/\nu_l$ and $R_\epsilon = k^2/\nu_l \epsilon$; the y in R_k is the normal distance from the nearest wall.

Hence the distance y of all the cell centres from the nearest wall are first determined and stored in the array GWDIST. These, together with the existing values of k , are used to calculate the value of R_k for each cell in the domain under study. The values of R_ϵ are also obtained using existing values of k and ϵ . The values of R_k and R_ϵ so calculated are temporarily stored in the 'EARTH' arrays EASP3 and EASP5 and used in evaluating f_μ . The values of f_μ are then used to evaluate the turbulent kinematic viscosity ν_t . The values of ν_t are then stored in the 'EARTH' array AUX(VIST).

The coding sequences required for the determination of the turbulent kinematic viscosity are inserted in section 5 of group 9 of 'GROUND'.

iii) Calculation of the functions f_1 and f_2

The functions f_1 (equation 2.19) and f_2 (equation 2.20) are required in the determination of the source term S_ϵ of the ϵ equation (table 3.1). The values of the functions f_1 and f_2 obtained are stored temporarily in the 'EARTH' arrays EASP4 and EASP6 for use in later sections.

The coding sequences required are also inserted in section 5 of group 9, immediately after the coding

sequences for the calculation of the turbulent kinematic viscosity.

iv) Calculation of the source term for the k equation

In 'PHOENICS', the source term for a general variable ϕ is expressed in a linearized form as:

$$S = C(V_a - \phi) \quad (4.1)$$

where C is called the coefficient part of the linearized source term and V_a is called the value part of the linearized source term.

Thus, for the k equation, the source term (table 3.1) is given by:

$$\begin{aligned} S &= \mu_t G - \rho \epsilon \\ &= \rho \frac{C_D}{C_\mu} \frac{\mu_t}{f_\mu l^2} \left(\frac{C_\mu}{C_D} f_\mu l^2 G - k \right) \end{aligned} \quad (4.2)$$

Equation (4.2) dictates that the coefficient is $\frac{C_D}{C_\mu} \frac{\mu_t}{f_\mu l^2}$ and the value is $\frac{C_\mu}{C_D} f_\mu l^2 G$.

The coding sequences for the evaluation of the coefficient of the source term is included in section 10 of group 13 of 'GROUND', and that for the calculation of the value of the source term is included in section 21 of group 13.

v) Calculation of the source term for the ϵ equation

For the ϵ equation, the source term (table 3.1) is given by:

$$\begin{aligned} S &= \frac{\epsilon}{K} (f_1 C_1 \mu_t G - f_2 C_2 \rho \epsilon) \\ &= f \frac{C_D}{C_u} \frac{C_2}{l^2} \frac{f_2}{f_u} U_t \left[\frac{C_1}{C_2} \frac{f_1}{f_2} U_t G - \epsilon \right] \end{aligned} \quad (4.3)$$

Thus, the coefficient is $\frac{C_D}{C_u} \frac{C_2}{l^2} \frac{f_2}{f_u} U_t$ and the value is $\frac{C_1}{C_2} \frac{f_1}{f_2} U_t G$.

The corresponding coding sequences for the coefficient is inserted in section 10 of group 13 while that for the value is in section 21 of the same group.

vi) Wall boundary conditions

Close to solid walls, viscous effects predominate over the turbulent ones, and there are two methods of accounting for the near-wall regions in numerical methods for computing turbulent flow. One method is the modelling of the low-Reynolds-number phenomena, and the other is the use of wall functions.

a) Low-Reynolds-number modelling

The Lam and Bremhorst k - ϵ model is a low-Reynolds-number turbulence model and is thus valid for the whole domain under investigation, including the near-wall regions. In this model, the velocity components and the value of k are specified to be zero at the wall. However,

ϵ is finite at the wall, and is given by (47):

$$\epsilon = \nu_t \frac{\partial^2 k}{\partial y^2} \quad (4.4)$$

The variation of k and ϵ near the wall may be expanded in a Taylor series. By retaining only the first term in the expressions, equation (4.4) is equivalent to:

$$\epsilon = \frac{2 \nu_t k}{y^2} \quad (4.5)$$

Thus, Parry (60) recommended that, as the boundary conditions for the k equation and ϵ equation, a zero value is assigned at the wall for the k equation, and $\epsilon = \frac{2 \nu_t k}{y^2}$ for the ϵ equation for the grid cell close to the wall.

Boundary conditions are introduced in "PHOENICS" by way of sources $S = C(V_a - \phi)$ (equation 4.1). When the boundary condition dictates that the value of ϕ at a grid point should be fixed, V_a is set to the desired value and C is set to a very large number. For then, equation (3.3) reduces to :

$$\begin{aligned} \phi_p &= (\sum a_{nb} \phi_{nb} + V_a C) / (a_p + C) \\ &= V_a \end{aligned}$$

because $V_a \times C$ is much larger than all other terms in the numerator and C is much larger than all other terms in

the denominator.

Thus, to implement the boundary condition for ϵ in accordance with Parry's recommendation, the 'value' of the source term is set equal to $2\nu_1 k/y_2$, and the 'coefficient' is set to be 10^{10} , a very large number. The corresponding coding sequences for the 'value' of the source term used in the boundary condition is inserted in section 22 of group 13.

b) The wall-function method

The wall function formulae (36, 61) are used in this method, and when used with the Low-Reynolds-number model, the distance between the wall and the first grid node can be very small.

For the near wall grid nodes, the following algebraic relations are employed when the wall function method is used:

$$\begin{aligned} u^+ &= y^+ && \text{for } y^+ < 11.5 \\ u^+ &= \frac{1}{\chi} \ln(Ey^+) && \text{for } y^+ \geq 11.5 \end{aligned} \quad (4.6)$$

$$k = u_\tau^2 / \sqrt{c_\mu} \quad (4.7)$$

$$\epsilon = u_\tau^3 / \chi y \quad (4.8)$$

where $y^+ = u_\tau y / \nu$, $u^+ = u / u_\tau$, $u_\tau = \sqrt{(\tau_w / \rho)}$, y is the normal distance from the wall, u is the resultant velocity parallel to the wall, and τ_w is the wall shear stress.

κ is the von Karman's constant ($\kappa = 0.435$) and E is a roughness parameter ($E = 9$ for smooth walls).

The above relationships are embodied in "PHOENICS" as one of the standard features.

4.3 Modelling of flow through a conical entrance orifice plate

The Lam-Bremhorst $k-\epsilon$ model was applied to the flow through a conical entrance orifice plate. The flow was assumed to be steady and axi-symmetric; and cylindrical polar-coordinates were used in the numerical modelling.

4.3.1 Geometry

The computational test section containing the orifice plate is shown in figure 4.1. The domain is divided into regular cylindrical-polar grids. Variable grid spacing was used. The grids were concentrated in regions of large velocity gradients; i.e. in the area of the orifice plate in the axial direction, and close to the pipe wall and to the orifice lip in the radial direction.

The conical entrance orifice plate was created by declaring the appropriate regions of the computational test section to be inaccessible to the fluid. In "PHOENICS", the area A in the diffusion and convection terms, and the volume V_0 in the source terms of the

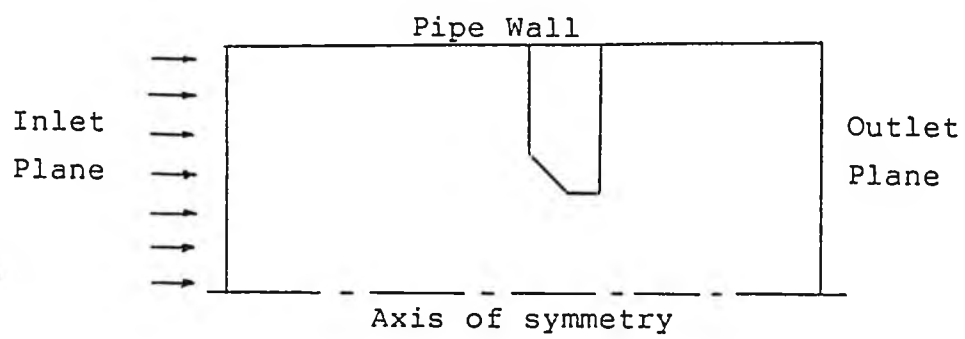


Fig. 4.1 The computational test section

finite-domain equation may differ from the products of the cell-side lengths which represent the nominal cell-face areas and volumes. Thus,

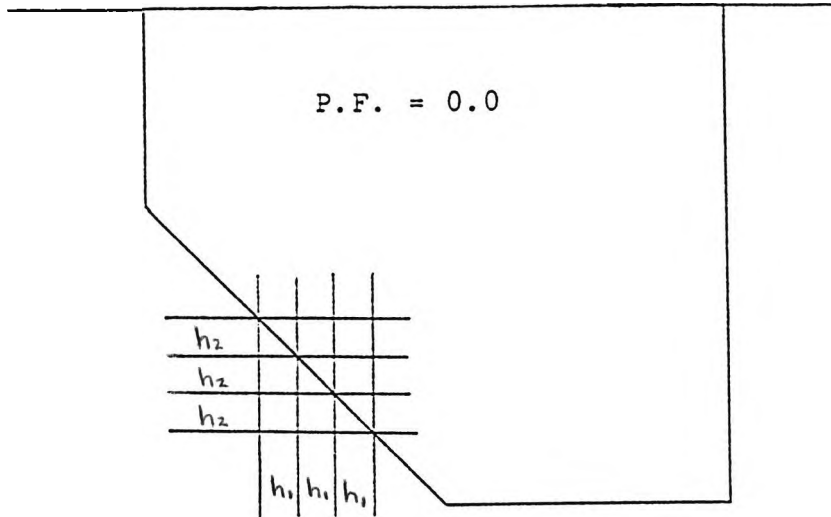
$$A = A_{\text{nom}} \times f_A$$

$$V_o = V_{\text{nom}} \times f_v$$

where A_{nom} and V_{nom} stand for the nominal values, and f_A and f_v are the so-called 'porosity factors' to which the user of the computer code can ascribe values which may differ from unity. f_A can differ from cell to cell and from face to face. The volume porosity can also vary from cell to cell. A porosity factor of 0.0 has the effect of completely blocking off the appropriate part of the cylindrical integration domain, which a porosity factor of 1.0 indicates that no blockage is present, and the corresponding cell is freely accessible by the fluid.

Thus, the inaccessibility to the fluid of specified regions in the computational test section may be represented by way of porosity factors, which allow the extent of blockage of each cell face and all volume to be numerically expressed.

Figure 4.2 shows the use of porosity factors in creating the conical entrance orifice plate in the computational test section. The plate, with the exception of the conical part, is created by assigning a porosity



P.F. = 0.5 for cells corresponding to the conical surface

Fig. 4.2 Representation of the orifice plate by the use of porosity factor (P.F.)

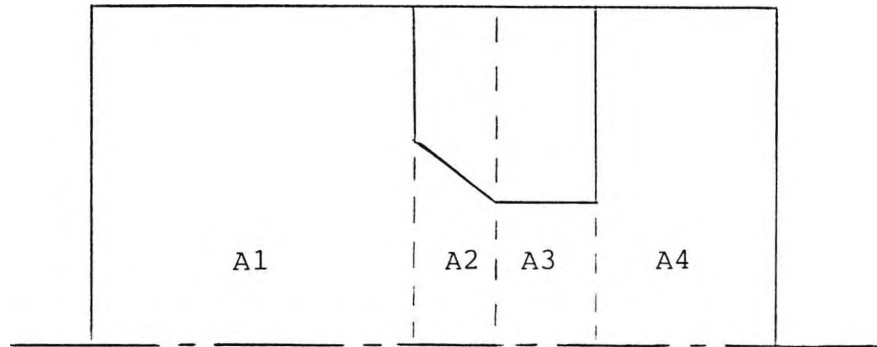
factor of 0.0 to the cells in the region of interest. The conical part is simulated by employing equal number of grid points in the axial and radial directions, and a porosity factor of 0.5 for cells in the region of interest. For a bevel angle of 45 degree, the lengths of the cells in the axial and radial directions are set to be equal ($h_1 = h_2$ in figure 4.2). All other cells in the integration domain are assigned a porosity factor of 1.0, indicating that no blockage is present.

4.3.2 Grid distribution

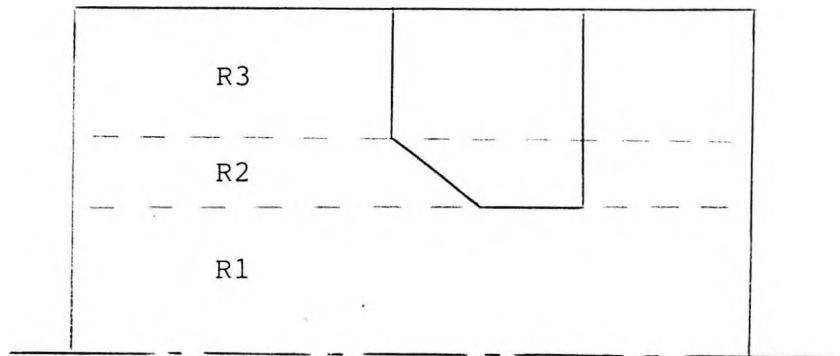
For the solution of the finite-domain equation, the computational test section has to be divided into regular cylindrical-polar grids. The distribution of grid lines were such that they concentrated in regions of large velocity gradient.

Thus, variable spacings were used in the axial direction in regions A_1 and A_4 (figure 4.3a), and for grids in the radial direction in regions R_1 and R_3 (figure 4.3b). The grids were concentrated axially in the area of the orifice plate and radially near the plate lip and pipe wall. The axial grid spacing in region A_3 also varied, with grids concentrated near the conical part of the orifice.

To simulate the conical part of the orifice, the number of cells in region A_2 in the axial direction is



a) Division of the computational test section into regions to describe the axial grid line distribution



b) Division of the computational test section into regions to describe the radial grid line distribution

Fig. 4.3 Grid line distribution

the same as the number of cells in region R_2 in the radial direction. The axial grid spacing in region A_2 is uniform; so is the radial grid spacing in region R_2 . These two spacings are set to be equal for a bevel angle of 45 degree.

4.3.3 Boundary conditions

The boundaries of the computational test section are shown in figure 4.4. There are a total of eight boundaries - the inlet plane (region 6) and outlet plane (region 7), the pipe wall (regions 1 and 2), the two faces of the orifice plate (regions 3 and 4), the lip of the orifice plate (region 5) and the axis of symmetry. The conditions of the variables at the boundaries have to be specified for the solution of the finite-domain equations.

i) Inlet plane (region 6)

At inlet, the axial velocity profile was assumed to be uniform with a magnitude v_z given by

$$v_z = \frac{Re_D \nu}{D}$$

where ν is the kinematic viscosity of the fluid, D is the pipe diameter and Re_D is the pipe Reynolds number.

The inlet profiles of turbulent kinetic energy k and its rate of dissipation ϵ were also assumed to be uniform and their magnitudes k_{in} and ϵ_{in} given by the

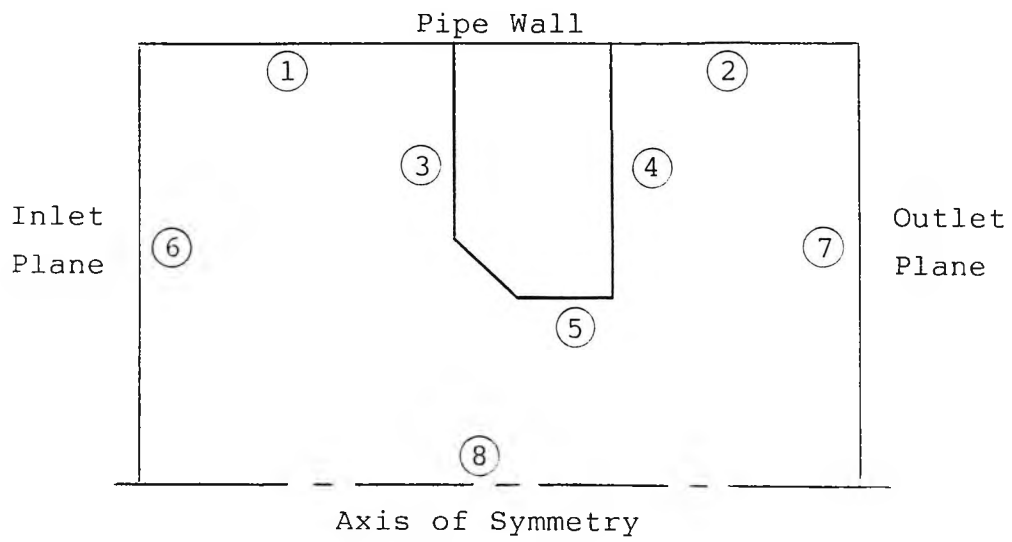


Fig. 4.4 Boundary regions of the computational test section

following relationship.

$$k_{in} = i v_z^2 \quad (4.9)$$

$$\epsilon_{in} = k_{in}^{1.5} / (\lambda R) \quad (4.10)$$

where i = intensity of turbulence

λ = length scale factor

R = pipe radius

ii) Outlet plane (region 7)

At the outlet plane, only the pressure needs to be specified. The pressure is taken to be constant with a numerical value of zero.

iii) At walls (regions 1, 2, 3, 4 and 5)

At the pipe wall, and at the orifice plate walls (except the bevelled part of the orifice), the wall-function method (or the low-Reynolds-number modelling method) (section 4.2.1) is used to specify the magnitudes of the velocity, turbulent kinetic energy and its rate of dissipation at the near wall grid nodes.

4.3.4 Auxiliary information

i) Under-relaxation

The system of finite-domain equations like equations (3.3) and (3.4) are only nominally linear. Because of the interlinkages and nonlinearities present in these

equations, the final solution has to be obtained by iteration. However, successive iteration does not always lead to a converged solution. The values of variables might drift away from what can be considered a reasonable solution and such divergence of the iterative process must be avoided.

To suppress the tendency to diverge, it is often necessary to slow down the changes in the values of the variables by using 'under-relaxation'. Two under-relaxation devices are incorporated as a standard feature of "PHOENICS" - the 'false-time-step under-relaxation' and the 'linear under-relaxation'.

a) 'false-time-step under-relaxation'

This under-relaxation practice adds $(\frac{\rho V_0}{\delta t_f})_p \phi_p^*$ to S_1 and $(\frac{\rho V_0}{\delta t_f})_p$ to a_p in equation (3.3). Thus, the finite-domain equation becomes

$$\phi_p = \frac{\sum a_{nb} \phi_{nb} + S_1 + (\frac{\rho V_0}{\delta t_f})_p \phi_p^*}{a_p + (\frac{\rho V_0}{\delta t_f})_p} \quad (4.11)$$

where V_0 is the cell volume, δt_f is the 'false-time-step', and ϕ_p^* is the value of ϕ_p from the previous iteration.

The smaller the value of δt_f , the greater will be the tendency for the finite-domain equation to imply

$$\phi_p = \phi_p^*$$

Thus, the solution is being slowed down and the divergence of the iterative solution procedure may be prevented.

b) 'linear under-relaxation'

Equation (3.3) can be rewritten as

$$\phi_p = \phi_p^* + [(\sum a_{nb}\phi_{nb} + S_1) / a_p - \phi_p^*]$$

where ϕ_p^* is the value of ϕ_p from the previous iteration. The terms in the square bracket represent the change in ϕ_p during two consecutive iterations. To slow down the change, an under-relaxation factor α can be used such that

$$\phi_p = \phi_p^* + \alpha [(\sum a_{nb}\phi_{nb} + S_1) / a_p - \phi_p^*] \quad (4.12)$$

when α is unity, no under-relaxation is effected. If α is close to zero, the value of ϕ_p changes only slowly, and thus the divergence of the iterative procedure may be prevented.

ii) Convergence

An iterative process is said to have converged when further iterations will not produce any change in the values of the dependent variables. Practically, the iterative process is terminated when some arbitrary

convergence criterion is satisfied. In "PHOENICS", the convergence is monitored through the use of residuals, which is a measure of how well the finite-domain equations are satisfied by the current values of the dependent variables. The residual R_ϕ of a variable ϕ at a node P can be calculated from

$$R_\phi = \sum a_{nb} \phi_{nb} + S_1 - a_p \phi_p \quad (4.13)$$

The residuals represent the error that need to be reduced and eliminated during the successive iterations.

"PHOENICS" calculates the sum of the absolute values of R_ϕ for all cells in the integration domain. To facilitate monitoring, the residuals are suitably normalised by a reference value. When the sum of the absolute values of the residual for a variable falls below the associated reference value, the solution for that variable is terminated. The values for that variable will still be updated and the residual calculated as the solution for other variables continues. When the residual goes above the associated reference value, the solution process for that variable will be activated again.

4.4 Tests on the conical entrance orifice plates

The Lam-Bremhorst $k-\epsilon$ model was chosen in the study of the characteristics of the conical entrance orifice plates. Other things that need to be looked into in the

simulation of flow through the orifice plates are the lengths of the solution domain on the upstream and downstream side of the orifice plate, and the distribution of the grid points in the domain under investigation. Also, the value of the residuals (equation 4.13) when the solution can be considered as converged has to be considered.

In the use of the conical entrance orifice plates as a flow measuring device, discharge coefficient is the quantity of primary interest. Therefore, a correct model can basically be said to have been obtained when the chosen lengths of the solution domain on the upstream and downstream side of the orifice plate are sufficiently large, so that any further increase in these lengths will not result in a change in the discharge coefficient; the grid distribution is sufficiently fine so that the discharge coefficient remains unchanged as the grid is further refined; the level of the residuals being sufficiently small so that the discharge coefficient remains constant with respect to changes in the residuals.

4.4.1 General information on the test cases

In the modelling of flow through orifice plates, most of the previous workers (16,17) tested the grid distribution of their models at only one β ratio. Then the grid distribution so obtained was used in models for

other β ratio orifice plates.

For the same grid distribution, the density of the grid in different regions of the solution domain would not be the same as the β ratio is altered. Therefore, error might occur in the numerical results obtained.

The limits of use for conical entrance orifice plates as specified in BS 1042 (section 1.2 : 1984) is for a β ratio of $0.1 \leq \beta \leq 0.316$, and for a pipe Reynolds number (R_{ed}) of $80 \leq R_{ed} \leq 60,000$. Thus, tests were performed at β ratios of 0.1, 0.2 and 0.3 and at a Reynolds number (R_{ed}) of 60,000, so as to determine the number of grids, and the upstream and downstream lengths of the orifice plates required for the model.

i) Physical case used in the tests

In all these tests, numerical results were obtained using a pipe 100 mm in diameter and with water as the working fluid. The density of water is taken to be 1000 kg/m^3 and its kinematic viscosity taken to be $10^{-6} \text{ m}^2/\text{s}$.

ii) Inlet and outlet conditions

At the inlet, the profiles for the axial velocity v_z , the turbulent kinetic energy k and its dissipation rate ϵ need to be specified for the solution procedure. Thus, a uniform profile was specified at the inlet for the distribution of velocity v_z , turbulent kinetic energy

k and its rate of dissipation ϵ .

- the inlet velocity V_z was set to be equal to 600 mm/s so as to attain a pipe Reynolds number of 60,000.
- the kinetic energy of turbulence k is given by equation (4.9), with the level of turbulence intensity i set arbitrarily to a small value of 0.003.
- the corresponding value of dissipation rate ϵ was determined from the equation $\epsilon = \frac{0.09 k^{1.5}}{0.03 R}$ where R is the pipe radius (62). Thus, the length scale factor λ in equation (4.10) is equal to 0.333.

At the outlet, a constant pressure was prescribed and was given a numerical value of zero.

iii) Monitoring of convergence of the solution procedure

The convergence of the solution procedure is monitored through the use of residuals (equation 4.13). To facilitate monitoring, the residuals were normalised by a reference value.

For the pressure p, the residual is the sum of the absolute values of the cell-wise volumetric continuity errors. In the test runs, the residual for p was normalised by dividing it with a reference value given by $1.25 \times 10^{-3} \times Q_v$, where Q_v is the volume rate of flow in

the pipe. The reference value for the axial velocity V_z is $2.5 \times 10^{-3} \times V_z \times Q_m$, where Q_m is the mass rate of flow in the pipe. The reference value for the radial velocity V_r is $1.25 \times 10^{-2} \times V_z \times Q_m$. The reference value for the turbulence kinetic energy k is $2.5 \times 10^2 \times k_{in} \times Q_m$, where k_{in} is the value of k at the inlet. The reference value for the dissipation rate ϵ is $2.5 \times 10^5 \times \epsilon_{in} \times Q_m$, where ϵ_{in} is the value of ϵ at the inlet.

The reference values were chosen arbitrarily, but were such that the magnitudes of the normalised residuals for the variables would not be too far away from each other. Otherwise, the solution of some variables would stop while the values of other variables were still far from being converged. This might lead to divergence.

For the test cases considered, the fluid flow was predominantly in the axial direction. It was observed that the normalised residual for the axial velocity V_z gave a good indication about the convergence of the pressure field. Also, in the use of conical entrance orifice plates as a flow measuring device, the discharge coefficient will be the parameter of primary interest. Thus, the normalised residual for V_z was plotted against the discharge coefficient in figures 4.5 to 4.7 in order to show the convergence of the solution procedure.

4.4.2 Tests on the $\beta = 0.1$ conical entrance orifice plates

i) Grid distribution

To determine the number of grids required for the model, simulation was performed with three different grids. The computational test section was divided into regions as depicted in figure 4.3, and the number of grids in each region is given in table 4.1. The grids in regions A2 and R2, which correspond to the conical part of the orifice plate, were uniformly spaced. The grid distribution in other regions were non-uniform, being more concentrated near the walls.

	No. of grid nodes							Total no. of grid nodes (axial x radial)
	A1	A2	A3	A4	R1	R2	R3	
Test no. 1	38	12	24	38	9	12	30	112 x 51
Test no. 2	38	15	30	38	9	15	30	121 x 54
Test no. 3	62	20	40	62	12	20	40	184 x 72

Table 4.1 Grid distribution for the computational test section
(β ratio = 0.1)

ii) Upstream and downstream lengths

The lengths of the solution domain upstream and downstream of the orifice plate were specified to be 30 D and 16 D respectively in tests number 1 and 2, where D is the pipe diameter. The corresponding values were 40 D and 20 D for test number 3, with the density of grid more than 40 % greater than that in test number 2.

iii) Under-relaxation

To suppress the tendency of the solution to diverge, under-relaxation factors had to be used. 'Linear under-relaxation' was applied to the pressure while 'false-time-step under-relaxation' was applied to other variables. The values of the under-relaxation factors used were varied during the course of solution to prevent divergence or to accelerate convergence. The range of values of under-relaxation factors used were 0.1 to 0.5 for the pressure p , 0.01 to 0.001 for the axial velocity V_z , 0.01 for the radial velocity V_r , 0.1 to 0.001 for the turbulence kinetic energy k and 0.1 for the rate of dissipation ϵ .

iv) Results

Figure 4.5 shows the variation of the discharge coefficient (corner tappings) with the normalised residual for the axial velocity V_z for the three grid distributions shown in table 4.1. It can be seen that the discharge coefficient becomes asymptotically constant as the residual is reduced and the solution can be considered to be well converged when the magnitude of the residual has reduced to below 10. The number of iterations required for the solution varied from about 60,000 to over 100,000 sweeps, depending on the grid distribution used. The variation of the discharge coefficients with the normalised residuals of all the variables are given in tables 4.2 to 4.4.

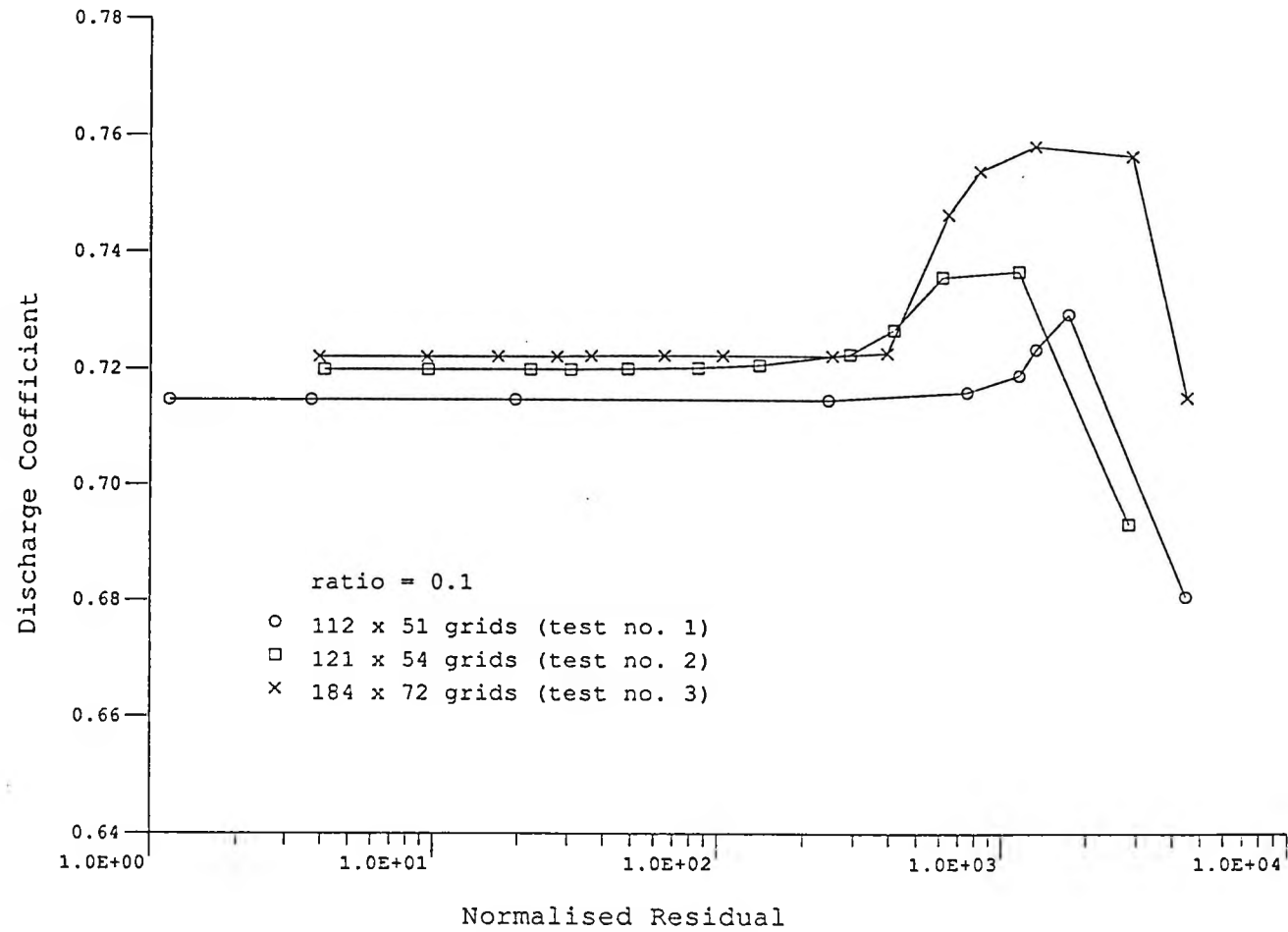


Fig. 4.5 Variation of the Discharge Coefficient with the Normalised Residual for the axial velocity component

Normalised Residuals					Discharge Coefficient		
P	V_r	V_z	K	ϵ	corner tappings	flange tappings	D & 1/2 D tappings
3.009E+1	1.481E+2	4.487E+3	6.358E+3	2.489E+5	0.6808	0.6806	0.6803
2.987E+1	1.280E+2	1.765E+3	5.725E+3	1.545E+5	0.7295	0.7294	0.7291
2.996E+1	4.378E+1	1.349E+3	4.278E+2	8.753E+3	0.7235	0.7234	0.7233
4.742E+1	2.084E+1	1.172E+3	3.506E+2	1.005E+4	0.7190	0.7190	0.7189
3.532E+1	1.121E+1	7.640E+2	1.428E+2	4.438E+3	0.7161	0.7161	0.7159
1.748E+1	7.734E+0	2.474E+2	1.027E+2	3.599E+3	0.7147	0.7146	0.7145
1.433E+1	4.444E+0	1.976E+1	1.826E+1	5.412E+2	0.7147	0.7146	0.7145
1.314E+1	3.886E+0	3.739E+0	4.849E+1	1.505E+3	0.7147	0.7146	0.7145
3.150E+0	1.310E+0	1.165E+0	2.949E+0	8.407E+1	0.7147	0.7146	0.7145

Table 4.2 Variation of normalised residuals with discharge coefficients
(β ratio = 0.1 test no. 1)

Normalised Residuals					Discharge Coefficient		
P	V_r	V_z	K	ϵ	corner tappings	flange tappings	D & 1/2 D tappings
4.933E+1	5.537E+2	2.854E+3	9.033E+3	3.408E+5	0.6932	0.6932	0.6930
2.273E+1	3.364E+2	1.173E+3	1.729E+4	6.827E+5	0.7368	0.7367	0.7365
3.532E+1	1.718E+2	6.246E+2	1.234E+4	3.477E+5	0.7358	0.7357	0.7356
2.493E+1	5.376E+1	4.225E+2	9.270E+2	2.355E+4	0.7268	0.7268	0.7266
2.182E+1	7.699E+0	2.946E+2	3.733E+2	1.049E+4	0.7226	0.7226	0.7225
3.595E+1	6.840E+0	1.419E+2	1.393E+2	4.376E+3	0.7207	0.7207	0.7206
3.696E+1	5.477E+0	8.646E+1	8.888E+1	2.947E+3	0.7202	0.7201	0.7201
3.480E+1	3.779E+0	4.920E+1	2.060E+1	1.520E+2	0.7200	0.7199	0.7198
2.226E+1	3.086E+0	3.102E+1	2.025E+1	5.718E+2	0.7199	0.7198	0.7198
2.630E+1	2.686E+0	2.233E+1	2.089E+1	5.154E+2	0.7199	0.7198	0.7197
9.972E-1	7.446E-1	9.673E+0	1.103E+2	3.886E+3	0.7199	0.7198	0.7197
8.652E-1	3.413E-1	4.150E+0	7.154E+0	1.237E+2	0.7199	0.7198	0.7197

Table 4.3 Variation of normalised residuals with discharge coefficients
(β ratio = 0.1 test no. 2)

Normalised Residuals					Discharge Coefficient		
P	V_r	V_z	K	ϵ	corner tappings	flange tappings	D & 1/2 D tappings
2.083E+0	5.249E+2	4.589E+3	7.332E+3	5.890E+5	0.7152	0.7150	0.7147
7.393E-1	3.723E+2	2.974E+3	9.271E+3	6.985E+5	0.7566	0.7564	0.7561
9.695E-1	2.351E+2	1.355E+3	6.965E+3	3.254E+5	0.7583	0.7581	0.7580
7.404E-1	2.003E+2	8.564E+2	2.586E+3	9.509E+4	0.7540	0.7538	0.7536
8.544E-1	1.036E+2	6.582E+2	5.135E+2	8.228E+3	0.7465	0.7464	0.7462
3.827E+0	3.851E+0	3.989E+2	2.791E+2	1.252E+4	0.7228	0.7228	0.7227
4.863E+0	4.021E+0	2.558E+2	1.715E+2	8.082E+3	0.7223	0.7223	0.7222
4.951E+0	3.427E+0	1.057E+2	3.277E+1	1.371E+3	0.7223	0.7223	0.7222
3.506E+0	3.013E+0	6.595E+1	4.682E+1	1.826E+3	0.7223	0.7223	0.7222
3.991E+0	2.643E+0	3.664E+1	5.577E+1	2.469E+3	0.7222	0.7221	0.7221
3.831E+0	2.425E+0	2.773E+1	2.983E+1	1.248E+3	0.7221	0.7220	0.7221
7.014E+0	2.265E+0	1.717E+1	5.520E+1	2.999E+3	0.7221	0.7220	0.7220
7.161E+0	1.764E+0	9.576E+0	2.513E+1	1.183E+3	0.7221	0.7220	0.7220
3.548E+0	7.696E-1	3.986E+0	6.177E+0	1.689E+2	0.7221	0.7220	0.7220

Table 4.4 Variation of normalised residuals with discharge coefficients
(β ratio = 0.1 test no. 3)

From tables 4.2 to 4.4, it can be seen that the discharge coefficients obtained in run number 2 (121 x 54 grids) differ from that obtained in run number 3 (184 x 72 grids) by only about 0.3 %. Thus the results obtained using the grid distribution in run number 2 (121 x 54 grids) can be regarded to be grid-independent. The value of the discharge coefficient (corner tapplings) obtained with this grid distribution is 0.7199, which differs from the BS value of 0.734 (BS 1042: section 1.2 : 1984) by 1.92 %.

In order to confirm that sufficient lengths were specified for the upstream and downstream distances in the model, another test run was conducted using an upstream length of 150 D and a downstream length of 106 D. In this test, the axial grid distribution in the region of the orifice plate and the radial grid distribution was identical to that of run number 2. The results obtained are compared with run number 2 in table 4.5.

Upstream length	Downstream length	No. of grid nodes							Discharge Coefficient		
		A1	A2	A3	A4	R1	R2	R3	Corner tapplings	Flange tapplings	D & 1/2 D tapplings
30 D	16 D	38	15	30	38	9	15	30	0.7199	0.7198	0.7197
150 D	106 D	83	15	30	133	9	15	30	0.7196	0.7196	0.7195

Table 4.5 Effect of upstream and downstream lengths
(β ratio = 0.1)

Thus, an upstream length of 30 D and a downstream length of 16 D as used in run number 2 would be suffi-

cient distances to be used in the model.

In all the above tests, the results were obtained using the 'wall-function method' in specifying the wall boundary conditions.

4.4.3 Tests on the $\beta = 0.2$ conical entrance orifice plates

i) Grid distribution

To determine the number of grids required for the model, simulation was performed with three different grids. The computational test section was divided into regions as depicted in figure 4.3, and the number of grids in each region was given in table 4.6. The grids in region A2 and R2, which correspond to the conical part of the orifice plate, were uniformly spaced. The grid distribution in other region were non-uniform, being more concentrated near the walls.

	No. of grid nodes							Total no. of grid nodes (axial x radial)
	A1	A2	A3	A4	R1	R2	R3	
Test no. 1	38	15	30	38	8	15	19	121 x 42
Test no. 2	38	21	42	38	8	21	19	139 x 48
Test no. 3	62	32	64	62	10	32	28	220 x 70

Table 4.6 Grid distribution for the computational test section
(β ratio = 0.2)

ii) Upstream and downstream lengths

The lengths of the solution domain upstream and

downstream of the orifice plate were specified to be 30 D and 16 D respectively in test number 1 and 2, where D is the pipe diameter. The corresponding values were 40 D and 20 D for test number 3, with the grid density more than 40% greater than that in test number 2.

iii) Under-relaxation

Under-relaxation factors had to be used to suppress the tendency to diverge. 'Linear under-relaxation' was applied to the pressure, while 'false-time-step under-relaxation' was applied to other variables. The values of the under-relaxation factors were varied during the course of solution to combat divergence or to accelerate convergence. The range of values used were 0.1 to 0.5 for the pressure p , 0.001 to 0.0001 for the axial velocity V_z , 0.01 to 0.001 for the radial velocity V_r , 0.1 to 0.001 for the turbulence kinetic energy k and 0.1 for the rate of dissipation ϵ .

iv) Results

Figure 4.6 shows the variation of the discharge coefficient (corner tappings) with the normalised residual for V_z for the three grid distributions given in table 4.6. It can be seen that the discharge coefficient becomes asymptotically constant as the residual is reduced and the solution can be considered to be converged when the magnitude of the residual has reduced to below 10. The number of iterations required for the

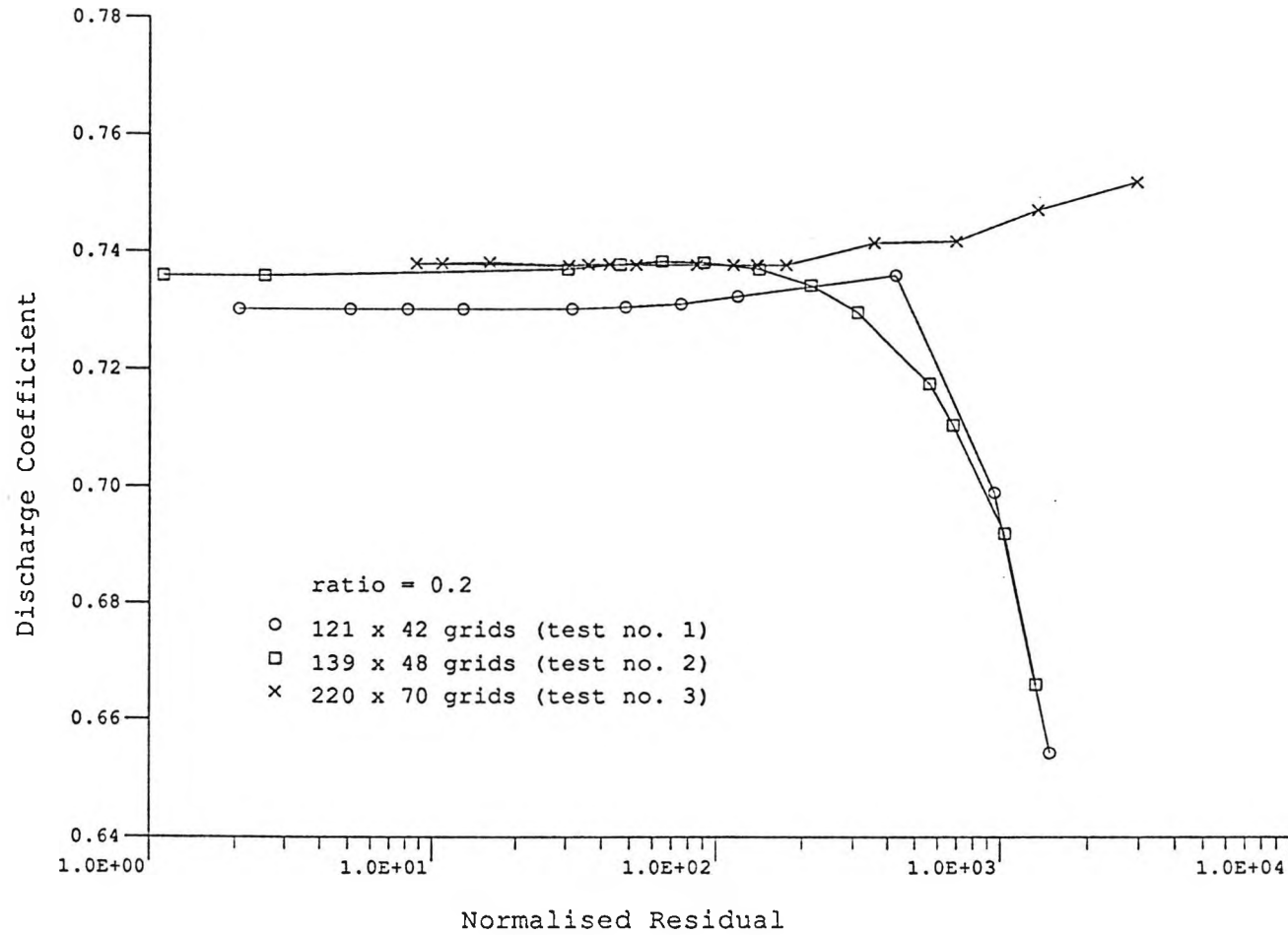


Fig. 4.6 Variation of the Discharge Coefficient with the Normalised Residual for the axial velocity component

Normalised Residuals					Discharge Coefficient		
P	V_r	V_z	K	ϵ	corner tappings	flange tappings	D & 1/2 D tappings
2.857E+1	1.096E+2	1.490E+3	3.525E+3	1.959E+4	0.6543	0.6541	0.6538
2.619E+1	8.744E+1	9.642E+2	3.318E+3	1.551E+4	0.6990	0.6987	0.6984
1.389E+1	5.341E+1	4.361E+2	3.728E+3	1.337E+4	0.7359	0.7357	0.7355
1.025E+1	1.161E+1	1.204E+2	8.818E+1	3.716E+2	0.7323	0.7324	0.7320
5.448E+0	6.183E+0	7.638E+1	4.749E+1	2.025E+2	0.7310	0.7309	0.7307
5.475E+0	3.491E+0	4.865E+1	1.506E+1	6.363E+1	0.7305	0.7304	0.7301
4.638E+0	2.168E+0	3.176E+1	5.982E+0	2.493E+1	0.7302	0.7302	0.7299
7.634E+0	1.254E+0	1.300E+1	5.656E-1	1.513E+0	0.7302	0.7301	0.7299
7.533E+0	1.037E+0	8.192E+0	2.645E+0	1.101E+1	0.7302	0.7301	0.7299
3.353E+0	8.969E-1	5.105E+0	1.276E+0	5.230E+0	0.7302	0.7301	0.7299
7.377E+0	7.930E-1	2.065E+0	1.432E+0	5.748E+0	0.7302	0.7301	0.7299

Table 4.7 Variation of normalised residuals with discharge coefficients
(β ratio = 0.2 test no. 1)

Normalised Residuals					Discharge Coefficient		
P	V_r	v_z	K	ϵ	corner tappings	flange tappings	D & 1/2 D tappings
5.615E+0	3.659E+1	1.337E+3	2.622E+2	1.462E+3	0.6660	0.6659	0.6654
9.739E+0	4.573E+1	1.048E+3	1.630E+5	7.487E+5	0.6920	0.6918	0.6913
5.697E+0	2.892E+1	6.892E+2	1.357E+2	6.411E+2	0.7105	0.7103	0.7097
5.713E+0	2.641E+1	5.694E+2	1.075E+2	4.859E+2	0.7175	0.7172	0.7168
6.810E+0	1.975E+1	3.165E+2	6.830E+1	2.862E+2	0.7296	0.7294	0.7291
5.453E+0	1.567E+1	2.169E+2	4.525E+1	1.830E+2	0.7342	0.7340	0.7337
4.485E+0	1.155E+1	1.437E+2	2.646E+1	9.733E+1	0.7370	0.7368	0.7364
5.257E+0	7.741E+0	9.166E+1	1.244E+1	3.999E+1	0.7381	0.7379	0.7377
6.493E+0	5.671E+0	6.545E+1	1.171E+1	3.840E+1	0.7383	0.7382	0.7378
4.446E+0	2.281E+0	4.664E+1	5.675E+0	1.729E+1	0.7378	0.7379	0.7375
5.009E+0	1.254E+0	3.072E+1	5.621E+0	2.049E+1	0.7370	0.7369	0.7368
4.520E+0	4.178E-1	2.541E+0	2.734E+0	8.834E+0	0.7359	0.7358	0.7357
6.662E+0	3.184E-1	1.118E+0	9.232E-1	3.883E+0	0.7359	0.7358	0.7355

Table 4.8 Variation of normalised residuals with discharge coefficients
(β ratio = 0.2 test no. 2)

Normalised Residuals					Discharge Coefficient		
P	V_r	V_z	K	ϵ	corner tappings	flange tappings	D & 1/2 D tappings
3.485E+2	8.766E+2	3.051E+3	2.537E+2	9.603E+2	0.7520	0.7524	0.7521
5.115E+2	5.285E+2	1.381E+3	1.719E+2	9.750E+2	0.7472	0.7473	0.7473
4.675E+2	2.528E+2	7.140E+2	1.180E+2	7.240E+2	0.7418	0.7419	0.7419
8.178E+1	4.446E+1	3.653E+2	2.447E+2	1.689E+3	0.7415	0.7417	0.7416
8.627E+0	1.413E+0	1.785E+2	8.790E+1	5.890E+1	0.7377	0.7378	0.7377
8.647E+0	1.018E+0	1.413E+2	6.905E+0	3.240E+1	0.7377	0.7378	0.7375
9.556E+0	8.165E-1	1.165E+2	5.358E+0	2.438E+1	0.7377	0.7376	0.7376
1.231E+1	6.528E-1	8.682E+1	5.721E+0	2.478E+1	0.7377	0.7376	0.7376
1.167E+1	6.408E-1	5.306E+1	1.771E+0	1.082E+1	0.7377	0.7376	0.7376
1.088E+1	5.962E-1	4.289E+1	1.313E+0	7.462E+0	0.7378	0.7377	0.7375
6.980E-1	4.054E-1	3.618E+1	6.520E-1	2.550E+0	0.7378	0.7377	0.7375
1.069E+1	6.231E-1	3.098E+1	7.320E+1	2.519E+2	0.7376	0.7375	0.7375
1.457E+1	8.112E-1	1.620E+1	3.864E+1	1.908E+2	0.7382	0.7381	0.7379
1.258E+1	6.475E-1	1.093E+1	3.751E+1	1.553E+2	0.7380	0.7379	0.7377
2.812E+0	6.957E-1	8.827E+0	4.258E+1	2.318E+2	0.7380	0.7379	0.7377

Table 4.9 Variation of normalised residuals with discharge coefficients
(β ratio = 0.2 test no. 3)

solution varied from about 10,000 sweeps for the coarser grids to over 70,000 sweeps for the finer grids. The variation of the discharge coefficients with the normalised residuals are given in tables 4.7 to 4.9.

From tables 4.7 to 4.9, it can be seen that the discharge coefficient obtained in run number 2 (139 x 48 grids) differs from that obtained in run number 3 (220 x 70 grids) by less than 0.3 %. Thus, the results obtained using the grid distribution in run number 2 (139 x 48 grids) can be regarded to be grid-independent. The value of the discharge coefficient (corner tappings) obtained with this grid distribution is 0.7359, which differs from the BS value of 0.734 (BS 1042 : section 1.2 : 1984) by only 0.26 %.

To confirm that sufficient upstream and downstream lengths were used in the model, a test run as conducted using an upstream length of 150 D and a downstream length of 106 D. In this test, the axial grid distribution in the region of the orifice plate and the radial grid distribution was identical to that of run number 2. The results obtained are compared with run number 2 in table 4.10.

Upstream length	Downstream length	No. of grid nodes							Discharge Coefficient		
		A1	A2	A3	A4	R1	R2	R3	Corner tappings	Flange tappings	D & 1/2 D tappings
30 D	16 D	38	21	42	38	8	21	19	0.7359	0.7358	0.7355
150 D	106 D	83	21	42	133	8	21	19	0.7353	0.7353	0.7350

Table 4.10 Effect of upstream and downstream lengths
(B ratio = 0.2)

Thus, an upstream lengths of 30 D and a downstream length of 16 D as used in run number 2 would be sufficient distances to be used in the model.

In all the above tests, the 'wall-function method' was used in specifying the wall boundary condition. An additional test run was conducted with the wall boundary condition specified by the 'low Reynolds-number modelling method' and using the same grid distribution as in run number 3. The value of the discharge coefficient (corner tappings) thus obtained was 0.4670.

4.4.4 Tests on the $\beta = 0.3$ conical entrance orifice plates

i) Grid distribution

To determine the number of grids required for the model, simulation was again performed with three different grids. The computational test section was divided into regions as depicted in figure 4.3, and the number of grids in each region was given in table 4.11. The grids in regions A2 and R2, which correspond to the conical part of the orifice plate, were uniformly spaced. The grid distribution in other region were non-uniform, being more concentrated near the walls.

	No. of grid nodes							Total no. of grid nodes (axial x radial)
	A1	A2	A3	A4	R1	R2	R3	
Test no. 1	38	20	40	38	8	20	13	136 x 41
Test no. 2	38	25	50	38	8	25	13	151 x 46
Test no. 3	62	35	70	62	10	35	17	229 x 62

Table 4.11 Grid distribution for the computational test section
(β ratio = 0.3)

ii) Upstream and downstream lengths

The lengths of the solution domain upstream and downstream of the orifice plate were specified to be 30 D and 16 D respectively in tests number 1 and 2, where D is the pipe diameter. The corresponding values were 40 D and 20 D for test number 3, with the grid density more than 40 % greater than that in test number 2.

iii) Under-relaxation

Under-relaxation factors were used to suppress divergence. 'Linear under-relaxation' was applied to the pressure while 'false-time-step under-relaxation' was applied to other variables. The values of the factors used were varied during the course of solution in order to combat divergence or to accelerate convergence. The range of values used were 0.5 for the pressure p , 0.01 to 0.05 for the axial velocity V_z and the radial velocity V_r , 0.1 for the turbulence kinetic energy k and the rate of dissipation ϵ .

iv) Results

Figure 4.7 shows the variation of the discharge coefficient (corner tappings) with the normalised residual for the axial velocity V_z for the three grid distributions shown in table 4.11. It can be seen that the discharge coefficient becomes asymptotically constant as the residual is reduced and the solution can be considered to be converged when the magnitude of the residual has reduced to below 5. The number of iterations required for the solution varied from about 15,000 sweeps for the coarser grids to over 100,000 sweeps for the finer grids. The variation of the discharge coefficients with the normalised residuals of all the variables are given in tables 4.12 to 4.14.

From table 4.12 to 4.14, it can be seen that the discharge coefficients obtained in run number 2 (151 x 46 grids) differs from that obtained in run number 3 (229 x 62 grids) by less than 0.18 %. Thus, the results obtained using the grid distribution in run number 2 (151 x 46 grids) can be regarded to be grid-independent. The value of the discharge coefficient (corner tappings) obtained with this grid distribution is 0.7451, which differs from the BS value of 0.734 (BS 1042: section 1.2: 1984) by 1.51%.

To confirm that sufficient upstream and downstream lengths were used in the model, a test run was conducted

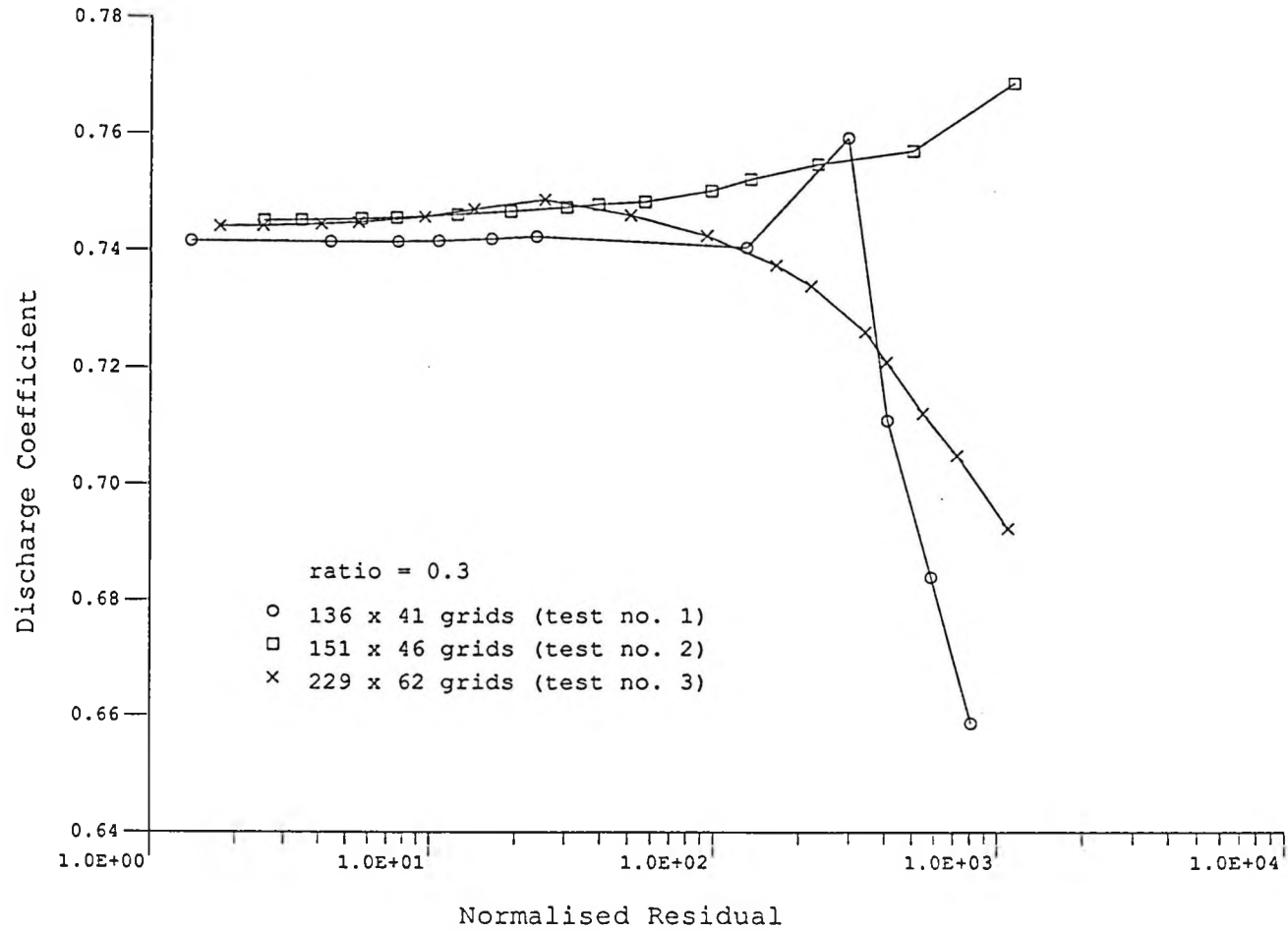


Fig. 4.7 Variation of the Discharge Coefficient with the Normalised Residual for the axial velocity component

Normalised Residuals					Discharge Coefficient		
P	V_r	V_z	K	ϵ	corner tappings	flange tappings	D & 1/2 D tappings
3.692E+1	3.963E+1	8.108E+2	6.945E+4	1.115E+5	0.6588	0.6587	0.6584
2.791E+1	3.603E+1	5.896E+2	1.359E+5	2.179E+5	0.6840	0.6838	0.6837
3.142E+1	2.540E+1	4.138E+2	6.279E+4	8.982E+4	0.7110	0.7109	0.7106
2.643E+1	2.601E+1	3.035E+2	1.321E+5	1.781E+5	0.7592	0.7592	0.7590
2.239E+1	1.203E+1	1.318E+2	1.061E+4	1.009E+4	0.7404	0.7404	0.7402
4.510E+0	3.567E+0	2.409E+1	1.897E+2	2.872E+2	0.7423	0.7422	0.7420
3.359E+0	3.154E+0	1.668E+1	3.872E+1	5.286E+1	0.7419	0.7417	0.7416
3.066E+0	2.263E+0	1.086E+1	9.811E+0	1.460E+1	0.7416	0.7415	0.7413
3.402E+0	1.708E+0	7.758E+0	2.200E+0	2.478E+0	0.7415	0.7415	0.7413
2.945E+0	1.041E+0	4.447E+0	2.552E+0	3.019E+0	0.7415	0.7415	0.7413
2.296E+0	3.891E-1	1.399E+0	4.979E-1	5.720E-1	0.7416	0.7415	0.7414

Table 4.12 Variation of normalised residuals with discharge coefficients
(β ratio = 0.3 test no. 1)

Normalised Residuals					Discharge Coefficient		
P	V_r	V_z	K	ϵ	corner tappings	flange tappings	D & 1/2 D tappings
1.147E+1	5.787E+1	1.179E+3	1.086E+3	1.608E+3	0.7686	0.7703	0.7698
3.200E+0	3.169E+1	5.149E+2	2.182E+2	3.313E+2	0.7570	0.7579	0.7581
2.836E+0	1.725E+1	2.367E+2	6.115E+1	8.923E+1	0.7547	0.7554	0.7554
2.997E+0	8.415E+0	1.364E+2	2.528E+1	3.463E+1	0.7521	0.7525	0.7526
2.401E+0	3.439E+0	9.948E+1	1.250E+1	1.686E+1	0.7501	0.7503	0.7505
2.900E+0	5.660E-1	5.791E+1	8.977E+0	1.311E+1	0.7482	0.7483	0.7484
2.236E+0	2.489E-1	3.978E+1	9.877E+0	1.605E+1	0.7478	0.7477	0.7478
3.158E+0	1.597E-1	3.083E+1	6.899E+0	1.107E+1	0.7473	0.7473	0.7473
3.270E+0	1.517E-1	1.947E+1	5.699E+0	8.650E+0	0.7466	0.7466	0.7466
3.305E+0	1.705E-1	1.261E+1	2.408E+0	3.542E+0	0.7461	0.7460	0.7459
2.862E+0	1.539E-1	7.648E+0	2.053E+0	2.962E+0	0.7456	0.7456	0.7454
2.666E+0	1.471E-1	5.716E+0	9.071E-1	1.254E+0	0.7454	0.7453	0.7452
2.442E+0	1.353E-1	3.496E+0	2.787E+0	3.847E+0	0.7452	0.7452	0.7449
2.367E+0	1.310E-1	2.550E+0	4.169E-1	4.317E-1	0.7451	0.7451	0.7449

Table 4.13 Variation of normalised residuals with discharge coefficients
(β ratio = 0.3 test no. 2)

Normalised Residuals					Discharge Coefficient		
P	V _r	V _z	K	ε	corner tappings	flange tappings	D & 1/2 D tappings
1.207E+1	3.600E+1	1.104E+3	2.361E+2	5.665E+2	0.6924	0.6914	0.6907
5.365E+0	2.157E+1	7.305E+2	5.490E+1	1.330E+2	0.7050	0.7040	0.7033
4.978E+0	1.550E+2	5.535E+2	1.177E+2	9.794E+1	0.7122	0.7111	0.7103
5.298E+0	9.342E+0	4.118E+2	1.036E+2	5.606E+1	0.7210	0.7201	0.7193
5.492E+0	6.330E+0	3.463E+2	2.066E+1	3.627E+1	0.7261	0.7251	0.7243
5.438E+0	4.121E+0	2.234E+2	1.805E+1	3.044E+1	0.7339	0.7330	0.7320
5.082E+0	3.436E+0	1.676E+2	1.715E+1	2.721E+1	0.7374	0.7365	0.7356
4.719E+0	3.460E+0	9.577E+1	1.225E+1	1.724E+1	0.7424	0.7416	0.7407
4.441E+0	4.060E+0	5.163E+1	9.159E+0	1.092E+1	0.7459	0.7454	0.7445
5.150E+0	3.108E+0	2.580E+1	3.519E+0	1.368E+0	0.7486	0.7483	0.7476
4.955E+0	1.046E+0	1.443E+1	2.027E+0	1.182E+0	0.7470	0.7469	0.7465
4.322E+0	4.616E-1	9.688E+0	2.207E+0	1.617E+0	0.7457	0.7456	0.7452
4.843E+0	3.371E-1	5.590E+0	9.273E+0	1.344E+1	0.7448	0.7447	0.7443
4.763E+0	3.600E-1	4.119E+0	9.306E+0	1.575E+1	0.7445	0.7444	0.7440
4.922E+0	3.580E-1	2.532E+0	3.112E+0	5.485E+0	0.7442	0.7441	0.7437
5.175E+0	3.601E-1	1.770E+0	7.318E+0	1.278E+1	0.7441	0.7440	0.7436

Table 4.14 Variation of normalised residuals with discharge coefficients
(β ratio = 0.3 test no. 3)

using an upstream length of 150 D and a downstream length of 106 D. In this test, the axial grid distribution in the region of the orifice plate and the radial grid distribution was identical to that of run number 2. The results obtained are compared with run number 2 in table 4.15.

Upstream length	Downstream length	No. of grid nodes							Discharge Coefficient		
		A1	A2	A3	A4	R1	R2	R3	Corner tappings	Flange tappings	D & 1/2 D tappings
30 D	16 D	38	25	50	38	8	25	13	0.7451	0.7451	0.7449
150 D	106 D	83	25	50	133	8	25	13	0.7445	0.7444	0.7443

Table 4.15 Effect of upstream and downstream lengths
(β ratio = 0.3)

Thus, an upstream length of 30 D and a downstream length of 16 D as used in run number 2 would be sufficient distances to be used in the model.

The 'wall-function method' was used in specifying the wall boundary condition in all the above tests. An additional test run was carried out with the wall boundary conditions specified by the 'low-Reynolds number modelling method', using the same grid distribution as in run number 2. The value of the discharge coefficient (corner tappings) thus obtained was 0.5148.

4.4.5 Concluding remarks on the tests

Tests were conducted on conical entrance orifice plates with β ratios of 0.1, 0.2 and 0.3. The grid

distributions for the solution to be grid-independent were determined, and these were 121 x 54 grids for $\beta = 0.1$, 139 x 48 grids for $\beta = 0.2$ and 151 x 46 grids for $\beta = 0.3$. These grid distributions and the ones with higher grid density (i.e. 184 x 72 grids for $\beta = 0.1$, 220 x 70 grids for $\beta = 0.2$ and 229 x 62 grids for $\beta = 0.3$) would be used in the study of the characteristics of the conical entrance orifice plates.

The tests also showed that, with the wall boundary conditions specified by the 'low-Reynolds-number modelling' method, the discharge coefficients obtained deviate significantly from the BS value of 0.734. Chen (63) had similar observation on the use of 'low-Reynolds-number modelling' method in specifying wall boundary conditions in his investigation on the natural convection in a large-scale air-filled cavity. He used both the 'low-Reynolds-number modelling' method and the 'wall-function' method, and found that the results obtained with the first method deviated from the experimental data.

The 'low-Reynolds-number modelling' method probably need a much finer grid distribution near the walls than the 'wall-function' method to give the correct result. Thus, only the 'wall-function' method would be used in specifying the wall boundary conditions in the investigation of the characteristics of the conical entrance orifice plates.

A typical Q1 file, which supplied all information as to what is to be simulated to 'EARTH", is given in Appendix B.

CHAPTER 5

APPLICATIONS OF THE MODEL

5.1 Introduction

The development of the model for the conical entrance orifice plate flow sensor was discussed in the last chapter. Tests were performed at a Reynolds number (Re_D) of 60,000, and the grid distributions required for the solution to be regarded as grid-independent were determined. These grid distributions (i.e. 121 x 54 grids for $\beta = 0.1$, 139 x 48 grids for $\beta = 0.2$ and 151 x 46 grids for $\beta = 0.3$) and the ones with larger number of grids (i.e. 184 x 72 grids for $\beta = 0.1$, 220 x 70 grids for $\beta = 0.2$ and 229 x 62 grids for $\beta = 0.3$) are used in the present chapter to investigate the characteristics of the conical entrance orifice plate flow sensors.

5.2 Effect of Reynolds number on the discharge coefficient

5.2.1 Computed discharge coefficients

Table 5.1 shows the computed discharge coefficients against the Reynolds number (Re_D) for various β ratio. It can be seen from the table that the discharge coefficients vary with the Reynolds number and with the β ratio. This is also evident from figures 5.1 to 5.3.

In order to measure the pressure difference across the orifice plate, BS 1042 : Section 1.2 specified that

β	Reynolds Number	Discharge Coefficient		
		Corner tappings	Flange tappings	D & 1/2 D tappings
0.1	80	0.7139 (-2.74 %)	0.7139	0.7139
	1,000	0.7211 (-1.76 %)	0.7211	0.7211
	2,000	0.7215 (-1.70 %)	0.7215	0.7215
	4,000	0.7214 (-1.72 %)	0.7214	0.7214
	6,000	0.7203 (-1.87 %)	0.7203	0.7203
	10,000	0.7186 (-2.10 %)	0.7186	0.7186
	30,000	0.7190 (-2.04 %)	0.7190	0.7189
	60,000	0.7199 (-1.92 %)	0.7198	0.7197
0.2	80	0.7200 (-1.91 %)	0.7201	0.7199
	1,000	0.7379 (0.53 %)	0.7379	0.7379
	2,000	0.7410 (0.95 %)	0.7410	0.7410
	4,000	0.7428 (1.20 %)	0.7428	0.7428
	6,000	0.7390 (0.68 %)	0.7390	0.7390
	10,000	0.7438 (1.34 %)	0.7438	0.7436
	30,000	0.7356 (0.22 %)	0.7355	0.7352
	60,000	0.7359 (0.26 %)	0.7358	0.7355
0.3	80	0.7239 (-1.38 %)	0.7242	0.7239
	1,000	0.7476 (1.85 %)	0.7476	0.7476
	2,000	0.7520 (2.45 %)	0.7521	0.7522
	4,000	0.7545 (2.79 %)	0.7547	0.7547
	6,000	0.7556 (2.94 %)	0.7557	0.7557
	10,000	0.7492 (2.07 %)	0.7493	0.7497
	30,000	0.7457 (1.59 %)	0.7456	0.7454
	60,000	0.7451 (1.51 %)	0.7451	0.7449

* value in bracket is the percentage variation of the discharge coefficient from that given in BS 1042 : Section 1.2 : 1984

Table 5.1 Variation of discharge coefficient with Reynolds number

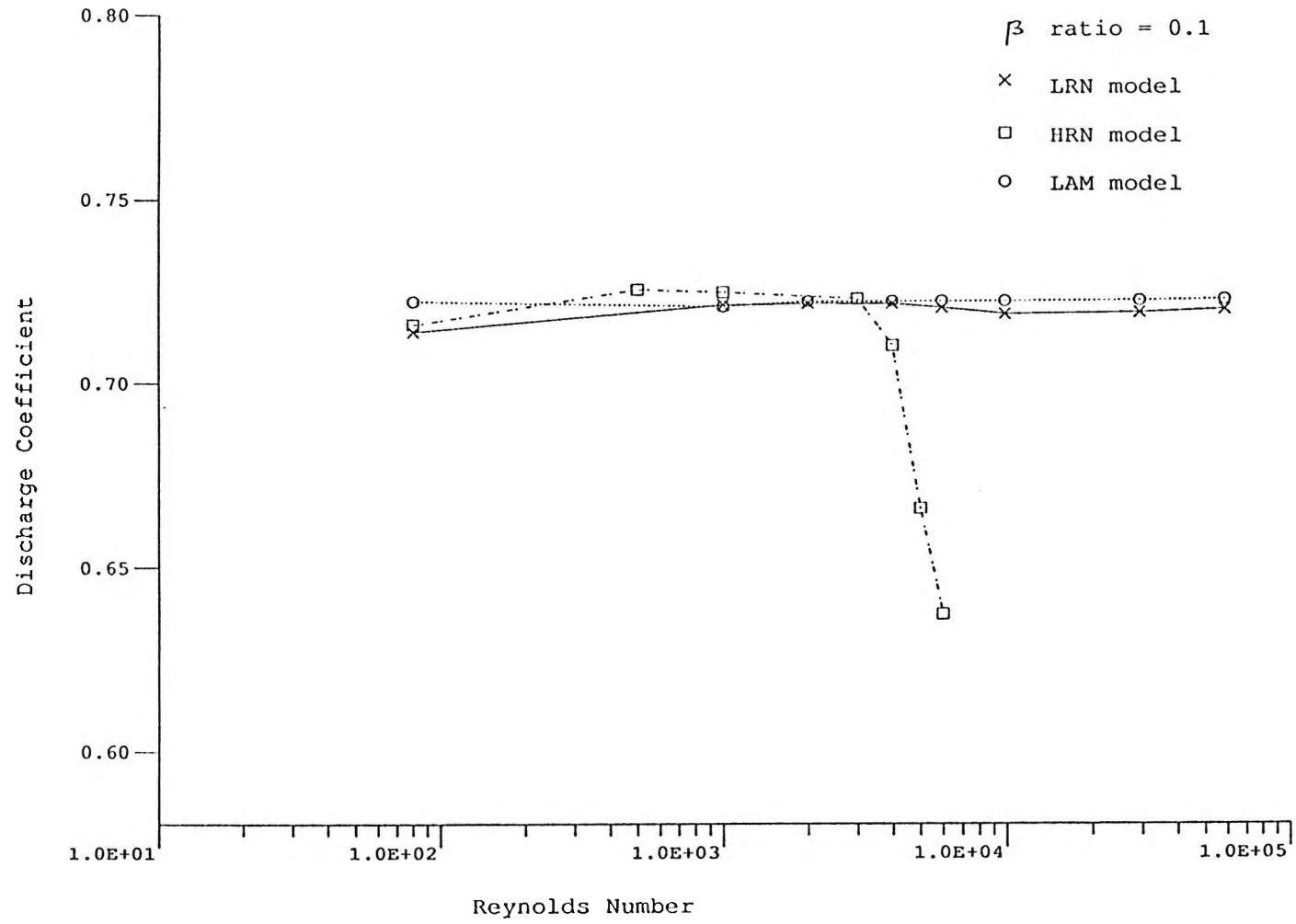


Fig. 5.1 Variation of the computed discharge coefficient with Reynolds number

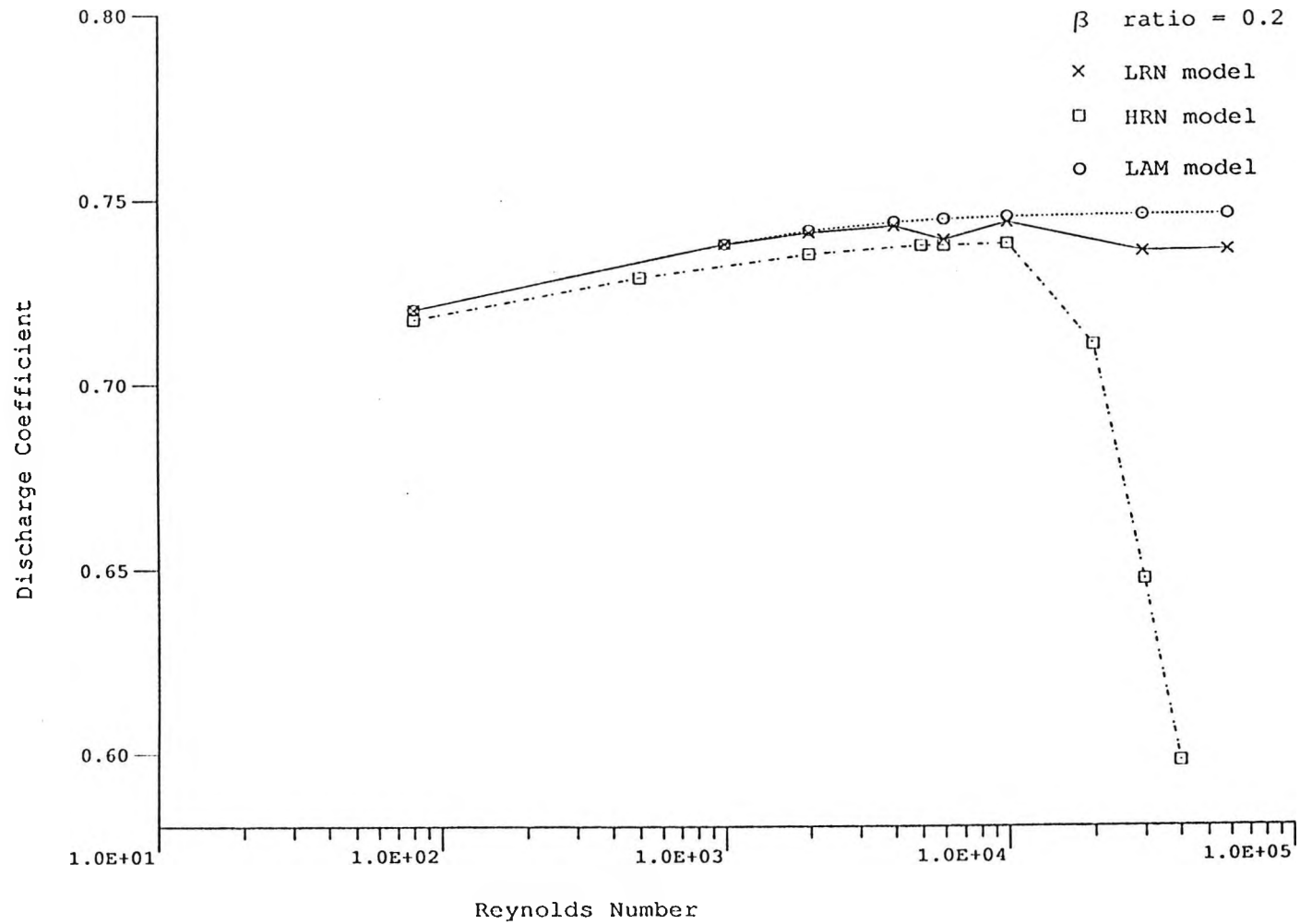


Fig. 5.2 Variation of the computed discharge coefficient with Reynolds number

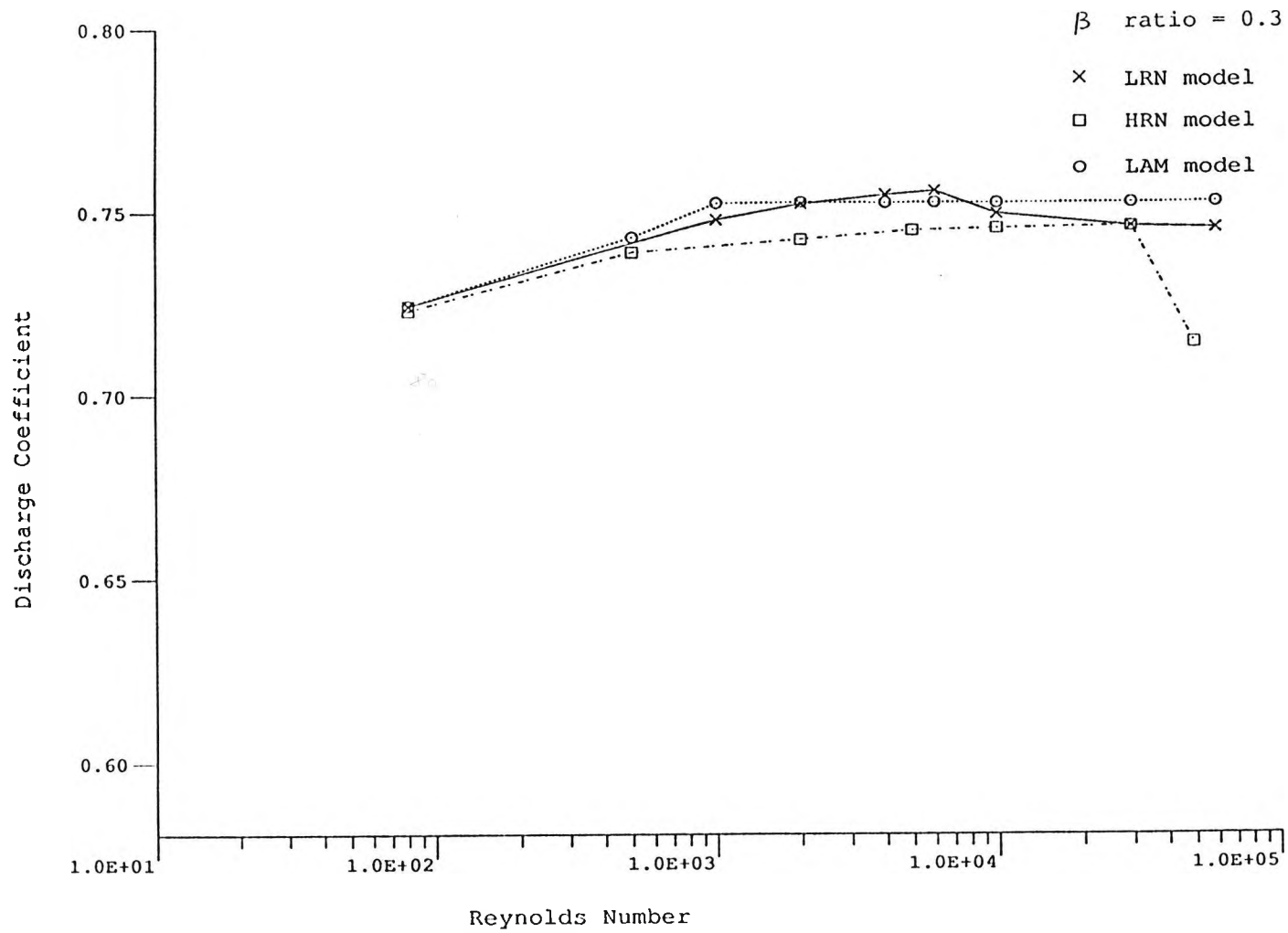


Fig. 5.3 Variation of the computed discharge coefficient with Reynolds number

corner tapplings shall be used with conical entrance orifice plates, and the discharge coefficient given is based on the use of corner tapplings. However, it can be seen from table 5.1 that the discharge coefficients obtained from the computed pressure at locations corresponding to the use of corner tapplings, flange tapplings and $D \& \frac{1}{2} D$ tapplings are almost identical, with difference occuring only at the fourth digit after the decimal point.

Thus, the computed results suggest that, in addition to corner tapplings as specified in BS 1042 : Section 1.2, flange tapplings and $D \& \frac{1}{2} D$ tapplings can also be used as pressure tapplings with the conical entrance orifice plate flow sensors in flow measurement, and that there is practically no difference in the discharge coefficients for each type of tapplings.

The variation of the computed discharge coefficients with Reynolds number (Re_p) is also shown in figures 5.1 to 5.3. Since the discharge coefficients are almost identical for the three types of tapplings, only the results obtained using corner tapplings are presented in the figures.

Besides the Lam-Bremhorst $k-\epsilon$ model (LRN model), results were also obtained using the standard $k-\epsilon$ model (HRN model) and by assuming laminar flow in the computa-

tional test section (LAM model). The discharge coefficients (corner tappings) obtained by using the different models are also presented in figures 5.1 to 5.3.

From these figures, it can be seen that for the HRN model, the discharge coefficients obtained vary significantly with the Reynolds number as the Reynolds number gets larger, and that the discharge coefficients differ significantly from the BS value of 0.734 at these larger Reynolds numbers. Apparently, the flow is locally behaving more viscously than that indicated by the Reynolds number.

For the LRN model and LAM model, the discharge coefficients obtained vary with the Reynolds number in approximately the same manner. As would be expected, the difference between the discharge coefficients obtained by the two models is very small at the lower Reynolds numbers, with the difference gets larger as the Reynolds number is increased. This is particularly evident in figure 5.2 and 5.3, which show the computed results for $\beta = 0.2$ and 0.3 .

5.2.2 Comparison with experimental results

In order to test and verify the validity of the model, the computed discharge coefficients have to be compared with available experimental results. Only limited experimental results had been published on the

performance of conical entrance orifice plates (23-27). Of the available information, those reported by Stoll and Zientara (24) and Turton (26) covered a wide range of Reynolds numbers and β ratio. The others were concerned only with a limited range. Thus, the results reported by Stoll and Zientara and Turton are used to test the model.

Figures 5.4 to 5.6 show the comparison of the computed discharge coefficient with the experimental results reported by Stoll and Zientara and Turton. The results are all based on the use of corner tapplings. It can be seen from these figures that the discharge coefficients predicted by the LRN model are lower than most of the experimental results for $\beta = 0.1$. For $\beta = 0.2$ and 0.3 , the predicted discharge coefficients are lower than most of the experimental values for the lower Reynolds numbers, and higher than most of the experimental values for the larger Reynolds numbers. In general, the predicted discharge coefficients can be said to fall within the range of values obtained experimentally. The comparison of the computed discharge coefficient with the experimental results can be considered to be reasonable and trends of the discharge coefficient predicted by the LRN model parallel the published results.

The difference between the predicted discharge coefficients and the experimental results might partly be due to the geometry of the conical entrance orifice

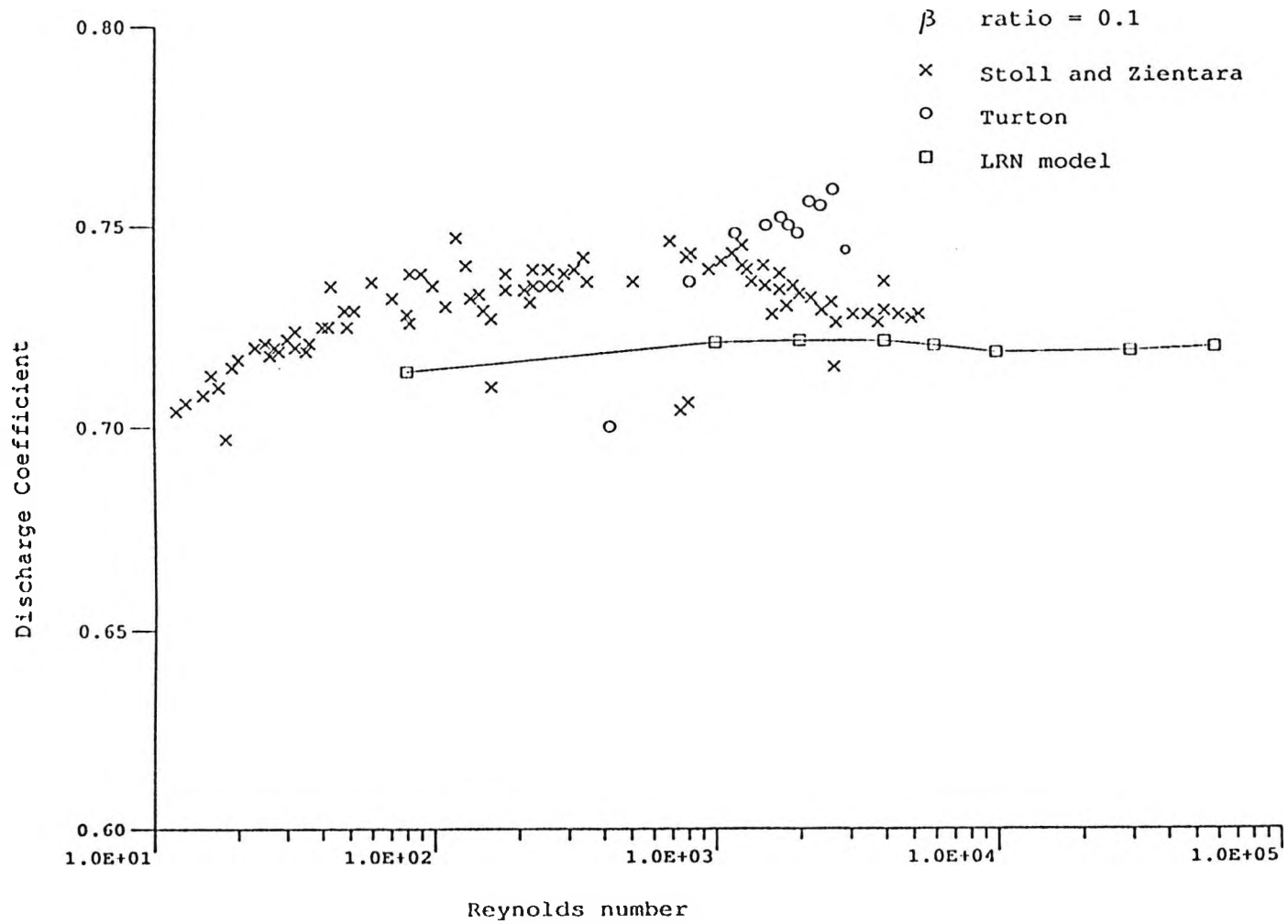


Fig. 5.4 Comparison of the computed discharge coefficient with experimental results

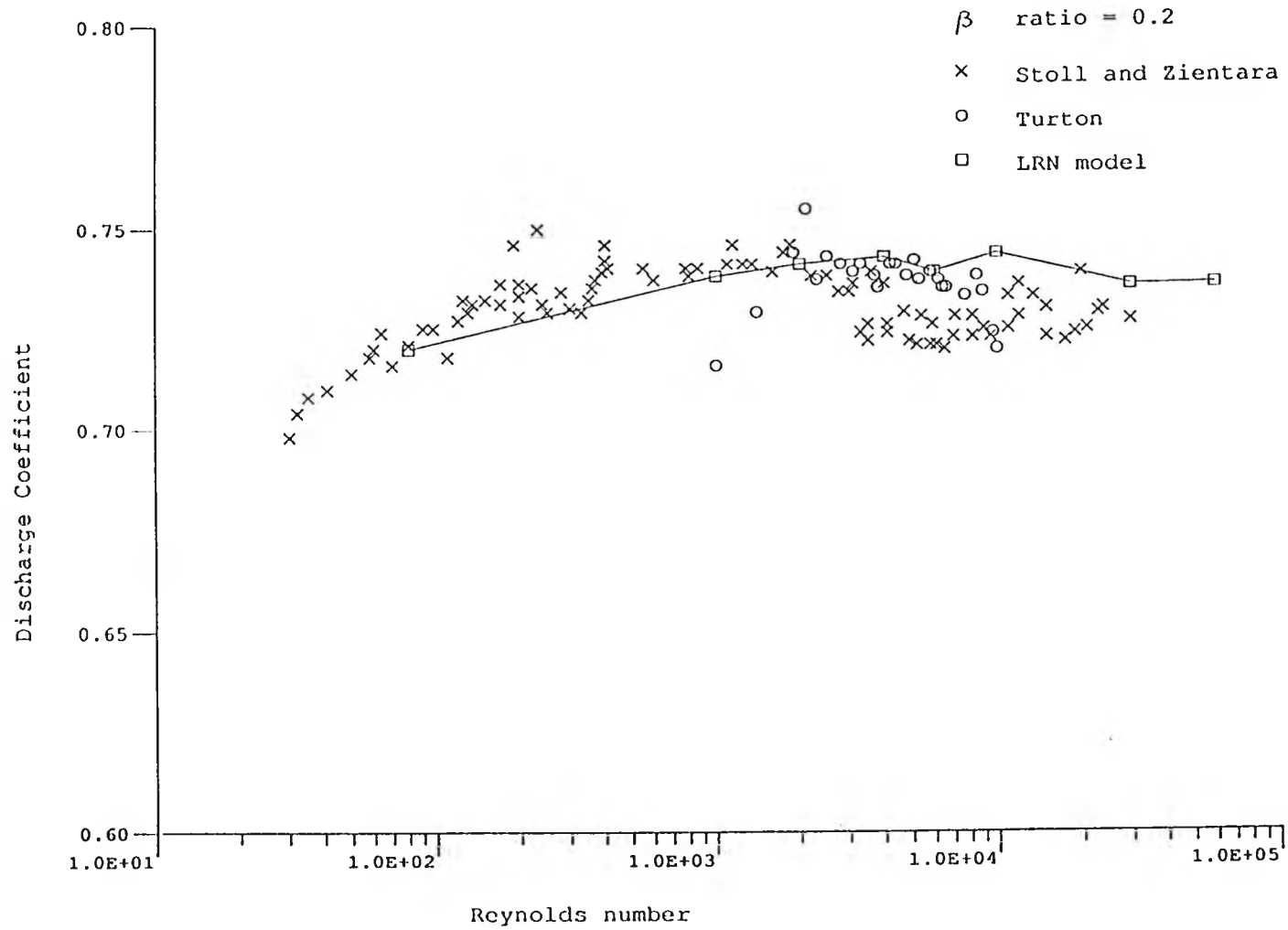


Fig. 5.5 Comparison of the computed discharge coefficient with experimental results

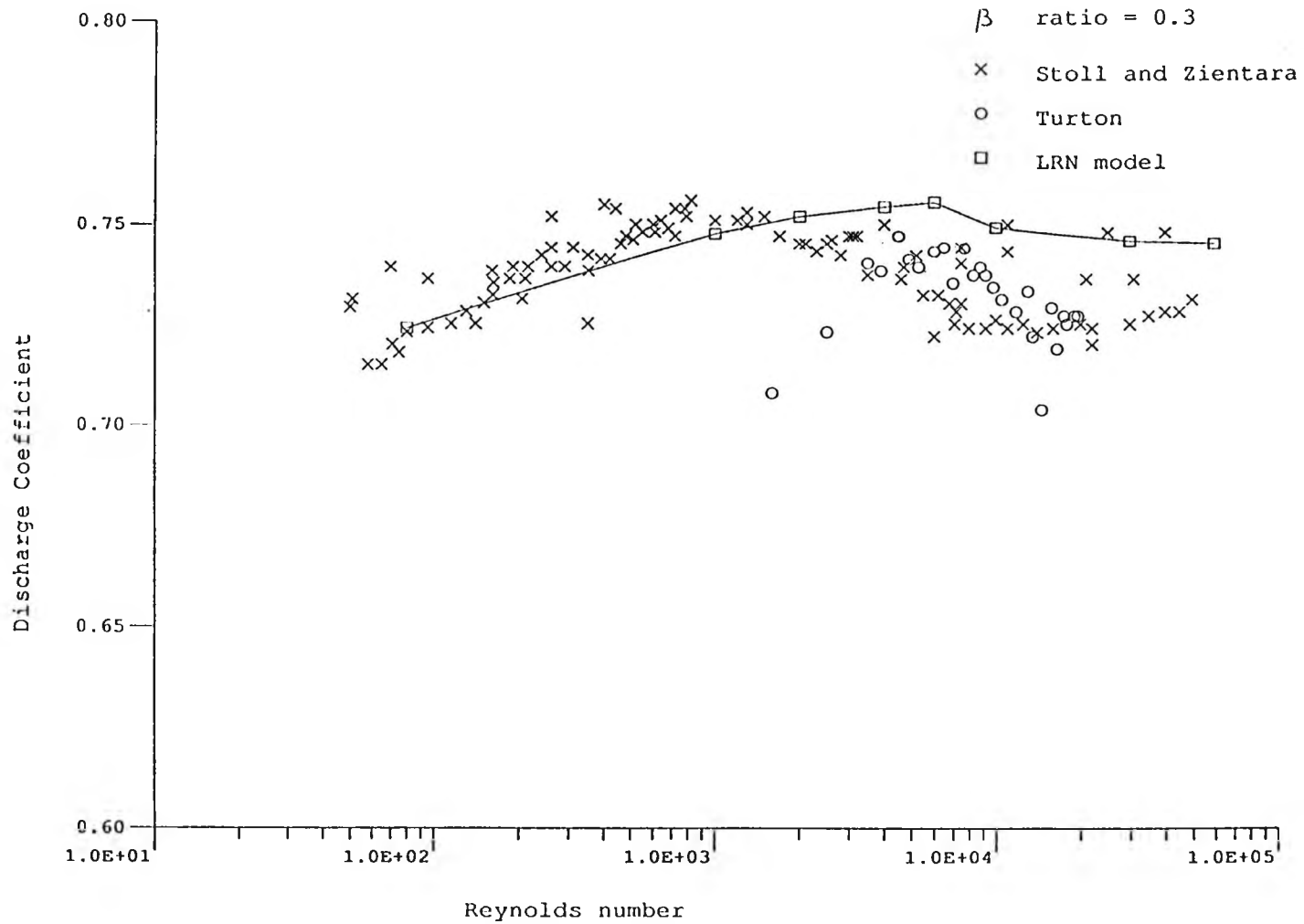


Fig. 5.6 Comparison of the computed discharge coefficient with experimental results

plates used. In the numerical model, the geometry and dimensions as specified in BS 1042 : Section 1.2 were used. However, the work reported by Stoll and Zientara was on conical entrance orifice plates similar to the KENT P.L. type orifice. The geometry of the KENT plate is a function of β , although at low values of β , the dimensions of the KENT plate are within the limits specified in BS 1042 : Section 1.2. Stoll and Zientara gave information on the dimensions of one set of plates tested, and some of these dimensions were outside the limits specified in BS 1042. The results presented by Turton were on plates manufactured in accordance with BS 1042 : Section 1.2. However, as reported by Turton, it was difficult to observe the dimensional tolerances specified and most of the plates used in the experiment had dimensions outside the limits given in BS 1042. Since the actual dimensions of the orifice plates used in the experiments are not exactly the same as that used in the numerical model, difference between the computed discharge coefficients and the experimental results might be expected.

5.2.3 Comparison with values given in British Standard

BS 1042 : Section 1.2 : 1984 limits the use of conical entrance orifice plates to values of β between 0.1 and 0.316, and for Reynolds numbers between 80 and 60,000. The revision of BS 1042 : Section 1.2 in 1989 further limits the use of conical entrance orifice plates

to Reynolds numbers between 80 and $2 \times 10^5 \beta$. A constant discharge coefficient of $0.734 \pm 2 \%$ is given in both editions of BS 1042 : Section 1.2.

The variation of the computed discharge coefficients from the value given in the British Standard is shown in table 5.1. The same information is also plotted in figure 5.7. From the figure, it can be seen that the difference between the computed discharge coefficients and the value given in the British Standard is a function of Reynolds number and the β ratio, and the LRN model predicted the discharge coefficient to within $\pm 3 \%$ of the value stated in BS 1042 : Section 1.2.

Figure 5.7 and table 5.1 also show that the greatest difference between the predicted and given value of discharge coefficient occurs at a Reynolds number below 10,000. For Reynolds numbers between 10,000 and 60,000, the discharge coefficients as predicted by the LRN model are within $\pm 2.1 \%$ of the value given in the Standard for all the three β ratios investigated. This results suggest that the conical entrance orifice plates can be used for Reynolds numbers up to 60,000, as asserted in the earlier edition (1984) of BS 1042 : Section 1.2, and if the discharge coefficient is taken as a function of β , the tolerance on the discharge coefficient can be reduced.

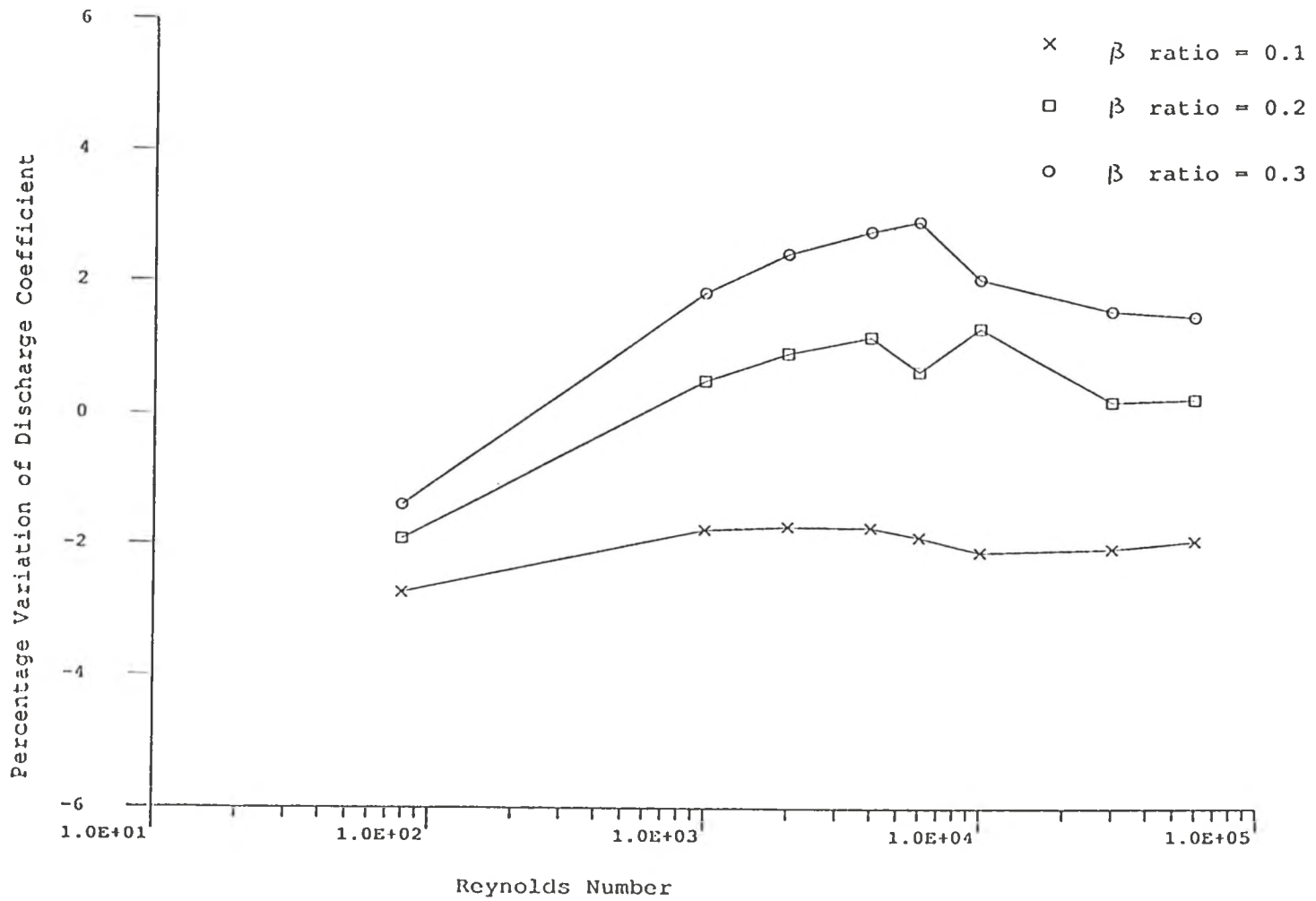


Fig. 5.7 Variation of the computed discharge coefficient from that given in BS 1042 : Section 1.2

5.3 Pressure profile and flow pattern through the conical entrance orifice plate

5.3.1 Variation of wall pressure along pipe

Figure 5.8 to 5.13 show the variation of wall pressure along the pipe as predicted by the LRN model for values of β from 0.1 to 0.3, and for Reynolds numbers between 80 and 60,000. From such pressure profiles, it is possible to compute the discharge coefficients with any particular choice of pressure tapings.

The streamwise distribution of static pressure along the pipe wall is shown in figures 5.8 and 5.9 for a Reynolds number of 60,000 and 30,000 respectively. Evident from the figures are the pressure drop caused by the presence of the orifice plate, and the location of the point of minimum pressure downstream of the orifice.

Figures 5.10(a) to 5.10(c) present the variation of wall pressure along the pipe for a Reynolds number of 10,000 for the three β ratios under investigation. It can be seen from these figures that the pressure minima evident in figures 5.8 and 5.9 can no longer be observed for $\beta = 0.1$ and 0.3. Downstream of the orifice, the computed wall pressure remains almost constant up to the outlet plane for these two β ratios.

Figures 5.11(a) to 5.11(g) show the streamwise wall pressure distribution for a Reynolds number of 6,000 as

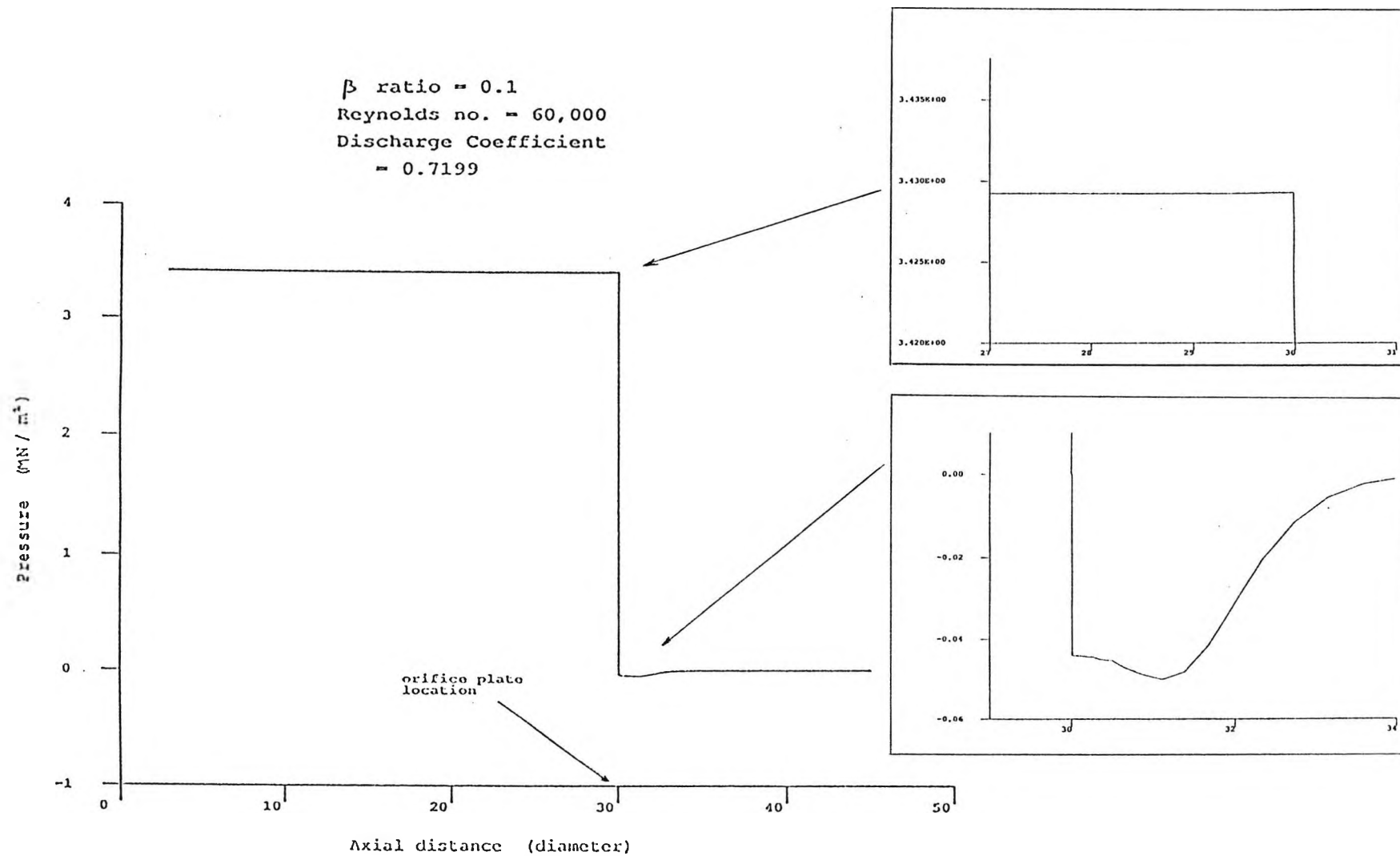


Fig. 5.8(a) Variation of the predicted wall pressure along the pipe

β ratio = 0.2
 Reynolds no. = 60,000
 Discharge Coefficient
 = 0.7359

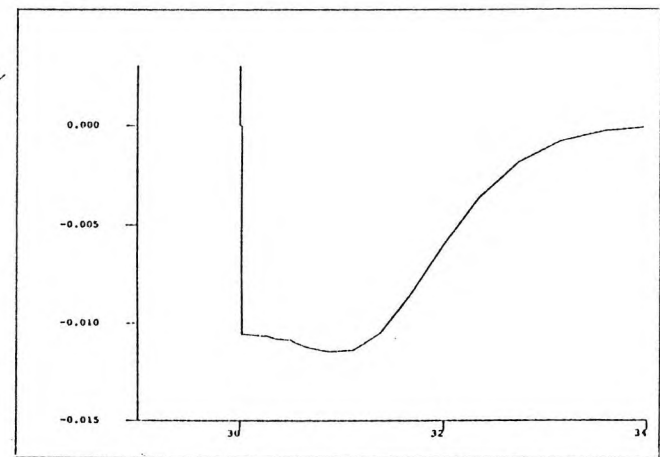
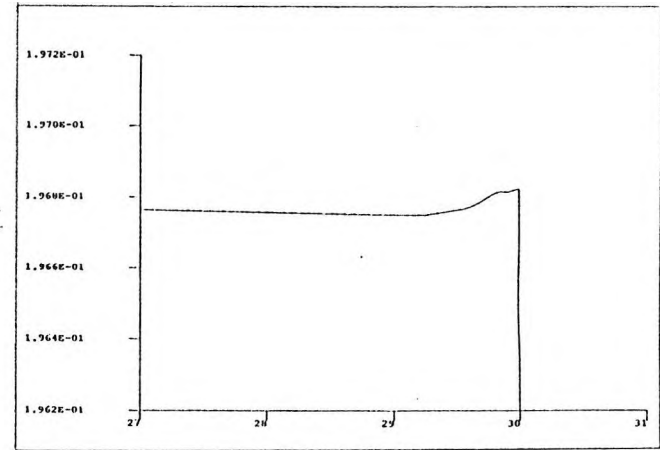
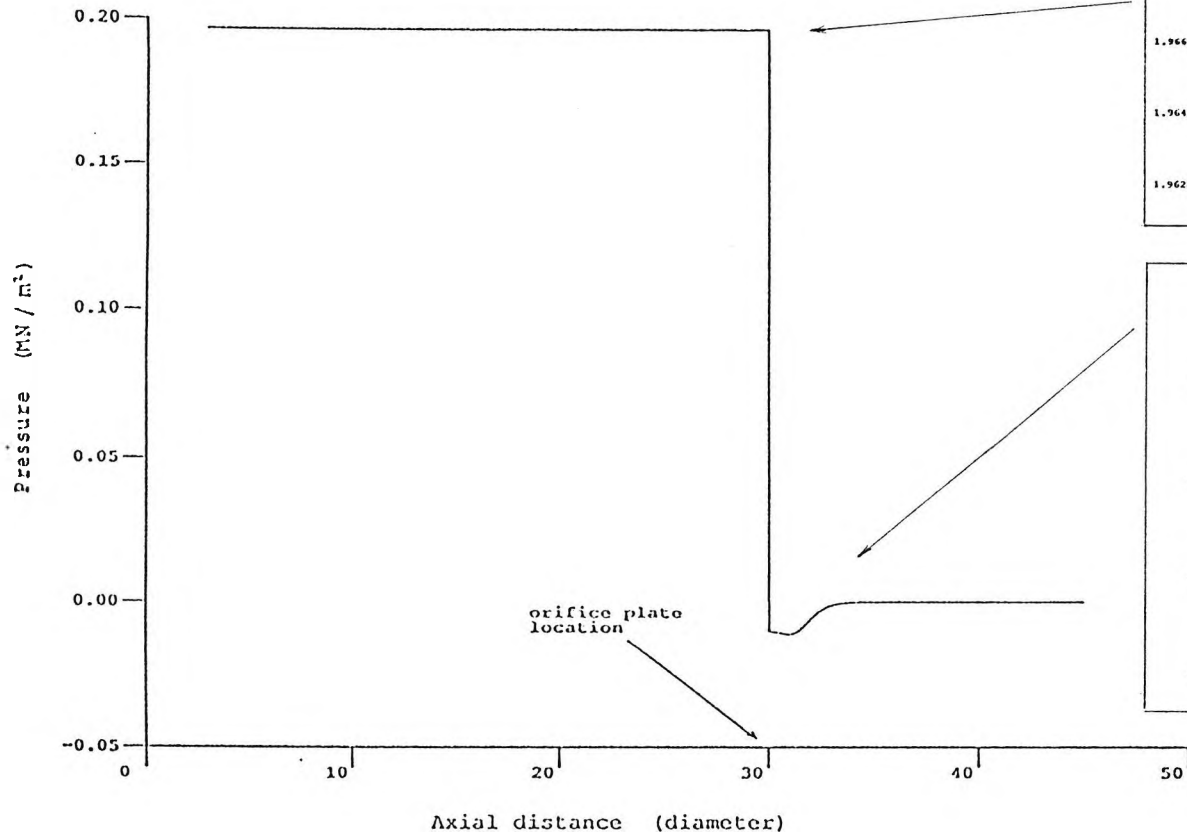


Fig. 5.8(b) Variation of the predicted wall pressure along the pipe

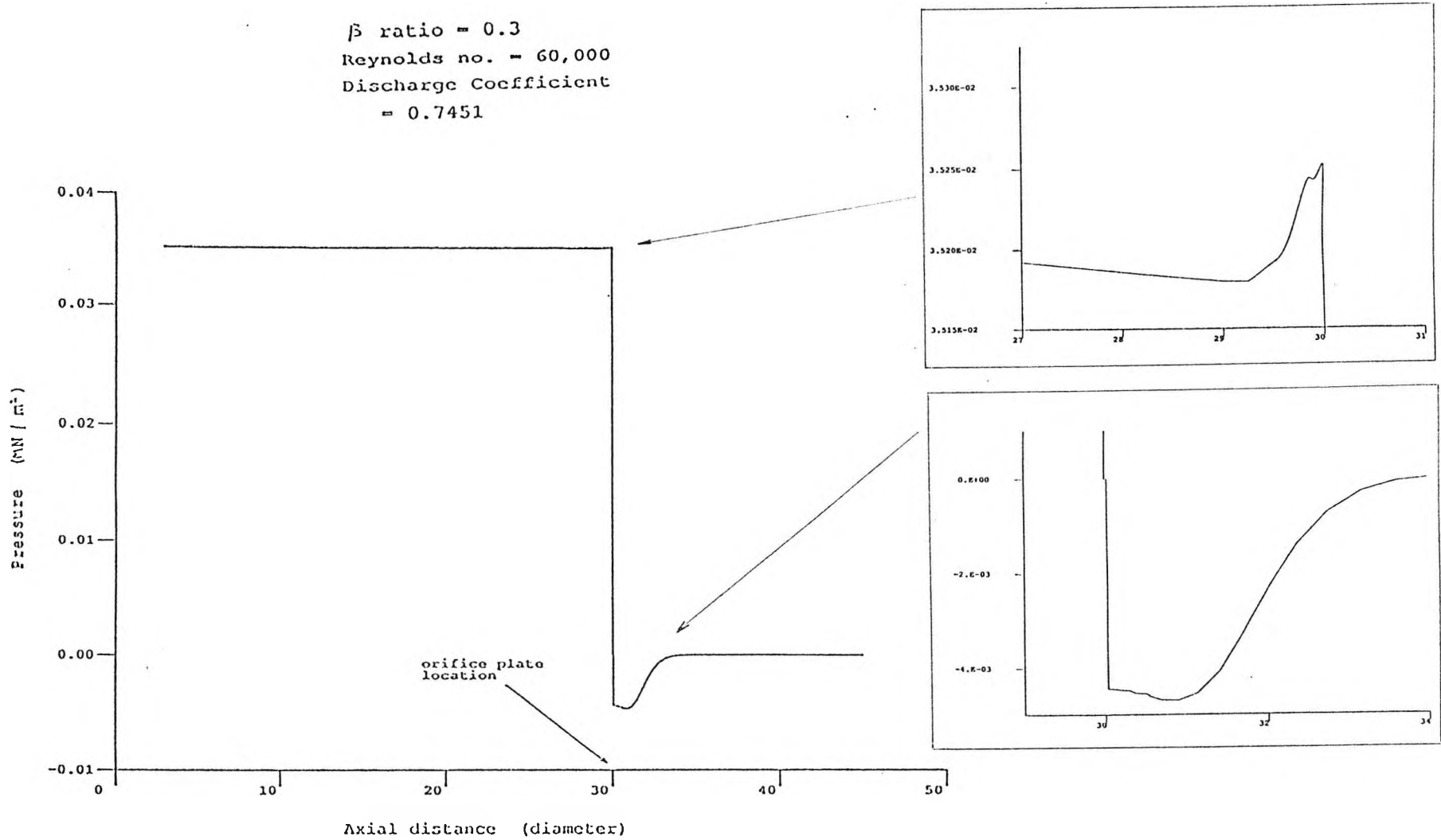


Fig. 5.8(c) Variation of the predicted wall pressure along the pipe

β ratio = 0.1
Reynolds no. = 30,000
Discharge Coefficient
= 0.7190

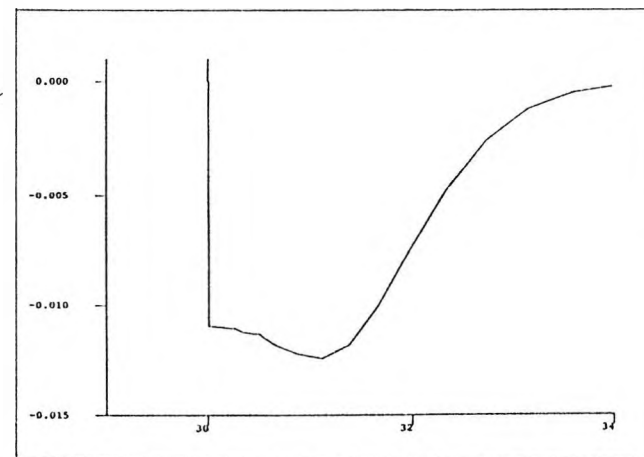
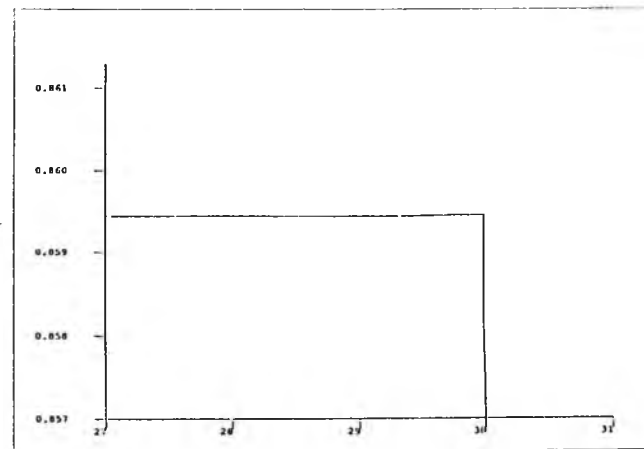
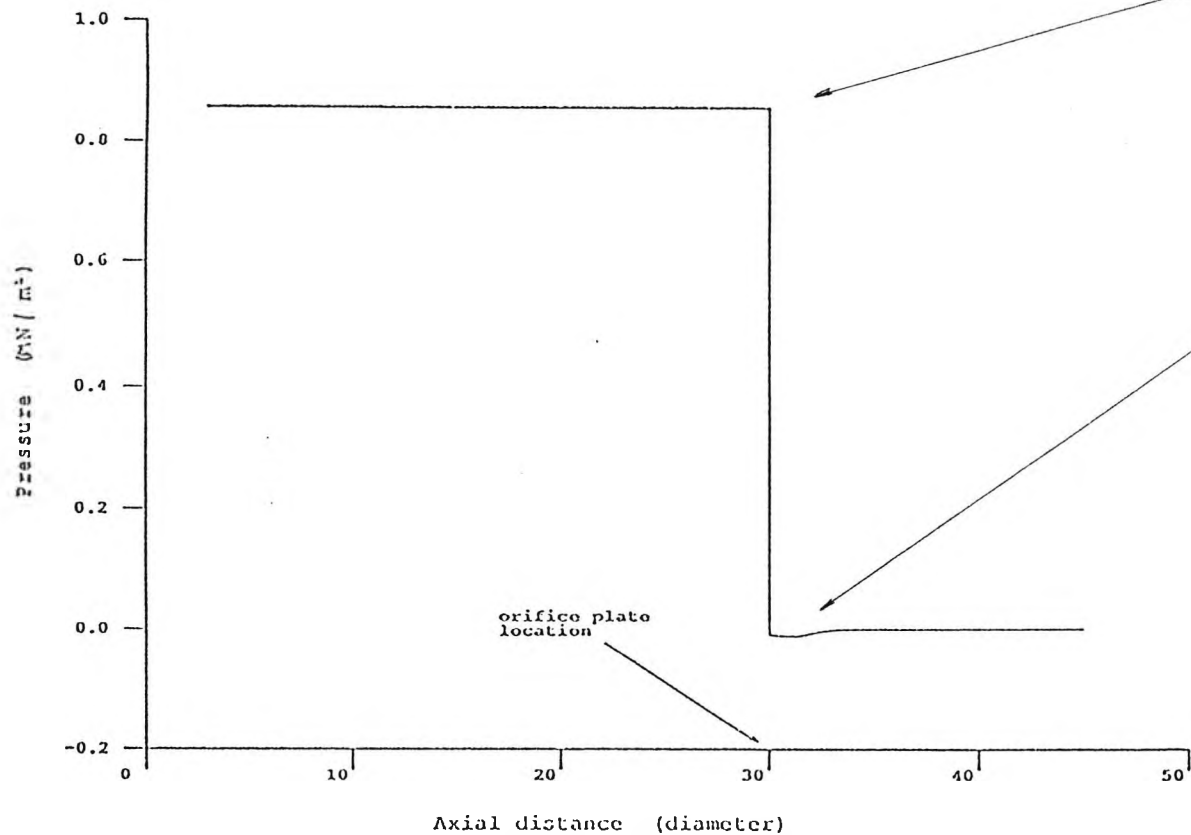


Fig. 5.9(a) Variation of the predicted wall pressure along the pipe

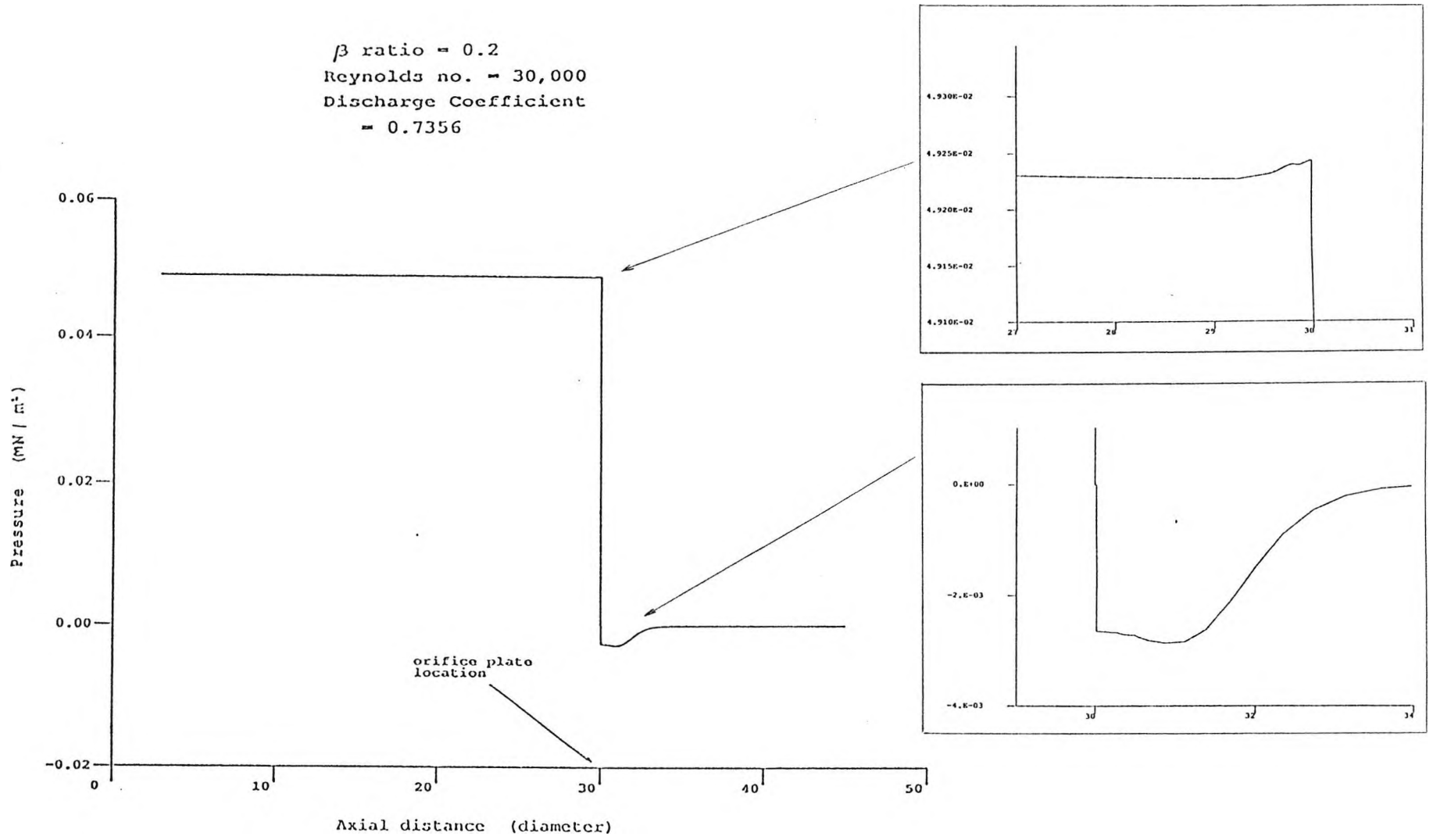


Fig. 5.9(b) Variation of the predicted wall pressure along the pipe

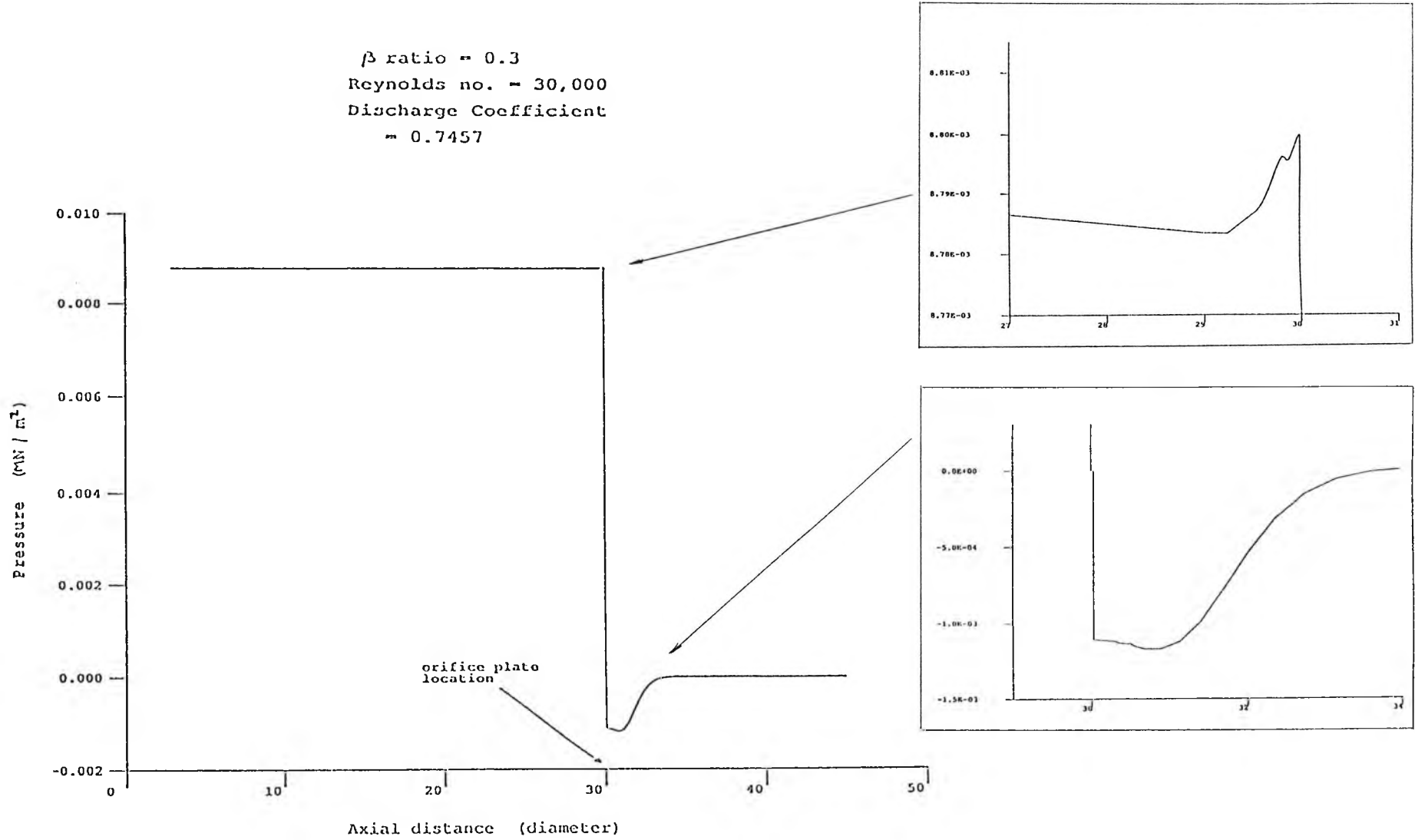


Fig. 5.9(c) Variation of the predicted wall pressure along the pipe

β ratio = 0.1
 Reynolds no. = 10,000
 Discharge Coefficient
 = 0.7186

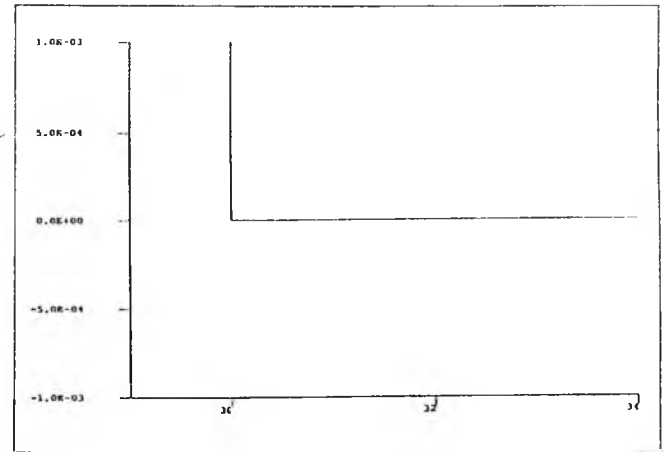
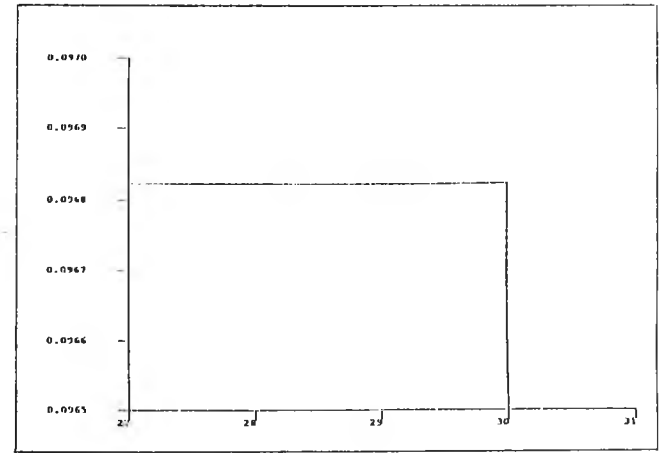
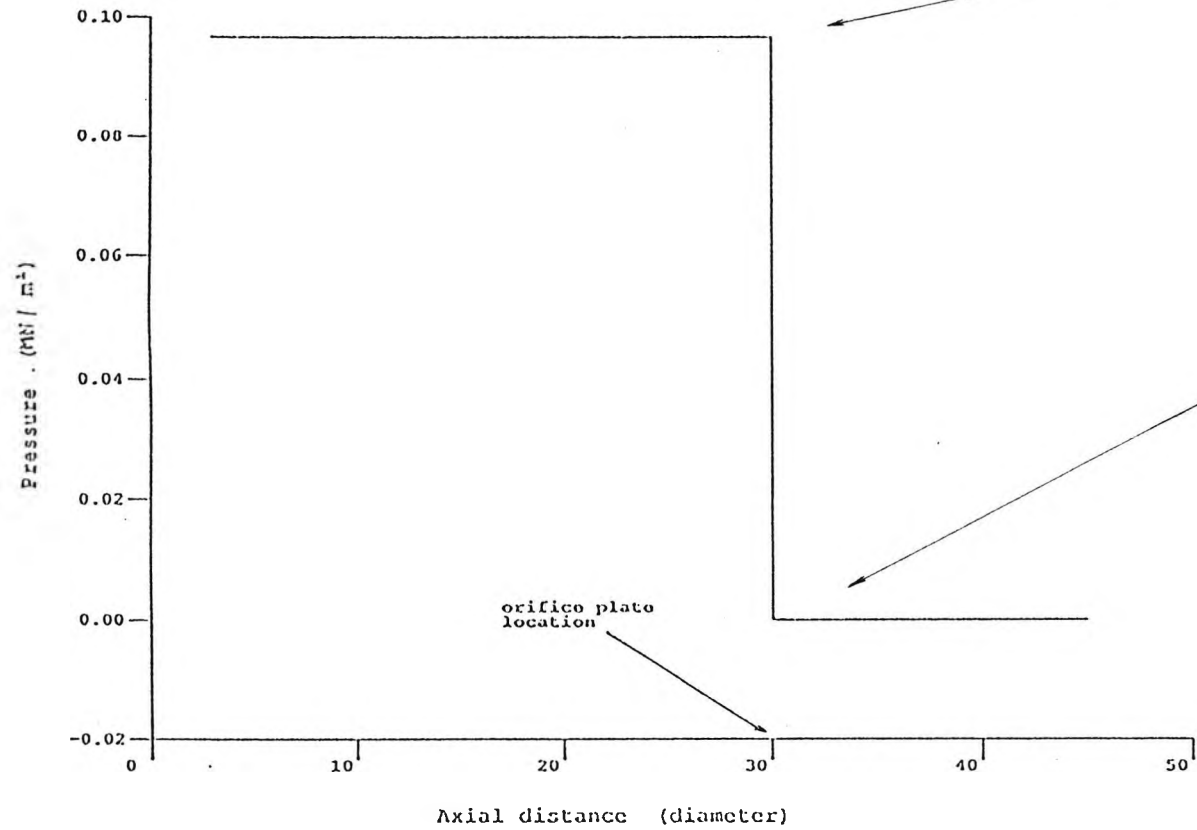


Fig. 5.10(a) Variation of the predicted wall pressure along the pipe

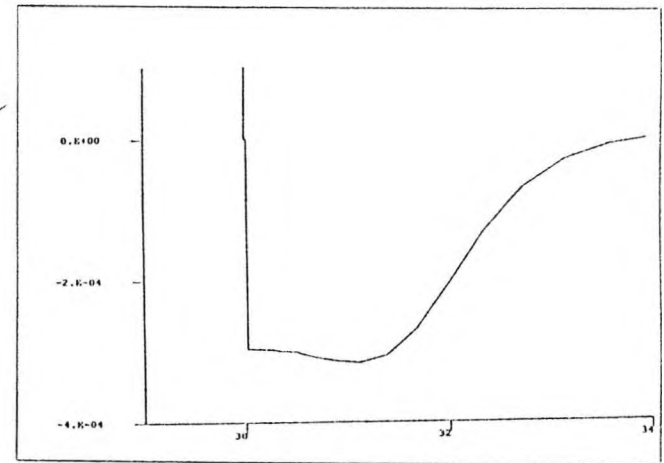
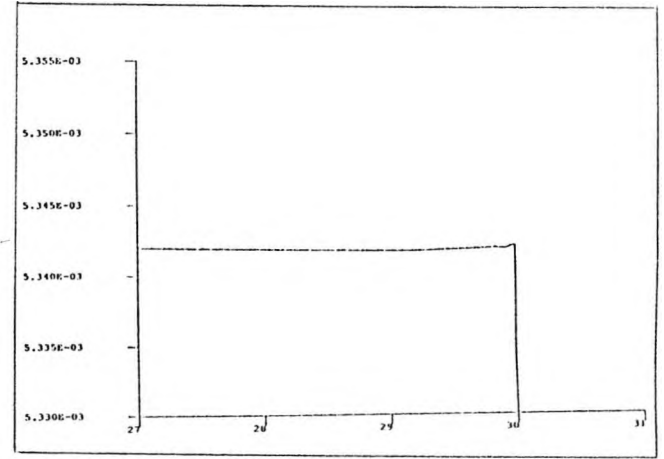
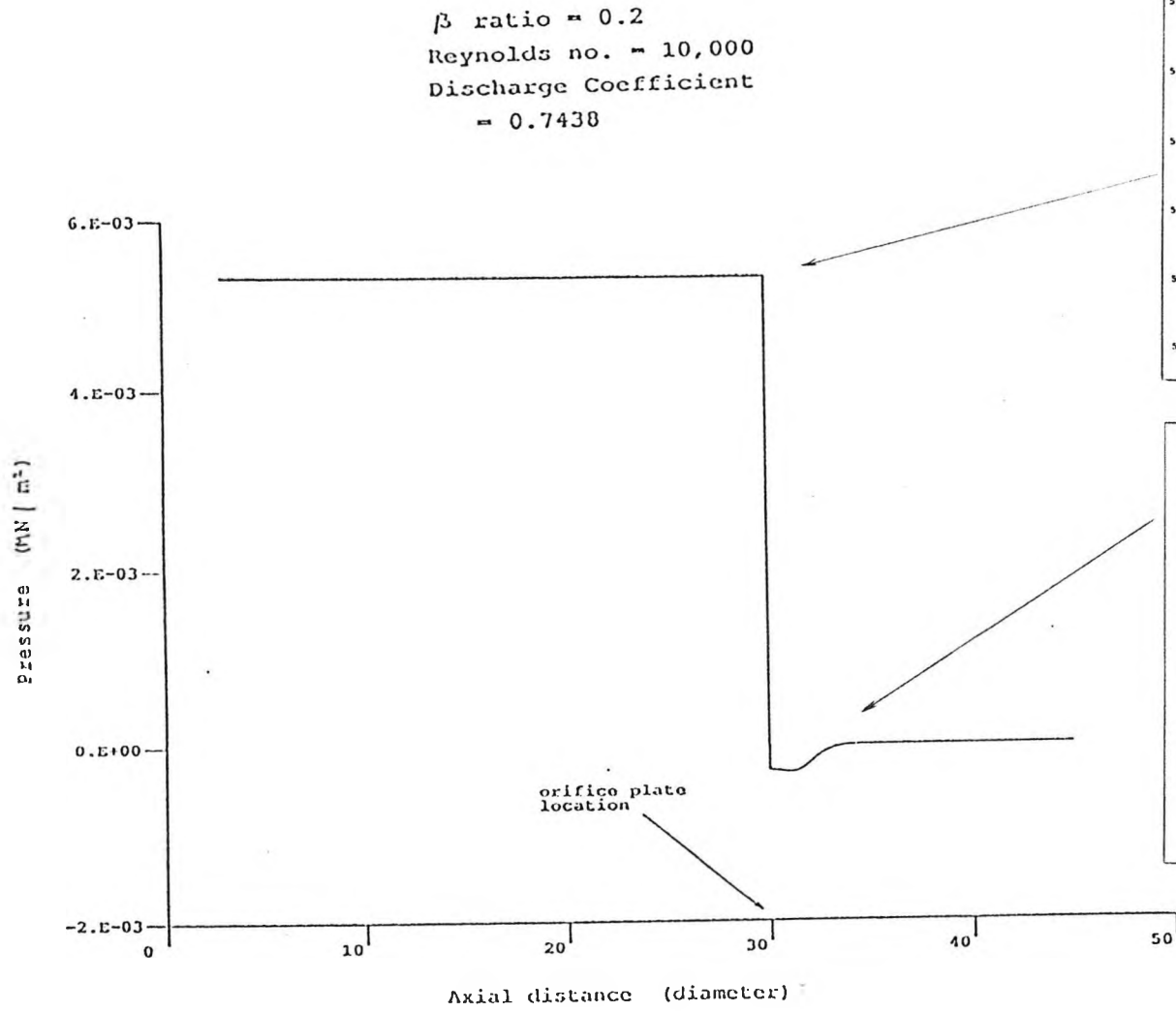


Fig. 5.10(b) Variation of the predicted wall pressure along the pipe

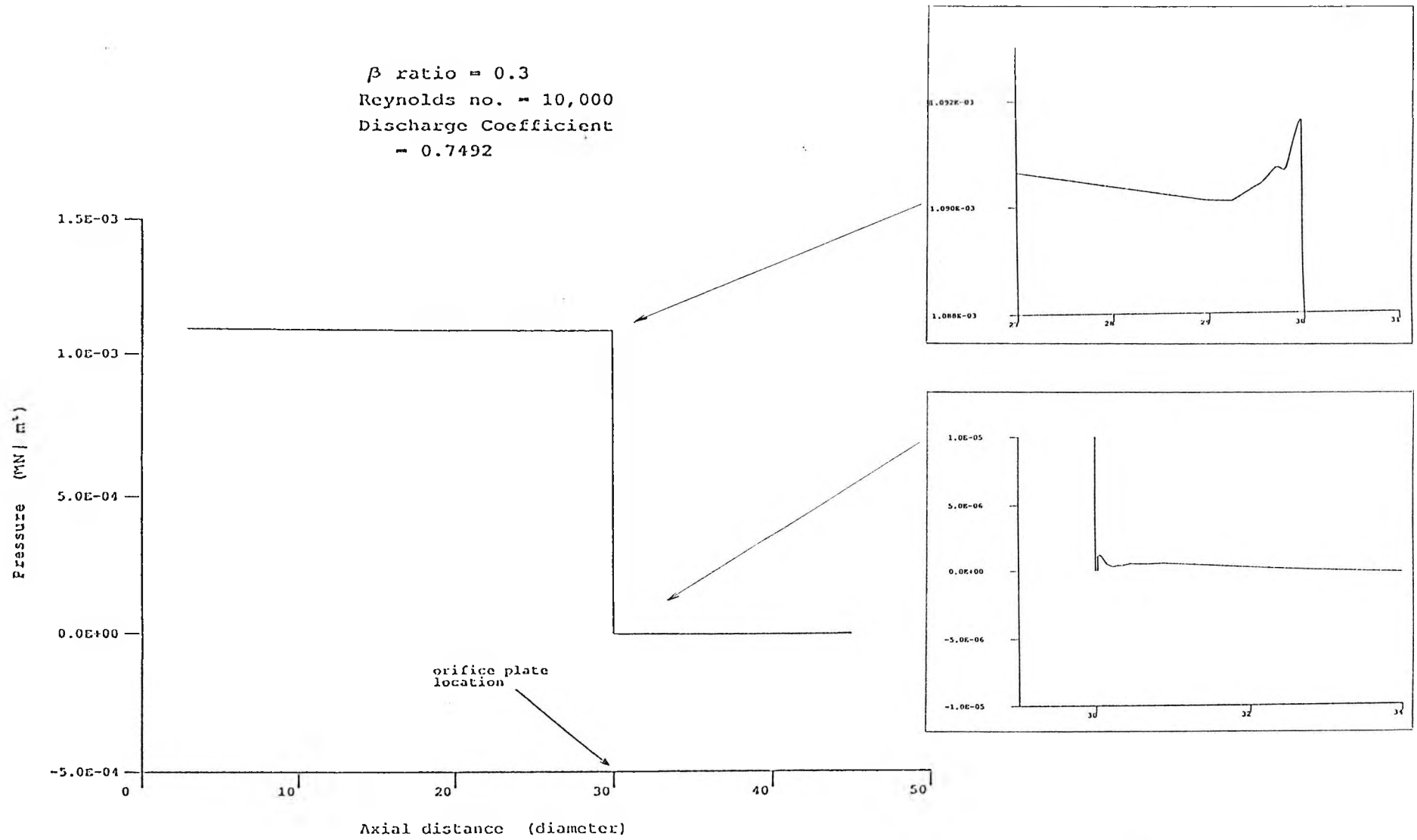


Fig. 5.10(c) Variation of the predicted wall pressure along the pipe

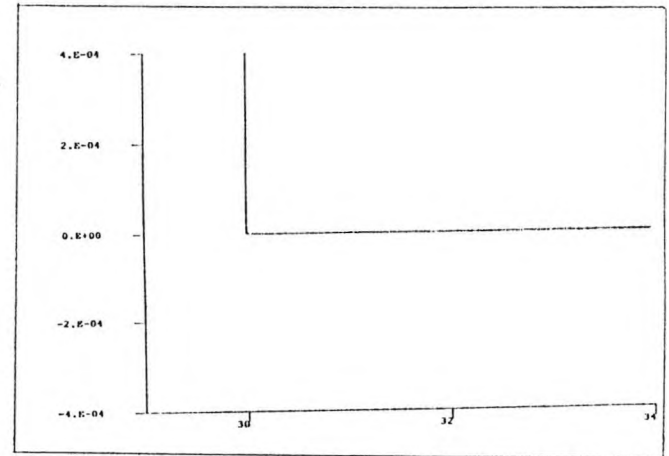
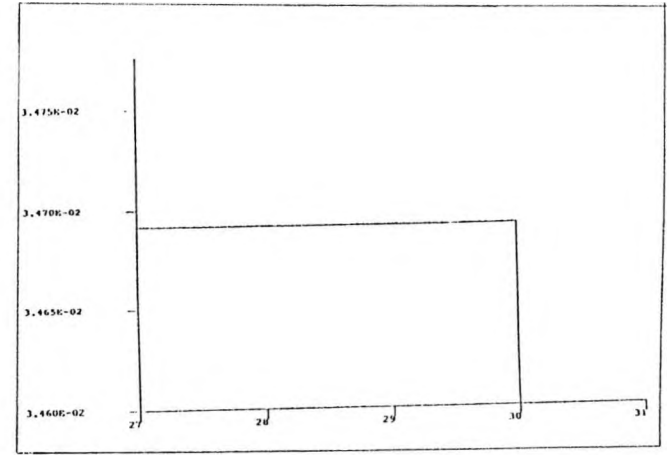
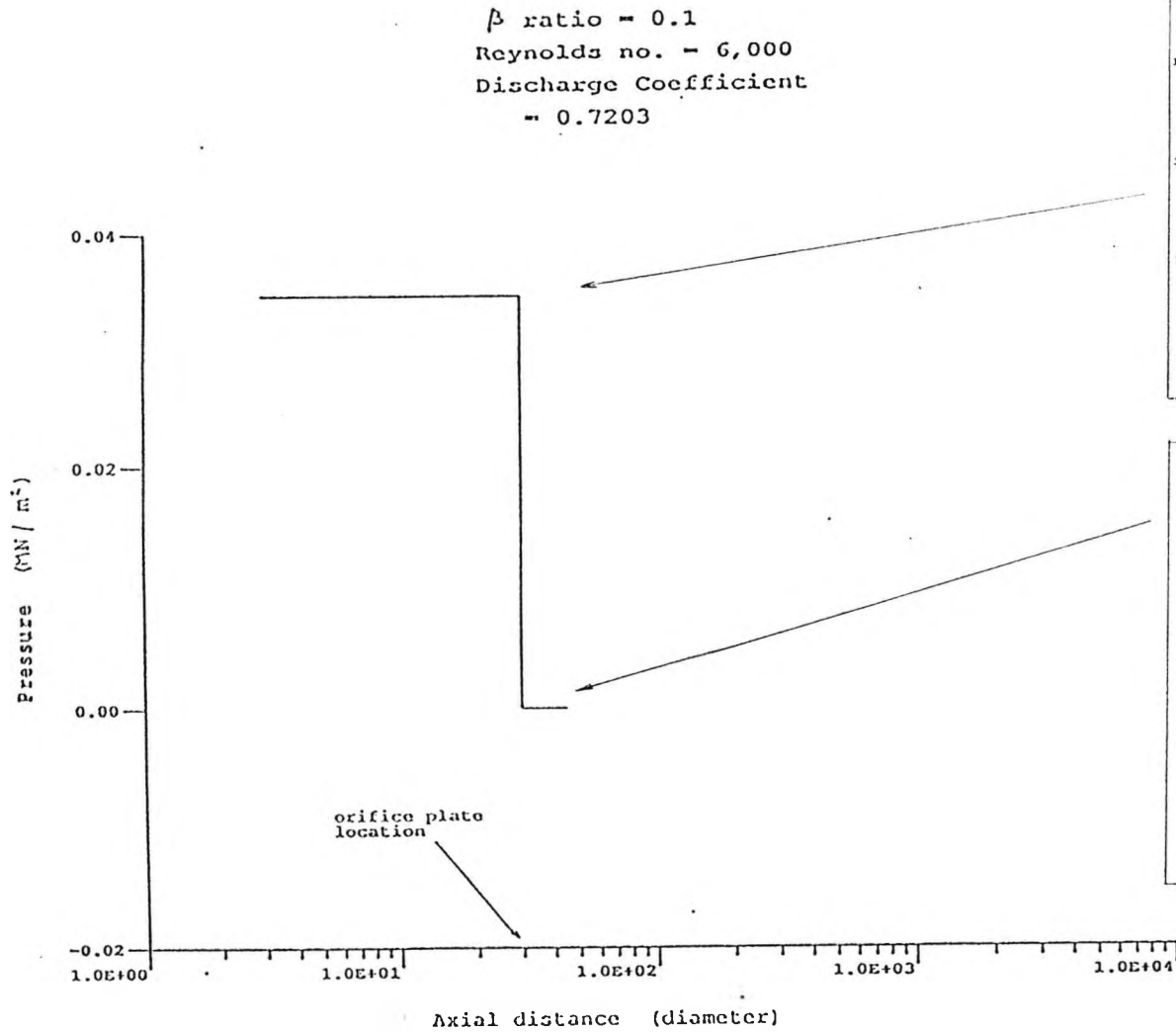


Fig. 5.11(a) Variation of the predicted wall pressure along the pipe

β ratio = 0.1
 Reynolds no. = 6,000
 Discharge Coefficient
 = 0.7208
 Downstream length
 = 1506 D

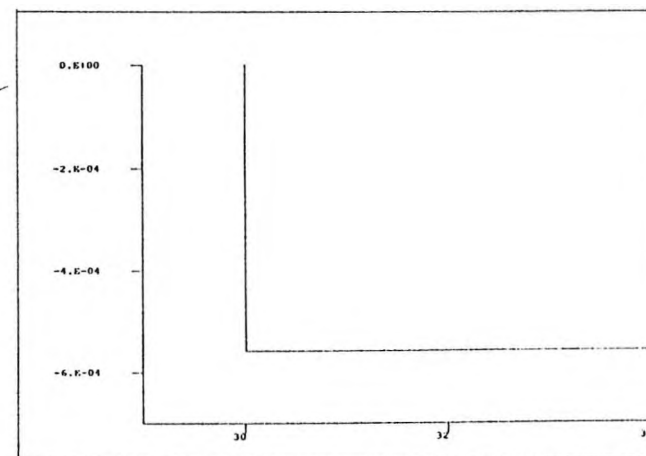
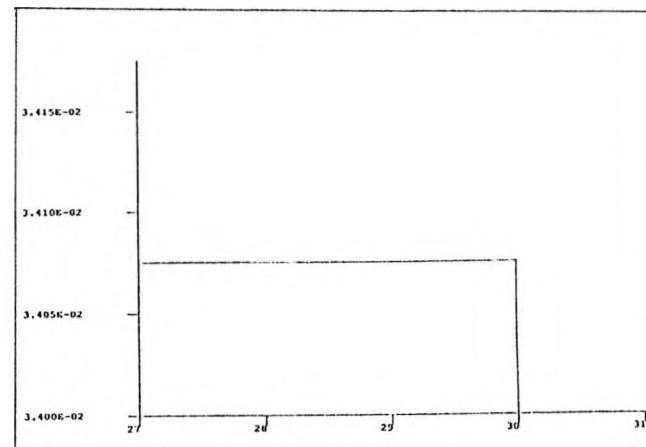
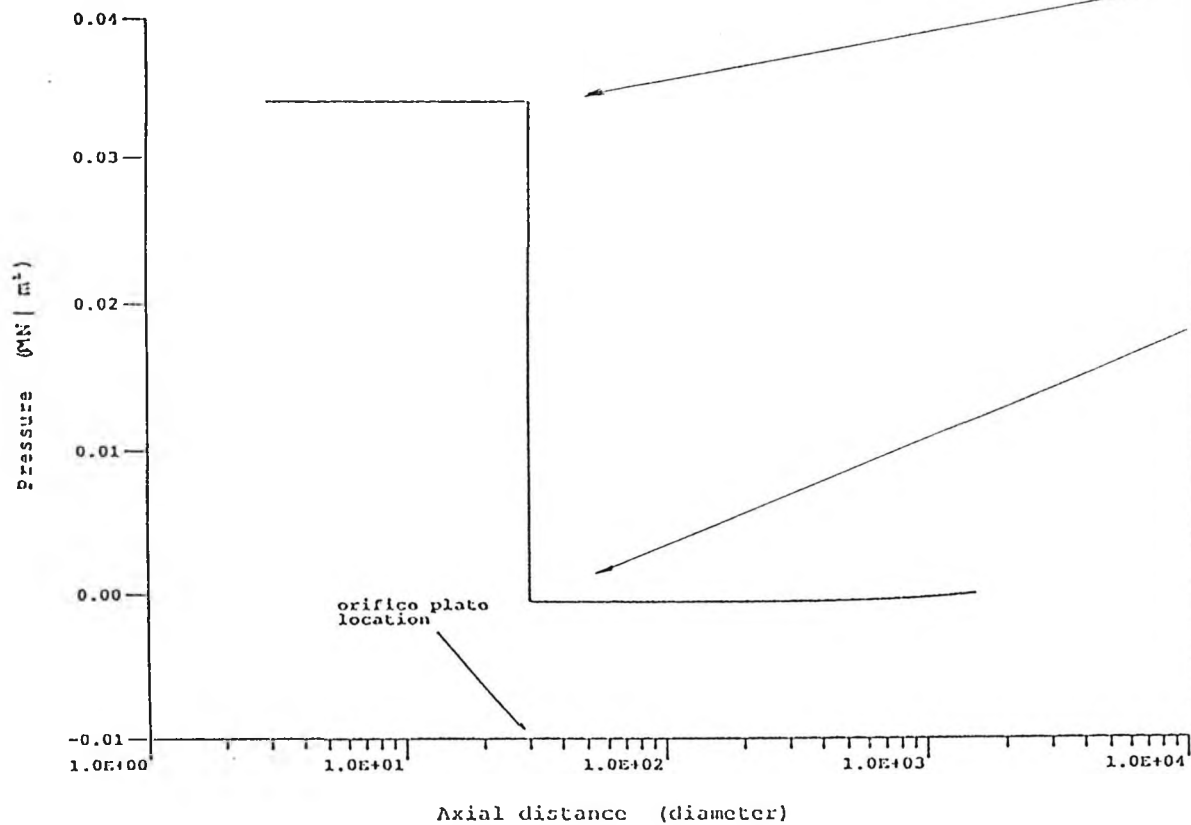


Fig. 5.11(b) Variation of the predicted wall pressure along the pipe

β ratio = 0.2
 Reynolds no. = 6,000
 Discharge Coefficient
 = 0.7390

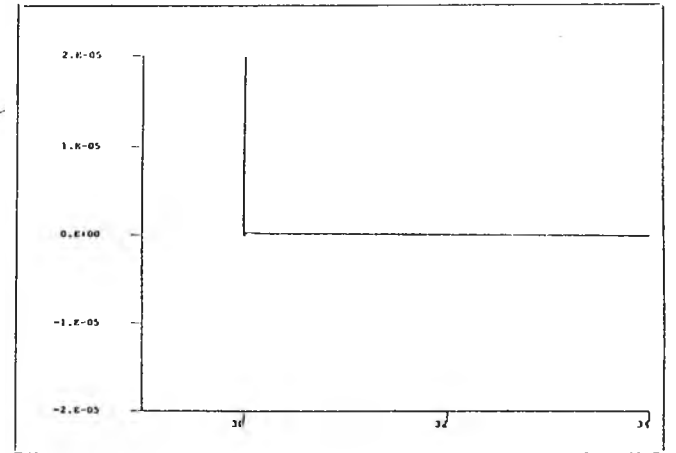
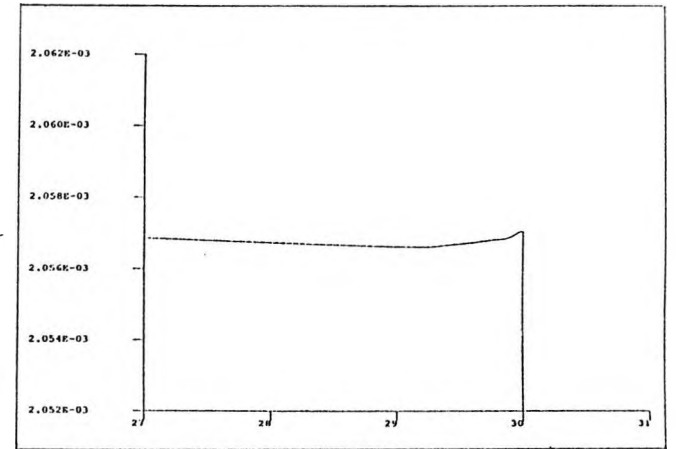
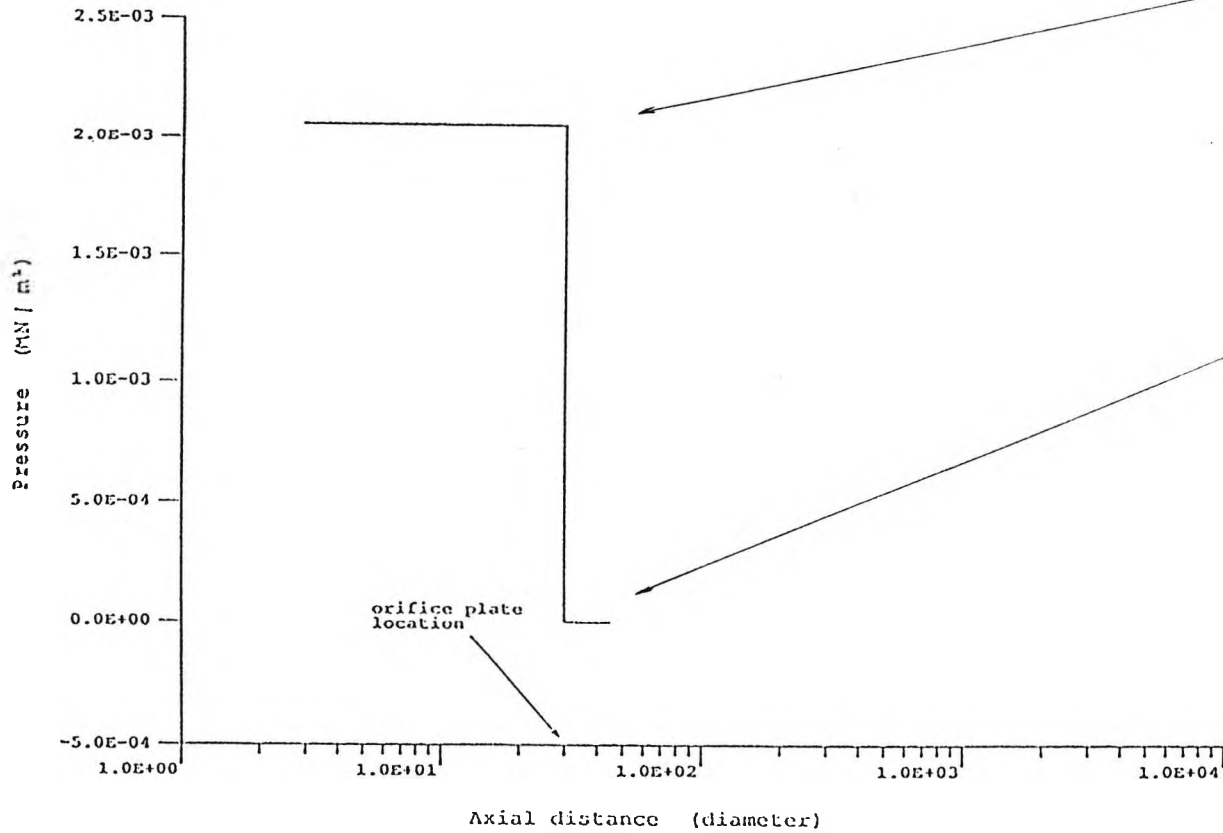


Fig. 5.11(c) Variation of the predicted wall pressure along the pipe

β ratio = 0.2
 Reynolds no. = 6,000
 Discharge Coefficient
 = 0.7389
 Downstream length
 = 606 D

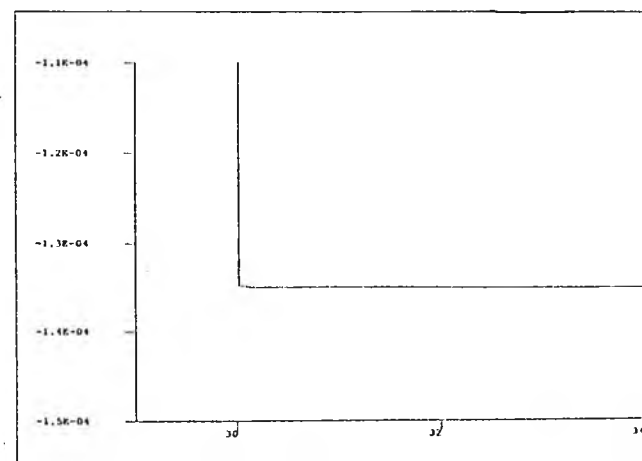
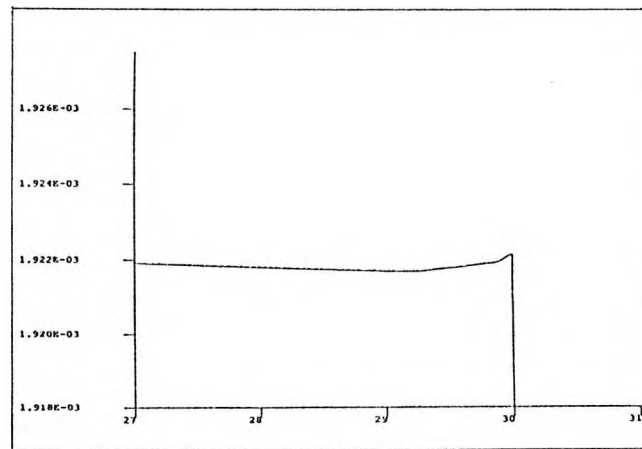
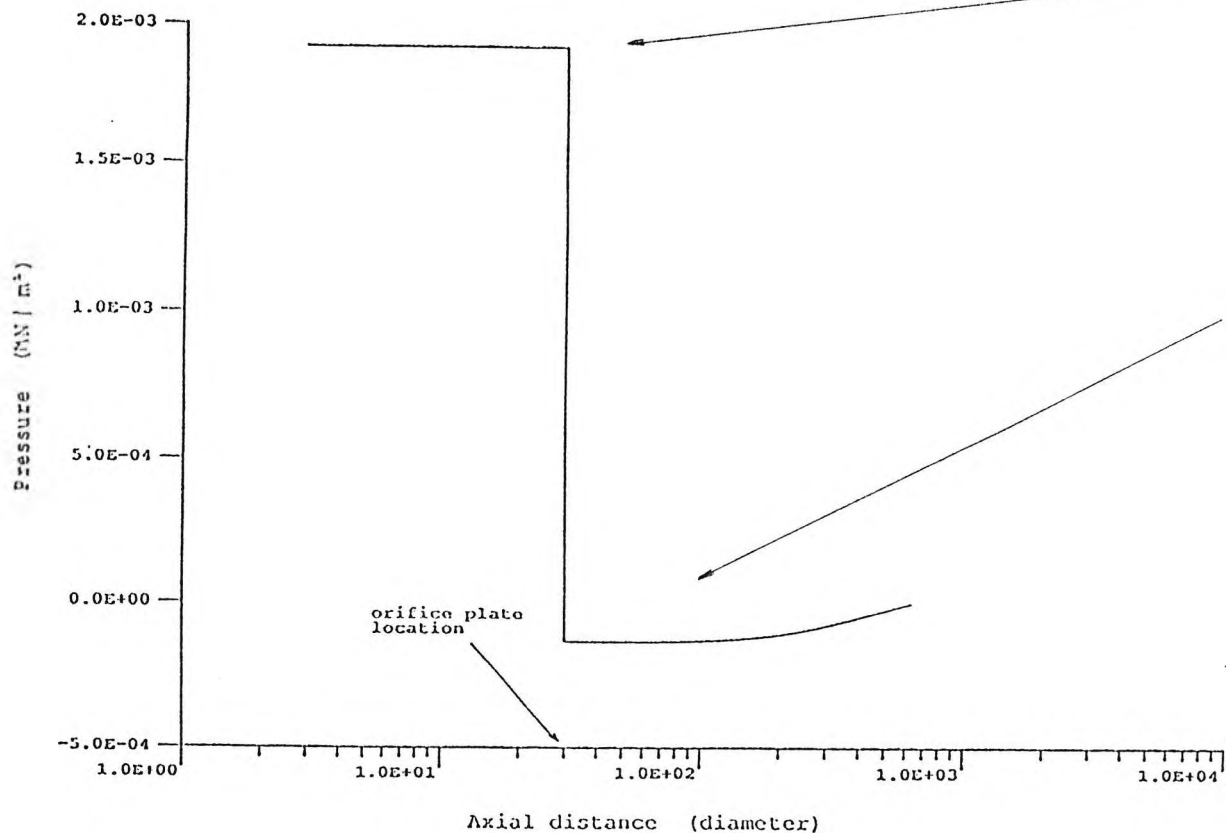


Fig. 5.11(d) Variation of the predicted wall pressure along the pipe

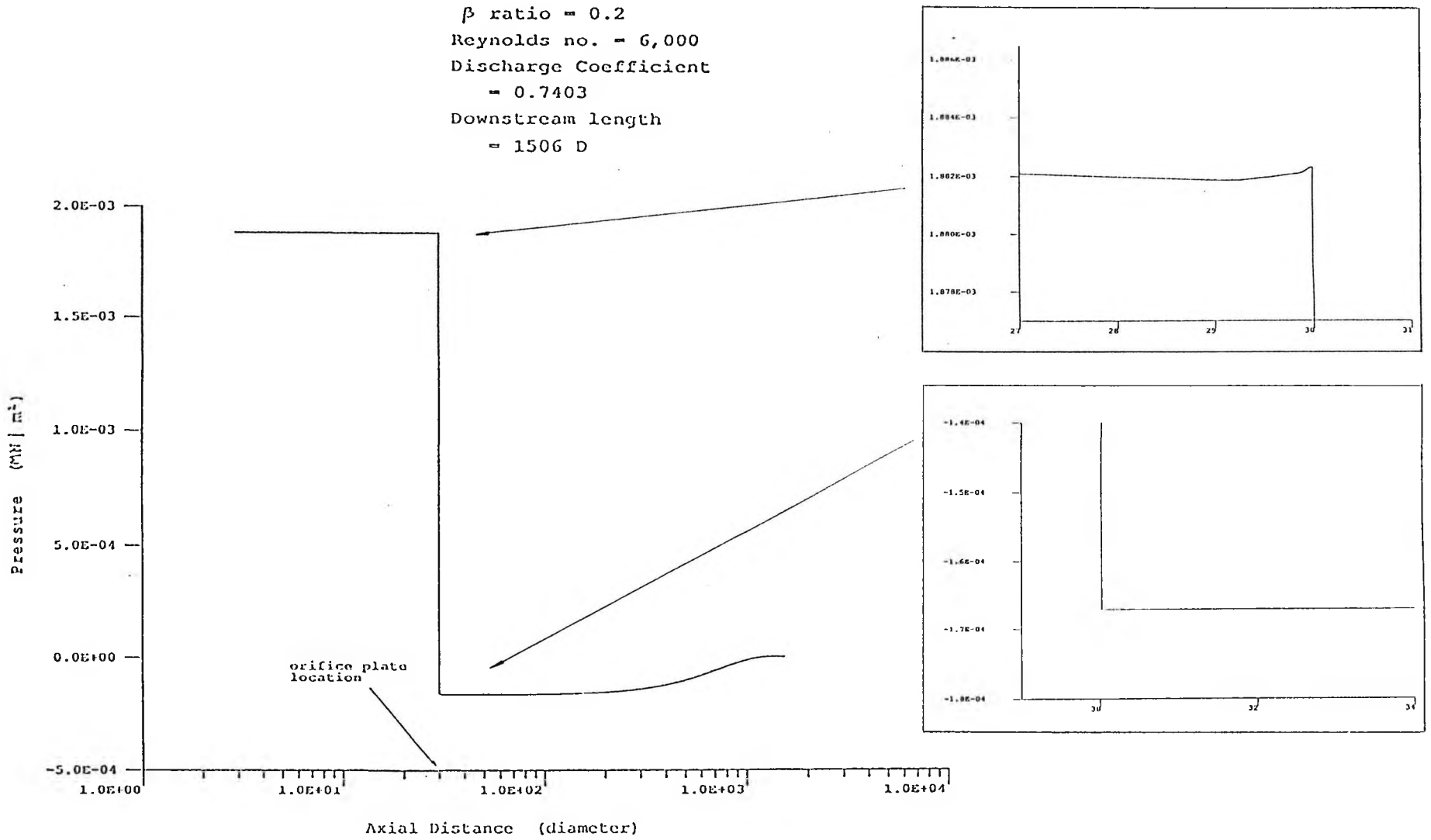


Fig. 5.11(c) Variation of the predicted wall pressure along the pipe

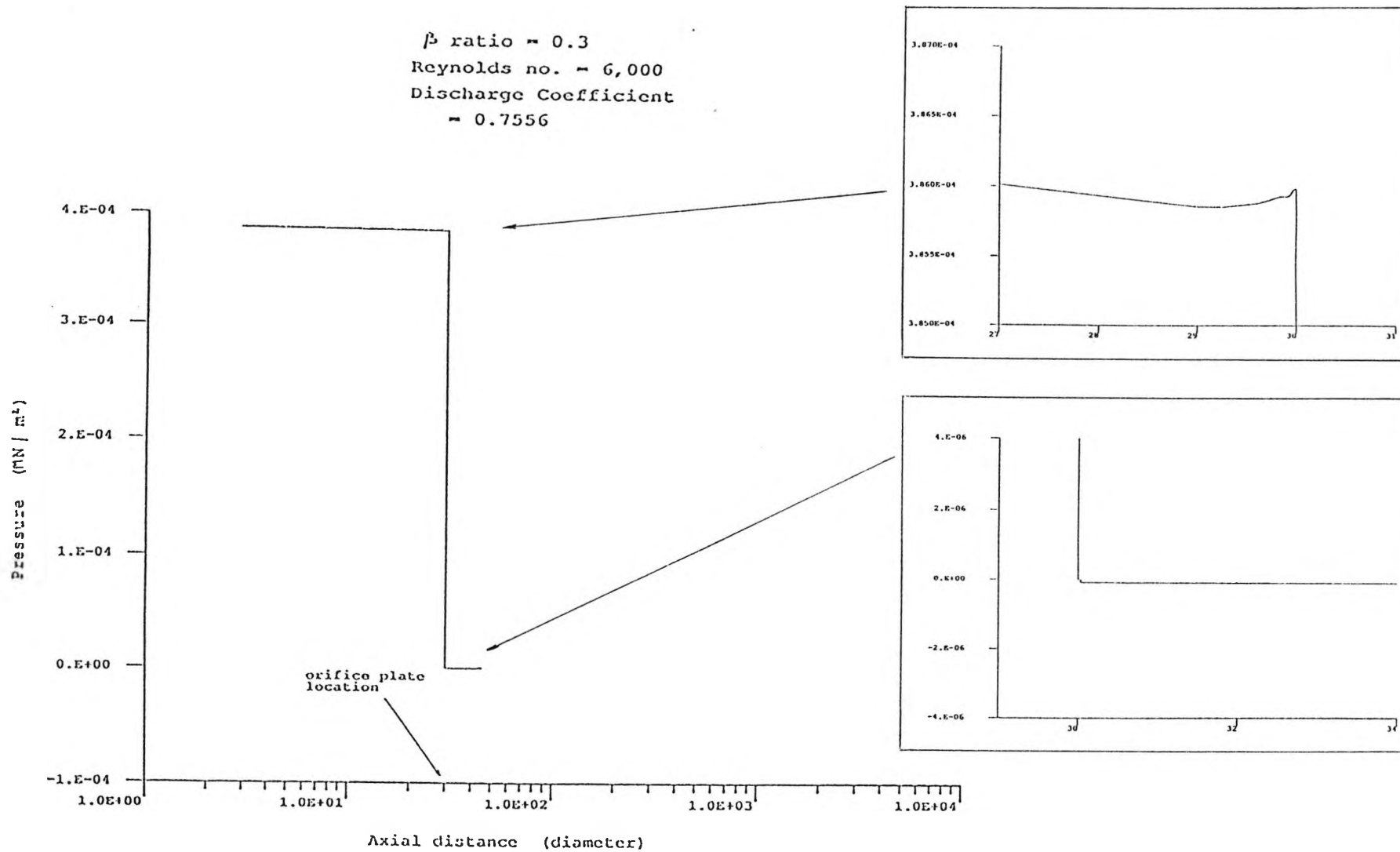


Fig. 5.11(F) Variation of the predicted wall pressure along the pipe

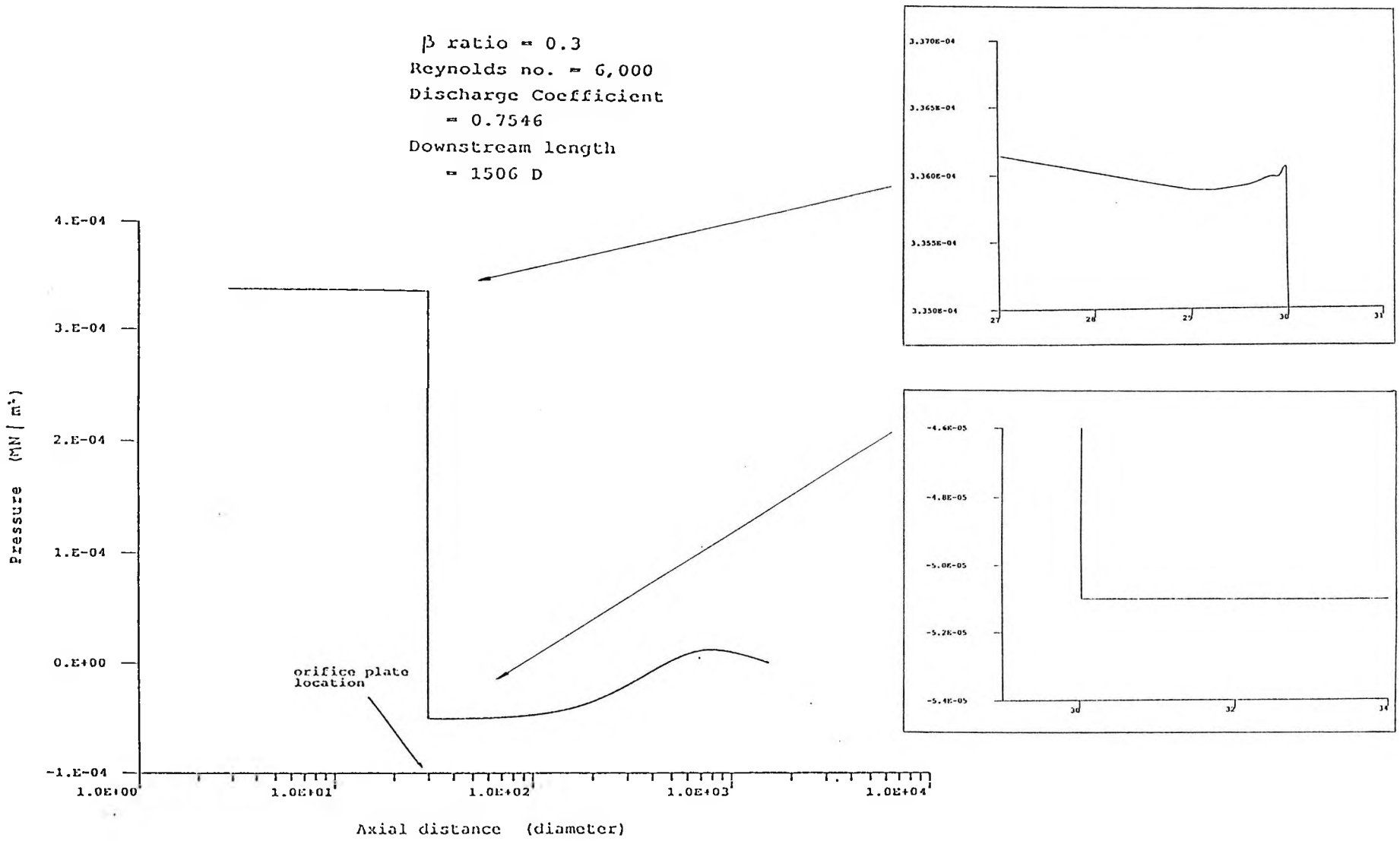


Fig. 5.11(g) Variation of the predicted wall pressure along the pipe

computed by the LRN model. The effect of increasing the downstream pipe length on the pressure profile can also be seen from these figures. As the downstream pipe length increased, the presence of a minimum wall pressure at the intersection of the orifice plate and the pipe wall becomes obvious. The same can be observed in figures 5.12 and 5.13 which show the streamwise wall pressure distribution for a Reynolds number of 1,000 and 80 respectively. For flows at higher Reynolds number, the pressure minima is located at some distance downstream of the orifice plate as is evident in figures 5.8 and 5.9. The move in the location of the pressure minima upstream to the orifice plate at low Reynolds numbers was also noted by Mattingly and Davis (13) in their study of laminar flow through square edged orifice. Mattingly and Davis interpreted this as viscous effects at low Reynolds numbers.

Although the downstream pressure profile changes as the downstream pipe length increases from 16 D, the computed discharge coefficient remains practically constant for a given Reynolds number and β ratio, and is not affected by the downstream pressure profile changes as can be seen from figures 5.11 to 5.13.

From the wall pressure profiles, it can be seen that there is very little difference in the pressure differentials at locations corresponding to the use of

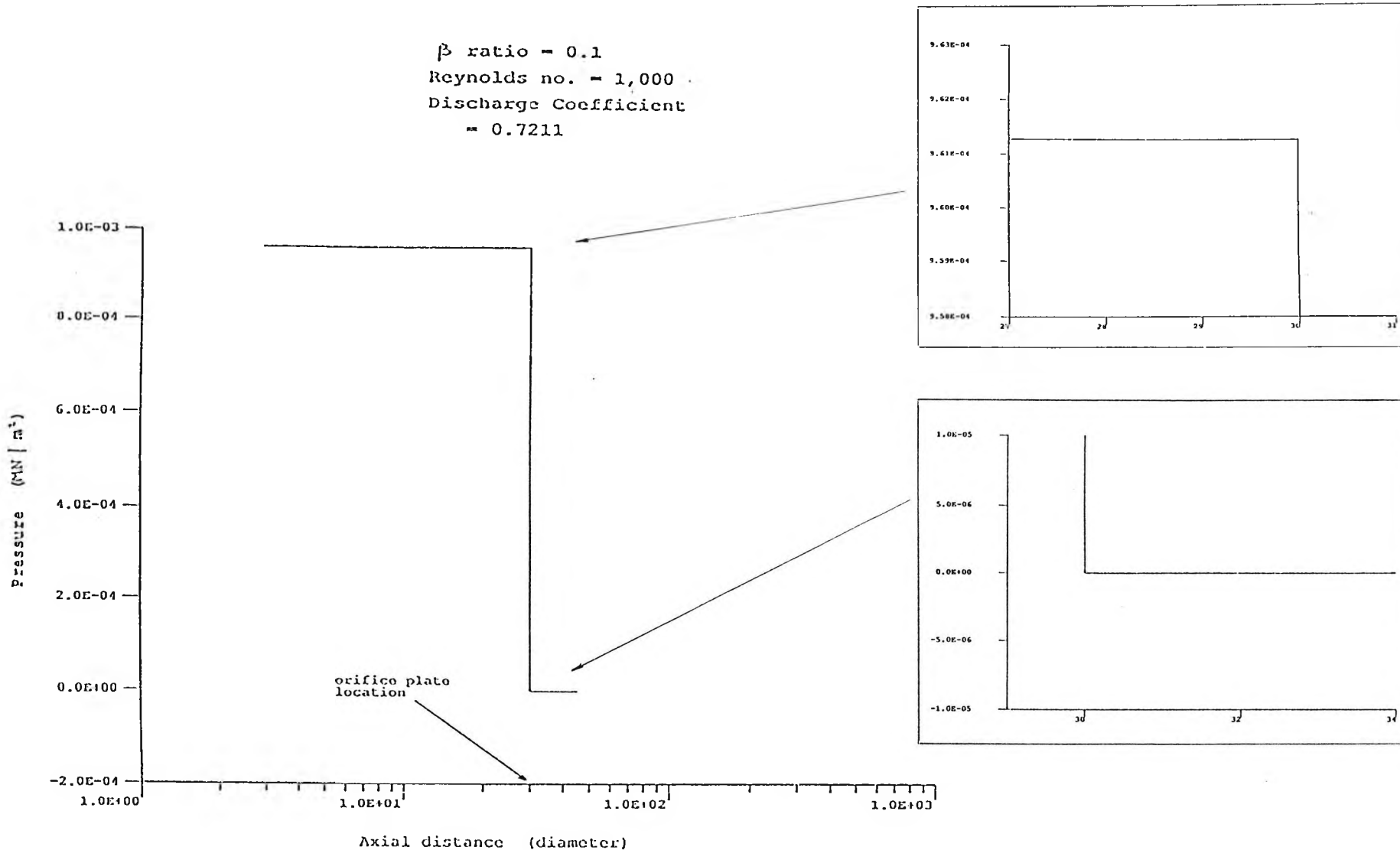


Fig. 5.12(a) Variation of the predicted wall pressure along the pipe

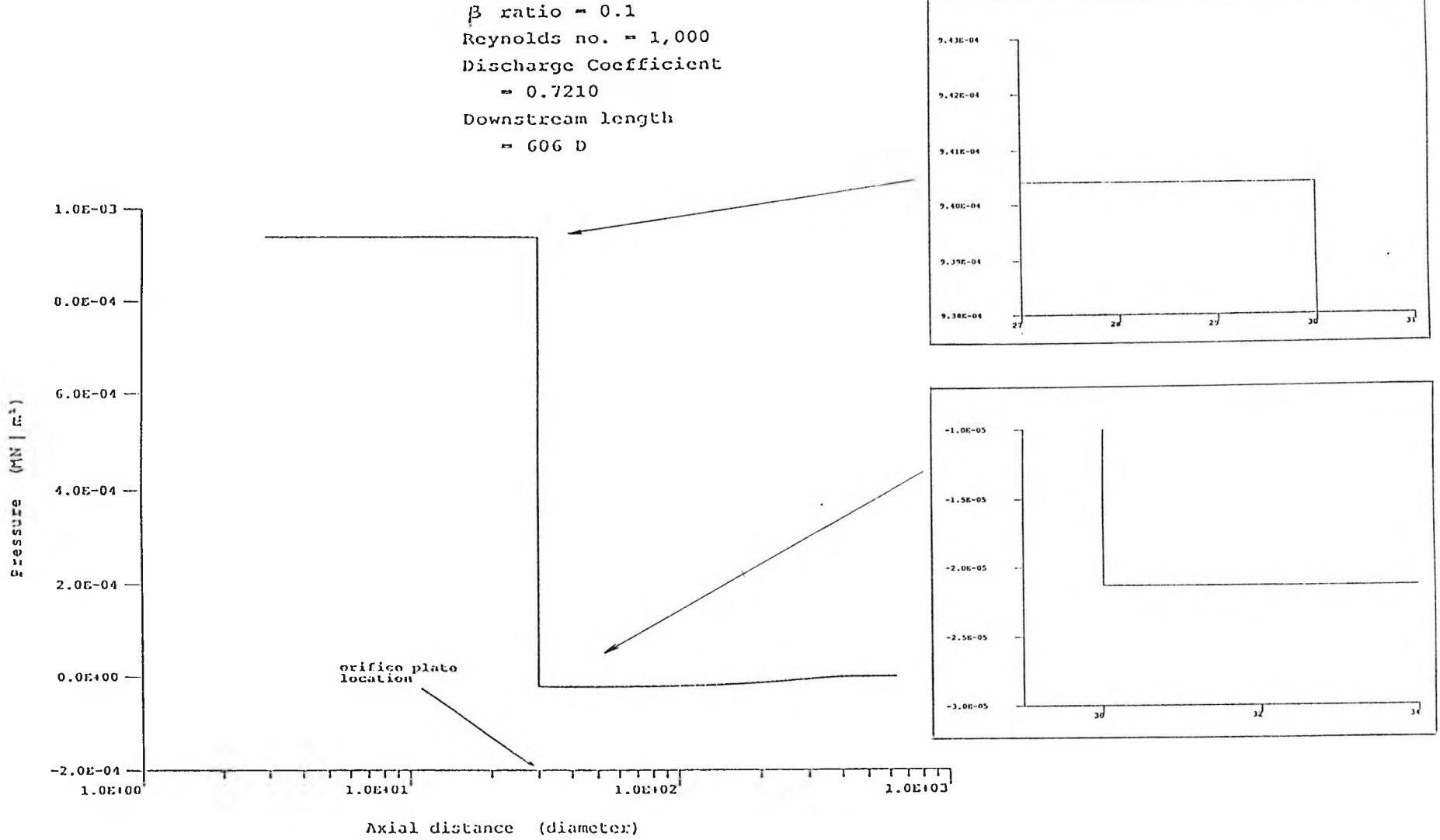


Fig. 5.12(b) Variation of the predicted wall pressure along the pipe

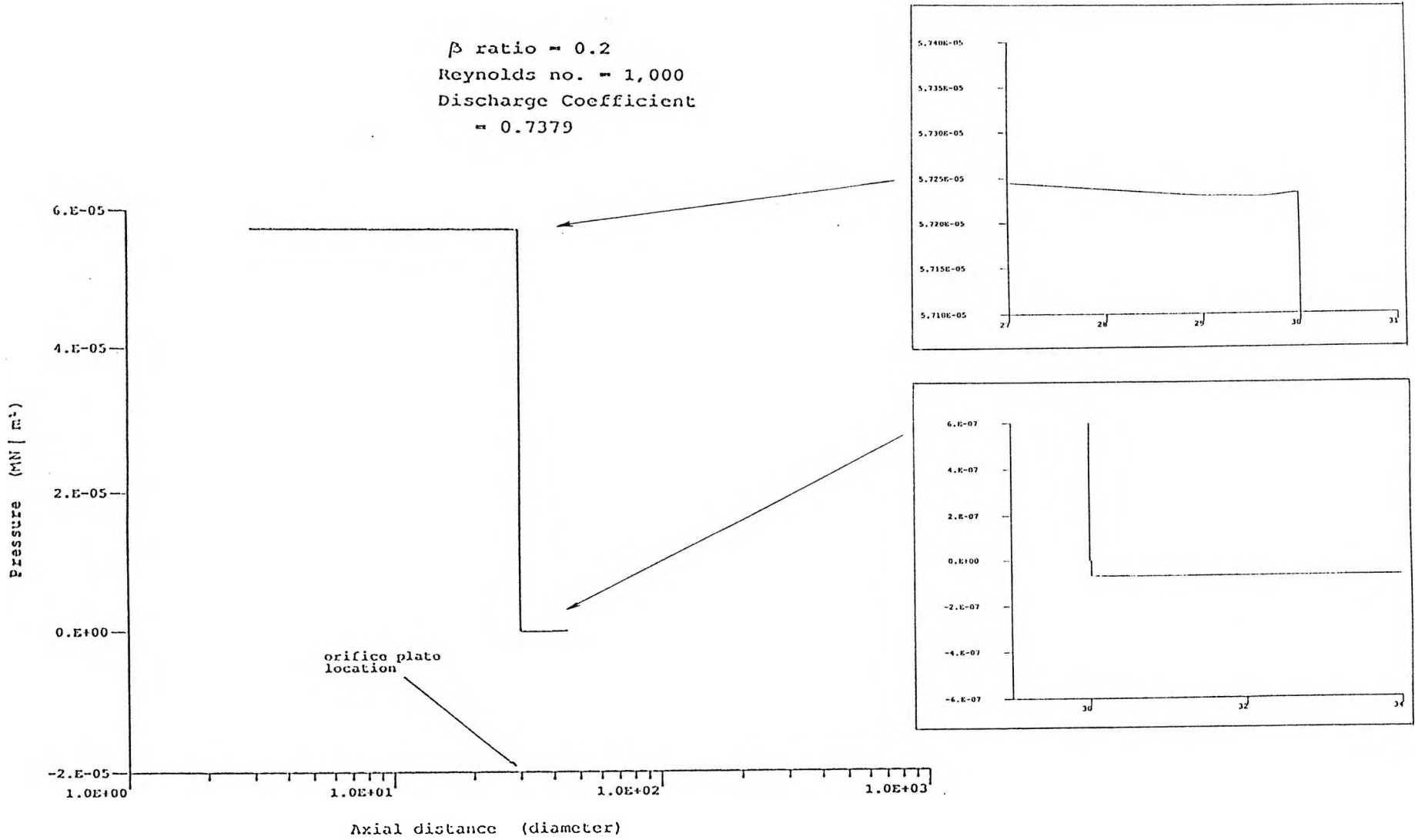


Fig. 5.12(c) Variation of the predicted wall pressure along the pipe

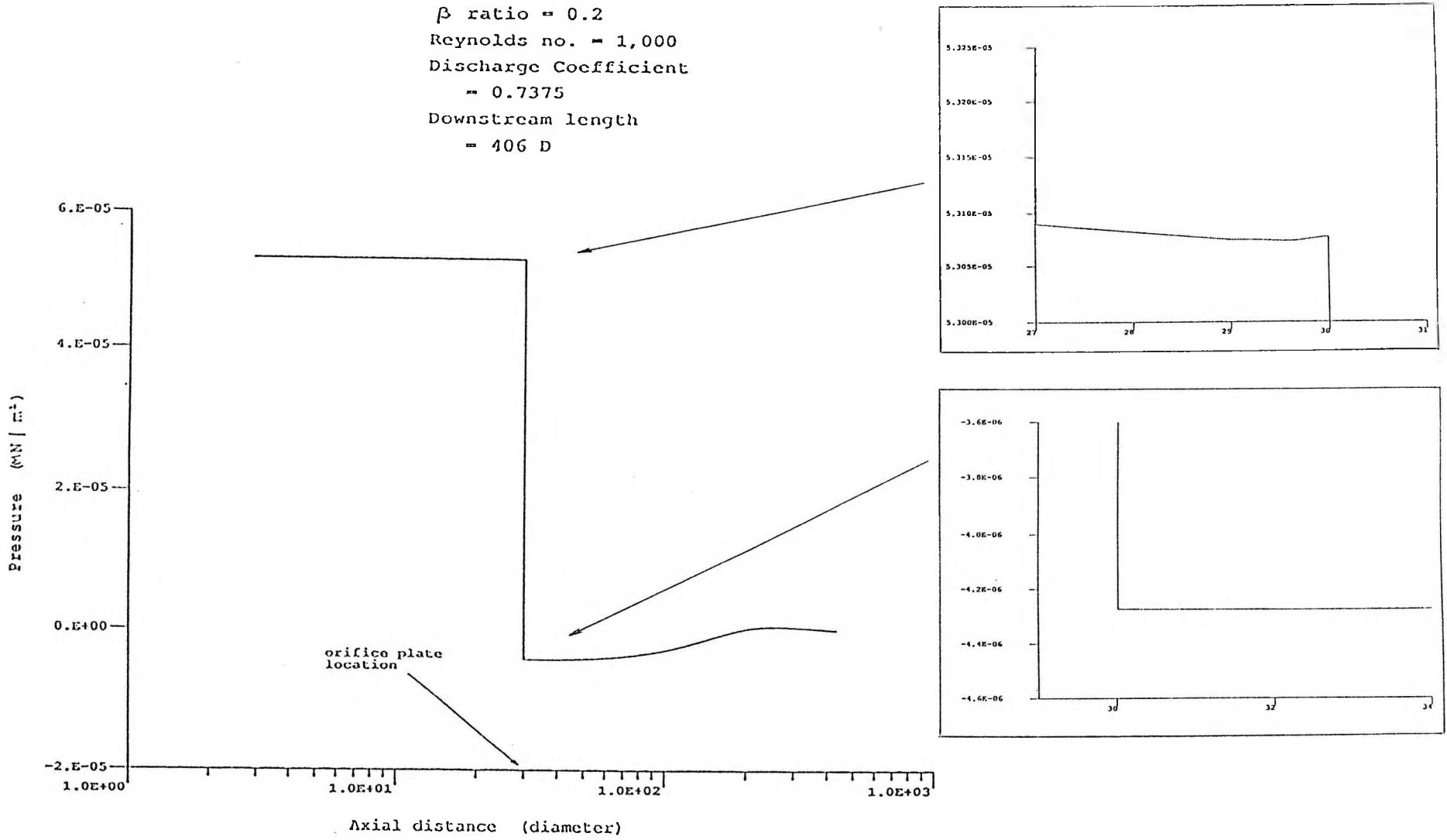


Fig. 5.12(d) Variation of the predicted wall pressure along the pipe

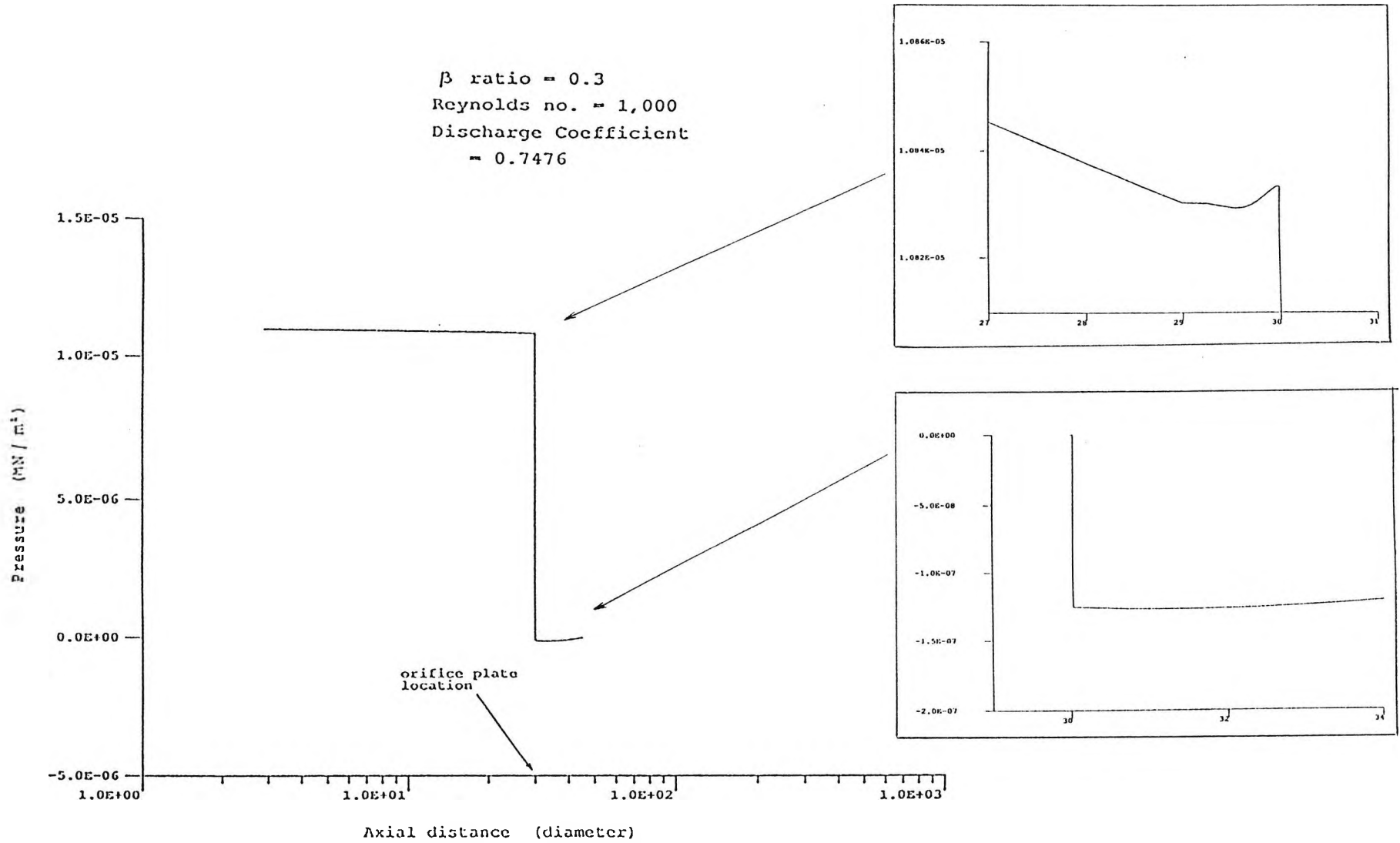


Fig. 5.12(e) Variation of the predicted wall pressure along the pipe

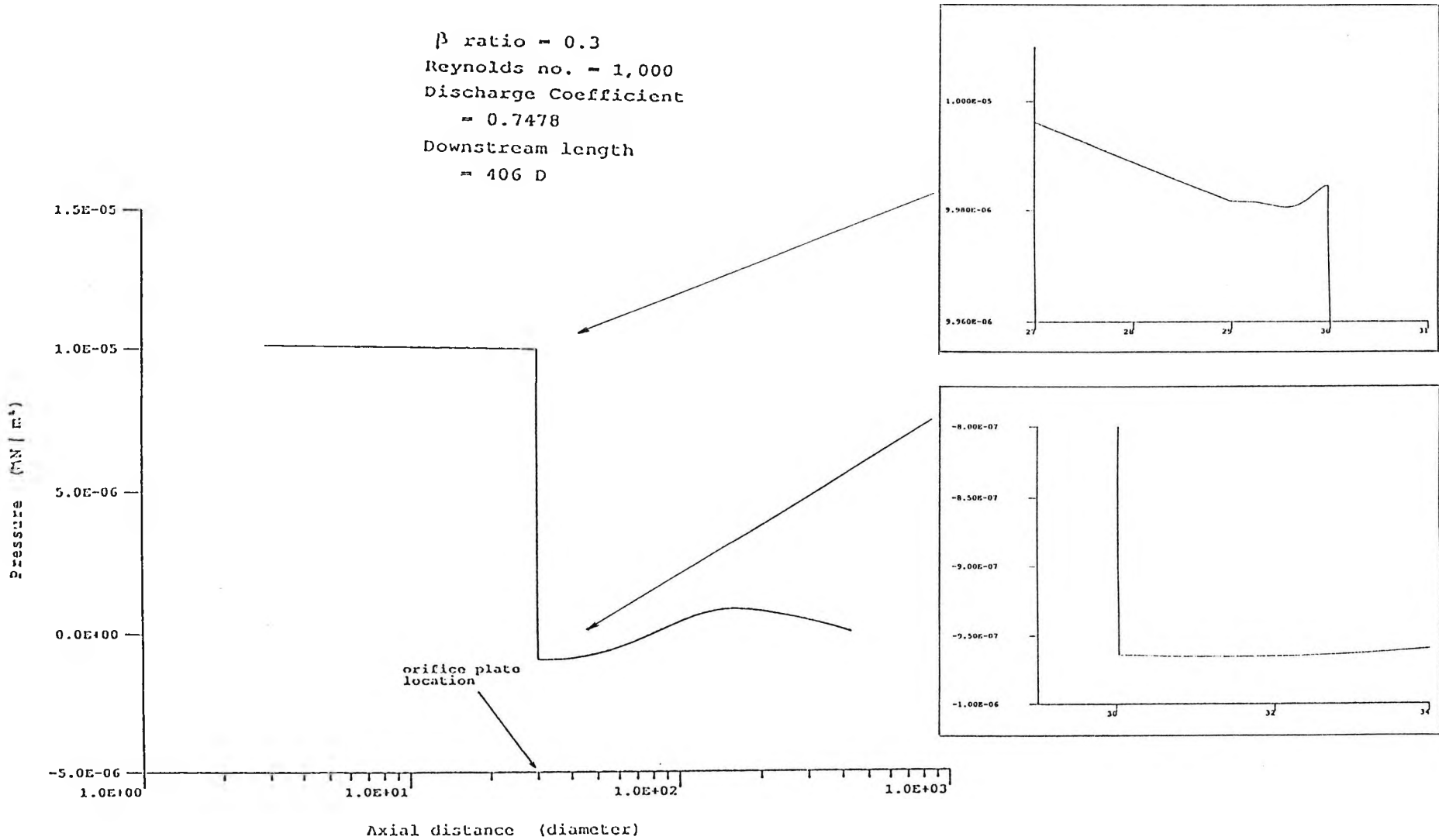


Fig. 5.12(f) Variation of the predicted wall pressure along the pipe

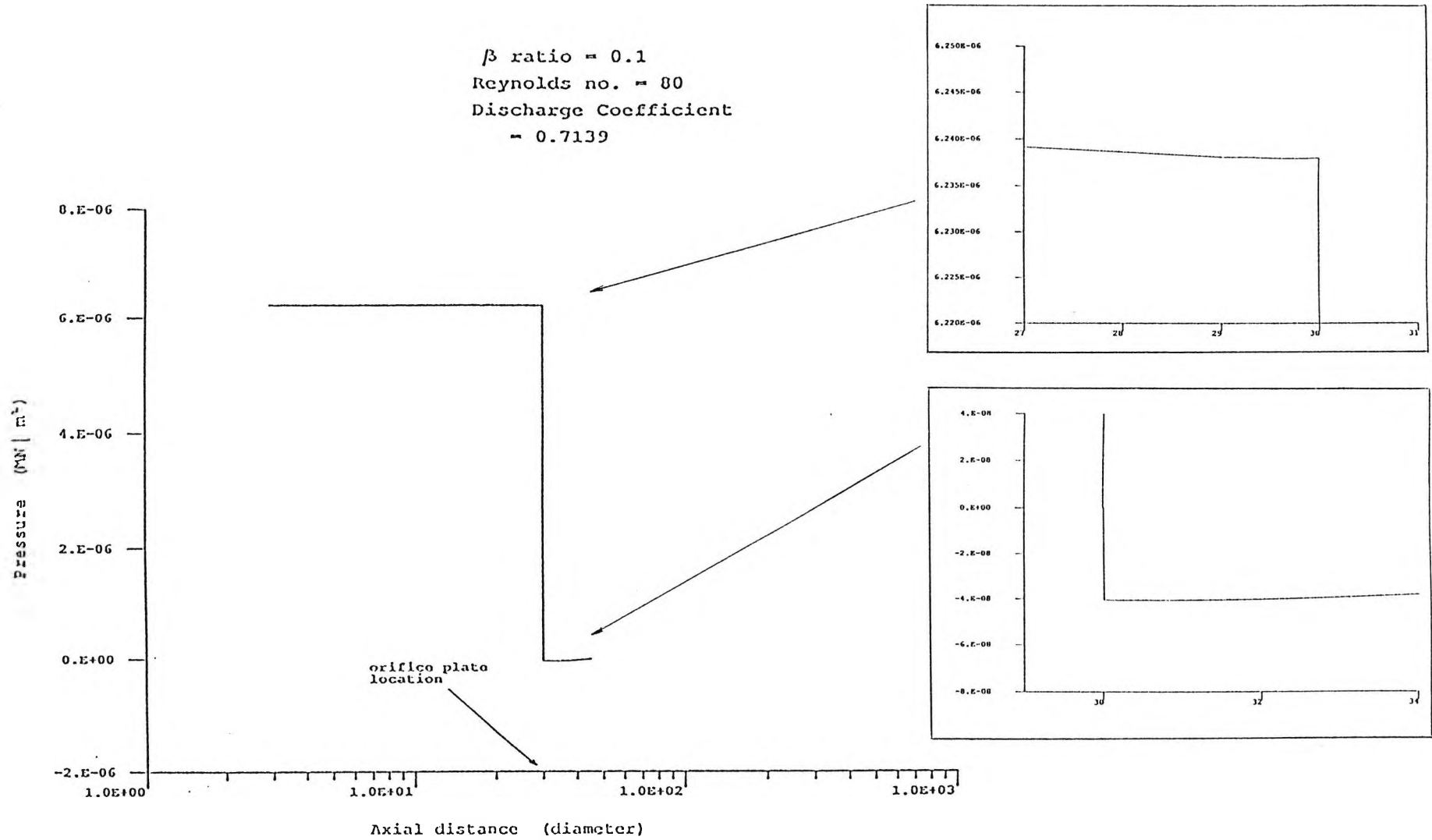


Fig. 5.13(a) Variation of the predicted wall pressure along the pipe

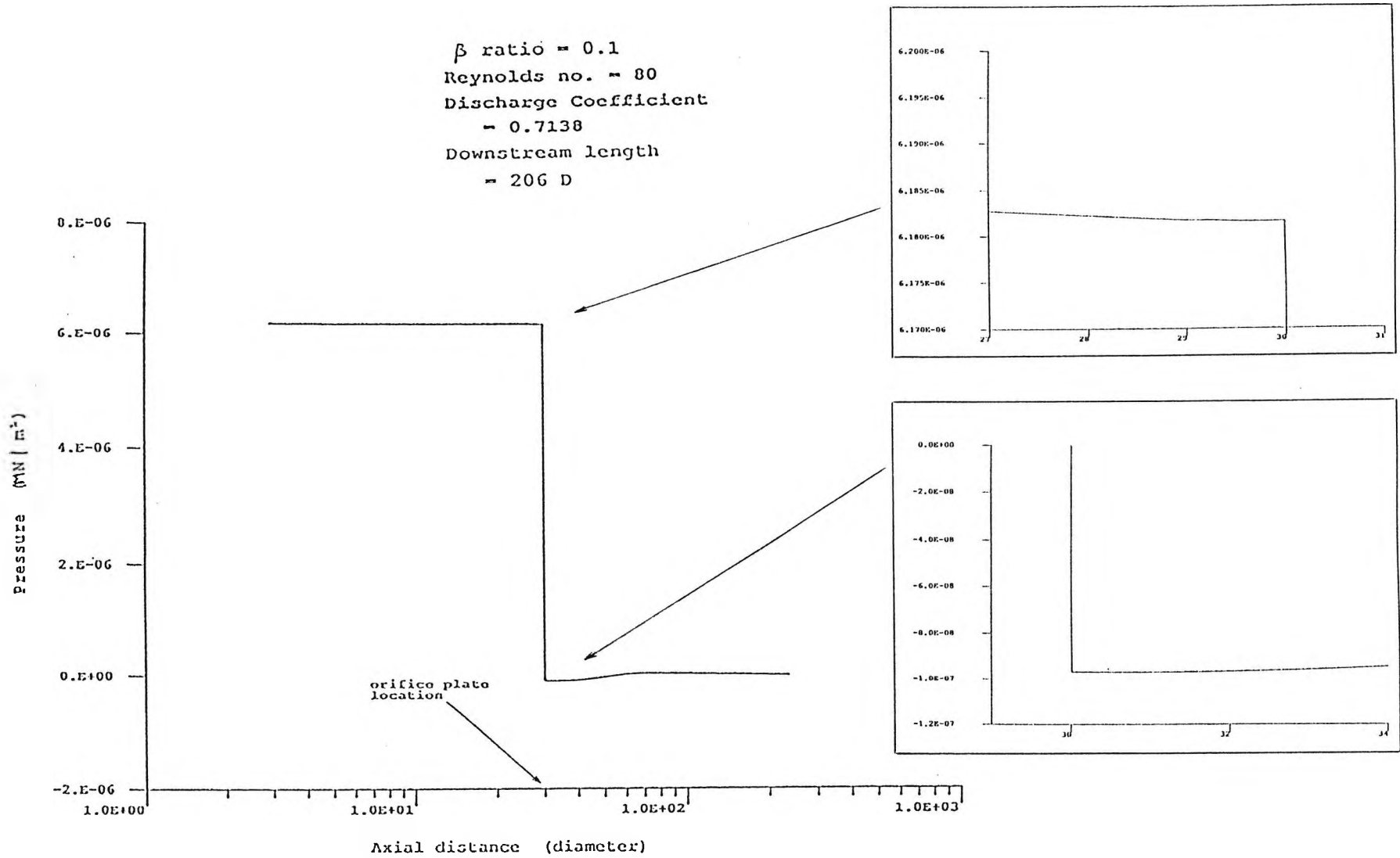


Fig. 5.13(b) Variation of the predicted wall pressure along the pipe

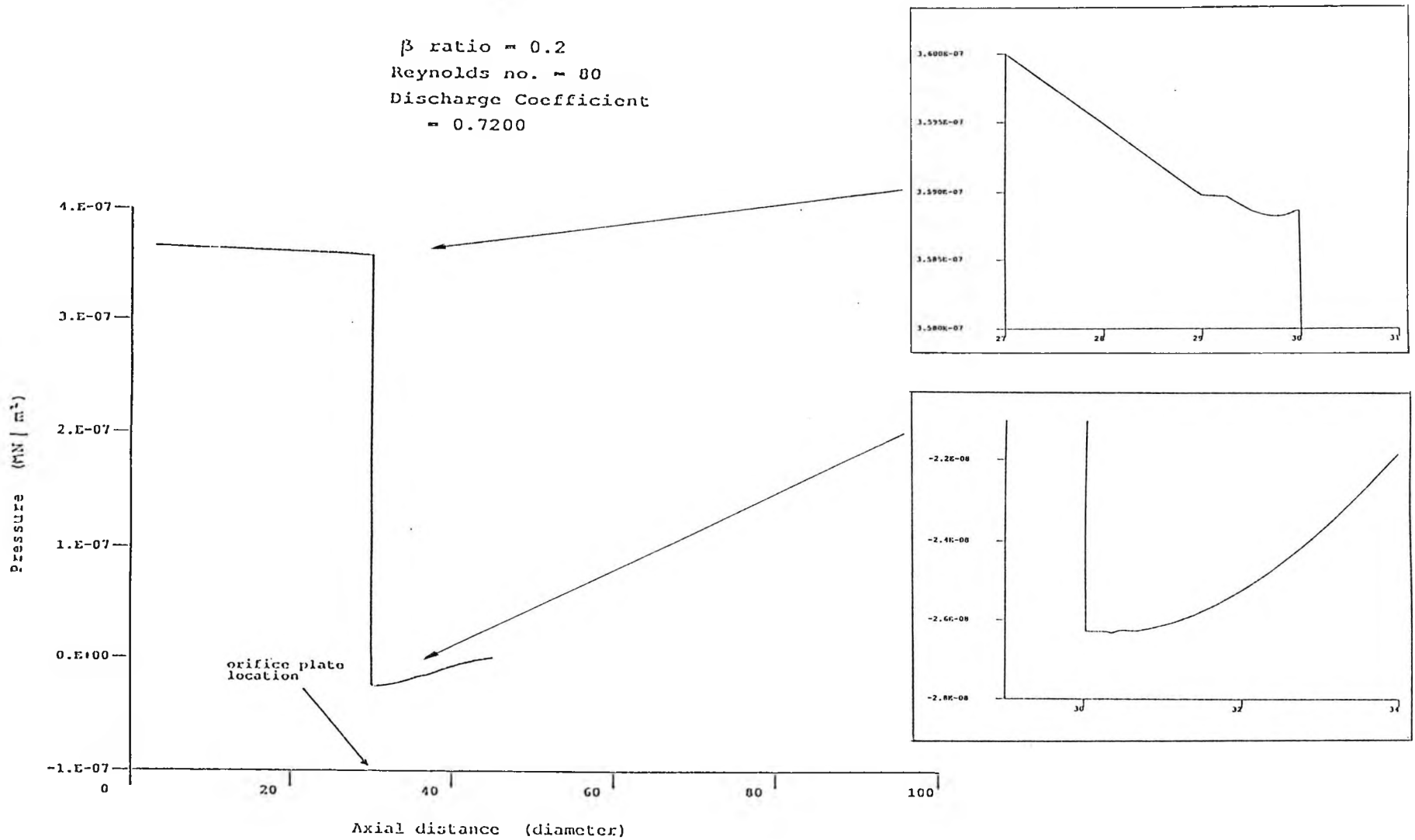


Fig. 5.13(c) Variation of the predicted wall pressure along the pipe

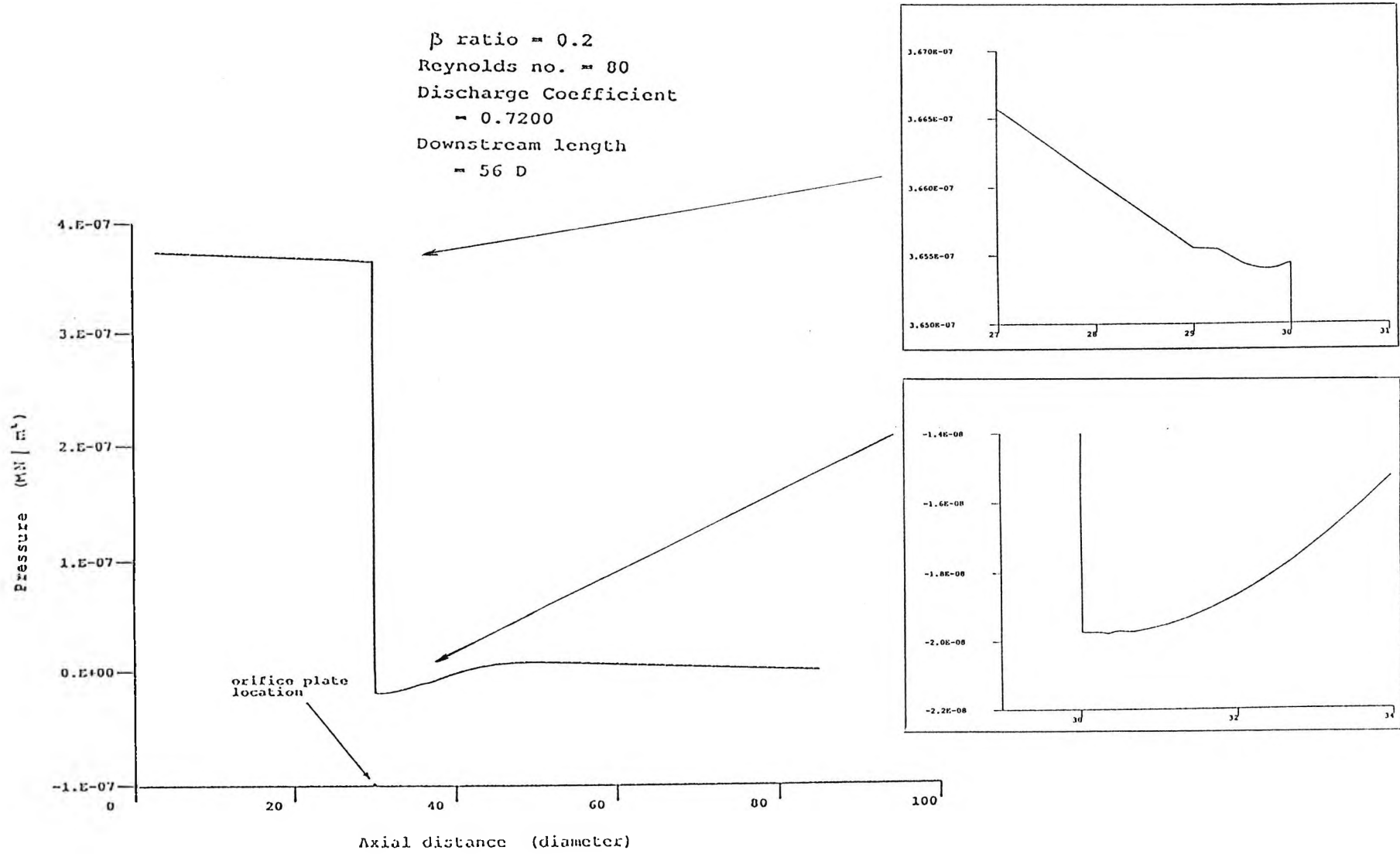


Fig. 5.13(d) Variation of the predicted wall pressure along the pipe

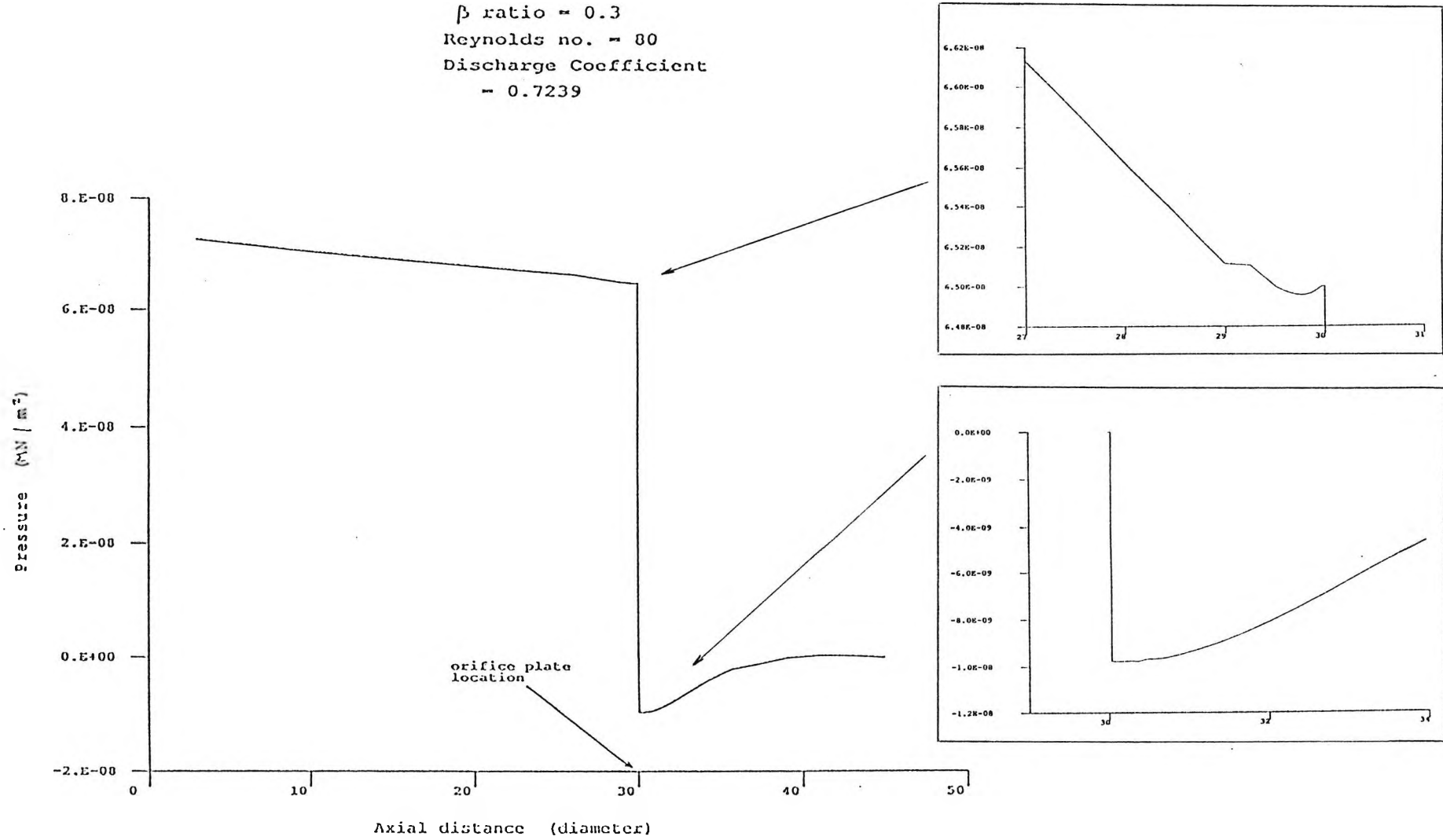


Fig. 5.13(e) Variation of the predicted wall pressure along the pipe

corner, flange and D & $\frac{1}{2}$ D pressure tapplings. Thus, the computed discharge coefficients for these three pressure tapplings are almost identical, as is shown in table 5.1.

For comparison with the LRN model, the variation of wall pressure along the pipe as computed by the LAM model is presented in figures 5.14(a) to 5.14(c) for $\beta = 0.3$ and Reynolds numbers of 80, 30,000 and 60,000. For a Reynolds number of 80, there is the expected good agreement between the LRN model and the LAM model, as is evident by comparing figure 5.13(e) with figure 5.14(a). However, at the Reynolds numbers of 30,000 and 60,000, the LAM model cannot predict the presence of the pressure minima as can be seen by comparing figure 5.9(c) with figure 5.14(b), and figure 5.8(c) with figure 5.14(c). The pressure remains almost constant downstream of the orifice plate. The LAM model is not used in the present investigation.

5.3.2 Flow pattern through the orifice

Figure 5.15(a) shows the flow pattern as predicted by the LRN model through a conical entrance orifice plate for $\beta = 0.2$ and for a Reynolds number of 30,000. For clarity of the velocity vector plot, a grid-scaling factor of 20 was applied in the radial direction. The grid-scaling factor for the axial direction was unity. Shown in the figure is the general pattern of flow convergence through the orifice plate and the jet flow

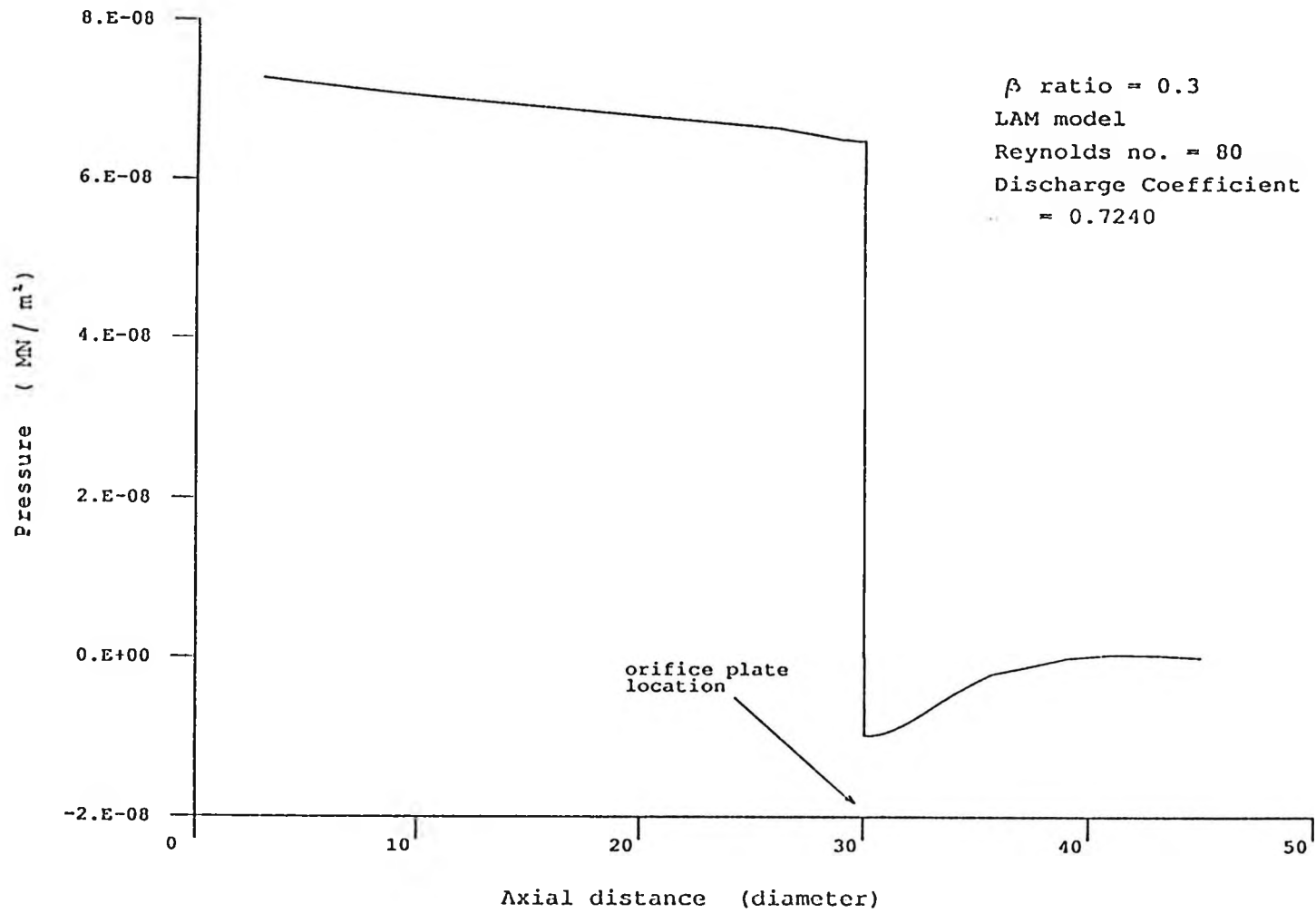


Fig. 5.14(a) Variation of the predicted wall pressure along the pipe

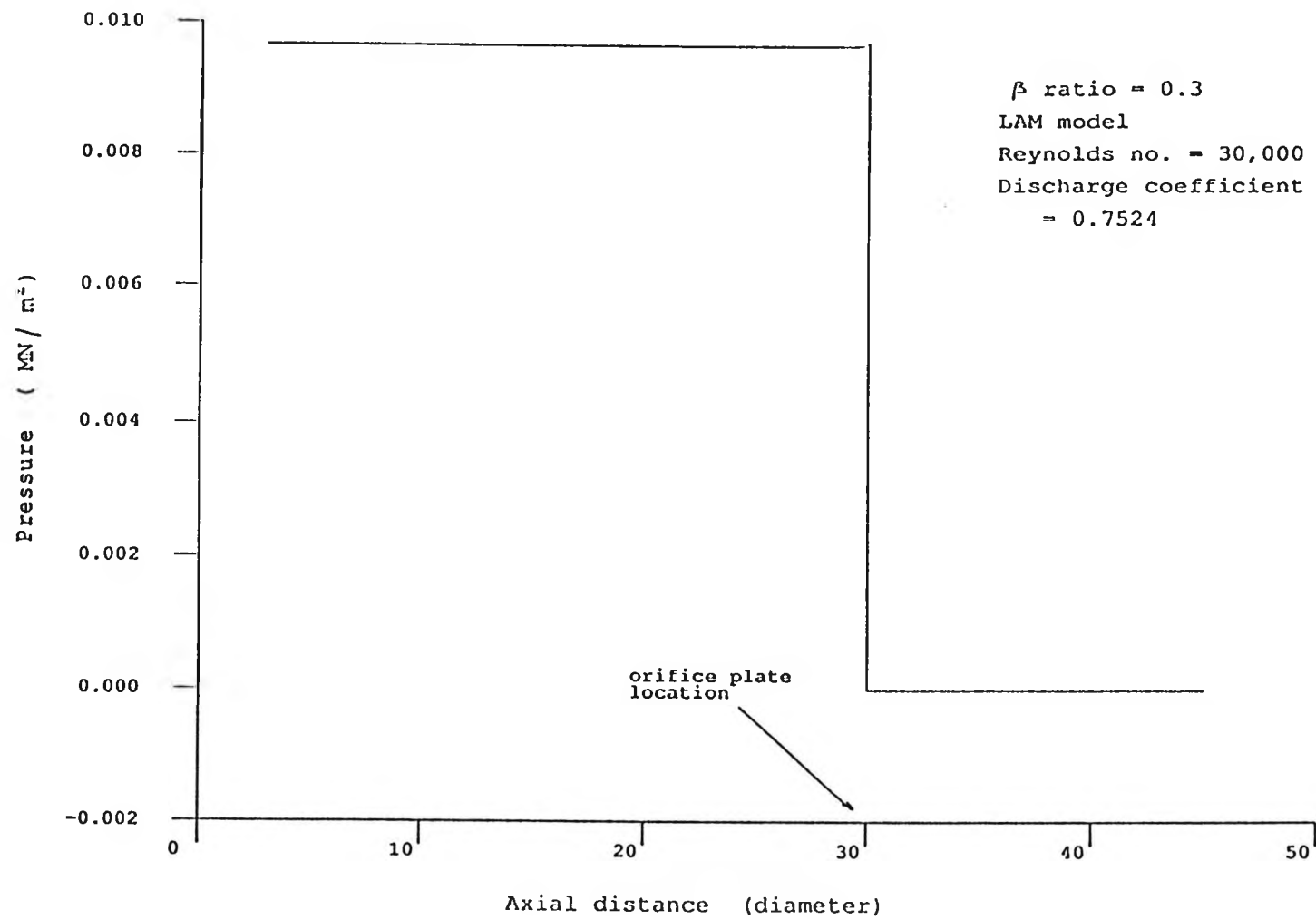


Fig. 5.14(b) Variation of the predicted wall pressure along the pipe

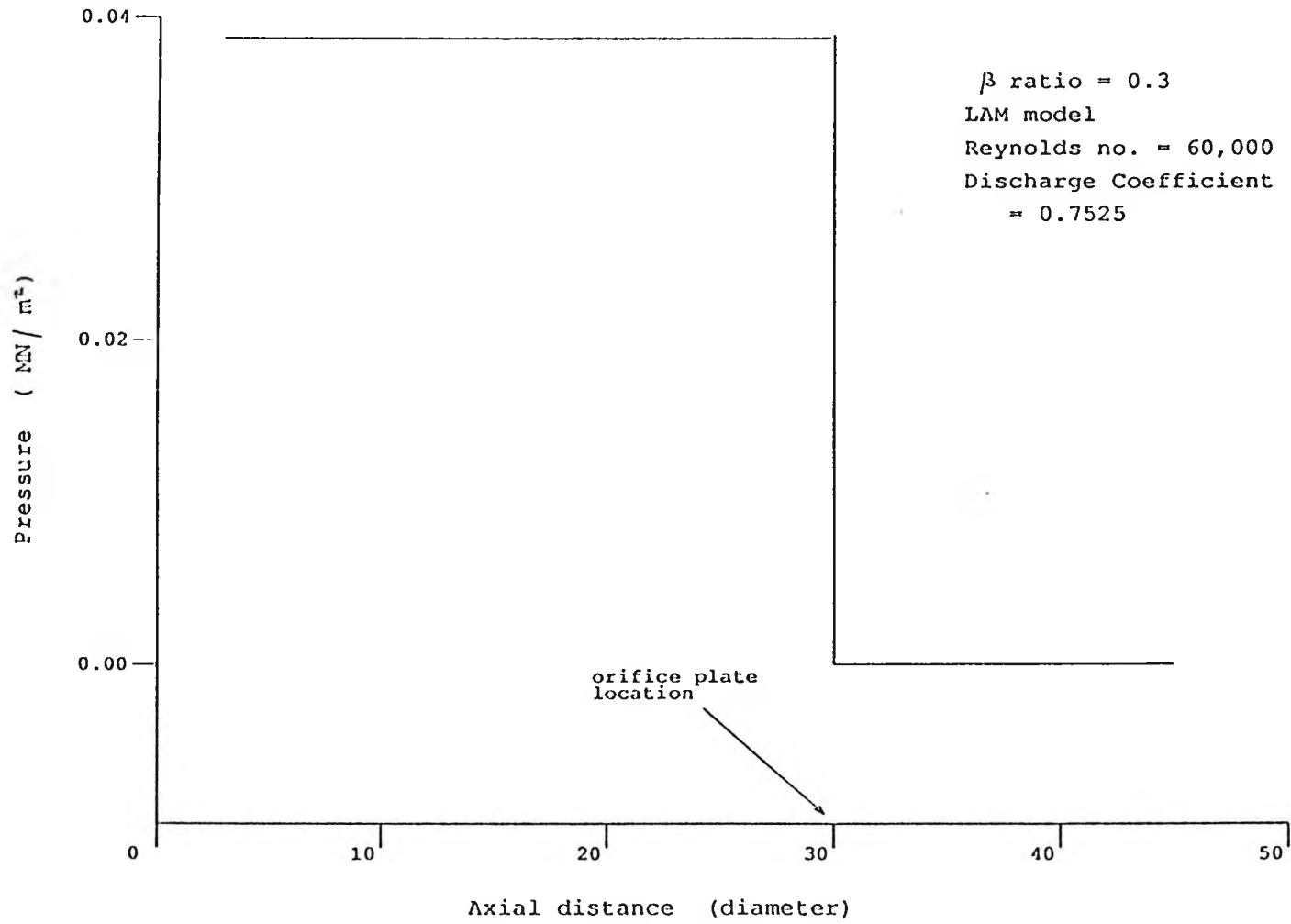


Fig. 5.14(c) Variation of the predicted wall pressure along the pipe

β RATIO = 0.2 REYNOLDS NO. = 30,000 (GRID STRETCHED 20 TIMES IN THE Y DIRECTION)

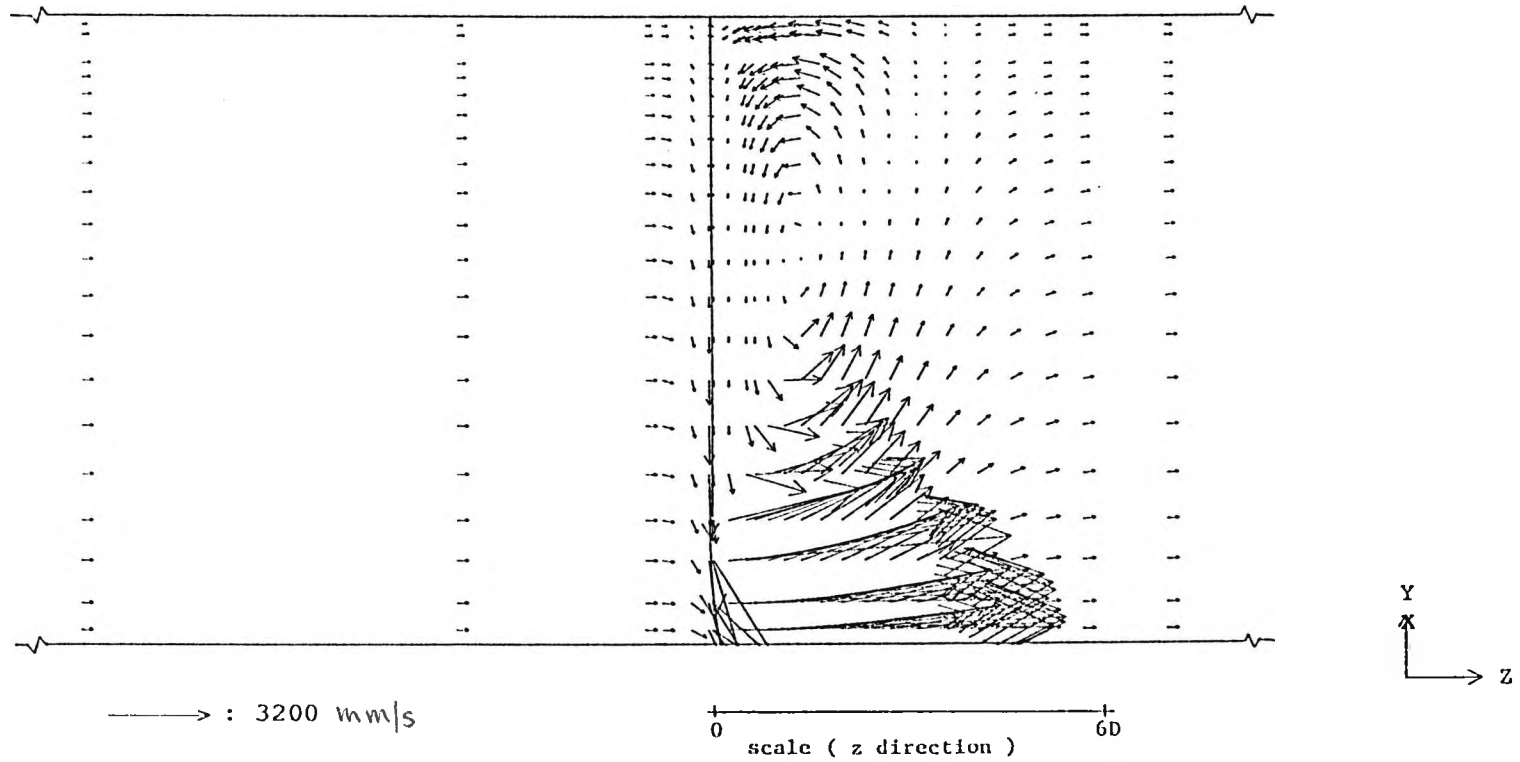


Fig. 5.15(a) Predicted velocity vector for flow through conical entrance orifice

downstream of the plate. Also evident from the figure is the presence of a recirculating eddy downstream of the orifice plate. Figure 5.15(b) shows the magnified view of the corners immediately upstream and downstream of the orifice plate, and the presence of a recirculating eddy at the upstream corner can be clearly seen.

As can be seen from the axial pressure profile plots presented in section 5.3.1, relatively significant pressure changes might occur streamwise in the region immediately downstream of the orifice plate. Thus, the flow pattern there may be of interest.

The changes in the flow pattern downstream of the orifice plate with Reynolds number are shown in figures 5.16 to 5.18 for different values of β . For clarity of the velocity vector plots, grid-scaling factors between 15 to 25 were employed to scale the dimension of the grids in the radial direction in these figures. The grid-scaling factor for the axial direction was unity.

Figures 5.16(a) to 5.16(f) present the velocity vector plots for $\beta = 0.3$. A recirculating eddy can be seen in the corner produced by the pipe wall and the downstream surface of the orifice plate in figures 5.16(a) and 5.16(b), corresponding to a Reynolds number of 60,000 and 30,000 respectively. As the Reynolds number is reduced, the extent of the recirculating zone exceed

β RATIO = 0.2 REYNOLDS NO. = 30,000 (GRID STRETCHED 5 TIMES IN THE Y DIRECTION)

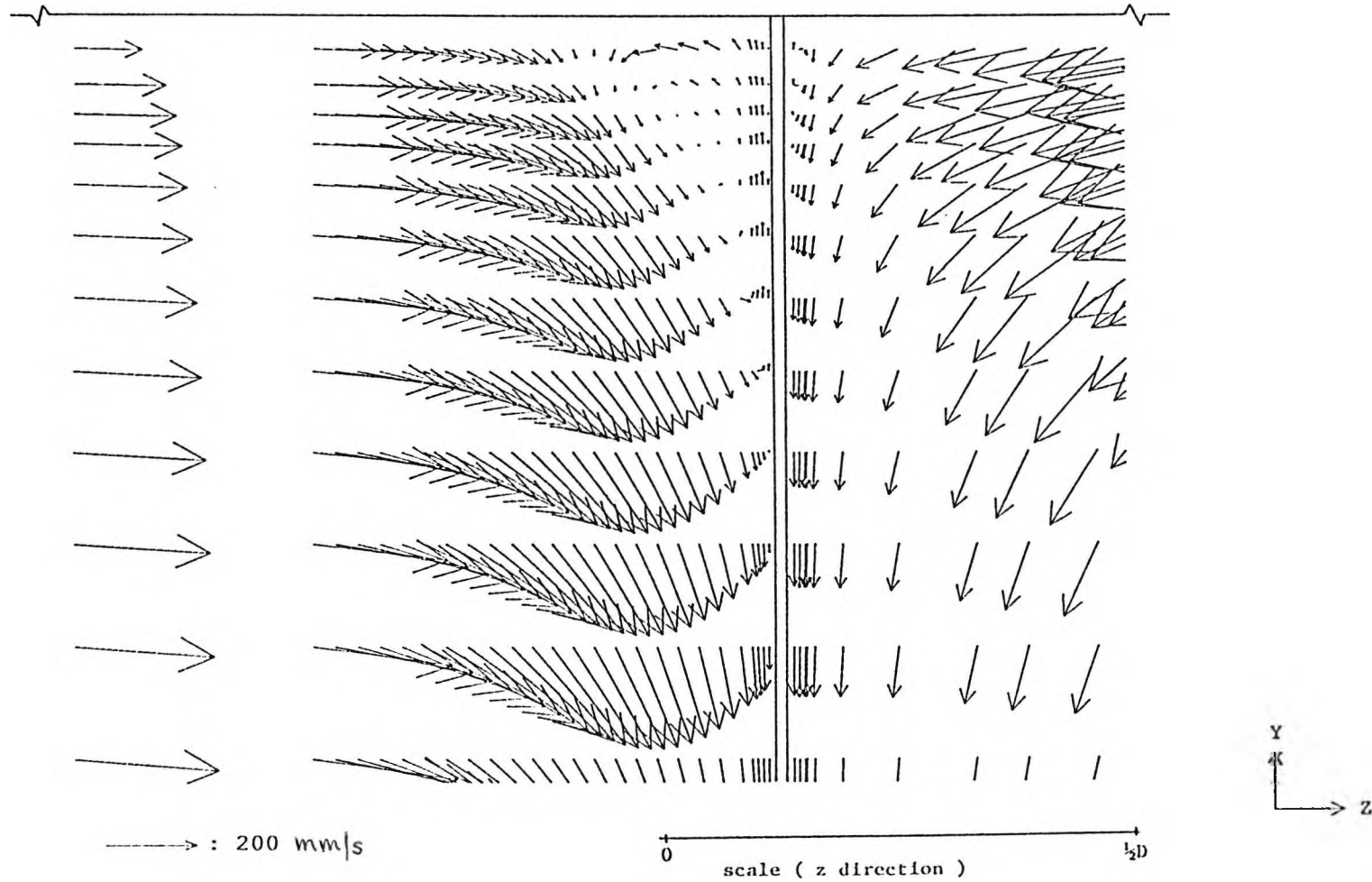


Fig. 5.15(b) Predicted velocity vector at the corners of the conical entrance orifice

β RATIO = 0.3 REYNOLDS NO. = 60,000 (GRID STRETCHED 15 TIMES IN THE Y DIRECTION)

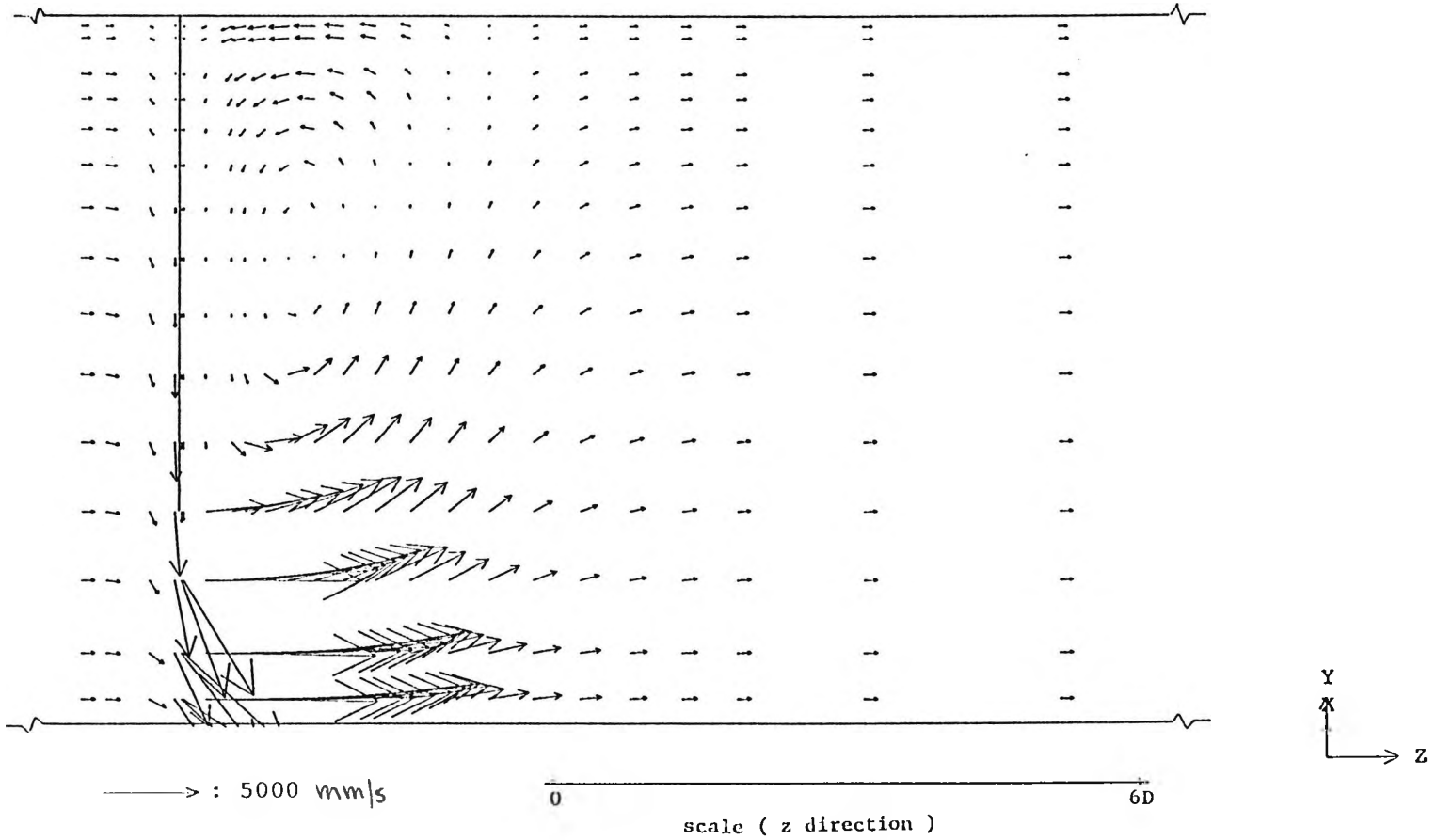


Fig. 5.16(a) Predicted velocity vector for flow through conical entrance orifice

β RATIO = 0.3 REYNOLDS NO. = 30,000 (GRID STRETCHED 15 TIMES IN THE Y DIRECTION)

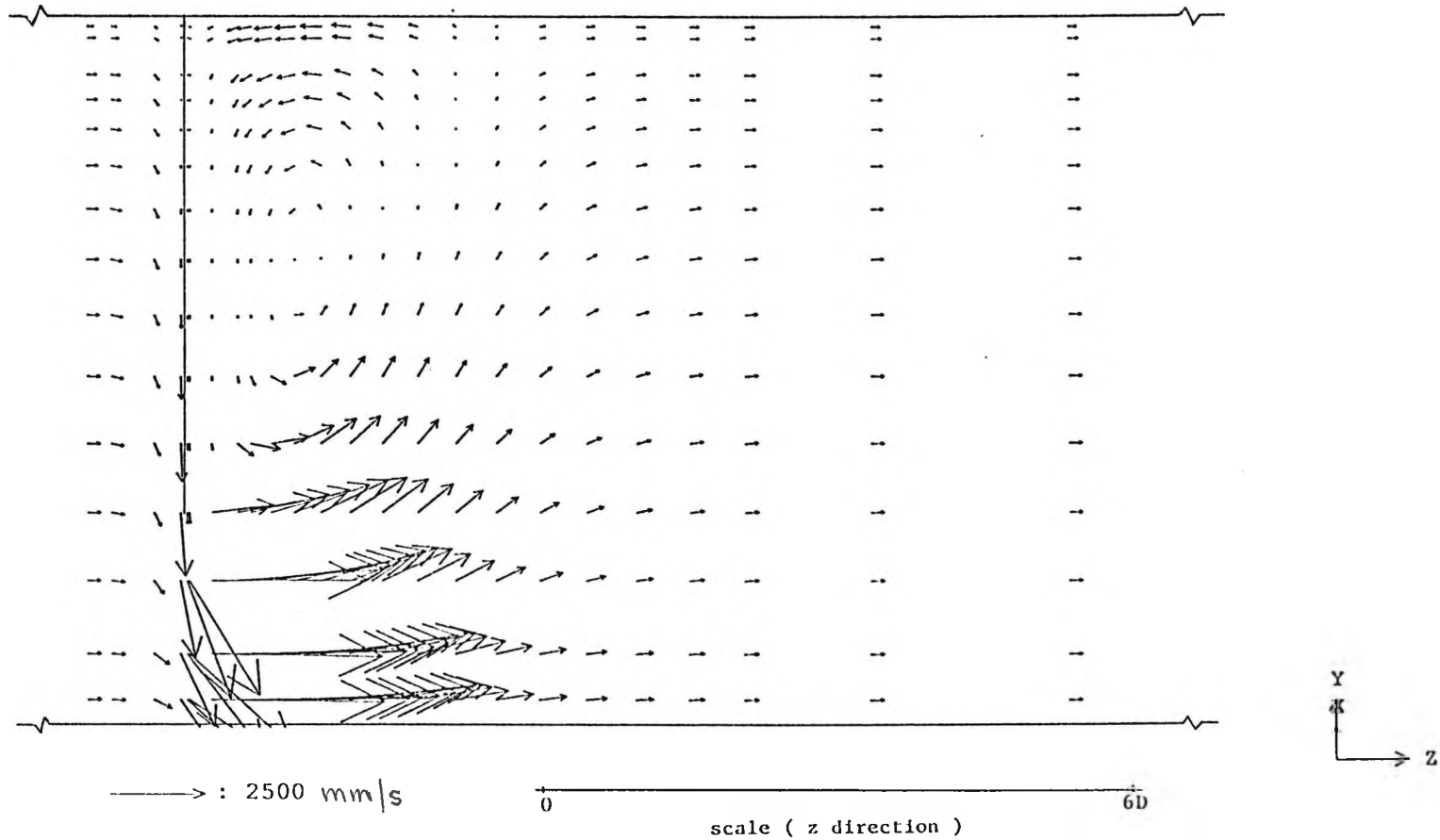
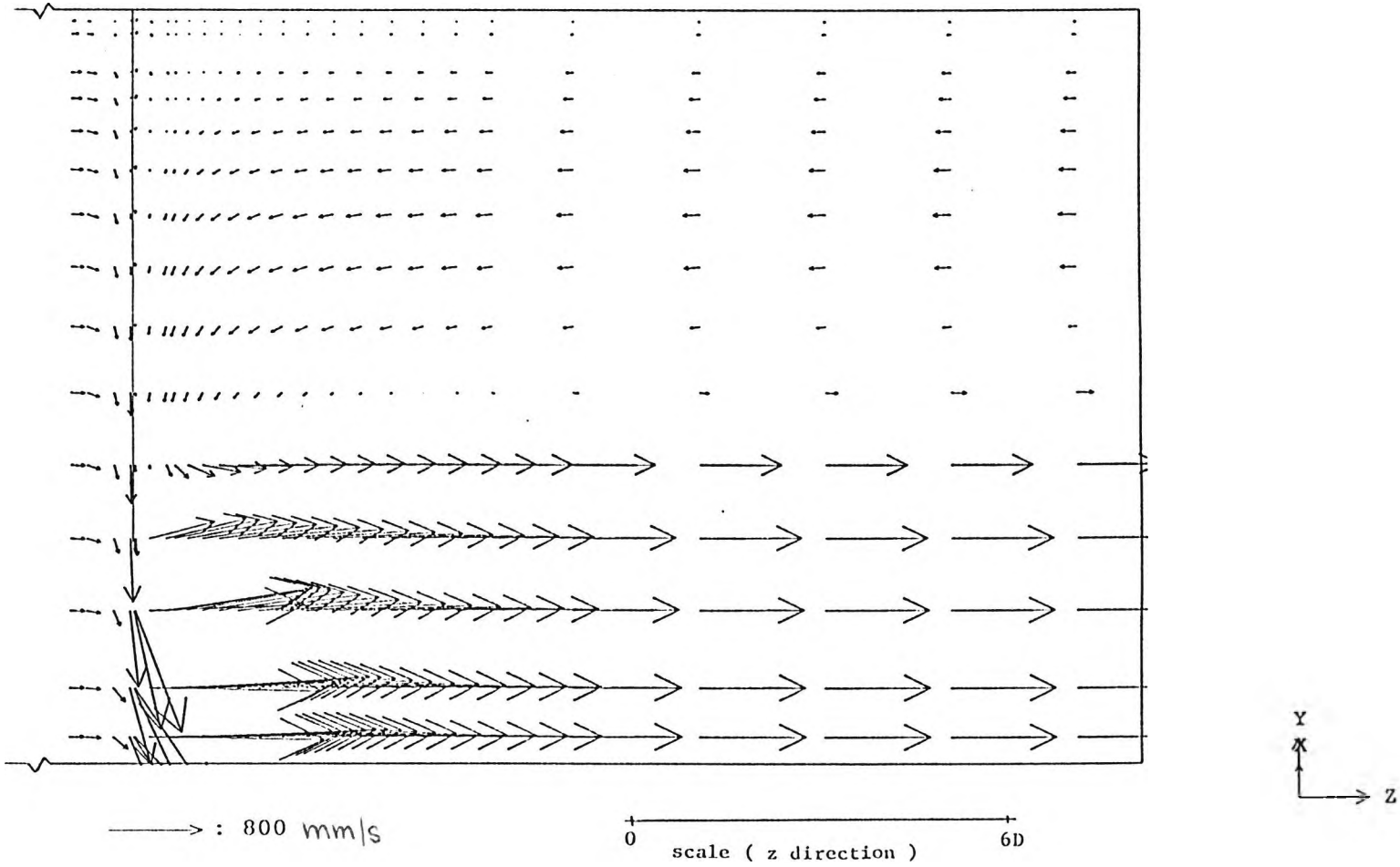


Fig. 5.16(b) Predicted velocity vector for flow through conical entrance orifice

β RATIO = 0.3 REYNOLDS NO. = 10,000 (GRID STRETCHED 25 TIMES IN THE Y DIRECTION)



150

Fig. 5.16(c) Predicted velocity vector for flow through conical entrance orifice

β RATIO = 0.3 REYNOLDS NO. = 6,000 (GRID STRETCHED 25 TIMES IN THE Y DIRECTION)

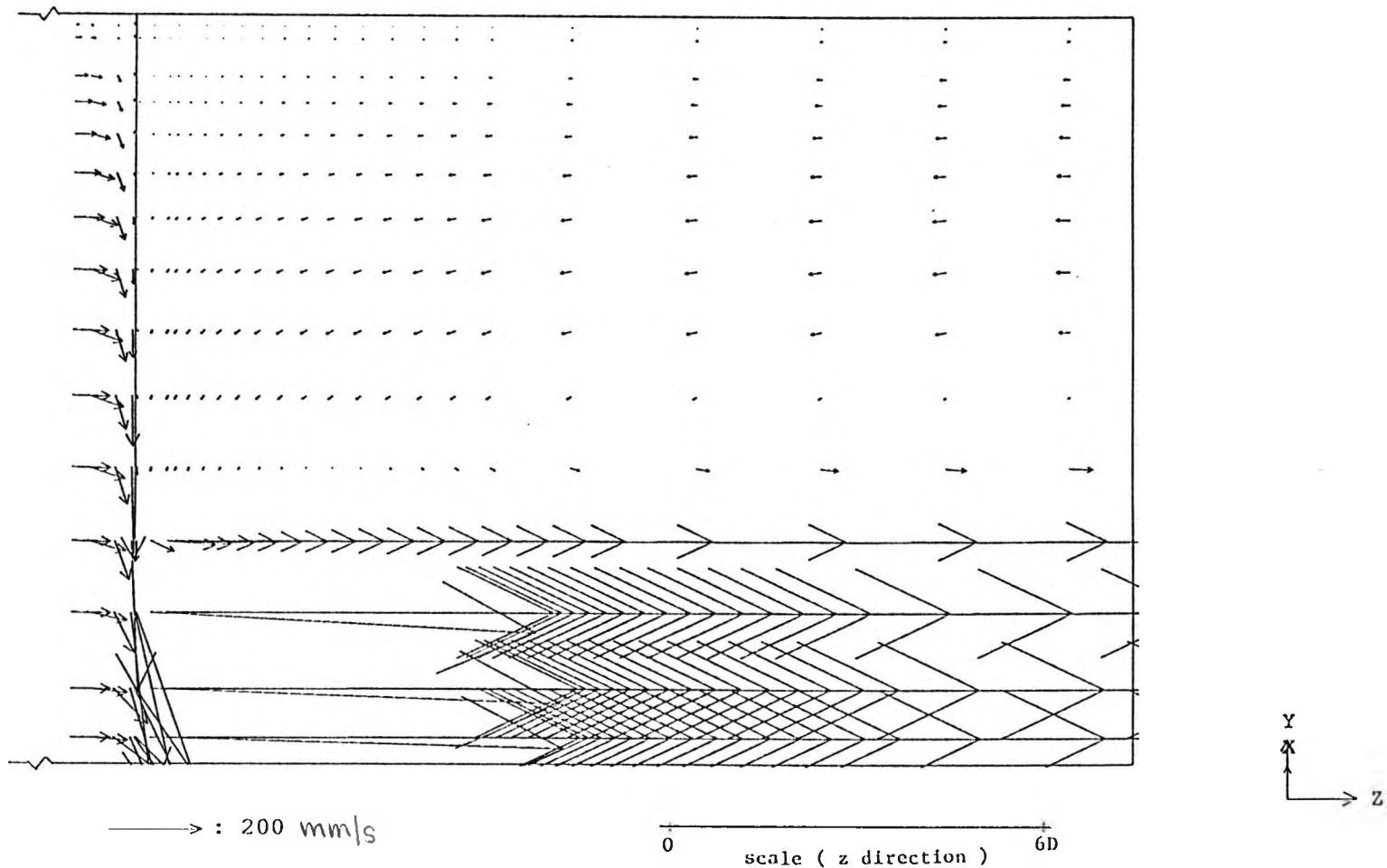


Fig. 5.16(d) Predicted velocity vector for flow through conical entrance orifice

β RATIO = 0.3 REYNOLDS NO. = 1,000 (GRID STRETCHED 25 TIMES IN THE Y DIRECTION)

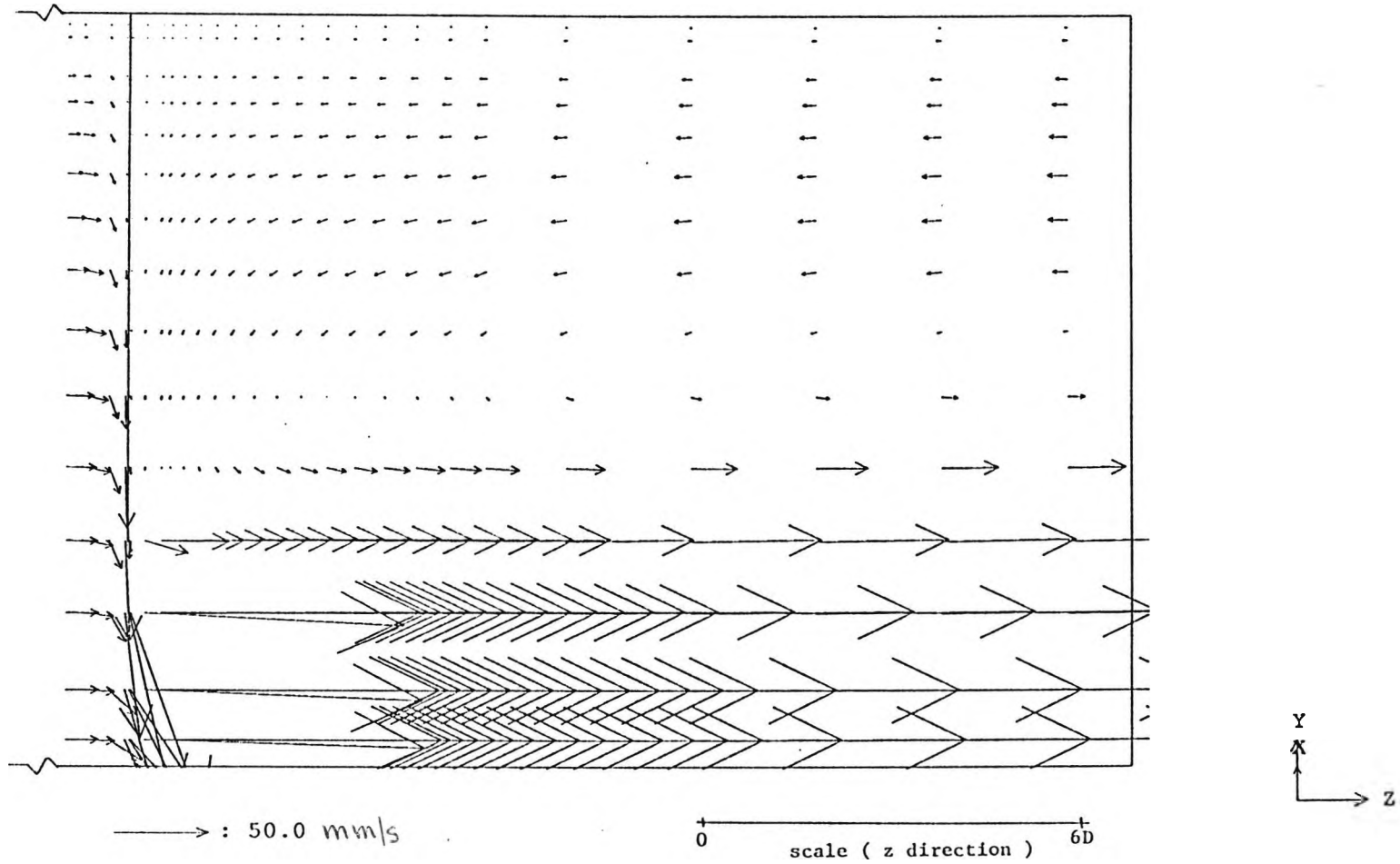


Fig. 5.16(e) Predicted velocity vector for flow through conical entrance orifice

β RATIO = 0.3 REYNOLDS NO. = 80 (GRID STRETCHED 25 TIMES IN THE Y DIRECTION)

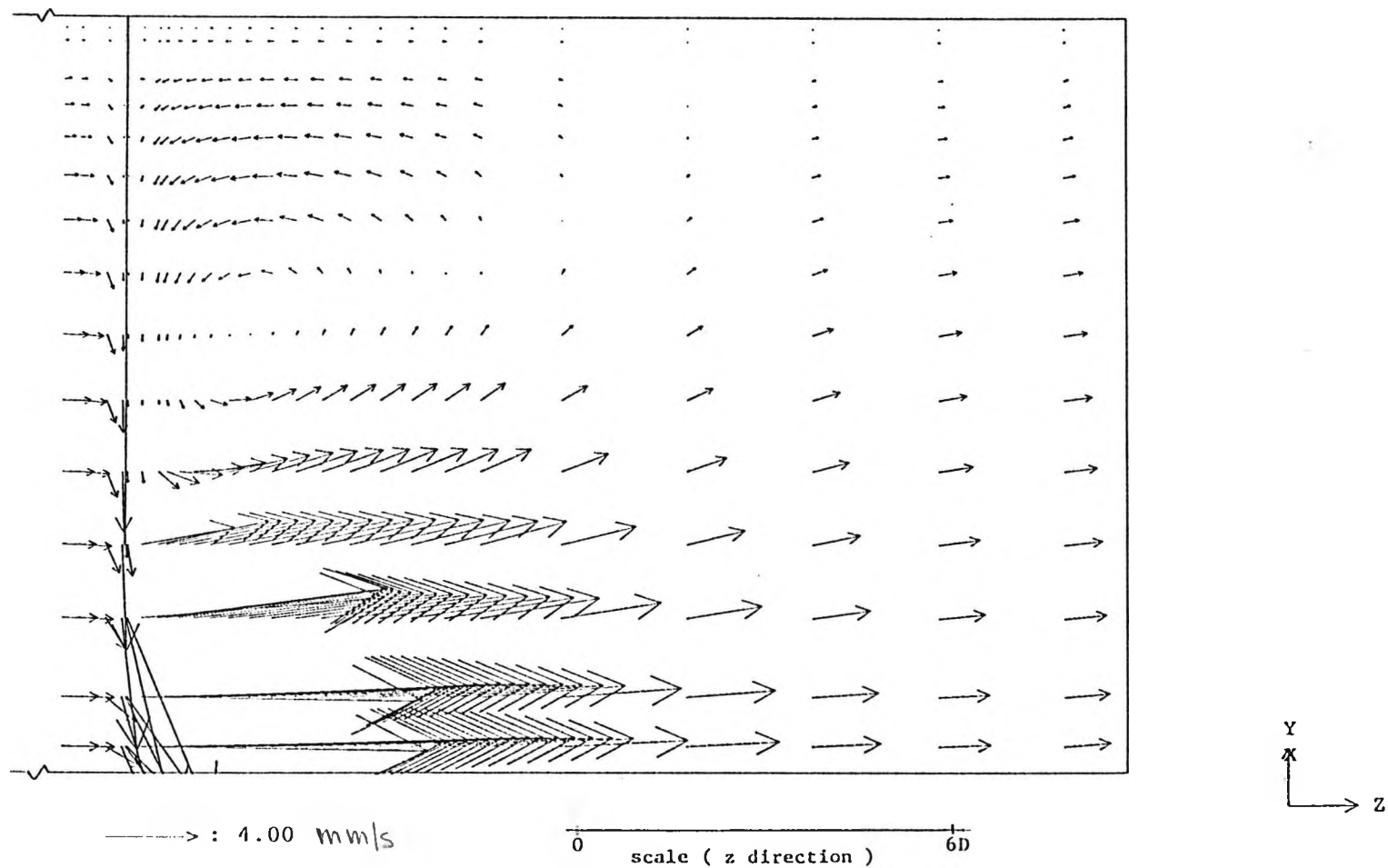


Fig. 5.16(f) Predicted velocity vector for flow through conical entrance orifice

the downstream length of the pipe used in the simulation. This can be seen from figures 5.16(c), 5.16(d) and 5.16(e), corresponding to a Reynolds number of 10,000, 6,000 and 1,000 respectively. At a Reynolds number of 80, however, an entire recirculating eddy can again be seen in the downstream corner, as is evident from figure 5.16(f).

The flow pattern downstream of the orifice plate at different Reynolds numbers are shown in figures 5.17 and 5.18 for $\beta = 0.2$ and 0.1 respectively. The flow pattern varies with the Reynolds number in about the same manner as that observed for $\beta = 0.3$.

5.3.3 Recirculation zone downstream of the conical entrance orifice plate

The results presented in figures 5.16 to 5.18 used a downstream length of $16 D$, and as shown in section 5.3.2, the extent of the recirculation zone may be larger than the downstream pipe length of $16 D$ used depending on the β ratio and Reynolds numbers. Thus, for some of these cases, results were also obtained using a longer downstream pipe length. The length of the downstream recirculation zone, which is the distance of the reattachment point from the orifice plate, is shown in table 5.2 for various Reynolds numbers and β ratio.

From table 5.2, it can be seen that, for a constant

β RATIO = 0.2 REYNOLDS NO. = 60,000 (GRID STRETCHED 15 TIMES IN THE Y DIRECTION)

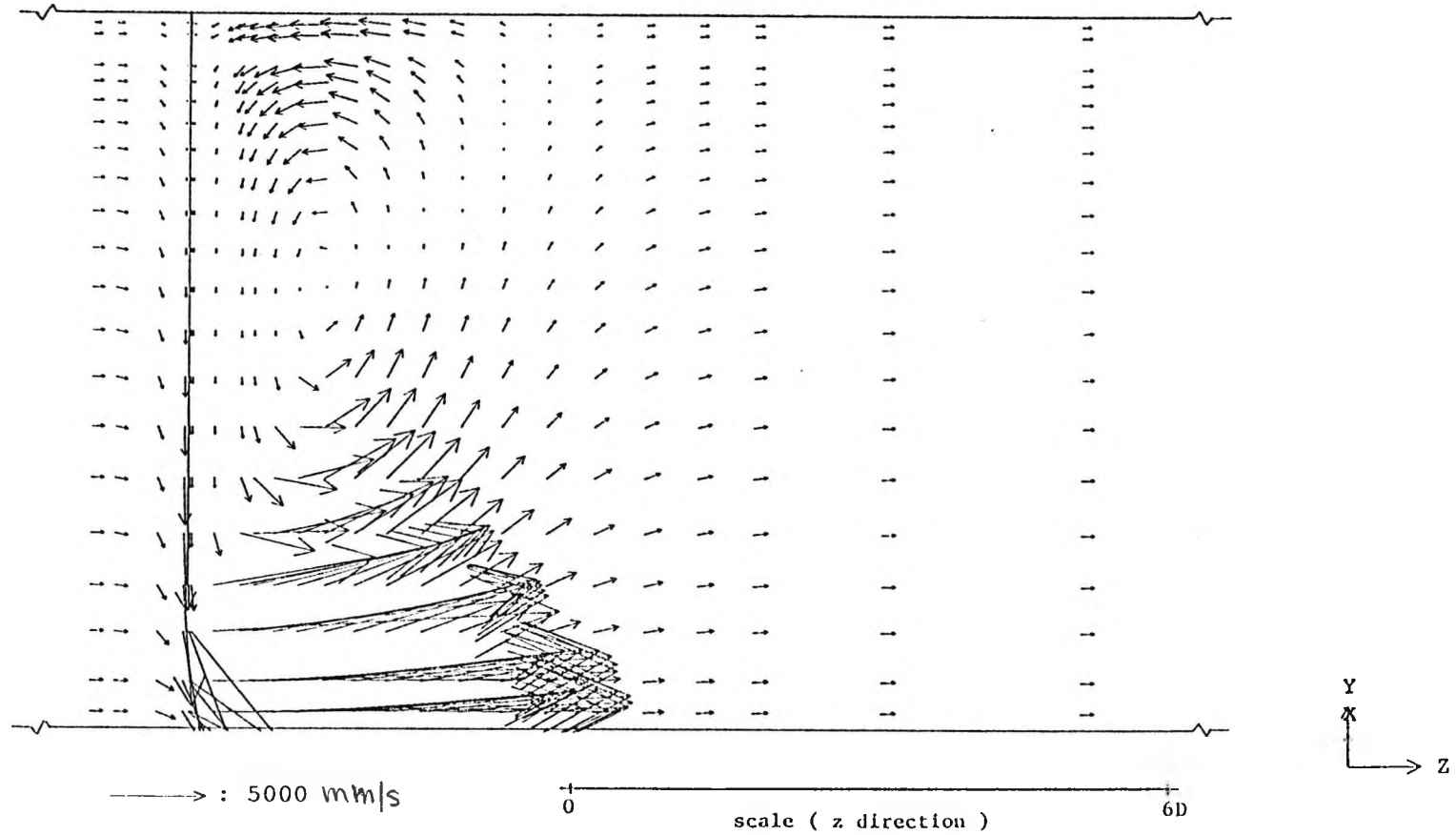


Fig. 5.17(a) Predicted velocity vector for flow through conical entrance orifice

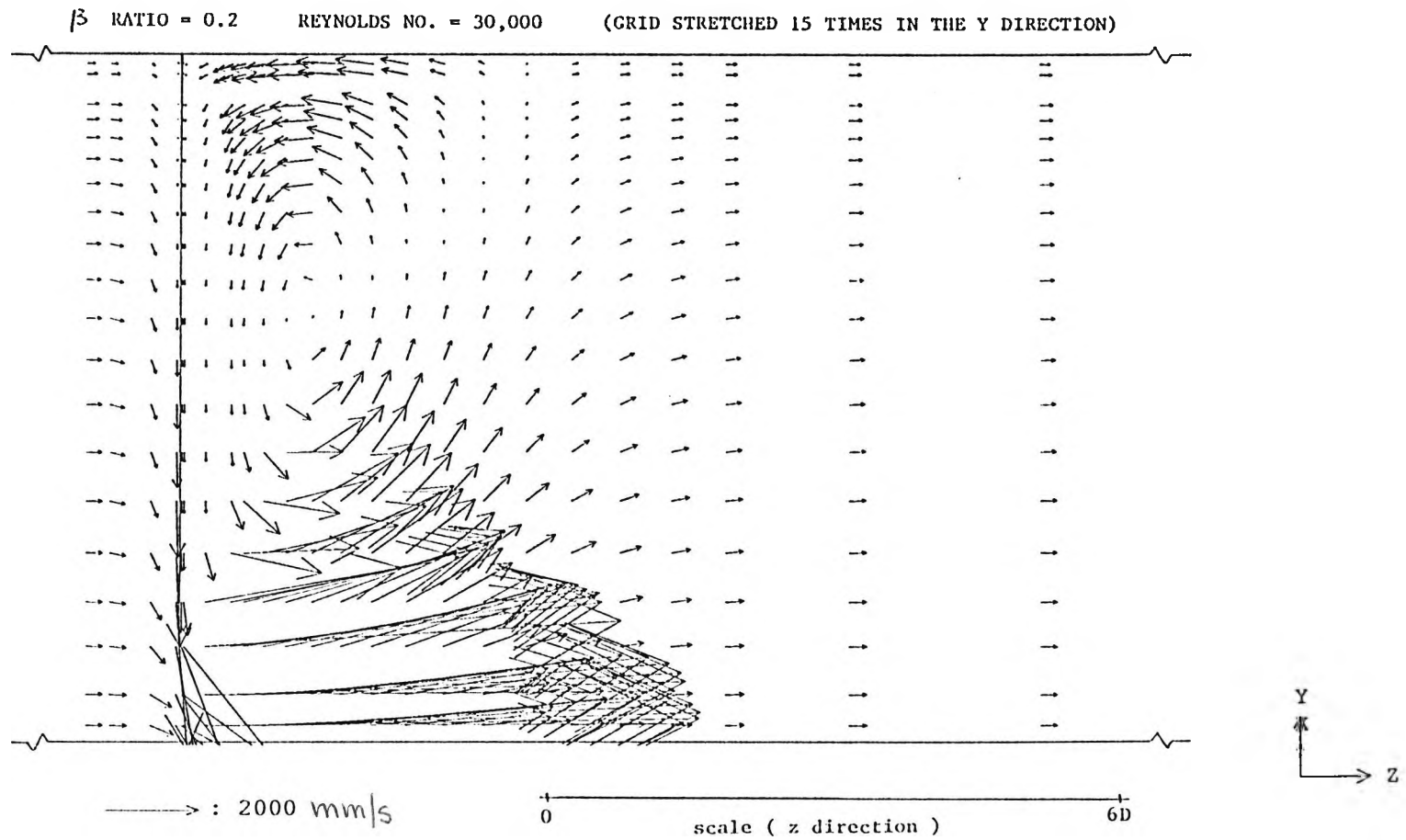


Fig. 5.17(b) Predicted velocity vector for flow through conical entrance orifice

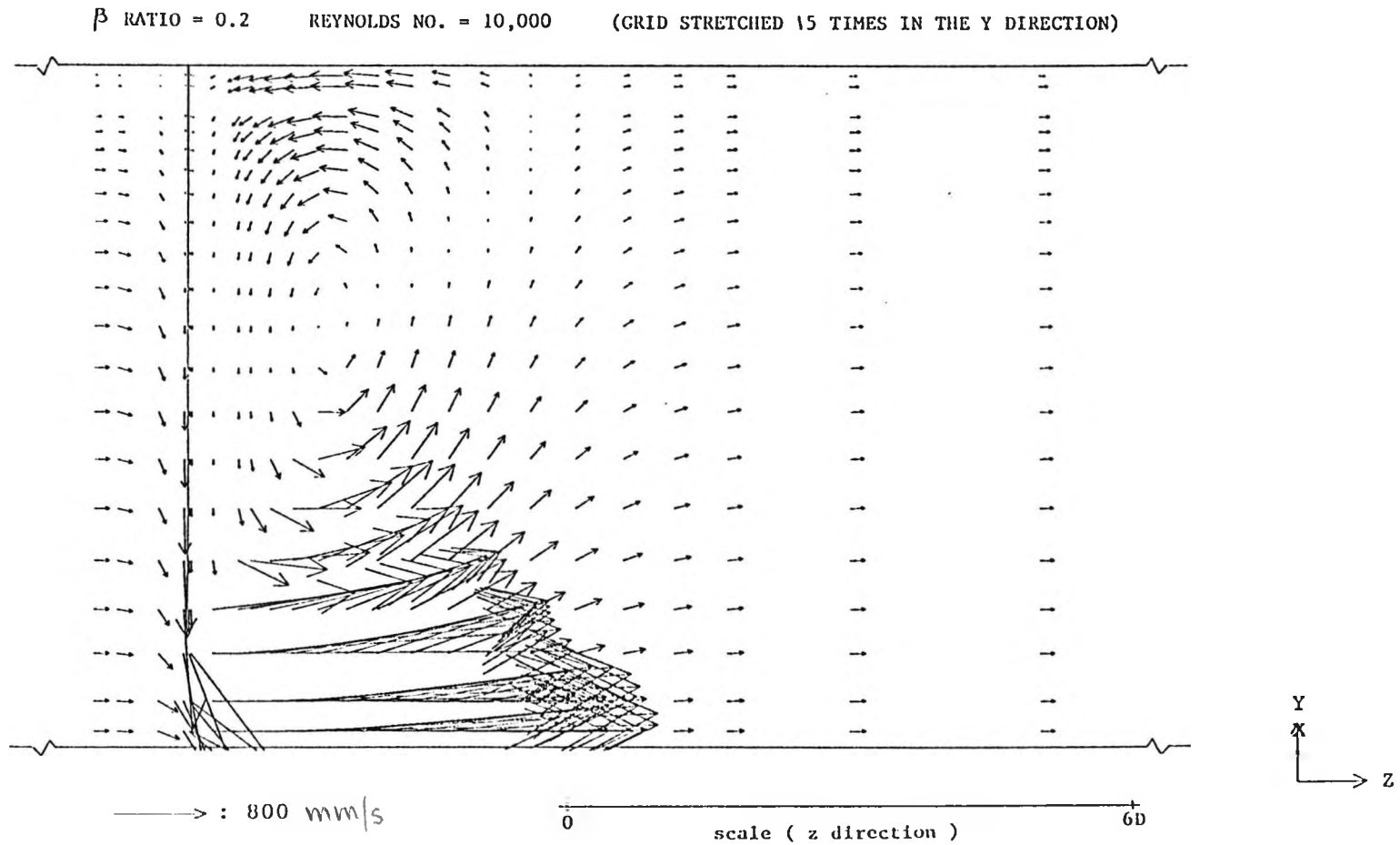


Fig. 5.17(c) Predicted velocity vector for flow through conical entrance orifice

β RATIO = 0.2 REYNOLDS NO. = 6,000 (GRID STRETCHED 25 TIMES IN THE Y DIRECTION)

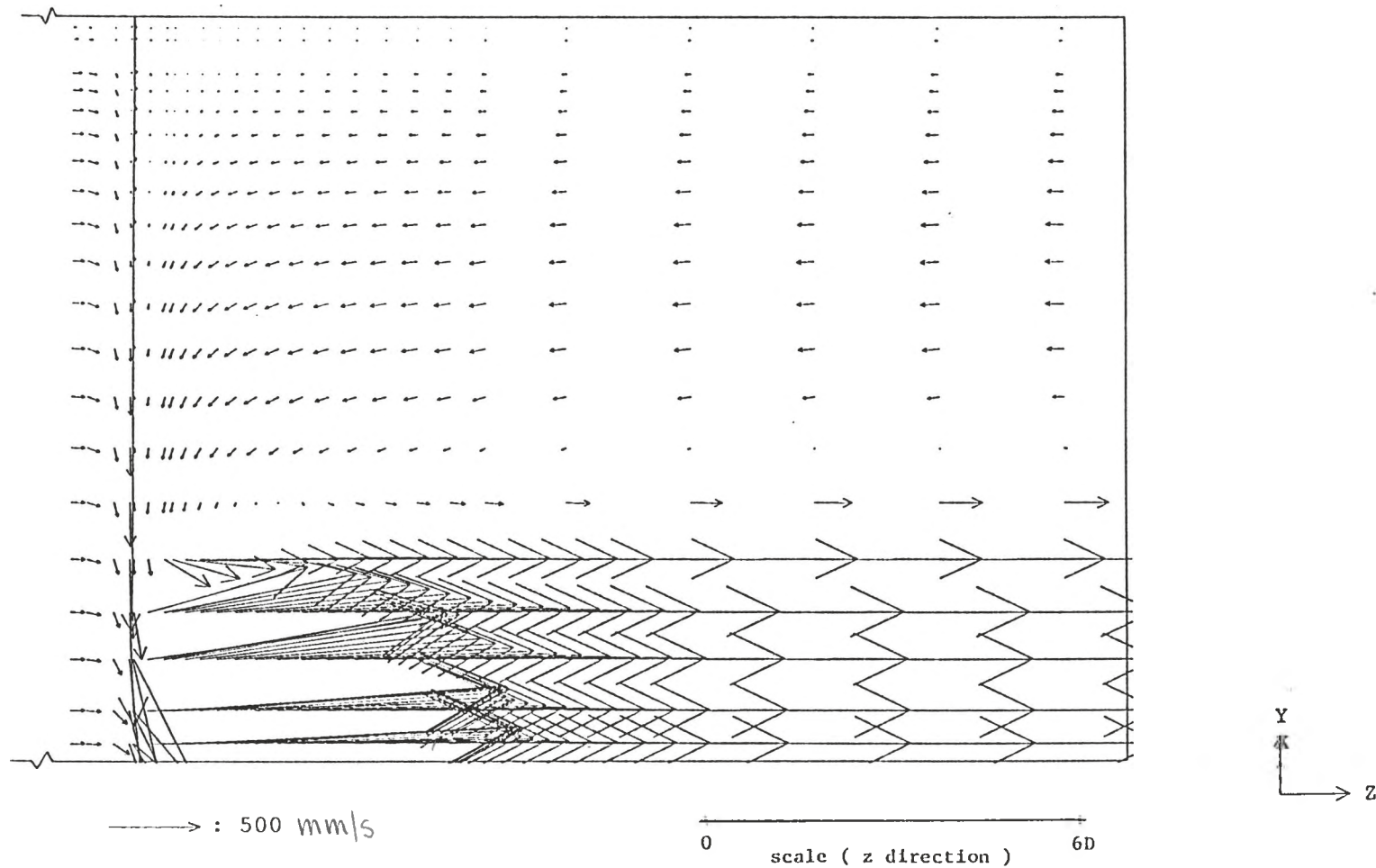


Fig. 5.17(d) Predicted velocity vector for flow through conical entrance orifice

β RATIO = 0.2 REYNOLDS NO. = 1,000 (GRID STRETCHED 25 TIMES IN THE Y DIRECTION)

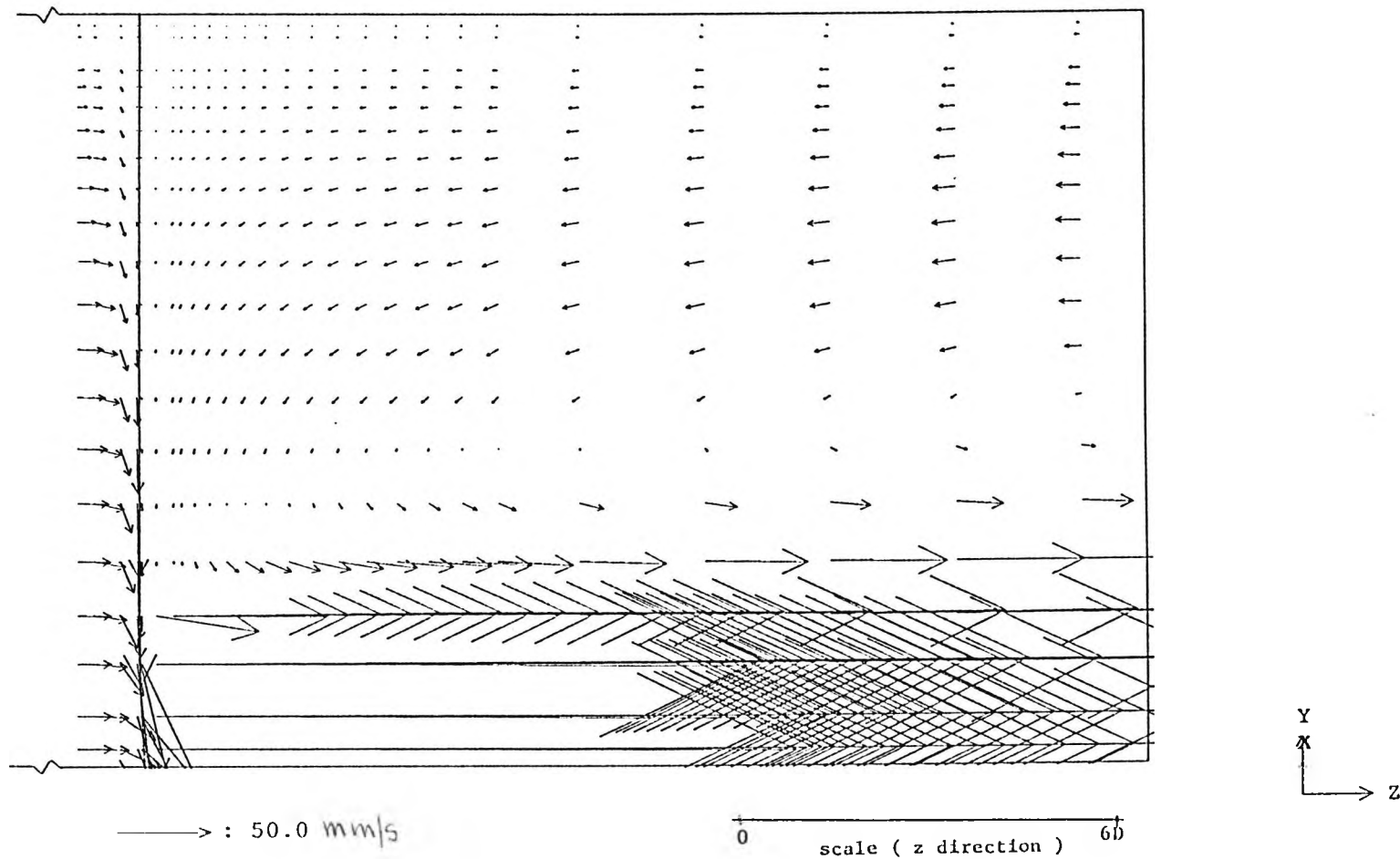


Fig. 5.17(e) Predicted velocity vector for flow through conical entrance orifice

β RATIO = 0.2 REYNOLDS NO. = 80 (GRID STRETCHED 25 TIMES IN THE Y DIRECTION)

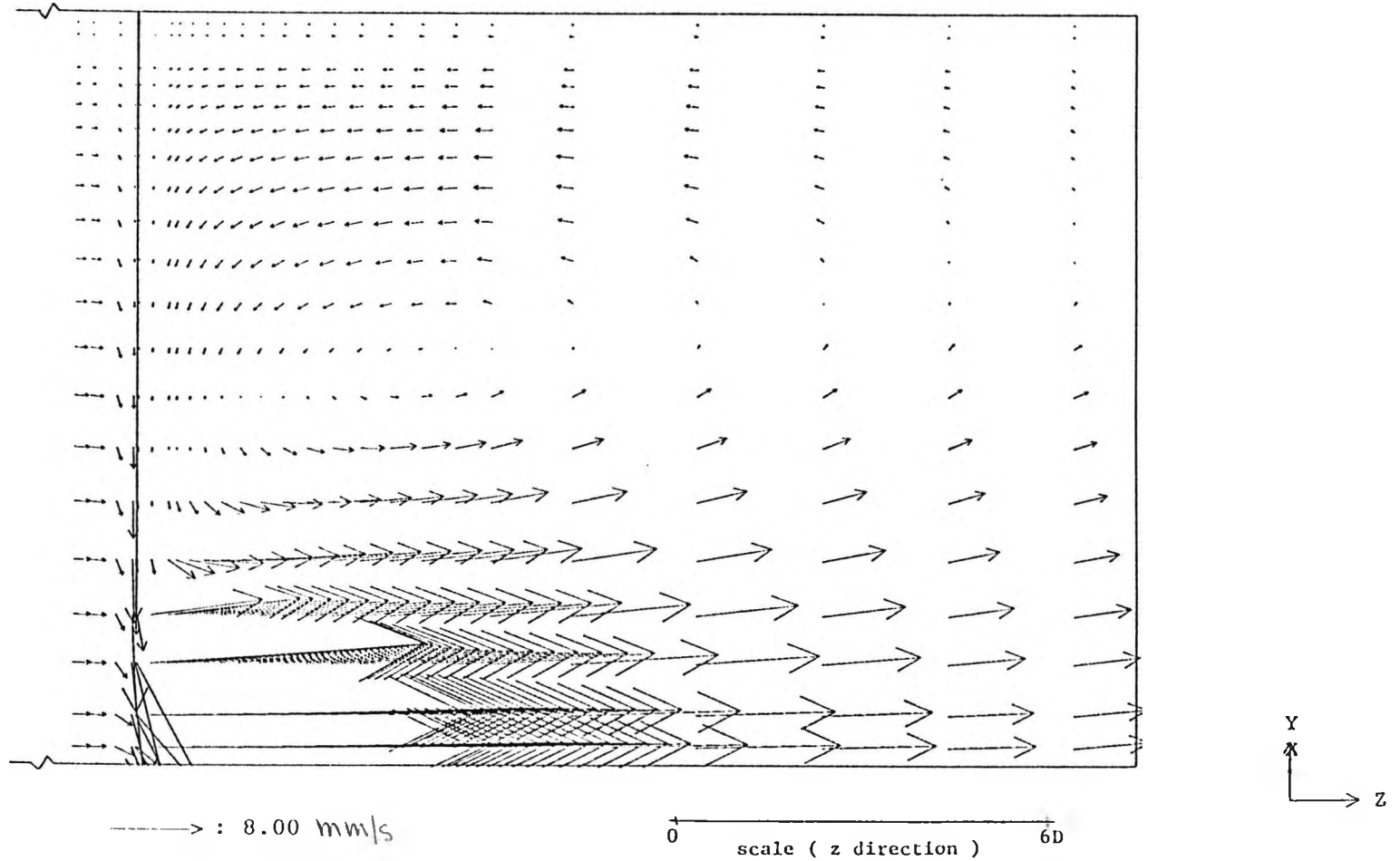


Fig. 5.17(f) Predicted velocity vector for flow through conical entrance orifice

β RATIO = 0.1 REYNOLDS NO. = 60,000 (GRID STRETCHED 15 TIMES IN THE Y DIRECTION)

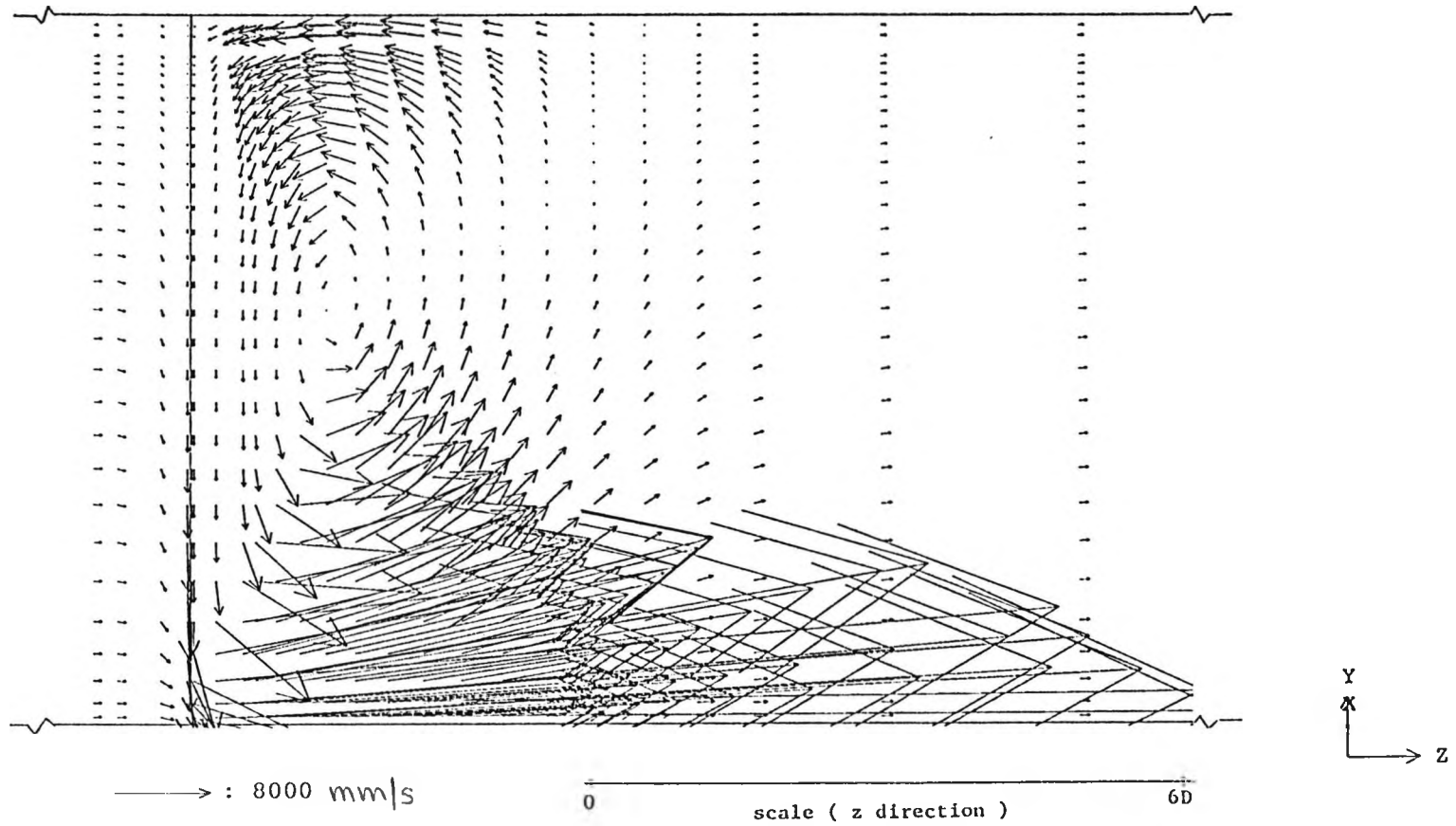


Fig. 5.18(a) Predicted velocity vector for flow through conical entrance orifice

β RATIO = 0.1 REYNOLDS NO. = 30,000 (GRID STRETCHED 15 TIMES IN THE Y DIRECTION)

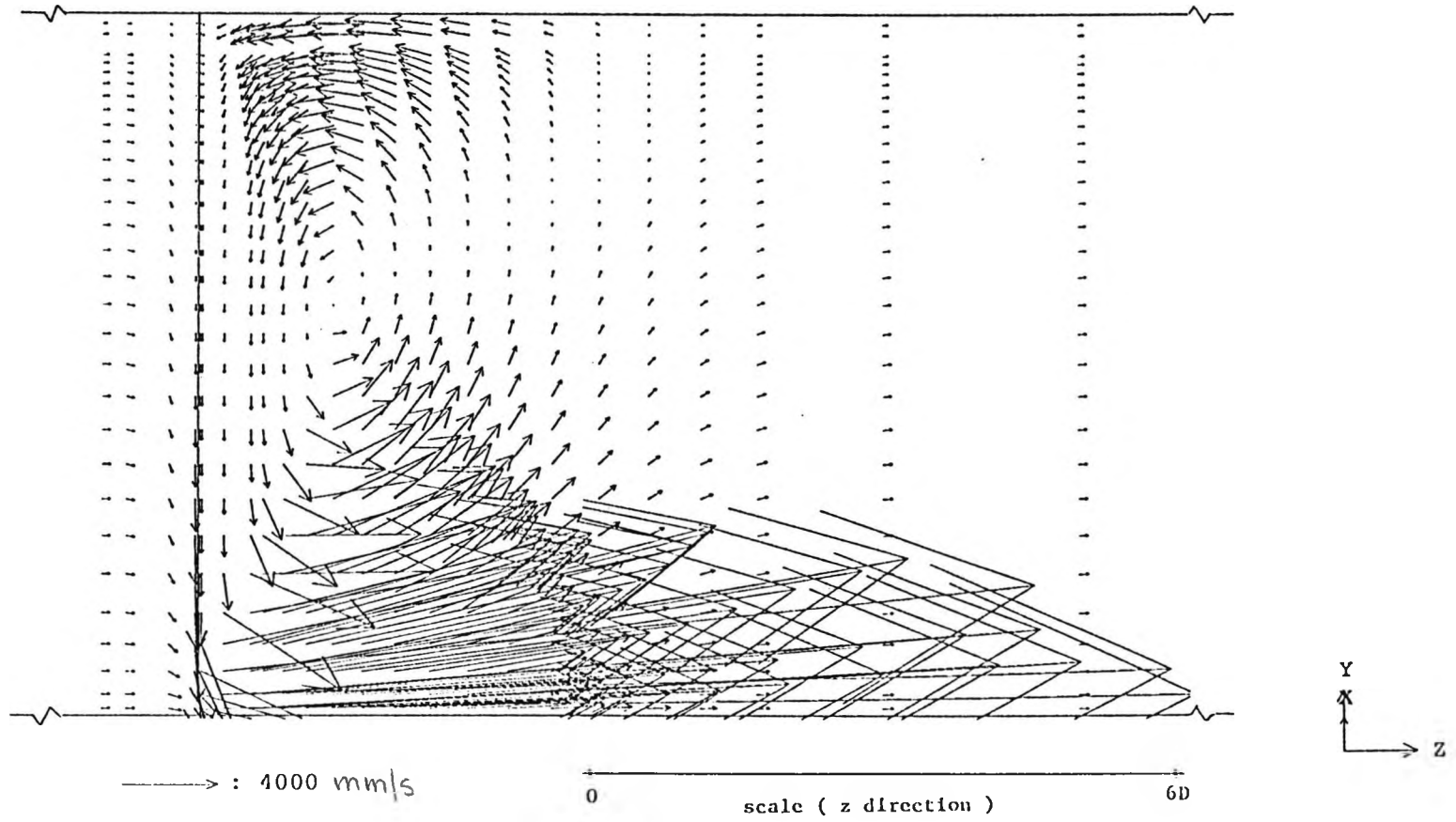


Fig. 5.18(b) Predicted velocity vector for flow through conical entrance orifice

β RATIO = 0.1 REYNOLDS NO. = 10,000 (GRID STRETCHED 25 TIMES IN THE Y DIRECTION)

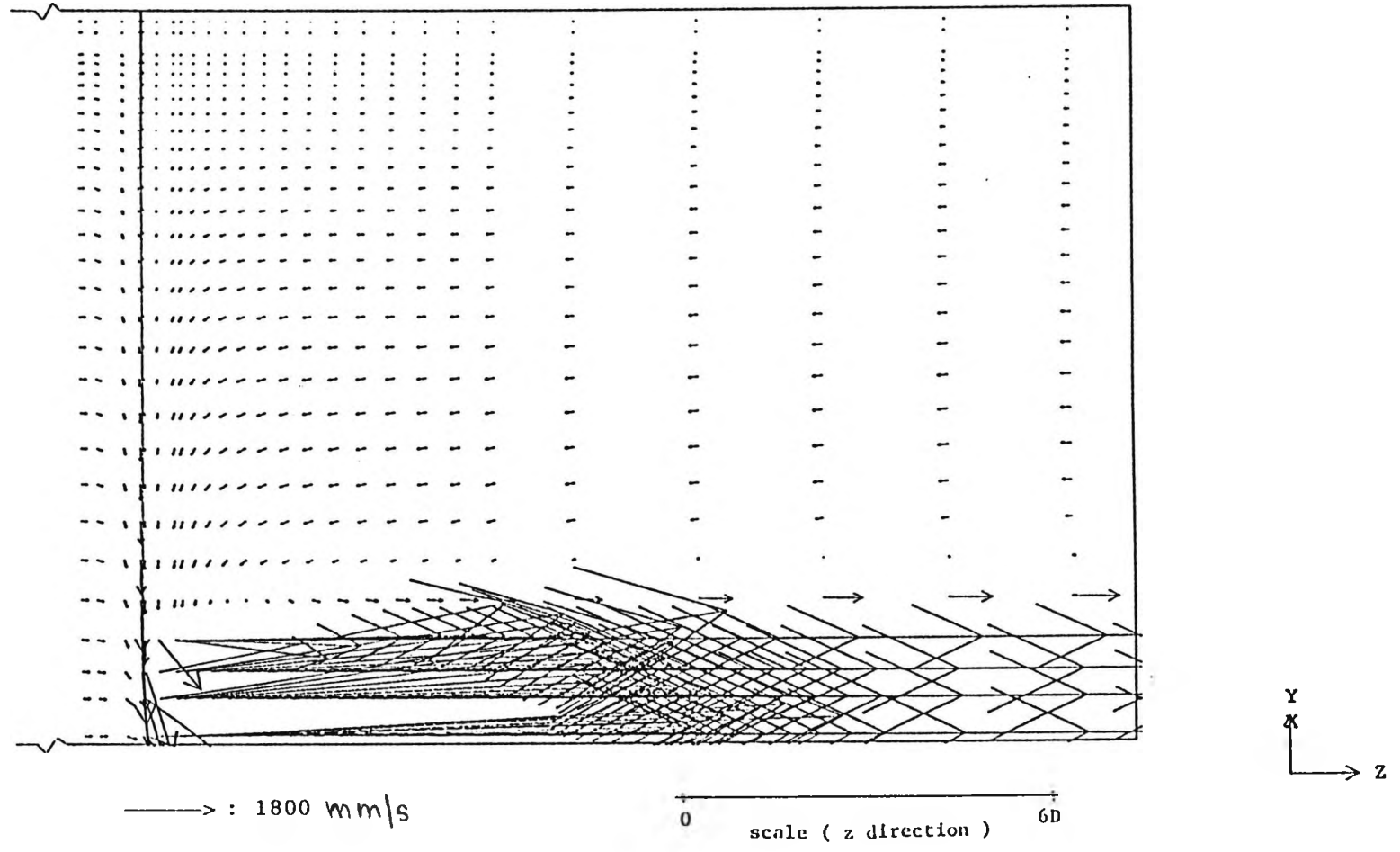


Fig. 5.18(c) Predicted velocity vector for flow through conical entrance orifice

β RATIO = 0.1 REYNOLDS NO. = 6,000 (GRID STRETCHED 25 TIMES IN THE Y DIRECTION)

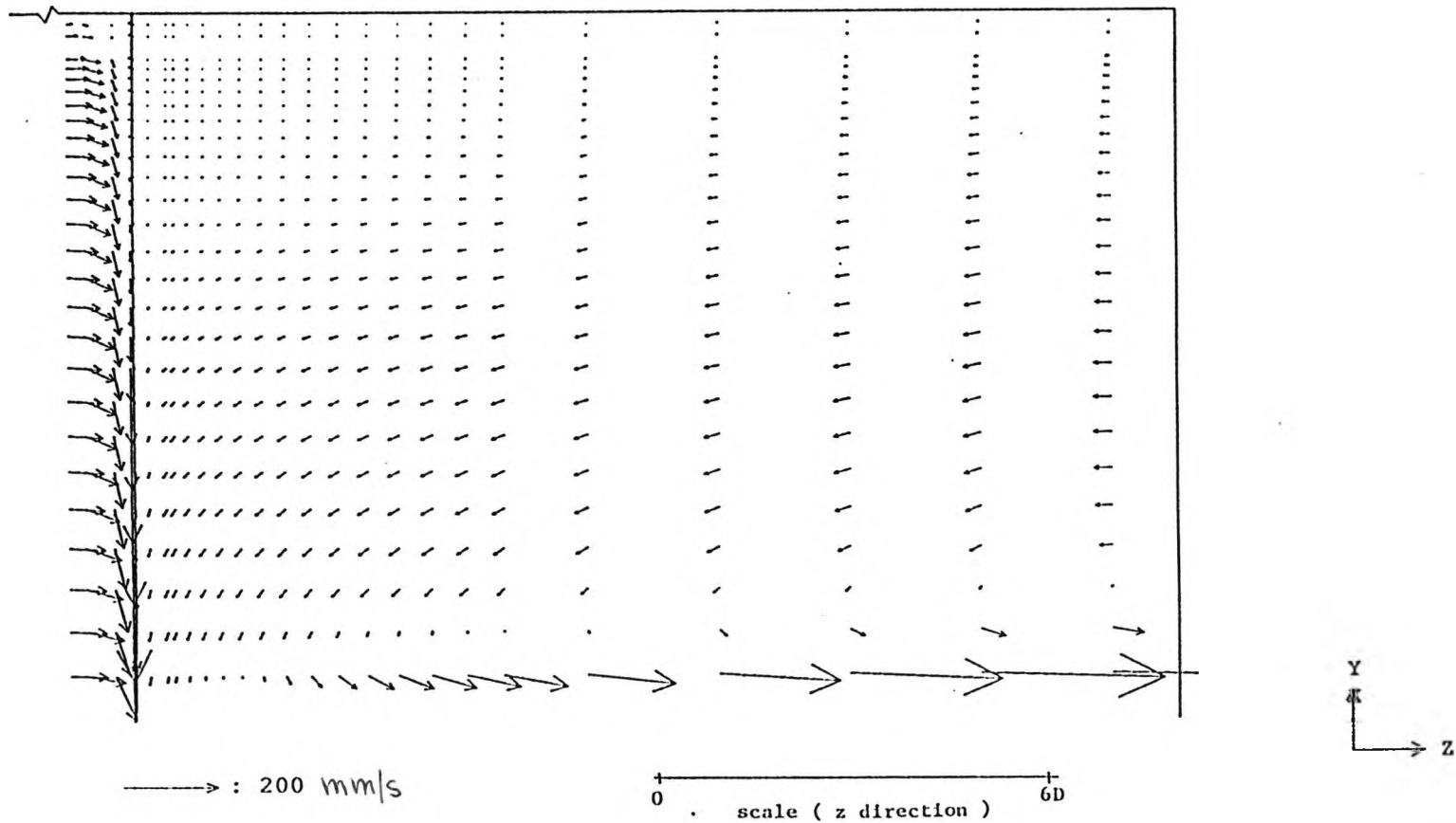


Fig. 5.18(d) Predicted velocity vector for flow through conical entrance orifice

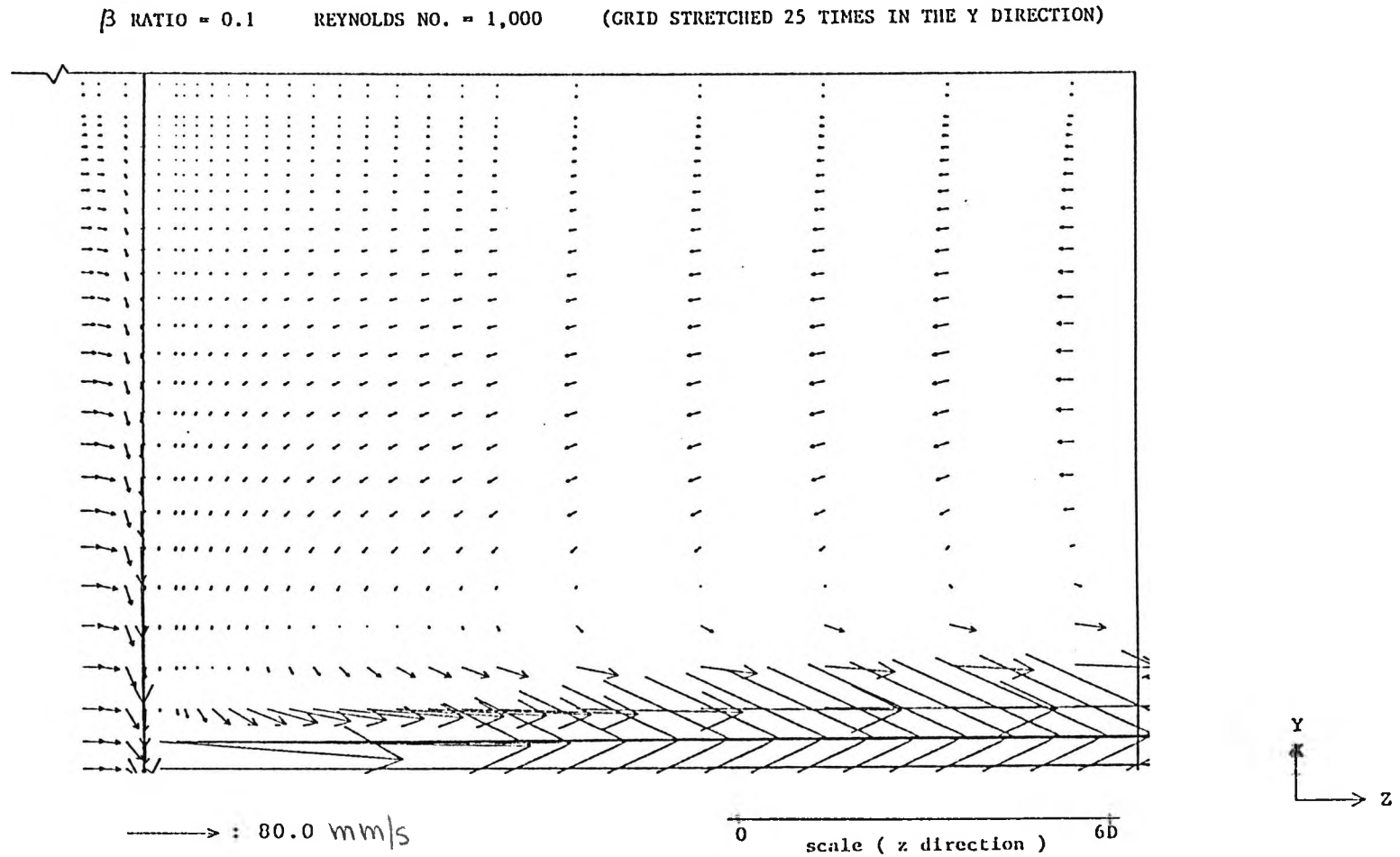


Fig. 5.18(e) Predicted velocity vector for flow through conical entrance orifice

β RATIO = 0.1 REYNOLDS NO. = 80 (GRID STRETCHED 25 TIMES IN THE Y DIRECTION)

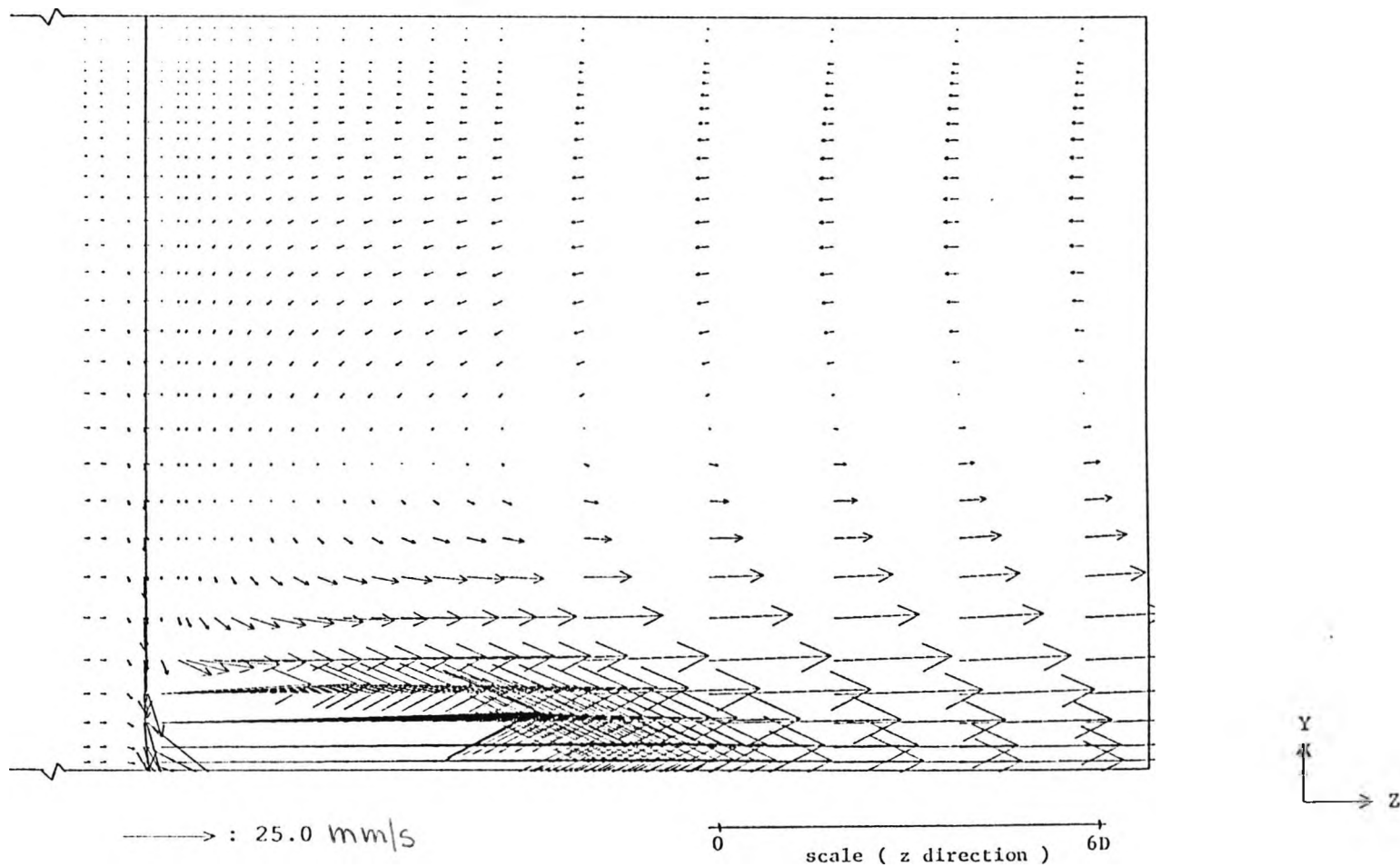


Fig. 5.18(f) Predicted velocity vector for flow through conical entrance orifice

β ratio	Reynolds Number	upstream length	downstream length	length of downstream recirculation zone
0.1	80	30 D	206 D	38.0 D
	1,000	30 D	606 D	416.0 D
	6,000	30 D	1506 D	> 1506.0 D
	10,000	30 D	16 D	> 16.0 D
	30,000	30 D	16 D	4.1 D
	60,000	30 D	16 D	4.1 D
0.2	80	30 D	56 D	16.0 D
	1,000	30 D	406 D	202.0 D
	6,000	30 D	1506 D	1188.0 D
	10,000	30 D	16 D	3.2 D
	30,000	30 D	16 D	3.2 D
	60,000	30 D	16 D	3.2 D
0.3	80	30 D	16 D	8.0 D
	1,000	30 D	406 D	108.0 D
	6,000	30 D	1506 D	638.0 D
	10,000	30 D	16 D	> 16.0 D
	30,000	30 D	16 D	2.8 D
	60,000	30 D	16 D	2.8 D

Table 5.2 Length of the downstream recirculation zone

β ratio and for the Reynolds numbers investigated, the recirculating eddy lengthens with Reynolds number at low Reynolds numbers. At high Reynolds numbers, however, the size of the eddy remains approximately constant and becomes smaller than that observed at the lower Reynolds numbers.

Little information is available on how the size of the recirculating eddy will vary with Reynolds number for flows through orifice for the range of Reynolds number given in table 5.2. Therefore, no direct comparison with other results can be made. However, the trend observed in table 5.2 agree qualitatively with that observed by Ghoniem (64) who studied the flow over a rearward-facing step. The structure of the recirculation zone forming behind a rearward-facing step in a channel was computed for Reynolds number in the 50-5000 range. It was observed that the recirculation zone length increases with Reynolds number, reaching a maximum at transition, and then decay to a shorter length at the turbulent range.

For constant Reynolds number, the recirculating eddy lengthens with decreasing β as is observed from table 5.2. The same trend was reported by other workers (13, 16) although for different ranges of β ratio and Reynolds number.

5.4 Effect of turbulence intensity and length scale factor

The simulation of the conical entrance orifice plate flow sensor was performed using a uniform profile for all quantities at the pipe inlet. In particular, empirical relationships (equations 4.9 and 4.10) were used to assign values to k and ϵ at the inlet ($k_{in} = iV_z^2$ and $\epsilon_{in} = k_{in}^{1.5}/\lambda R$).

The intensity of turbulence i and length scale factor λ used in the simulation was 0.003 and 0.333 respectively. These are typical values used in specifying inlet conditions for internal flows without swirl (65). However, the actual values for these quantities will vary depending on the particular situation when the conical entrance orifice plate is employed in flow measurement. Thus, the inlet value of i and λ are varied to investigate their effect on the discharge coefficient.

Table 5.3 shows the effect of changing the turbulence intensity i and length scale factor λ for $\beta = 0.2$ and $Re_0 = 10,000$. A uniform inlet profile of k and ϵ was used in test no. 1 to test no. 8. However, for test nos. 9 and 10, a 2-step profile was used for k . For the upper half of the inlet plane, the value of i was specified to be 0.1 in both cases; the values of i for the lower half of the inlet plane were 0.01 and 0.001 respectively for test nos. 9 and 10.

$\beta = 0.2$						
test no.	Reynolds Number	i	λ	Discharge Coefficient		
				Corner tappings	Flange tappings	D & 1/2 D tappings
1	10,000	0.001	0.03	0.7438 (0.00 %)	0.7438 (0.00 %)	0.7436 (0.00 %)
2	10,000	0.001	0.333	0.7439 (0.01 %)	0.7438 (0.00 %)	0.7436 (0.00 %)
3	10,000	0.003	0.03	0.7438 (0.00 %)	0.7437 (-0.01 %)	0.7435 (-0.01 %)
4	10,000	0.003	0.333	0.7438 (0.00 %)	0.7438 (0.00 %)	0.7436 (0.00 %)
5	10,000	0.003	1.0	0.7438 (0.00 %)	0.7438 (0.00 %)	0.7436 (0.00 %)
6	10,000	0.03	0.333	0.7438 (0.00 %)	0.7437 (-0.01 %)	0.7435 (-0.01 %)
7	10,000	0.1	0.333	0.7438 (0.00 %)	0.7437 (-0.01 %)	0.7435 (-0.01 %)
8	10,000	0.1	1.0	0.7438 (0.00 %)	0.7438 (0.00 %)	0.7436 (0.00 %)
9	10,000	0.01 - 0.1 (2 - step profile)	0.333	0.7438 (0.00 %)	0.7437 (-0.01 %)	0.7435 (-0.01 %)
10	10,000	0.001 - 0.1 (2 - step profile)	0.333	0.7439 (0.01 %)	0.7438 (0.00 %)	0.7436 (0.00 %)

* value in bracket is the percentage deviation of the discharge coefficient from that of test no. 4

Table 5.3 Variation of discharge coefficient with turbulence intensity i and length scale factor λ

It can be seen from table 5.3 that there is very little variation in the computed discharge coefficients for the range of values of i and λ investigated. The deviation of the discharge coefficient from the reference value (with $i = 0.003$ and $\lambda = 0.333$) is within 0.01 %.

Table 5.4 shows the results for $\beta = 0.2$ and for a Reynolds number of 60,000. The deviation from the reference value is within 0.04 %.

Table 5.5 presents the results for $\beta = 0.1$ and 0.3 with $Re_p = 60,000$. The deviation of the discharge coefficient is within 0.07 % of the reference value.

Thus, it can be seen that, for the range of values considered, the variation in the inlet values of i and λ has very little effect on the discharge coefficient of conical entrance orifice plate. This is in agreement with the observation by McVeigh (25) that the conical entrance orifice plate is comparatively insensitive to upstream effects.

5.5 Effects of geometric tolerances on conical entrance orifice plate

The British Standard for conical entrance orifice plates specifies a conic entrance angle F of $45^\circ \pm 1^\circ$. The thickness of the conical entrance J is specified to be $0.084d \pm 0.003d$ and the axial length of the parallel

$\beta = 0.2$						
test no.	Reynolds Number	i	λ	Discharge Coefficient		
				Corner tappings	Flange tappings	D & 1/2 D tappings
1	60,000	0.001	0.03	0.7360 (0.01 %)	0.7358 (0.00 %)	0.7355 (0.00 %)
2	60,000	0.001	0.333	0.7358 (-0.01 %)	0.7358 (0.00 %)	0.7355 (0.00 %)
3	60,000	0.003	0.03	0.7359 (0.00 %)	0.7358 (0.00 %)	0.7355 (0.00 %)
4	60,000	0.003	0.333	0.7359 (0.00 %)	0.7358 (0.00 %)	0.7355 (0.00 %)
5	60,000	0.003	1.0	0.7358 (-0.01 %)	0.7358 (0.00 %)	0.7355 (0.00 %)
6	60,000	0.03	0.333	0.7359 (0.00 %)	0.7358 (0.00 %)	0.7355 (0.00 %)
7	60,000	0.1	0.333	0.7358 (-0.01 %)	0.7358 (0.00 %)	0.7355 (0.00 %)
8	60,000	0.1	1.0	0.7356 (-0.04 %)	0.7355 (-0.04 %)	0.7353 (-0.03 %)
9	60,000	0.01 - 0.1 (2 - step profile)	0.333	0.7359 (0.00 %)	0.7358 (0.00 %)	0.7355 (0.00 %)
10	60,000	0.001 - 0.1 (2 - step profile)	0.333	0.7359 (0.00 %)	0.7358 (0.00 %)	0.7355 (0.00 %)

* value in bracket is the percentage deviation of the discharge coefficient from that of test no. 4

Table 5.4 Variation of discharge coefficient with turbulence intensity i and length scale factor λ

β	test no.	Reynolds Number	i	λ	Discharge Coefficient		
					Corner tappings	Flange tappings	D & 1/2 D tappings
0.1	1	60,000	0.001	0.03	0.7196 (-0.04 %)	0.7195 (-0.04 %)	0.7194 (-0.04 %)
	2	60,000	0.003	0.333	0.7199 (0.00 %)	0.7198 (0.00 %)	0.7197 (0.00 %)
	3	60,000	0.1	1.0	0.7196 (-0.04 %)	0.7196 (-0.03 %)	0.7195 (-0.03 %)
0.3	1	60,000	0.001	0.03	0.7453 (0.03 %)	0.7452 (0.01 %)	0.7450 (0.01 %)
	2	60,000	0.003	0.333	0.7451 (0.00 %)	0.7451 (0.00 %)	0.7449 (0.00 %)
	3	60,000	0.1	1.0	0.7447 (-0.05 %)	0.7446 (-0.07 %)	0.7445 (-0.05 %)

* value in bracket is the percentage deviation of the discharge coefficient from that of test no. 2 for each β ratio

Table 5.5 Variation of discharge coefficient with turbulence intensity i and length scale factor λ

bore e is specified to be $0.021d \pm 0.003d$, where d is the diameter of the orifice. From a manufacturing point of view, the observance of the dimensional tolerances associated with the conical entrance orifice plate can be a time-consuming exercise, especially for small pipe diameters, because the tolerance is a function of orifice diameters. In fact, many of the available experimental results on conical entrance orifice plates were obtained on plates with dimensions outside the limits specified in the British Standard.

Therefore, the LRN model developed in chapter 4 is used to investigate the effects of variation in the thickness of the conical entrance J , the axial length of the parallel bore e and the conic entrance angle F on the discharge coefficient.

At each value of β , the simulation was performed with two different grid distributions (121 x 54 grids and 184 x 72 grids for $\beta = 0.1$; 139 x 48 grids and 220 x 70 grids for $\beta = 0.2$; 151 x 46 grids and 229 x 62 grids for $\beta = 0.3$). For values of J , e and F smaller than the nominal values specified in BS 1042 : Section 1.2 (i.e. $J = 0.084d$, $e = 0.021d$ and $F = 45^\circ$), the grid distributions with smaller number of grids were used. The distributions with larger number of grids were used for values of J , e and F larger than that specified. This is to ensure that the grid density in the region of interest

is sufficient for the solution to be regarded as grid-independent, as determined in chapter 4.

Since the discharge coefficients obtained by simulation may differ from the true value by several percent, it is desirable to have a reference discharge coefficient against which the effects of variation in geometry can be estimated. Thus, for a given grid distribution, the computed discharge coefficient with values of J , e and F equal to the nominal values specified in the British Standard (i.e. $J = 0.084d$, $e = 0.021d$ and $F = 45^\circ$) is used as the reference discharge coefficient. By comparing the reference discharge coefficient with that obtained for different values of J , e and F , the effects of variation in these quantities on the discharge coefficient can be estimated.

5.5.1 Effect of variation in the thickness of the conical entrance

BS 1042 : Section 1.2 specifies the thickness of the conical entrance J to be $0.084d \pm 0.003d$. The effect of variation in the thickness of the conical entrance is given in table 5.6 and also in figures 5.19(a) to 5.19(c). These results were obtained with $e = 0.021d$ and $F = 45^\circ$, the nominal values specified in the British Standard. With the value of J within the limits specified in the Standard (i.e. $J = 0.084d \pm 0.003d$), table 5.6 shows that the deviation of the discharge coefficient

β	Thickness of Conical Entrance	Percentage Deviation		
		Reynolds no. = 80	Reynolds no. = 10,000	Reynolds no. = 60,000
0.1	0.055 d	-2.51 %	-2.05 %	-2.31 %
	0.060 d	-1.95 %	-1.57 %	-1.74 %
	0.070 d	-1.00 %	-0.79 %	-0.86 %
	0.081 d	-0.20 %	-0.15 %	-0.18 %
	0.084 d	0.00 %	0.00 %	0.00 %
	0.087 d	0.18 %	0.15 %	0.15 %
	0.100 d	0.81 %	0.68 %	0.76 %
	0.110 d	1.17 %	1.00 %	1.14 %
	0.115 d	1.34 %	1.15 %	1.30 %
0.2	0.050 d	-2.93 %	-2.73 %	-2.68 %
	0.060 d	-1.85 %	-1.59 %	-1.64 %
	0.070 d	-0.96 %	-0.78 %	-0.87 %
	0.081 d	-0.18 %	-0.13 %	-0.16 %
	0.084 d	0.00 %	0.00 %	0.00 %
	0.087 d	0.17 %	0.11 %	-0.23 %
	0.100 d	0.80 %	0.46 %	0.26 %
	0.110 d	1.17 %	0.62 %	0.68 %
	0.120 d	1.49 %	0.70 %	0.88 %
	0.130 d	1.77 %	0.81 %	1.03 %
0.3	0.050 d	-2.78 %	-2.52 %	-2.51 %
	0.055 d	-2.24 %	-2.02 %	-2.00 %
	0.060 d	-1.75 %	-1.54 %	-1.56 %
	0.070 d	-0.93 %	-0.77 %	-0.82 %
	0.081 d	-0.17 %	-0.15 %	-0.20 %
	0.084 d	0.00 %	0.00 %	0.00 %
	0.087 d	0.24 %	0.19 %	0.09 %
	0.100 d	0.84 %	0.47 %	0.50 %
	0.110 d	1.22 %	0.60 %	0.71 %
	0.120 d	1.52 %	0.69 %	0.91 %

* The discharge coefficient for a thickness of 0.084d is used as the reference value for calculating the percentage deviation; d is the orifice diameter.

Table 5.6 Percentage deviation of the discharge coefficient from the reference value with changes in the thickness of the conical entrance

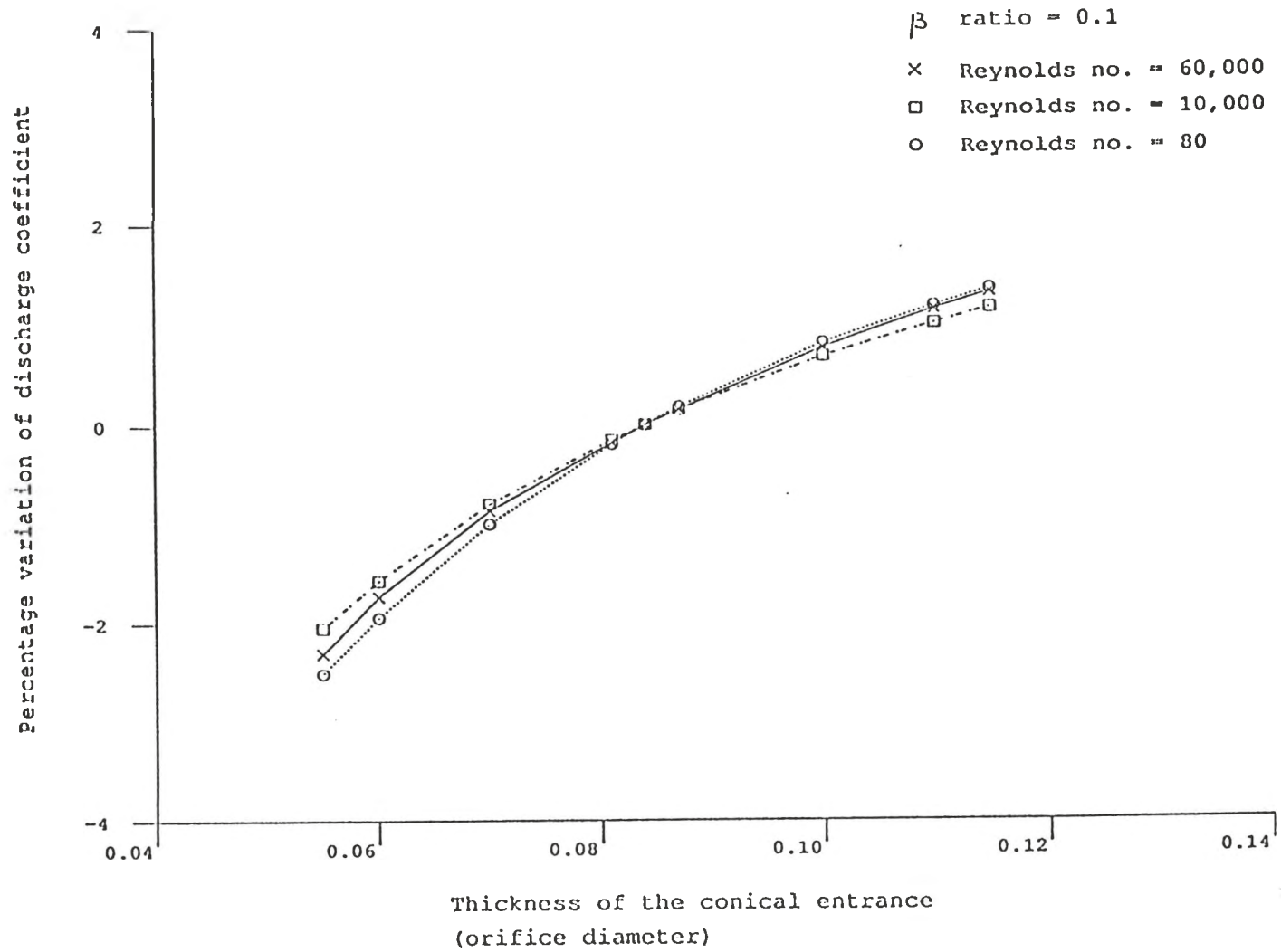


Fig. 5.19(a) Variation of the discharge coefficient with the thickness of the conical entrance

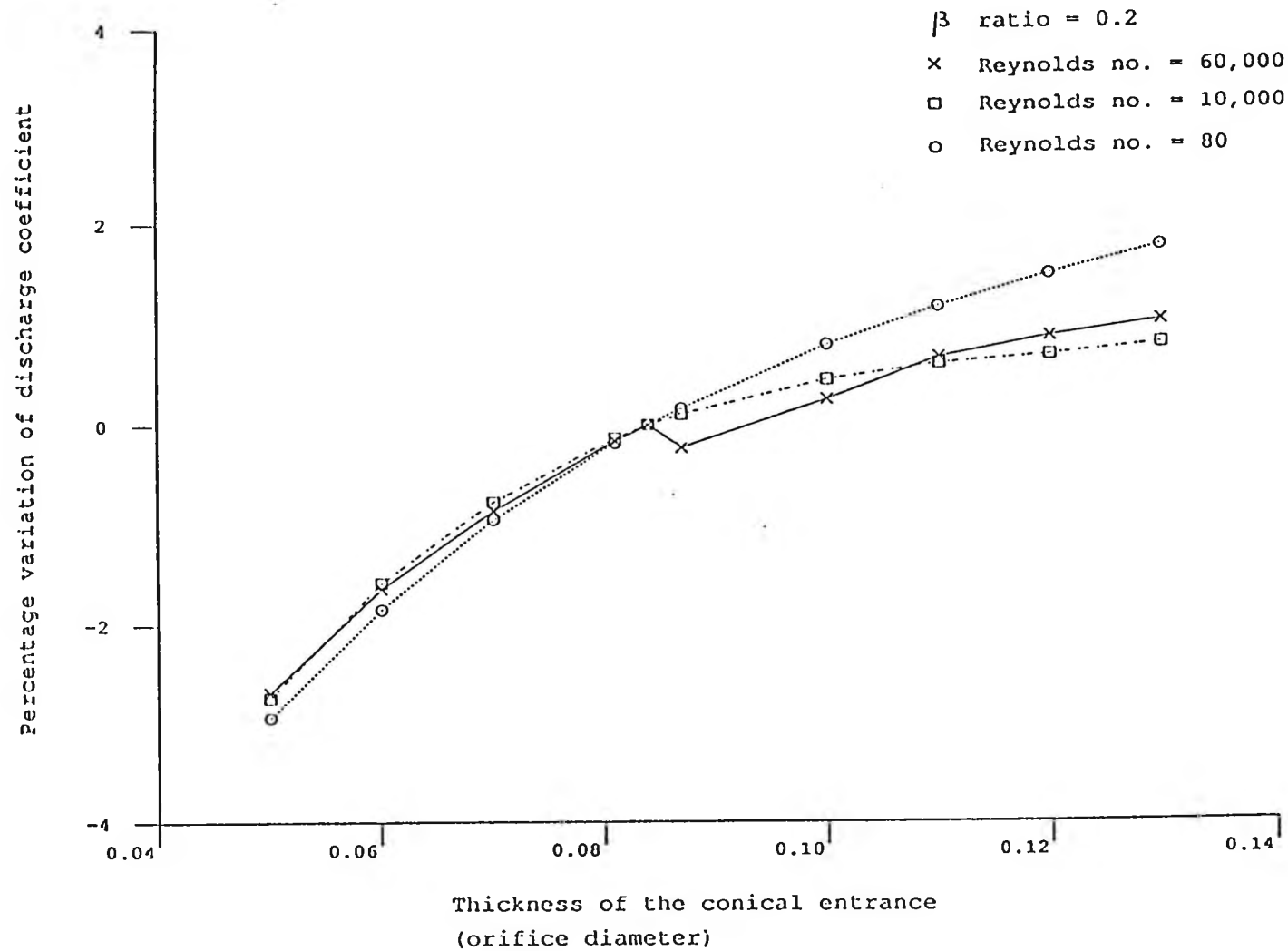


Fig. 5.19(b) Variation of the discharge coefficient with the thickness of the conical entrance

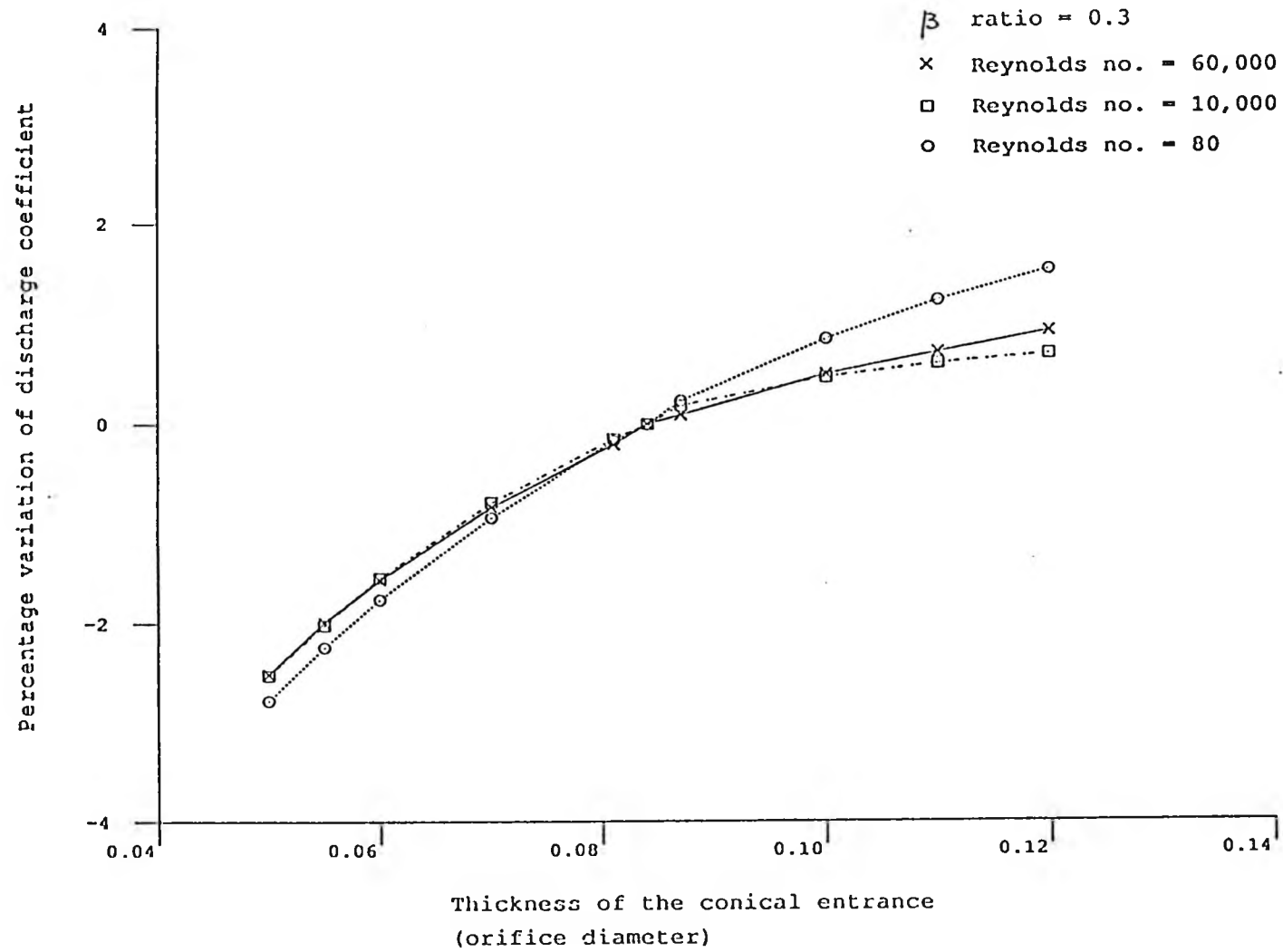


Fig. 5.19(c) Variation of the discharge coefficient with the thickness of the conical entrance

from the reference value is within $\pm 0.24 \%$ for the β ratios and Reynolds numbers investigated.

From figures 5.19(a) to 5.19(c), it can be seen that the general trend is for the deviation of the discharge coefficient from the reference value to increase as J moves away from the nominal value of 0.084d specified in the Standard and the discharge coefficient increases with the thickness of the conical entrance J for the range of J tested. Since the axial length of the parallel bore e is kept constant at $0.021d$, an increase in the value of J means an increase in the thickness of the orifice plate. Thus, the results agree with the trend observed by Kastner and McVeigh (23), who conducted tests on seven conical entrance orifice plates (with a nominal value of $\beta = 0.2$) of different thickness at Reynolds numbers below 3,000. They found that the discharge coefficient increased with increasing thickness of the plates. However, no information was provided as to whether the increase in thickness was due to an increase in J or e .

5.5.2 Effect of variation in the axial length of the parallel bore

The axial length of the parallel bore e is specified in BS 1042 : Section 1.2 to be $0.021d \pm 0.003d$. The effect of variation in the axial length of the parallel bore is given in table 5.7 and also in figures 5.20(a) to

β	Axial length of Parallel Bore	Percentage Deviation		
		Reynolds no. = 80	Reynolds no. = 10,000	Reynolds no. = 60,000
0.1	0.015 d	-0.88 %	-0.38 %	-0.22 %
	0.016 d	-0.73 %	-0.32 %	-0.18 %
	0.017 d	-0.59 %	-0.25 %	-0.13 %
	0.018 d	-0.43 %	-0.18 %	-0.10 %
	0.021 d	0.00 %	0.00 %	0.00 %
	0.024 d	0.29 %	0.80 %	0.57 %
	0.0255 d	0.43 %	1.23 %	0.90 %
	0.027 d	0.57 %	1.65 %	1.25 %
	0.028 d	0.66 %	1.90 %	1.45 %
	0.029 d	0.74 %	2.13 %	1.68 %
0.2	0.013 d	-0.90 %	-1.04 %	-0.88 %
	0.015 d	-0.67 %	-0.71 %	-0.64 %
	0.018 d	-0.32 %	-0.32 %	-0.30 %
	0.021 d	0.00 %	0.00 %	0.00 %
	0.024 d	0.21 %	0.30 %	-0.04 %
	0.027 d	0.39 %	0.56 %	0.42 %
	0.030 d	0.55 %	0.86 %	0.58 %
	0.032 d	0.65 %	1.07 %	0.72 %
0.3	0.013 d	-0.57 %	-1.22 %	-0.97 %
	0.015 d	-0.41 %	-0.87 %	-0.70 %
	0.018 d	-0.18 %	-0.41 %	-0.35 %
	0.021 d	0.00 %	0.00 %	0.00 %
	0.024 d	0.24 %	0.28 %	0.23 %
	0.027 d	0.33 %	0.51 %	0.48 %
	0.030 d	0.44 %	0.69 %	0.73 %

* The discharge coefficient for an axial length of 0.021d is used as the reference value for calculating the percentage deviation; d is the orifice diameter.

Table 5.7 Percentage deviation of the discharge coefficient from the reference value with changes in the axial length of the parallel bore

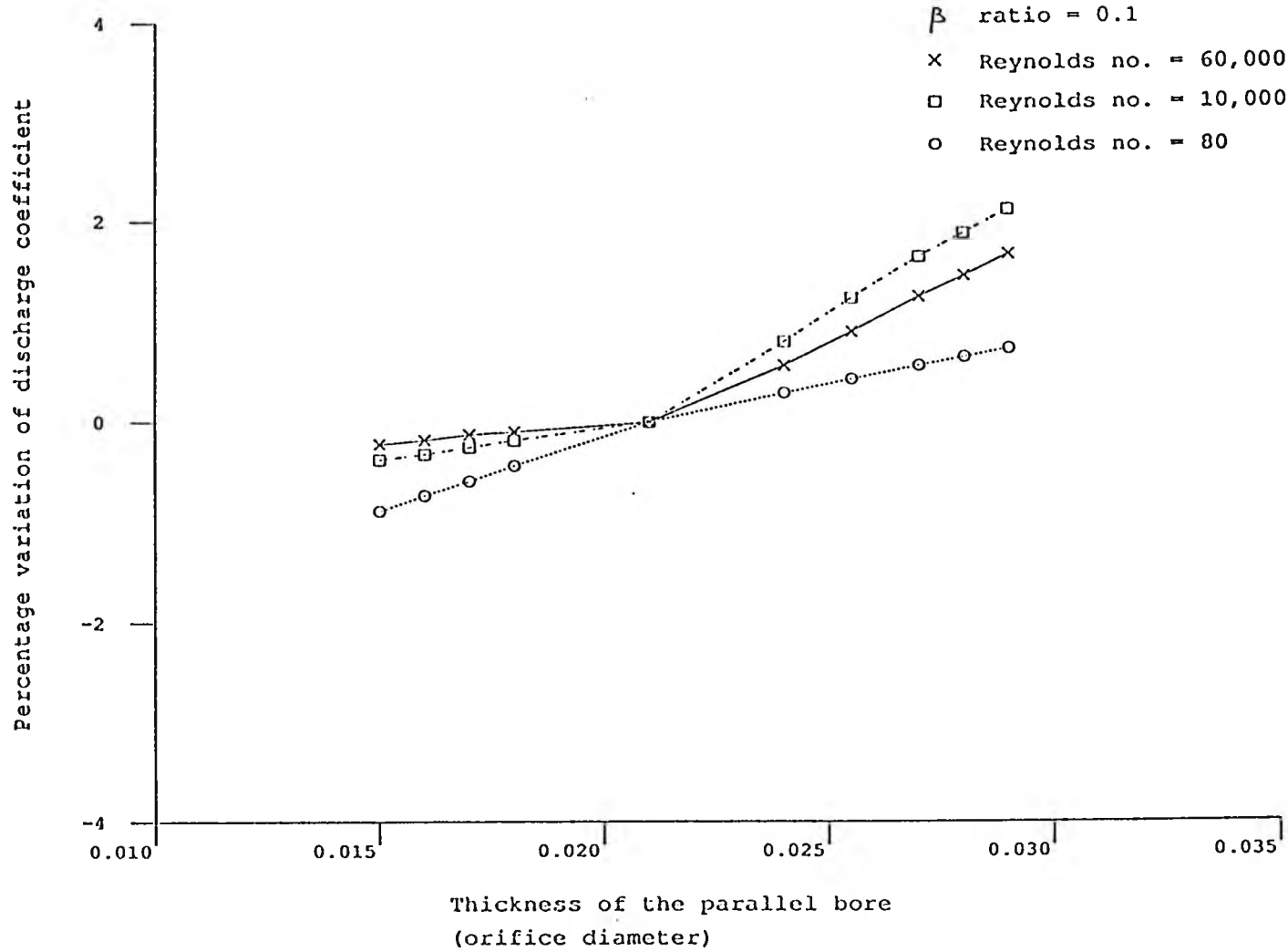


Fig. 5.20(a) Variation of the discharge coefficient with the thickness of the parallel bore

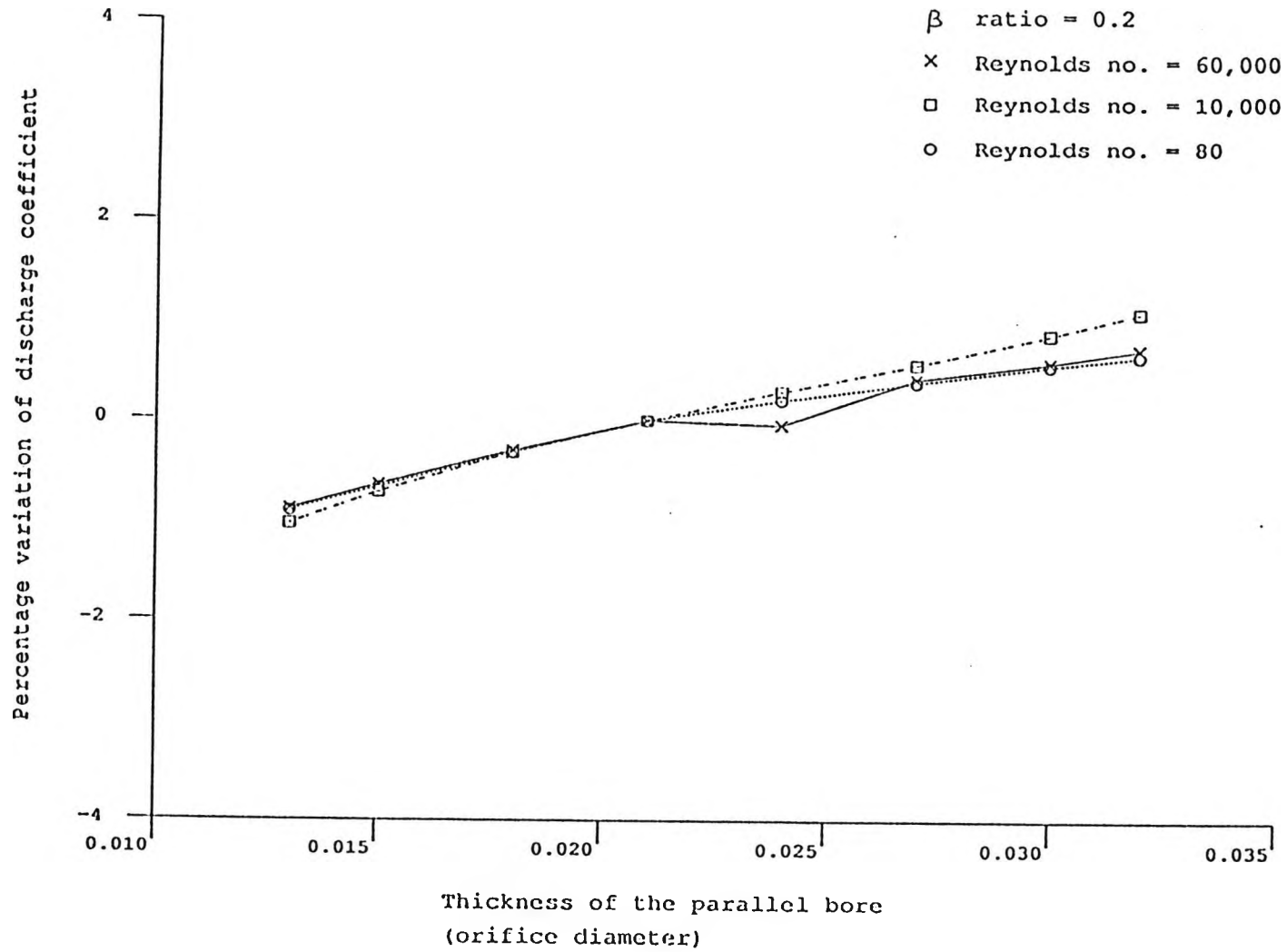


Fig. 5.20(b) Variation of the discharge coefficient with the thickness of the parallel bore

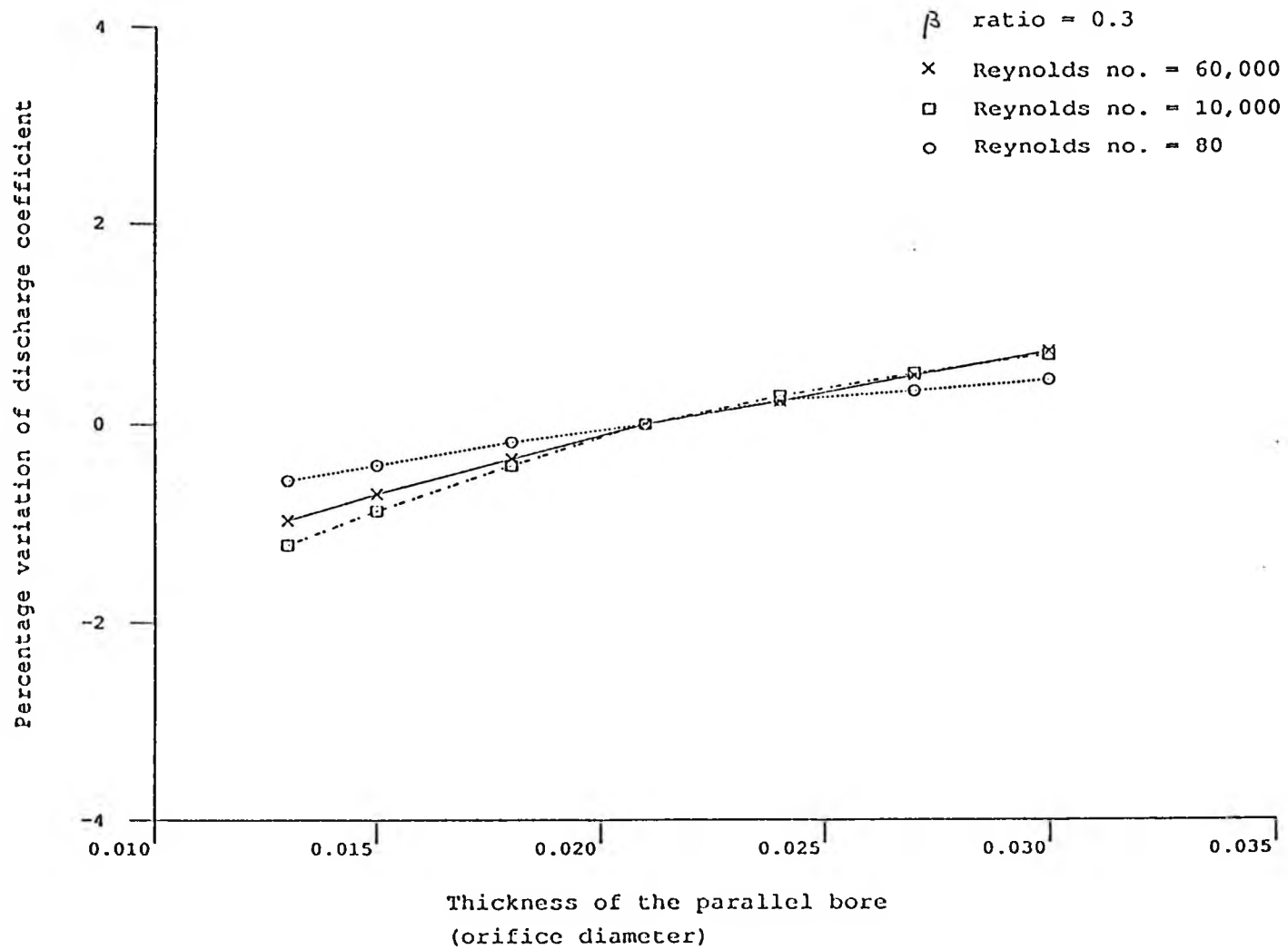


Fig. 5.20(c) Variation of the discharge coefficient with the thickness of the parallel bore

5.20(c). These results were obtained with $J = 0.084d$ and $F = 45^\circ$, the nominal values specified in the Standard. With the value of e within the limits specified in the Standard (i.e. $e = 0.021d \pm 0.003d$), table 5.7 shows that the variation of the discharge coefficient from the reference value is within $\pm 0.80\%$ for the β ratios and Reynolds numbers investigated.

From figures 5.20(a) to 5.20(c), it can be seen that the general trend is for the deviation of the discharge coefficient from the reference value to increase as e moves away from the nominal value of $0.021d$ given in the Standard and the discharge coefficient increases with the axial length of the parallel bore e for the range of e investigated. An increase in the value of e implies a thicker plate as the thickness of the conical entrance J is kept fixed at $0.084d$. Thus, the results again agree with the trend observed by Kastner and McVeigh (23) as mentioned in section 5.5.1.

5.5.3 Effect of variation in the angle of the conical entrance

BS 1042 : Section 1.2 specifies the angle of the conical entrance F to be $45^\circ \pm 1^\circ$. The effect of variation in the angle of the conical entrance is given in table 5.8 and also in figures 5.21(a) to 5.21(c). These results were obtained with $J = 0.084d$ and $e = 0.021d$, the nominal values specified in the Standard. With the value

β	Angle of Conical Entrance	Percentage Deviation		
		Reynolds no. = 80	Reynolds no. = 10,000	Reynolds no. = 60,000
0.1	35	0.77 %	2.00 %	1.67 %
	40	0.56 %	1.25 %	1.20 %
	43	0.25 %	0.54 %	0.54 %
	44	0.13 %	0.28 %	0.28 %
	45	0.00 %	0.00 %	0.00 %
	46	-0.15 %	-0.26 %	-0.28 %
	47	-0.31 %	-0.50 %	-0.53 %
	50	-0.85 %	-1.15 %	-1.18 %
	55	-1.91 %	-2.31 %	-2.23 %
0.2	35	0.47 %	1.75 %	1.26 %
	40	0.36 %	1.30 %	0.86 %
	43	0.18 %	0.59 %	0.38 %
	44	0.10 %	0.31 %	0.20 %
	45	0.00 %	0.00 %	0.00 %
	46	-0.11 %	-0.35 %	-0.64 %
	47	-0.22 %	-0.74 %	-1.13 %
	50	-0.62 %	-1.83 %	-1.73 %
	55	-1.41 %	-3.54 %	-3.46 %
0.3	35	0.17 %	1.78 %	1.33 %
	40	0.21 %	1.11 %	0.87 %
	43	0.11 %	0.51 %	0.39 %
	44	0.07 %	0.27 %	0.17 %
	45	0.00 %	0.00 %	0.00 %
	46	-0.10 %	-0.41 %	-0.34 %
	47	-0.17 %	-0.81 %	-0.66 %
	50	-0.37 %	-1.96 %	-1.67 %
	55	-1.01 %	-3.98 %	-3.40 %

* The discharge coefficient for an angle of 45 degree is used as the reference value for calculating the percentage deviation.

Table 5.8 Percentage deviation of the discharge coefficient from the reference value with changes in the angle of the conical entrance

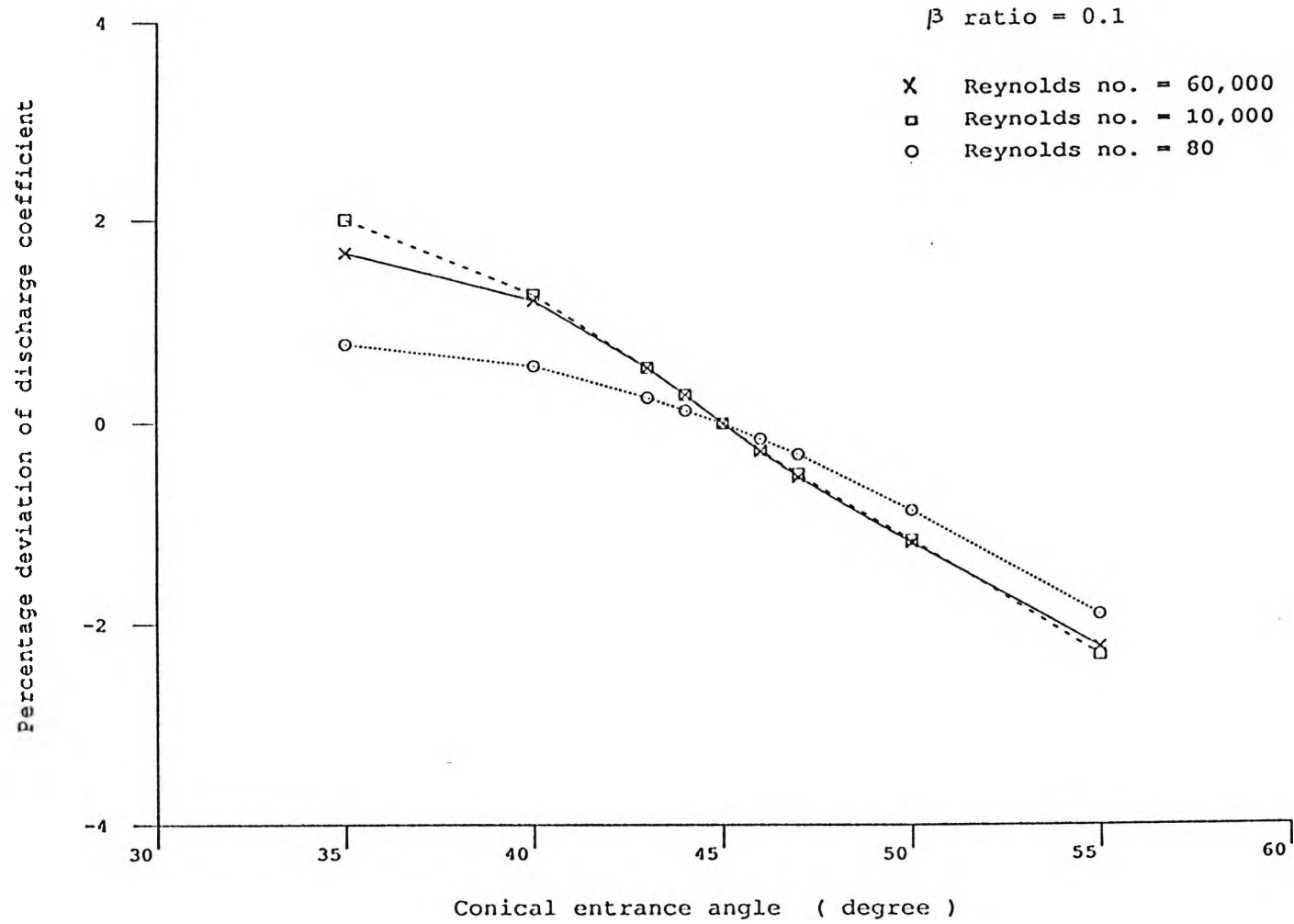


Fig. 5.21(a) Variation of the discharge coefficient with the conical entrance angle

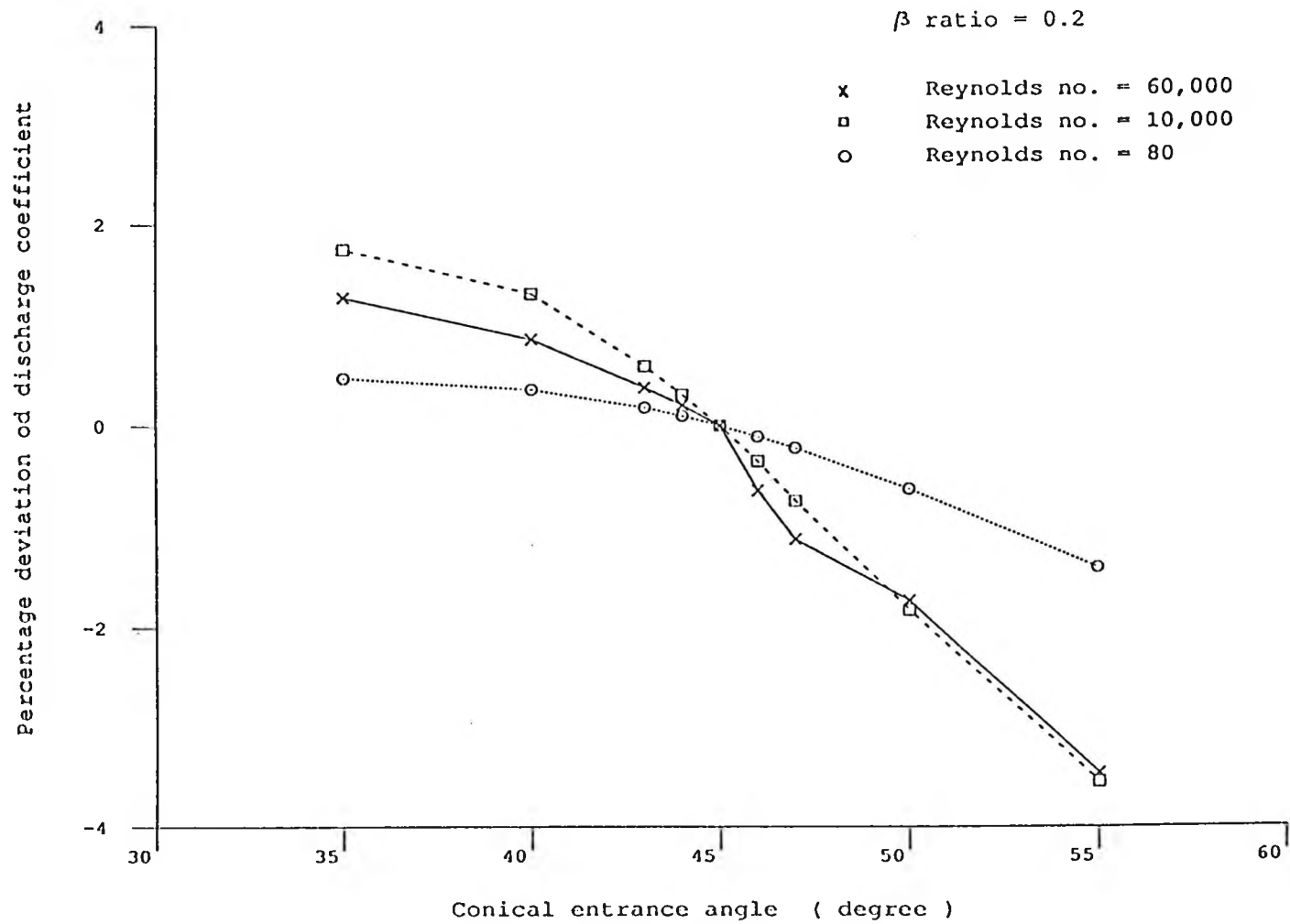


Fig. 5.21(b) Variation of the discharge coefficient with the conical entrance angle

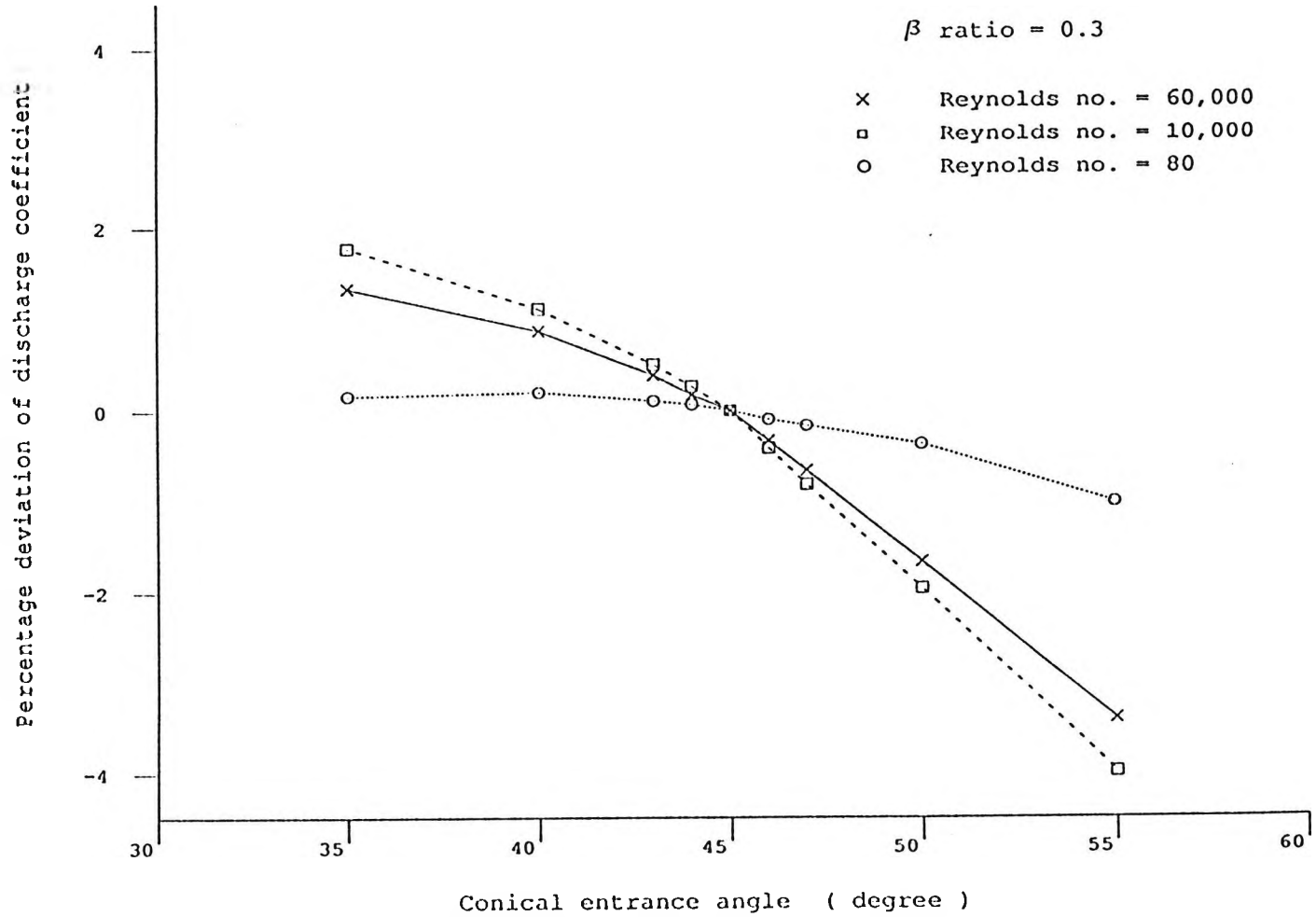


Fig. 5.21(c) Variation of the discharge coefficient with the conical entrance angle

of F within the limits specified in the British Standard (i.e. $F = 45^\circ \pm 1^\circ$), table 5.8 shows that the deviation of the discharge coefficient from the reference value is within $\pm 0.64 \%$ for the β ratios and Reynolds numbers investigated.

From figures 5.21(a) to 5.21(c), it can be seen that the general trend is for the deviation of the discharge coefficient from the reference value to increase as F moves away from the nominal value of 45° specified in the Standard, and the discharge coefficient decreases with an increase in the conic entrance angle for the range of F studied. This again agrees with the observation of Kastner and McVeigh (23) who noted an increase in the discharge coefficient for test plates with a smaller bevel angle in their experiments.

5.5.4 Concluding remarks

The effect of geometric tolerances on the discharge coefficient of the conical entrance orifice plate was simulated using the LRN model. With all other parameters kept fixed, the thickness of the conical entrance J , the axial length of the parallel bore e and the conic entrance angle F were varied from the nominal value as specified in BS 1042 : Section 1.2, one at a time, in order to estimate the effect of these variations on the discharge coefficient. For the range of β ratios and Reynolds numbers investigated, the variation of the

discharge coefficient is within $\pm 0.24\%$ of the reference value when J is allowed to vary within the limits specified in the Standard (e and F are kept constant at their nominal values). The corresponding value for e and F is $\pm 0.8\%$ and $\pm 0.64\%$ respectively when they are varied within the specified limits.

BS 1042 : Section 1.2 stated that the uncertainty on the value of the discharge coefficient is $\pm 2\%$ of 0.734 and the purpose of specifying the geometric tolerances for the orifice is to ensure that the discharge coefficient can be reproduced within the uncertainty stated in the Standard. The discharge coefficient, as computed by the LRN model, was shown to be a function of the β ratio (section 5.2.1). Thus, if the discharge coefficient of the conical entrance orifice plate is taken as a function of β , and with the same tolerance of $\pm 2\%$ on its value, then the specifications on the geometric tolerances can be more restrictive than are probably necessary.

Also, figures 5.19 and 5.20 show that the discharge coefficient increases with both J and e . For a given thickness ($e + J$) of the orifice plate, an increase in J must be accompanied by a decrease in e and vice versa. Thus, a positive deviation of the discharge coefficient caused by an increase in J or e will be partly offset by a negative deviation due to the accompanying decrease in

the other parameter. Therefore, for a given orifice plate thickness, the variation of the discharge coefficient will be smaller than that shown in figures 5.19 and 5.20 as J and e deviate from their nominal values. Hence, some latitude on the geometric tolerances as specified in the Standard may be allowed. This will facilitate the manufacture of the conical entrance orifice plates, as observance of the dimensional tolerances specified in the Standard can be a time-consuming exercise, especially for small pipe diameters, because the tolerance is a function of orifice diameter which depends on the pipe diameter for a given β .

CHAPTER 6

CONCLUSIONS

6.1 Introductory remarks

The flow through the conical entrance orifice plates depends on a number of parameters. The influence of these parameters on the performance of the orifice can be studied experimentally. But it will be very costly and time-consuming, if not impossible, to cover all possible combinations of these parameters in experiments. Alternatively, computer modelling can be used to study the performance of the conical entrance orifice plates. Widely ranging parameters can be introduced and evaluated, and, for selected cases, experiments can be carried out to validate the results obtained by simulation. The parameters can be varied one at a time, or in combinations with each other, so that their influence on the performance of the conical entrance orifice plate can be better understood.

The work presented in this thesis shows the applicability of a low Reynolds number $k-\epsilon$ model of turbulence in the simulation of flow through the conical entrance orifice plate.

6.2 Achievements of the present study

The achievements of the work presented in this thesis can be summarised as follows:

- 1) A model for conical entrance orifice plate flow sensor was developed making use of the Lam and Bremhorst $k-\epsilon$ model of turbulence and the 'PHOENICS' computer code. There is reasonable agreement between the discharge coefficient computed by the model and the published value (within $\pm 3\%$ of the value stated in BS 1042 : Section 1.2) for the β ratios and Reynolds numbers investigated.

- 2) The use of pressure tapplings other than corner tapplings was studied. BS 1042 : Section 1.2 stated that corner tapplings shall be used with conical entrance orifice plates. The present investigation indicated that flange tapplings and D & $\frac{1}{2}D$ tapplings can also be used, and that there is no significant difference between the discharge coefficients for the three types of pressure tapplings.

- 3) The effect of Reynolds number on the discharge coefficient was investigated. The present study indicated that, for the β ratios used in the study, the conical entrance orifice plates can be used for Reynolds numbers up to at least 60,000, the maximum Reynolds number tested in this investigation, which is beyond the limits specified in BS 1042 : Section 1.2 : 1989 for the smaller β ratios.

- 4) The discharge coefficient was computed with different values of β . The results indicated that the discharge coefficient is a function of β . If, instead of a constant value of 0.734 as is stated in the Standard, the discharge coefficient is given as a function of β , the uncertainty associated with the discharge coefficient can be reduced.

- 5) The effect of geometric tolerances on the discharge coefficient was explored. The results indicated that the dimensional tolerances specified in the British Standard for conical entrance orifice plate can be more restrictive than are probably necessary. Some latitude on the tolerances may be allowed, and this will make the manufacture of the conical entrance orifice plates an easier task.

6.3 Suggestions for future work

In the present study, the performance of conical entrance orifice plate flow sensor was simulated, and there are areas where the simulated results are at variance with that given in the British Standard.

As there are only limited experimental results available on the performance characteristics of conical entrance orifice plate, further experimental efforts would be required to better understand its performance characteristics and to verify the validity of the

simulated results. This should lead to a better utilization of conical entrance orifice plate as a low Reynolds number flow measuring device.

Although the model was developed for conical entrance orifice plate flow sensors, it can readily be modified to suit other types of orifice plates. Thus, the model can be used to investigate the behaviour of various orifice profiles and their potential as a low Reynolds number metering device explored.

REFERENCES

1. REEVE, A.
"What's New in the Flowmeter Line"
C & I, February 1990, pp. 45-49.
2. FOX, R. W. and McDONALD, A. T.
"Introduction to Fluid Mechanics" - 2nd Edition
John Wiley & Sons, 1978.
3. ASME JOINT COMMITTEE ON ORIFICE COEFFICIENTS OF
THE AMERICAN GAS ASSOCIATION
"History of Orifice Meters and the Calibration,
Construction and Operation for Metering"
ASME, New York, 1935.
4. WEYMOUTH, T. R.
"Measurement of Natural Gas"
Trans. ASME, 1912, 34, 1091-1110.
5. HICKSTEIN, E.O.
"The Flow of Air Through Thin-Plate Orifices"
Trans. ASME, 1915, 37, 765.
6. JUDDS, H.
"Experiments on Water Flow Through Pipe Orifices"
Trans. ASME, 1916, 38, 331-366.

7. HODGSON, J. L.
"The Commercial Metering of Air, Gas, and Steam"
Proc. Instn Civil Engineers, 1917, 204, 108-193.

8. HODGSON, J. L.
"The Laws of Similarity of Orifice and Nozzle
Flows"
Trans. ASME, 1929, 51, 303.

9. MILLS, R. D.
"Numerical Solutions of Viscous Flow Through a
Pipe Orifice at Low Reynolds Numbers"
J. Mech. Engrg. Sci., Vol. 10, No. 2, 1968,
pp. 133-140.

10. JOHANSEN, F. C.
"Flow Through Pipe Orifices at Low Reynolds
Numbers"
Proc. Royal Society, Vol. 126(A), 1930,
pp. 231-245.

11. KEITH, T. G.
"Finite Difference Solutions of Steady Laminar Flow
Through a Pipe Orifice"
Ph.D. Thesis, University of Maryland, 1971

12. KEITH, T. G. and JOHN, J. E. A.
"Calculated Orifice Plate Discharge Coefficients
at Low Reynolds Numbers"
Trans. ASME, J. of Fluids Engineering, June 1977,
pp. 424-425.
13. MATTINGLY, G. E. and DAVIS, R. W.
"Numerical Solutions for Laminar Orifice Flow"
Proc. ASME Winter Annual Meeting,
Paper No. 77-WA/FE-13, Georgia, 1977.
14. TUVE, G. L. and SPRENKLE, R. E.
"Orifice Discharge Coefficients for Viscous
Liquids"
Instruments, Vol. 6, 1933, pp. 201-206.
15. NIGRO, F. E. B., STRONG, A. B. and ALPAY, S. A.
"A Numerical Study of the Laminar Viscous In-
compressible Flow Through a Pipe Orifice"
Trans. ASME, J. of Fluids Engineering, Vol. 100,
Dec. 1978, pp. 467-472.
16. DAVIS, R. W. and MATTINGLY, G. E.
"Numerical Modelling of Turbulent Flow Through Thin
Orifice Plates"
Proc. of the Symposium on Flow in Open channels and
Closed Conduits held at NBS, Gaithersburg, MD,
February 1977, pp. 491-522.

17. HAFIZ, M.
"Computer Aided Mathematical Modelling of Turbulent Flow for Orifice Metering"
Ph.D. Thesis, City University, London, 1981.
18. PATEL, B. R. and SHEIKHOLESAMI, Z.
"Numerical Modelling of Turbulent Flow through Orifice Meters"
Int. Symposium on Fluid Flow Measurement,
Washington DC, Nov. 1986.
19. LANGSHOLT, M. and THOMASSEN, D.
"Computer Modelling of Fluid Flow Through Orifices"
Int. Conference on Flow Measurement in the mid 80's, Glasgow, June 1986, Paper 7.2.
20. READER-HARRIS, M. J.
"Computation of Flow Through Orifice Plates Downstream of Rough Pipework"
Int. Conference on Flow Measurement in the mid 80's, Glasgow, June 1986, Paper 7.3.
21. U.S. PATENT NO. 2,127,501, 23rd AUGUST 1938.
22. LINFORD, A.
"Flow Measurement and Meters" - 2nd Edition
C.E. and F.N. Spon Ltd., London, 1961, p.118

23. KASTNER, L. J. and McVEIGH, J. C.
"A Reassessment of Metering Orifices for Low Reynolds Numbers"
Proc. Instn. Mech. Engr., Vol. 180, Part 1,
No. 13, 1965-66, pp. 331-345
24. STOLL, H. W. and ZIENTARA, D.
"The Conic Entrance Orifice Plate, an Investigation of Its Performance Characteristics"
Flow, its Measurement and Control in Science and Industry, Instrument Society of America, Vol. 1, Part 2, pp. 517-522.
25. McVEIGH, J. C.
"The Effect of Installation Conditions on the Discharge Coefficient of the Conical Entrance Orifice Plate at Low Reynolds Numbers"
Flow, its Measurement and Control in Science and Industry, Instrument Society of America, Vol. 1, Part 2, 1974, pp. 533-537.
26. TURTON, R. K.
"A Note on Flow Through Conical Entrance Orifice Plates"
Conference on Fluid Flow Measurement in the mid 1970s, Glasgow, 1975, Paper A-3.

27. HO, Y. S. and LEUNG, T. P.
"Performance of Conical Entrance Orifice Plates
at Low Reynolds Numbers"
Int. J. Heat & Fluid Flow, Vol. 6, No. 2,
June 1985, pp. 122-125.
28. BS 1042; SECTION 1.2 : 1989.
29. BATCHELOR, G. K.
"An Introduction to Fluid Dynamics"
Cambridge University Press, 1967.
30. WELTY, J. R., WICKS, C. E. and WILSON, R. E.
"Fundamentals of Momentum, Heat, and Mass Transfer"
John Wiley & Sons, 1984.
31. HINZE, J. O.
"Turbulence" - 2nd Edition
McGraw-Hill, 1975
32. HARLOW, F. H. and NAKAYAMA, P. I.
"Transport of Turbulence Energy Decay Rate"
Los Alamos Science Lab., University of California,
Report LA-3854, 1968.

33. JONES, W. P. and LAUNDER, B. E.
"The Prediction of Laminarization with a 2-Equation Model of Turbulence"
Int. J. Heat & Mass Transfer, 15, 1972, p. 301.
34. JONES, W. P. and LAUNDER, B. E.
"The Calculation of Low-Reynolds-Number Phenomena with a 2-Equation Model of Turbulence"
Int. J. Heat & Mass Transfer, 16, 1973, p. 1119.
35. LAUNDER, B. E., MORSE, A. P., RODI, W. and SPALDING, D. B.
"The Prediction of Free-Shear Flows - a Comparison of the Performance of Six Turbulence Models"
Proc. NASA Langley Free Turbulent Shear Flow Conf., Vol. 1, NASA SP320, 1973.
36. LAUNDER, B. E. and SPALDING, D.B.
"The Numerical Computation of Turbulent Flows"
Computer Methods in Applied Mechanics and Engineering, Vol. 3, 1974, pp. 269-289.
37. TAYLOR, C., THOMAS, C. E. and MORGAN, K.
"Modelling Flow Over a Backward-Facing Step Using the F.E.M. and the Two-Equation Model of Turbulence"
Int. Journal for Numerical Methods in Fluids, Vol. 1, 1981, pp. 295-304.

38. MOON, L. F. and RUDINGER, G.
"Velocity Distribution in an Abruptly Expanding
Circular Duct"
J. of Fluids Engineering, Vol. 99, 1977,
pp. 226-230.
39. HABIB, M. A. and WHITELAW, J. H.
"The Calculation of Turbulent Flow in Wide-Angle
Diffusers"
Numerical Heat Transfer, Vol. 5, 1982, pp. 145-164.
40. DURST, F. and RASTOGI, A. K.
"Theoretical and Experimental Investigations of
Turbulent Flows with Separation"
Turbulent Shear Flow 2, 1980, pp. 208-219.
41. HANJALIC, K. and LAUNDER, B. E.
"A Reynolds Stress Model of Turbulence and its
Application to Thin Shear Flows"
J. of Fluid Mechanics, Vol. 52, Part 4, 1972,
pp. 609-638.
42. PATEL, V. C., RODI, W. and SCHEUERER, G.
"Turbulence Models for Near-Wall and Low Reynolds
Number Flows: A Review"
AIAA Journal, Vol. 23, Sept. 1985, pp. 1308-1319

43. CHIEN, K. Y.
"Predictions of Channel and Boundary-Layer Flows
with a Low-Reynolds-Number Turbulence Model"
AIAA Journal, Vol. 20, Jan. 1982, pp. 33-38.
44. DUTOYA, D. and MICHARD, P.
"A Program for Calculating Boundary Layers along
Compressor and Turbine Blades"
Numerical Methods in Heat Transfer, edited by
R. W. Lewis, K. Morgan and O. C. Zienkiewicz,
John Wiley and Sons, 1981, pp. 403-429.
45. HASSID, S. and POREH, M.
"A Turbulent Energy Dissipation Model for Flows
with Drag Reduction"
J. of Fluids Engineering, Vol. 100, 1978,
pp. 107-112.
46. HOFFMANN, G. H.
"Improved Form of the Low-Reynolds Number $k-\epsilon$
Turbulence Model"
Physics of Fluids, Vol. 18, 1975, pp. 309-312.
47. LAM, C. K. G. and BREMHORST, K.
"A Modified Form of the $k-\epsilon$ Model for Predicting
Wall Turbulence"
J. of Fluids Engineering, Vol. 103, 1981,
pp. 456-460.

48. LAUNDER, B. E. and SHARMA, B. I.
"Application of the Energy - Dissipation Model of
Turbulence to the Calculation of Flow Near a Spin-
ning Disc"
Letters in Heat and Mass Transfer, Vol. 1, 1974,
pp. 131-138.
49. REYNOLDS, W. C.
"Computation of Turbulent Flows"
Annual Review of Fluid Mechanics, Vol. 8,
1976, pp. 183-208.
50. WILCOX, D. C. and RUBESIN, W. M.
"Progress in Turbulence Modelling for Complex Flow
Fields Including Effects of Compressibility"
NASA Tech. Paper 1517, 1980.
51. PATANKAR, S. V. and SPALDING, D. B.
"A Calculation Procedure for Heat, Mass and Momen-
tum Transfer in Three-Dimensional Parabolic Flows"
Int. J. Heat Mass Transfer, Vol. 15, 1972,
pp. 1787-1806.

52. CARETTO, L. S., GOSMAN, A. D., PATANKAR, S. V. and SPALDING, D. B.
"Two Calculation Procedures for Steady, Three-Dimensional Flows with Recirculation"
Proc. 3rd Int. Conf. Numerical Methods in Fluid Mechanics, Paris, Vol. 2, 1972, pp. 60-68.
53. PATANKAR S. V.
"Numerical Prediction of Three-Dimensional Flows"
Studies in Convection: Theory, Measurement and Applications, Vol. 1, edited by B. E. Launder, Academic Press, London, 1975, pp. 1-78.
54. PATANKAR, S. V.
"A Calculation Procedure for Two-Dimensional Elliptic Situations"
Numerical Heat Transfer, Vol. 4, 1981, pp. 409-425.
55. PATANKAR, S. V.
"Numerical Heat Transfer and Fluid Flow"
McGraw-Hill, 1980.
56. SPALDING, D. B.
"Four Lectures on the PHOENICS Computer Code"
CFDU, Imperial College, London, Report CFD/82/5, 1982.

57. CHAM LIMITED
"Lecture Panels for PHOENICS Instruction Courses"
CHAM Limited, London, Technical Report TR/121,
September 1986.
58. ROSTEN, H. I. and SPALDING, D. B.
"PHOENICS - Beginner's Guide and User Manual"
CHAM Limited, London, Technical Report TR/100,
October 1986.
59. SPALDING, D. B.
"Mathematical Modelling of Fluid-Mechanics, Heat-
Transfer and Chemical-Reaction Processes"
CFDU, Imperial College, London, Report HTS/80/1,
1980.
60. PARRY, J. D.
Private Communication, CHAM Ltd., London, 1989.
61. WOLFGANG, RODI.
"Turbulence Models and Their Application in Hydraulics - a State of the Art Review" - 2nd Edition
International Association For Hydraulic Research,
1984.

62. KHALIL, E. E., SPALDING, D. B. and WHITELOW, J. H.
"The Calculation of Local Flow Properties in Two-Dimensional Furnaces"
Int. J. Heat Mass Transfer, Vol. 18, 1975,
pp. 775-791.
63. CHEN, Q.
"Construction of a Low Reynolds Number $k-\epsilon$ Model"
The PHOENICS Journal of Computational Fluids
Dynamics, Vol. 3, No. 3, 1990, pp. 228-326.
64. GHONIEM, A. F.
"Effect of Reynolds Number on the Structure of Recirculating Flow"
AIAA Journal, Vol. 25, No. 1, 1987, pp. 168-171.
65. NALLASAMY, M.
"Turbulence Models and Their Applications to the Prediction of Internal Flows : A Review"
Computers and Fluids, Vol. 15, No. 2, 1987,
pp. 151-194.

APPENDIX A

MODIFICATION TO SUBROUTINE 'GROUND'

```

C*****
C$DIR**GROUND
C$DIR**GROUND
      SUBROUTINE GROUND
C-----
C
C          *****
C          MATERIAL OMITTED
C          *****
C-----
CXXXXXXXXXXXXXXXXXXXXXXXXXXXXXXXXXXXXXXXXX USER SECTION STARTS:
C
CYSYSYSYSYSYSYSYSYSYS
      COMMON/TURB/CMU,CD,CMUCD,C1E,C2E,AK,EWAL
      REAL GINZ,LU1,LU2,DIAM,DCEZ,DZCE,DORT,DORR,DCEY,GY2
      INTEGER ZBO,YBC,YAC,ZCE,ZOT,ZAO
CYSYSYSYSYSYSYSYSYSYS
C-----
C
C          *****
C          MATERIAL OMITTED
C          *****
C-----
C 2   User dimensions own arrays here, for example:
C     DIMENSION UUH(10,10),UUC(10,10),UUX(10,10),UUZ(10)
C
CYSYSYSYSYSYSYSYSYSYS
      DIMENSION GVMZ(300,1),GYG(300,1),GHWY(300,1),GWDIST(300,1)
CYSYSYSYSYSYSYSYSYSYS
C-----
C
C          *****
C          MATERIAL OMITTED
C          *****
C-----
C*****
C
C--- GROUP 1. Run title and other preliminaries
C
      1 GO TO (1001,1002),ISC
      1001 CONTINUE
CYSYSYSYSYSYSYSYSYSYS
      CALL MAKE(EASP2)
      CALL MAKE(EASP3)
      CALL MAKE(EASP4)
      CALL MAKE(EASP5)
      CALL MAKE(EASP6)
      CALL MAKE(YG2D)
C-----COMMUNICATION WITH Q1
      CALL SUB4R(DCEY, RG(1),GY2, RG(2),LU1, RG(3),LU2, RG(4))
      CALL SUB4R(DIAM, RG(5),DCEZ, RG(6),GZCE, RG(7),DORT, RG(8))
      DORR=RG(9)
      ENUL=RG(10)
      CALL SUB3(ZBO,IG(1),YBC,IG(2),YAC,IG(3))
      CALL SUB3(ZCE,IG(4),ZOT,IG(6),ZAO,IG(7))
CYSYSYSYSYSYSYSYSYSYS
      RETURN
      1002 CONTINUE
      RETURN
C*****
C-----

```

```

C
C
C          *****
C          MATERIAL OMITTED
C          *****
C-----
C--- Group 9. Properties of the medium (or media)
C The sections in this group are arranged sequentially in their
C order of calling from EARTH. Thus, as can be seen from below,
C the temperature sections (10 and 11) precede the density
C sections (1 and 3); so, density formulae can refer to
C temperature stores already set.
C 9 GO TO (91,92,93,94,95,96,97,98,99,900,901,902,903),ISC
C*****
C-----
C
C          *****
C          MATERIAL OMITTED
C          *****
C-----
C 902 CONTINUE
C * ----- SECTION 12 -----
C For EL1.LE.GRND----- phase-1 length scale Index AUX(LEN1)
CYSYSYSYSYSYSYSYSYSYS
C-----THIS IS TO CALCULATE THE LENGTH SCALE OF TURBULENCE
C      CALL FN22(KE,1.E-10)
C      CALL FN22(EP,1.E-10)
C      CALL FN31(AUX(LEN1),KE,EP,CD,1.5,-1.0)
C      CALL FN22(AUX(LEN1),1.E-10)
C      CALL FN23(AUX(LEN1),1.E10)
CYSYSYSYSYSYSYSYSYSYS
C      RETURN
C-----
C
C          *****
C          MATERIAL OMITTED
C          *****
C-----
C 95 CONTINUE
C * ----- SECTION 5 -----
C For ENUT.LE.GRND--- reference turbulent kinematic viscosity.
CYSYSYSYSYSYSYSYSYSYS
C-----THIS IS TO CALCULATE THE DISTANCE FROM THE NEAREST WALL
C      GINZ=ZW-DZ/2.0
C      IF (IZ .LE. ZBO) THEN
C          DO 9510 IY=1,NY
C              IF (IY .LE. YBC) THEN
C                  GVWZ(IY,1)=ZWLAST-GINZ
C              ELSE IF (IY .GT. YBC .AND. IY .LT. YAC) THEN
C                  GVWZ(IY,1)=(LU1+LU2)*DIAM + (DCEZ*ZWLAST*(YAC-IY)/GZCE)
C                  -GINZ
C      ELSE
C          GVWZ(IY,1)=(LU1+LU2)*DIAM - GINZ
C      ENDIF
C      CONTINUE
C 9510 ELSE IF (IZ .GT. ZBO .AND. IZ .LE. (ZBO+ZCE)) THEN
C      DO 9520 IY=1,NY
C          IF (IY .LE. YBC) THEN
C              GVWZ(IY,1)=ZWLAST-GINZ
C          ELSE IF (IY .GT. YBC .AND. IY .LE. YAC-(IZ-ZBO)) THEN
C              GVWZ(IY,1)=(LU1+LU2)*DIAM + (DCEZ*ZWLAST*(YAC-IY)/GZCE)
C              -GINZ
C

```

```

        ELSE
          GVWZ(IY,1)=ZWLAST-GINZ
        ENDIF
9520    CONTINUE
        ELSE IF (IZ .GT. (ZBO+ZCE) .AND. IZ .LE. (ZBO+ZCE+ZOT)) THEN
          DO 9530 IY=1,NY
            GVWZ(IY,1)=ZWLAST-GINZ
9530    CONTINUE
        ELSE
          DO 9540 IY=1,NY
            IF (IY .LE. YBC) THEN
              GVWZ(IY,1)=ZWLAST-GINZ
            ELSE
              GVWZ(IY,1)=GINZ-(LU1+LU2)*DIAM-DCEZ*ZWLAST-
C          DORT*ZWLAST
        ENDIF
9540    CONTINUE
        ENDIF
C-----
        CALL GETYX(YG2D, GYG, 300, 1)
        IF (IZ .LE. ZBO) THEN
          DO 9550 IY=1,NY
            GHWY(IY,1)=YVLAST-GYG(IY,1)
9550    CONTINUE
        ELSE IF (IZ .GT. ZBO .AND. IZ .LE. (ZBO+ZCE)) THEN
          DO 9560 IY=1,NY
            IF (IY .LE. YAC-(IZ-ZBO)) THEN
              GHWY(IY,1)=DORR*YVLAST+DCEY*YVLAST*(ZBO+ZCE+1-IZ)/GY2
C          -GYG(IY,1)
            ELSE
              GHWY(IY,1)=YVLAST-GYG(IY,1)
            ENDIF
9560    CONTINUE
        ELSE IF (IZ .GT. (ZBO+ZCE) .AND. IZ .LT. ZAO) THEN
          DO 9570 IY=1,NY
            IF (IY .LE. YBC) THEN
              GHWY(IY,1)=DORR*YVLAST-GYG(IY,1)
            ELSE
              GHWY(IY,1)=YVLAST-GYG(IY,1)
            ENDIF
9570    CONTINUE
        ELSE
          DO 9580 IY=1,NY
            GHWY(IY,1)=YVLAST-GYG(IY,1)
9580    CONTINUE
        ENDIF
C-----
        DO 9590 IY=1,NY
          GWDIST(IY,1)=AMIN1(GVWZ(IY,1),GHWY(IY,1))
9590    CONTINUE
CYSYSYSYSYSYSYSYSYSYS
CCC
CYSYSYSYSYSYSYSYSYSYS
C-----THIS IS TO FIND THE TURBULENCE REYNOLDS NO. RK
        CALL SETYX(EASP2,GWDIST,NY,1)
        IF (IG(10) .EQ. 1) CALL FN0(C1,EASP2)
        CALL FN31(EASP3,KE,EASP2,1.0,0.5,1.0)
        CALL FN25(EASP3,1.0/ENUL)
        IF (IG(10) .EQ. 1) CALL FN0(C2,EASP3)
CYSYSYSYSYSYSYSYSYSYS
CCC
CYSYSYSYSYSYSYSYSYSYS
C-----THIS IS TO FIND THE FIRST FACTOR OF THE FUNCTION FMU
        CALL FN1(EASP4,1.0)

```

```

        CALL FN36(EASP4,EASP3,-1.0,-0.0165)
        CALL FN50(EASP4,2)
CYSYSYSYSYSYSYSYSYSYS
CCC
CYSYSYSYSYSYSYSYSYSYS
C-----THIS IS TO FIND THE TURBULENCE REYNOLDS NO. RT
        CALL FN22(EP,1.E-10)
        CALL FN56(EASP5,KE,KE,EP,1.0)
        CALL FN25(EASP5,1.0/ENUL)
        CALL FN22(EASP5,1.E-10)
        IF (IG(10) .EQ. 1) CALL FN0(C3,EASP5)
CYSYSYSYSYSYSYSYSYSYS
CCC
CYSYSYSYSYSYSYSYSYSYS
C-----THIS IS TO FIND THE SECOND FACTOR OF THE FUNCTION FMU
        CALL FN28(EASP3,EASP5,20.5)
        CALL FN33(EASP3,1.0)
CYSYSYSYSYSYSYSYSYSYS
CCC
CYSYSYSYSYSYSYSYSYSYS
C-----THIS IS TO COMBINE FIRST AND SECOND FACTORS TO FORM FMU
        CALL FN26(EASP3,EASP4)
C-----TO AVOID FMU GREATER THAN 1.0
        CALL FN23(EASP3,1.0)
        CALL FN22(EASP3,1.E-10)
        IF (IG(10) .EQ. 1) CALL FN0(C4,EASP3)
CYSYSYSYSYSYSYSYSYSYS
CCC
CYSYSYSYSYSYSYSYSYSYS
C-----THIS IS TO CALCULATE THE TURBULENT KINEMATIC VISCOSITY
        CALL FN22(KE,1.E-10)
        CALL FN31(AUX(VIST),KE,EP,CMUCD,2.0,-1.0)
        CALL FN26(AUX(VIST),EASP3)
CYSYSYSYSYSYSYSYSYSYS
CCC
CYSYSYSYSYSYSYSYSYSYS
C-----THIS IS TO CALCULATE THE FUNCTION F1 IN THE EP SOURCE TERM
C-----TO AVOID DIVISION BY ZERO
        CALL FN22(EASP3,1.E-10)
        CALL FN28(EASP4,EASP3,0.05)
        CALL FN21(EASP6,EASP4,EASP4,0.0,1.0)
        CALL FN26(EASP4,EASP6)
        CALL FN33(EASP4,1.0)
CYSYSYSYSYSYSYSYSYSYS
CCC
CYSYSYSYSYSYSYSYSYSYS
C-----COMBINE F1 WITH C1 OF THE STANDARD K-E EQUATION
        CALL FN25(EASP4,C1E)
        IF (IG(10) .EQ. 1) CALL FN0(C5,EASP4)
CYSYSYSYSYSYSYSYSYSYS
CCC
CYSYSYSYSYSYSYSYSYSYS
C-----THIS IS TO CALCULATE THE FUNCTION F2 IN THE EP SOURCE TERM
        CALL FN50(EASP5,2)
        CALL FN1(EASP6,1.0)
        CALL FN36(EASP6,EASP5,-1.0,-1.0)
CYSYSYSYSYSYSYSYSYSYS
CCC
CYSYSYSYSYSYSYSYSYSYS
C-----COMBINE F2 WITH C2 OF THE STANDARD K-E EQUATION
        CALL FN25(EASP6,C2E)
C-----TO AVOID DIVISION BY ZERO
        CALL FN22(EASP6,1.E-10)
        IF (IG(10) .EQ. 1) CALL FN0(C6,EASP6)

```

CYSYSYSYSYSYSYSYSYSYSYS
RETURN

C-----
C
C
C
C
C
C
C
C

MATERIAL OMITTED

C-----
C*****
C
C--- GROUP 13. Boundary conditions and special sources
C

13 CONTINUE
GO TO (130,131,132,133,134,135,136,137,138,139,1310,
11311,1312,1313,1314,1315,1316,1317,1318,1319,1320,1321),ISC

C-----
C
C
C
C
C
C
C

MATERIAL OMITTED

C-----
139 CONTINUE
C----- SECTION 10 ----- coefficient = GRND9
C

CYSYSYSYSYSYSYSYSYSYSYS
C-----THIS IS TO CALCULATE COEFFICIENT OF KE SOURCE IN LRN MODEL
CALL ONLYIF(KE,KE,'ALL')
CALL FN2(CO,AUX(VIST),0.0,CD/CMU)
CALL FN37(CO,AUX(LEN1),-2.0)
CALL FN27(CO,EASP3)

CYSYSYSYSYSYSYSYSYSYSYS
CCC
CYSYSYSYSYSYSYSYSYSYSYS
C-----THIS IS TO CALCULATE COEFFICIENT OF EP SOURCE IN LRN MODEL
CALL ONLYIF(EP,EP,'ALL')
CALL FN31(CO,AUX(VIST),AUX(LEN1),CD/CMU,1.0,-2.0)
CALL FN26(CO,EASP6)
CALL FN27(CO,EASP3)

CYSYSYSYSYSYSYSYSYSYSYS
RETURN

C-----
C
C
C
C
C
C
C

MATERIAL OMITTED

C-----
1320 CONTINUE
C----- SECTION 21 ----- value = GRND9
C

CYSYSYSYSYSYSYSYSYSYSYS
C-----THIS IS TO CALCULATE VALUE OF KE SOURCE IN LRN MODEL
CALL ONLYIF(KE,KE,'ALL')
CALL FN31(VAL,EASP1,AUX(LEN1),CMU/CD,1.0,2.0)
CALL FN26(VAL,EASP3)

CYSYSYSYSYSYSYSYSYSYSYS
CCC
CYSYSYSYSYSYSYSYSYSYSYS
C-----THIS IS TO CALCULATE VALUE OF EP IN LRN MODEL
CALL ONLYIF(EP,EP,'ALL')
CALL FN21(VAL,AUX(VIST),EASP1,0.0,1.0)
CALL FN26(VAL,EASP4)

```

      CALL FN27 (VAL, EASP6)
CYSYSYSYSYSYSYSYSYSYSYS
      RETURN
      1321 CONTINUE
C----- SECTION 22 ----- value = GRND10
C
CYSYSYSYSYSYSYSYSYSYSYS
C-----THIS IS THE BOUNDARY CONDITION FOR LRN MODEL FOR EP
      CALL ONLYIF (EP, EP, 'ALL')
      CALL FN1 (VAL, 2.0*ENUL)
      CALL FN26 (VAL, KE)
      CALL FN37 (VAL, EASP2, -2.0)
CYSYSYSYSYSYSYSYSYSYSYS
      RETURN
C*****
C-----
C
C          *****
C          MATERIAL OMITTED
C          *****
C-----
C*****
C
C
C--- GROUP 24. Dumps for restarts
      24 CONTINUE
      RETURN
      END

```

APPENDIX B

Q1 INPUT FILE

Q1 FILE

GROUP 1. Run title and other preliminaries

TEXT(LRN, BETA=0.2, W=600, TEST NO. 2, 139x48 GRIDS)
REAL(GRAD, DIAM, PLEN, PDFT, WIN, TKEIN, EPIN, DELCON)
REAL(DORR, DCEY, BETA, DCEZ, DORT, LU1, LU2, LU3, LD1, LD2, LD3)
REAL(A, GY1, GY2, GY3)
REAL(GZU1, GZU2, GZU3, GZD1, GZD2, GZD3)
REAL(GZCE, GZOT, GZOT1, GZOT2)
REAL(SPU1, SPU2, SUMU1, SUMU2, SUMBO, SUMAO, SUMD1, POW1, POW2, POWY)
REAL(SUMY1, SUMY2, SUMY3, ZD1F, TCE, TTH)
INTEGER(Y1, Y2, Y3)
INTEGER(YBC, YAC)
INTEGER(ZU1, ZU2, ZU3, ZD1, ZD2, ZD3)
INTEGER(ZCE, ZOT, ZAO, ZBO)
INTEGER(ZOT1, ZOT2)

DIAM=100.0;WIN=600.0
BETA=0.2; TCE=0.084; TTH=0.021

GROUP 2. Transience; time-step specification

GROUP 3. X-direction grid specification

CARTES=F

GROUP 4. Y-direction grid specification

GRAD=0.5*DIAM;YVLAST=GRAD

GY1=8.0;GY2=21.0;GY3=19.0
Y1=8;Y2=21;Y3=19
NY=Y1+Y2+Y3

DORR=BETA*DIAM/(2.0*YVLAST)
DCEY=TCE*BETA*DIAM/YVLAST

GRID DISTRIBUTION IN REGION R1

SUMY1=DORR
POWY=2.0
YFRAC(1) =SUMY1*(1.0-((GY1- 1.0)/GY1)**POWY)
YFRAC(2) =SUMY1*(1.0-((GY1- 2.0)/GY1)**POWY)
YFRAC(3) =SUMY1*(1.0-((GY1- 3.0)/GY1)**POWY)
YFRAC(4) =SUMY1*(1.0-((GY1- 4.0)/GY1)**POWY)
YFRAC(5) =SUMY1*(1.0-((GY1- 5.0)/GY1)**POWY)
YFRAC(6) =SUMY1*(1.0-((GY1- 6.0)/GY1)**POWY)
YFRAC(7) =SUMY1*(1.0-((GY1- 7.0)/GY1)**POWY)
YFRAC(8) =SUMY1

GRID DISTRIBUTION IN REGION R2

YFRAC(9) =SUMY1+1.0*DCEY/GY2
YFRAC(10) =SUMY1+2.0*DCEY/GY2
YFRAC(11) =SUMY1+3.0*DCEY/GY2
YFRAC(12) =SUMY1+4.0*DCEY/GY2
YFRAC(13) =SUMY1+5.0*DCEY/GY2
YFRAC(14) =SUMY1+6.0*DCEY/GY2
YFRAC(15) =SUMY1+7.0*DCEY/GY2
YFRAC(16) =SUMY1+8.0*DCEY/GY2
YFRAC(17) =SUMY1+9.0*DCEY/GY2
YFRAC(18) =SUMY1+10.0*DCEY/GY2
YFRAC(19) =SUMY1+11.0*DCEY/GY2
YFRAC(20) =SUMY1+12.0*DCEY/GY2
YFRAC(21) =SUMY1+13.0*DCEY/GY2
YFRAC(22) =SUMY1+14.0*DCEY/GY2

YFRAC(23)=SUMY1+15.0*DCEY/GY2
 YFRAC(24)=SUMY1+16.0*DCEY/GY2
 YFRAC(25)=SUMY1+17.0*DCEY/GY2
 YFRAC(26)=SUMY1+18.0*DCEY/GY2
 YFRAC(27)=SUMY1+19.0*DCEY/GY2
 YFRAC(28)=SUMY1+20.0*DCEY/GY2
 YFRAC(29)=SUMY1+DCEY
 SUMY2=SUMY1+DCEY

 GRID DISTRIBUTION IN REGION R3

SUMY3=1.0-DORR-DCEY-0.03
 YFRAC(30) =SUMY2+SUMY3*(1.0-(((GY3-1.0)- 1.0)/(GY3-1.0))**POWY)
 YFRAC(31) =SUMY2+SUMY3*(1.0-(((GY3-1.0)- 2.0)/(GY3-1.0))**POWY)
 YFRAC(32) =SUMY2+SUMY3*(1.0-(((GY3-1.0)- 3.0)/(GY3-1.0))**POWY)
 YFRAC(33) =SUMY2+SUMY3*(1.0-(((GY3-1.0)- 4.0)/(GY3-1.0))**POWY)
 YFRAC(34) =SUMY2+SUMY3*(1.0-(((GY3-1.0)- 5.0)/(GY3-1.0))**POWY)
 YFRAC(35) =SUMY2+SUMY3*(1.0-(((GY3-1.0)- 6.0)/(GY3-1.0))**POWY)
 YFRAC(36) =SUMY2+SUMY3*(1.0-(((GY3-1.0)- 7.0)/(GY3-1.0))**POWY)
 YFRAC(37) =SUMY2+SUMY3*(1.0-(((GY3-1.0)- 8.0)/(GY3-1.0))**POWY)
 YFRAC(38) =SUMY2+SUMY3*(1.0-(((GY3-1.0)- 9.0)/(GY3-1.0))**POWY)
 YFRAC(39) =SUMY2+SUMY3*(1.0-(((GY3-1.0)-10.0)/(GY3-1.0))**POWY)
 YFRAC(40) =SUMY2+SUMY3*(1.0-(((GY3-1.0)-11.0)/(GY3-1.0))**POWY)
 YFRAC(41) =SUMY2+SUMY3*(1.0-(((GY3-1.0)-12.0)/(GY3-1.0))**POWY)
 YFRAC(42) =SUMY2+SUMY3*(1.0-(((GY3-1.0)-13.0)/(GY3-1.0))**POWY)
 YFRAC(43) =SUMY2+SUMY3*(1.0-(((GY3-1.0)-14.0)/(GY3-1.0))**POWY)
 YFRAC(44) =SUMY2+SUMY3*(1.0-(((GY3-1.0)-15.0)/(GY3-1.0))**POWY)
 YFRAC(45) =SUMY2+SUMY3*(1.0-(((GY3-1.0)-16.0)/(GY3-1.0))**POWY)
 YFRAC(46) =SUMY2+SUMY3*(1.0-(((GY3-1.0)-17.0)/(GY3-1.0))**POWY)
 YFRAC(47) =SUMY2+SUMY3
 YFRAC(48) =SUMY2+SUMY3+0.03

 GROUP 5. Z-direction grid specification

UPSTREAM LENGTH
 LU1=29.5;LU2=0.5
 DOWNSTREAM LENGTH
 LD1=6.0;LD2=10.0
 TOTAL LENGTH
 PLEN=LU1+LU2+LD1+LD2;ZWLAST=PLEN*DIAM
 PRESSURE TAPPING WIDTH
 A=2.0/ZWLAST

 UPSTREAM GRID NO.

GZU1=5.0;GZU2=20.0
 ZU1=5;ZU2=20
 TOTAL NUMBER=(ZU1+2)+(ZU2+1)

 ORIFICE GRID NO.

GZCE=21.0;GZOT1=21.0;GZOT2=21.0
 GZOT=GZOT1+GZOT2
 ZCE=21;ZOT1=21;ZOT2=21
 ZOT=ZOT1+ZOT2

 DOWNSTREAM GRID NO.

GZD1=20.0;GZD2=5.0
 ZD1=20;ZD2=5
 TOTAL NUMBER=(ZD1+1+2)+ZD2

NZ=(ZU1+2)+(ZU2+1)+10+ZCE+ZOT+10+(ZD1+1+2)+ZD2
 DCEZ=TCE*BETA*DIAM/ZWLAST;DORT=TTH*BETA*DIAM/ZWLAST

GRID DISTRIBUTION IN REGION A1

SPU1=((LU1+LU2-1.0)/PLEN-A/2.0)/GZU1
 ZFRAC(1)=-GZU1;ZFRAC(2)=SPU1

```

PRESSURE TAPPING POSITION
ZFRAC(3)=1.0 ;ZFRAC(4)=A
-----
ZFRAC(5)=1.0 ;ZFRAC(6)=LU1/PLEN-SPU1*GZU1-A
SUMU1=LU1/PLEN
SUMU2=LU2/PLEN-A
ZFRAC(7)=GZU2/2.0;ZFRAC(8)=(LU2/PLEN-25.4/ZWLAST-A/2.0)/(GZU2/2.0)
-----
PRESSURE TAPPING POSITION
ZFRAC(9)=1.0 ;ZFRAC(10)=A
-----
ZFRAC(11)=GZU2/2.0;ZFRAC(12)=(25.4/ZWLAST-A/2.0-A)/(GZU2/2.0)
-----
PRESSURE TAPPING POSITION
ZFRAC(13)=10.0;ZFRAC(14)=A/10.0
*****
GRID DISTRIBUTION IN REGION A2
SUMBO=(LU1+LU2)/PLEN
ZFRAC(15)=GZCE;ZFRAC(16)=DCEZ/GZCE
*****
GRID DISTRIBUTION IN REGION A3
ZFRAC(17)=GZOT1;ZFRAC(18)=0.1*DORT/GZOT1
ZFRAC(19)=GZOT2;ZFRAC(20)=0.9*DORT/GZOT2
*****
GRID DISTRIBUTION IN REGION A4
SUMAO=SUMBO+DCEZ+DORT
-----
PRESSURE TAPPING POSITION
ZFRAC(21)=10.0;ZFRAC(22)=A/10.0
-----
SUMD1=LD1/PLEN-A-DCEZ-DORT
POW2=2.0
ZD1F=SUMD1/GZD1**POW2
ZFRAC(23)=1.0;ZFRAC(24)=ZD1F*(1.0**POW2)
ZFRAC(25)=1.0;ZFRAC(26)=ZD1F*(2.0**POW2-1.0**POW2)
ZFRAC(27)=1.0;ZFRAC(28)=ZD1F*(3.0**POW2-2.0**POW2)
ZFRAC(29)=1.0;ZFRAC(30)=(25.4/ZWLAST-A-A/2.0)-ZD1F*3.0**POW2
-----
PRESSURE TAPPING POSITION
ZFRAC(31)=1.0;ZFRAC(32)=A
-----
ZFRAC(33)=1.0;ZFRAC(34)=ZD1F*5.0**POW2-(25.4/ZWLAST-A)-A/2.0
ZFRAC(35)=1.0;ZFRAC(36)=(0.5/PLEN-DCEZ-DORT-A)-A/2.0-ZD1F*5.0**POW2
-----
PRESSURE TAPPING POSITION
ZFRAC(37)=1.0;ZFRAC(38)=A
-----
ZFRAC(39)=1.0;ZFRAC(40)=ZD1F*6.0**POW2-(0.5/PLEN-DCEZ-DORT-A)-A/2.0
ZFRAC(41)=1.0;ZFRAC(42)=ZD1F*(7.0**POW2-6.0**POW2)
ZFRAC(43)=1.0;ZFRAC(44)=ZD1F*(8.0**POW2-7.0**POW2)
ZFRAC(45)=1.0;ZFRAC(46)=ZD1F*(9.0**POW2-8.0**POW2)
ZFRAC(47)=1.0;ZFRAC(48)=ZD1F*(10.0**POW2-9.0**POW2)
ZFRAC(49)=1.0;ZFRAC(50)=ZD1F*(11.0**POW2-10.0**POW2)
ZFRAC(51)=1.0;ZFRAC(52)=ZD1F*(12.0**POW2-11.0**POW2)
ZFRAC(53)=1.0;ZFRAC(54)=ZD1F*(13.0**POW2-12.0**POW2)
ZFRAC(55)=1.0;ZFRAC(56)=ZD1F*(14.0**POW2-13.0**POW2)
ZFRAC(57)=1.0;ZFRAC(58)=ZD1F*(15.0**POW2-14.0**POW2)
ZFRAC(59)=1.0;ZFRAC(60)=ZD1F*(16.0**POW2-15.0**POW2)
ZFRAC(61)=1.0;ZFRAC(62)=ZD1F*(17.0**POW2-16.0**POW2)
ZFRAC(63)=1.0;ZFRAC(64)=ZD1F*(18.0**POW2-17.0**POW2)
ZFRAC(65)=1.0;ZFRAC(66)=ZD1F*(19.0**POW2-18.0**POW2)
ZFRAC(67)=1.0;ZFRAC(68)=ZD1F*(20.0**POW2-19.0**POW2)
SPU2=(LD2/PLEN)/GZD2
ZFRAC(69)=GZD2;ZFRAC(70)=SPU2

```

```

*****
GROUP 6. Body-fitted coordinates or grid distortion
GROUP 7. Variables stored, solved & named
SOLVE(P1,V1,W1,KE,EP)
SOLUTN(P1,Y,Y,Y,N,N,N)
SOLUTN(V1,Y,Y,Y,N,N,N)
SOLUTN(W1,Y,Y,Y,N,N,N)
SOLUTN(KE,Y,Y,N,N,N,N)
SOLUTN(EP,Y,Y,N,N,N,N)
STORE(ENUT)
ENUT=GRND
EL1=GRND4
PATCH(KESOURCE,PHASEM,1,NX,1,NY,1,NZ,1,1)
COVAL(KESOURCE,KE,GRND9,GRND9)
COVAL(KESOURCE,EP,GRND9,GRND9)
GENK=T
GROUP 8. Terms (in differential equations) & devices
DIFCUT=0.0
TERMS(P1,Y,Y,Y,N,Y,N); TERMS(V1,Y,Y,Y,N,Y,N)
TERMS(W1,Y,Y,Y,N,Y,N); TERMS(KE,Y,Y,Y,N,Y,N)
TERMS(EP,Y,Y,Y,N,Y,N)
GROUP 9. Properties of the medium (or media)
RHO1=1.0E-06;ENUL=1.0
GROUP 10. Inter-phase-transfer processes and properties
GROUP 11. Initialization of variable or porosity fields
TKEIN=0.003*WIN*WIN
EPIN=0.09*TKEIN**1.5/(0.03*GRAD)
FIINIT(P1)=1.0;FIINIT(W1)=0.5*WIN
FIINIT(V1)=0.0;FIINIT(KE)=0.3*TKEIN
FIINIT(EP)=0.3*EPIN
FIINIT(ENUT)=0.09*TKEIN*TKEIN/EPIN
RESTRT(ALL)
-----
GROUP 12. Convection and diffusion adjustments
GROUP 13. Boundary conditions and special sources
KELIN=0
ZBO=(ZU1+2)+(ZU2+1)+10
ZAO=ZBO+ZCE+ZOT+1
-----
PATCH(WALL1,NWALL,1,1,NY,NY,1,ZBO,1,1)
COVAL(WALL1,W1,GRND2,0.0);COVAL(WALL1,KE,GRND2,GRND2)
COVAL(WALL1,EP,GRND2,GRND2)
-----
PATCH(WALL2,NWALL,1,1,NY,NY,ZAO,NZ,1,1)
COVAL(WALL2,W1,GRND2,0.0);COVAL(WALL2,KE,GRND2,GRND2)
COVAL(WALL2,EP,GRND2,GRND2)
-----
PATCH(INLET,LOW,1,1,1,NY,1,1,1,1)
COVAL(INLET,P1,FIXFLU,WIN*RHO1);COVAL(INLET,W1,ONLYMS,WIN)
COVAL(INLET,KE,ONLYMS,TKEIN);COVAL(INLET,EP,ONLYMS,EPIN)
-----
PATCH(ZOUTLET,HIGH,1,1,1,NY,NZ,NZ,1,1)
COVAL(ZOUTLET,P1,FIXVAL,0.0)
-----
YBC=Y1
YAC=YBC+Y2+1
CONPOR(0.0,CELL,1,1,YAC,NY,(ZBO+1),ZBO+ZCE)
CONPOR(0.0,CELL,1,1,(YBC+1),NY,(ZBO+ZCE+1),(ZBO+ZCE+ZOT))
-----
PATCH(WALL3,HWALL,1,1,YAC,NY,ZBO,ZBO,1,1)
COVAL(WALL3,V1,GRND2,0.0);COVAL(WALL3,KE,GRND2,GRND2)
COVAL(WALL3,EP,GRND2,GRND2)
-----
PATCH(WALL4,NWALL,1,1,YBC,YBC,(ZBO+ZCE+1),(ZBO+ZCE+ZOT),1,1)

```

COVAL(WALL4,W1,GRND2,0.0);COVAL(WALL4,KE,GRND2,GRND2)
COVAL(WALL4,EP,GRND2,GRND2)

PATCH(WALL5,LWALL,1,1,YBC+1,NY,ZAO,ZAO,1,1)
COVAL(WALL5,V1,GRND2,0.0);COVAL(WALL5,KE,GRND2,GRND2)
COVAL(WALL5,EP,GRND2,GRND2)

USE OF POROSITY TO REPRESENT CONICAL PART OF ORIFICE

CONPOR(0.0,CELL,1,1,YAC- 1,YAC- 1,ZBO+ 2,ZBO+ZCE)
CONPOR(0.0,CELL,1,1,YAC- 2,YAC- 2,ZBO+ 3,ZBO+ZCE)
CONPOR(0.0,CELL,1,1,YAC- 3,YAC- 3,ZBO+ 4,ZBO+ZCE)
CONPOR(0.0,CELL,1,1,YAC- 4,YAC- 4,ZBO+ 5,ZBO+ZCE)
CONPOR(0.0,CELL,1,1,YAC- 5,YAC- 5,ZBO+ 6,ZBO+ZCE)
CONPOR(0.0,CELL,1,1,YAC- 6,YAC- 6,ZBO+ 7,ZBO+ZCE)
CONPOR(0.0,CELL,1,1,YAC- 7,YAC- 7,ZBO+ 8,ZBO+ZCE)
CONPOR(0.0,CELL,1,1,YAC- 8,YAC- 8,ZBO+ 9,ZBO+ZCE)
CONPOR(0.0,CELL,1,1,YAC- 9,YAC- 9,ZBO+10,ZBO+ZCE)
CONPOR(0.0,CELL,1,1,YAC-10,YAC-10,ZBO+11,ZBO+ZCE)
CONPOR(0.0,CELL,1,1,YAC-11,YAC-11,ZBO+12,ZBO+ZCE)
CONPOR(0.0,CELL,1,1,YAC-12,YAC-12,ZBO+13,ZBO+ZCE)
CONPOR(0.0,CELL,1,1,YAC-13,YAC-13,ZBO+14,ZBO+ZCE)
CONPOR(0.0,CELL,1,1,YAC-14,YAC-14,ZBO+15,ZBO+ZCE)
CONPOR(0.0,CELL,1,1,YAC-15,YAC-15,ZBO+16,ZBO+ZCE)
CONPOR(0.0,CELL,1,1,YAC-16,YAC-16,ZBO+17,ZBO+ZCE)
CONPOR(0.0,CELL,1,1,YAC-17,YAC-17,ZBO+18,ZBO+ZCE)
CONPOR(0.0,CELL,1,1,YAC-18,YAC-18,ZBO+19,ZBO+ZCE)
CONPOR(0.0,CELL,1,1,YAC-19,YAC-19,ZBO+20,ZBO+ZCE)
CONPOR(0.0,CELL,1,1,YAC-20,YAC-20,ZBO+21,ZBO+ZCE)

CONPOR(0.0,NORTH,1,1,YAC- 1,YAC- 1,ZBO+ 1,ZBO+ 1)
CONPOR(0.0,HIGH ,1,1,YAC- 1,YAC- 1,ZBO+ 1,ZBO+ 1)
CONPOR(0.5,CELL ,1,1,YAC- 1,YAC- 1,ZBO+ 1,ZBO+ 1)

CONPOR(0.0,NORTH,1,1,YAC- 2,YAC- 2,ZBO+ 2,ZBO+ 2)
CONPOR(0.0,HIGH ,1,1,YAC- 2,YAC- 2,ZBO+ 2,ZBO+ 2)
CONPOR(0.5,CELL ,1,1,YAC- 2,YAC- 2,ZBO+ 2,ZBO+ 2)

CONPOR(0.0,NORTH,1,1,YAC- 3,YAC- 3,ZBO+ 3,ZBO+ 3)
CONPOR(0.0,HIGH ,1,1,YAC- 3,YAC- 3,ZBO+ 3,ZBO+ 3)
CONPOR(0.5,CELL ,1,1,YAC- 3,YAC- 3,ZBO+ 3,ZBO+ 3)

CONPOR(0.0,NORTH,1,1,YAC- 4,YAC- 4,ZBO+ 4,ZBO+ 4)
CONPOR(0.0,HIGH ,1,1,YAC- 4,YAC- 4,ZBO+ 4,ZBO+ 4)
CONPOR(0.5,CELL ,1,1,YAC- 4,YAC- 4,ZBO+ 4,ZBO+ 4)

CONPOR(0.0,NORTH,1,1,YAC- 5,YAC- 5,ZBO+ 5,ZBO+ 5)
CONPOR(0.0,HIGH ,1,1,YAC- 5,YAC- 5,ZBO+ 5,ZBO+ 5)
CONPOR(0.5,CELL ,1,1,YAC- 5,YAC- 5,ZBO+ 5,ZBO+ 5)

CONPOR(0.0,NORTH,1,1,YAC- 6,YAC- 6,ZBO+ 6,ZBO+ 6)
CONPOR(0.0,HIGH ,1,1,YAC- 6,YAC- 6,ZBO+ 6,ZBO+ 6)
CONPOR(0.5,CELL ,1,1,YAC- 6,YAC- 6,ZBO+ 6,ZBO+ 6)

CONPOR(0.0,NORTH,1,1,YAC- 7,YAC- 7,ZBO+ 7,ZBO+ 7)
CONPOR(0.0,HIGH ,1,1,YAC- 7,YAC- 7,ZBO+ 7,ZBO+ 7)
CONPOR(0.5,CELL ,1,1,YAC- 7,YAC- 7,ZBO+ 7,ZBO+ 7)

CONPOR(0.0,NORTH,1,1,YAC- 8,YAC- 8,ZBO+ 8,ZBO+ 8)
CONPOR(0.0,HIGH ,1,1,YAC- 8,YAC- 8,ZBO+ 8,ZBO+ 8)
CONPOR(0.5,CELL ,1,1,YAC- 8,YAC- 8,ZBO+ 8,ZBO+ 8)

CONPOR(0.0,NORTH,1,1,YAC- 9,YAC- 9,ZBO+ 9,ZBO+ 9)
CONPOR(0.0,HIGH ,1,1,YAC- 9,YAC- 9,ZBO+ 9,ZBO+ 9)
CONPOR(0.5,CELL ,1,1,YAC- 9,YAC- 9,ZBO+ 9,ZBO+ 9)

CONPOR(0.0,NORTH,1,1,YAC-10,YAC-10,ZBO+10,ZBO+10)
CONPOR(0.0,HIGH,1,1,YAC-10,YAC-10,ZBO+10,ZBO+10)
CONPOR(0.5,CELL,1,1,YAC-10,YAC-10,ZBO+10,ZBO+10)

CONPOR(0.0,NORTH,1,1,YAC-11,YAC-11,ZBO+11,ZBO+11)
CONPOR(0.0,HIGH,1,1,YAC-11,YAC-11,ZBO+11,ZBO+11)
CONPOR(0.5,CELL,1,1,YAC-11,YAC-11,ZBO+11,ZBO+11)

CONPOR(0.0,NORTH,1,1,YAC-12,YAC-12,ZBO+12,ZBO+12)
CONPOR(0.0,HIGH,1,1,YAC-12,YAC-12,ZBO+12,ZBO+12)
CONPOR(0.5,CELL,1,1,YAC-12,YAC-12,ZBO+12,ZBO+12)

CONPOR(0.0,NORTH,1,1,YAC-13,YAC-13,ZBO+13,ZBO+13)
CONPOR(0.0,HIGH,1,1,YAC-13,YAC-13,ZBO+13,ZBO+13)
CONPOR(0.5,CELL,1,1,YAC-13,YAC-13,ZBO+13,ZBO+13)

CONPOR(0.0,NORTH,1,1,YAC-14,YAC-14,ZBO+14,ZBO+14)
CONPOR(0.0,HIGH,1,1,YAC-14,YAC-14,ZBO+14,ZBO+14)
CONPOR(0.5,CELL,1,1,YAC-14,YAC-14,ZBO+14,ZBO+14)

CONPOR(0.0,NORTH,1,1,YAC-15,YAC-15,ZBO+15,ZBO+15)
CONPOR(0.0,HIGH,1,1,YAC-15,YAC-15,ZBO+15,ZBO+15)
CONPOR(0.5,CELL,1,1,YAC-15,YAC-15,ZBO+15,ZBO+15)

CONPOR(0.0,NORTH,1,1,YAC-16,YAC-16,ZBO+16,ZBO+16)
CONPOR(0.0,HIGH,1,1,YAC-16,YAC-16,ZBO+16,ZBO+16)
CONPOR(0.5,CELL,1,1,YAC-16,YAC-16,ZBO+16,ZBO+16)

CONPOR(0.0,NORTH,1,1,YAC-17,YAC-17,ZBO+17,ZBO+17)
CONPOR(0.0,HIGH,1,1,YAC-17,YAC-17,ZBO+17,ZBO+17)
CONPOR(0.5,CELL,1,1,YAC-17,YAC-17,ZBO+17,ZBO+17)

CONPOR(0.0,NORTH,1,1,YAC-18,YAC-18,ZBO+18,ZBO+18)
CONPOR(0.0,HIGH,1,1,YAC-18,YAC-18,ZBO+18,ZBO+18)
CONPOR(0.5,CELL,1,1,YAC-18,YAC-18,ZBO+18,ZBO+18)

CONPOR(0.0,NORTH,1,1,YAC-19,YAC-19,ZBO+19,ZBO+19)
CONPOR(0.0,HIGH,1,1,YAC-19,YAC-19,ZBO+19,ZBO+19)
CONPOR(0.5,CELL,1,1,YAC-19,YAC-19,ZBO+19,ZBO+19)

CONPOR(0.0,NORTH,1,1,YAC-20,YAC-20,ZBO+20,ZBO+20)
CONPOR(0.0,HIGH,1,1,YAC-20,YAC-20,ZBO+20,ZBO+20)
CONPOR(0.5,CELL,1,1,YAC-20,YAC-20,ZBO+20,ZBO+20)

CONPOR(0.0,NORTH,1,1,YAC-21,YAC-21,ZBO+21,ZBO+21)
CONPOR(0.0,HIGH,1,1,YAC-21,YAC-21,ZBO+21,ZBO+21)
CONPOR(0.5,CELL,1,1,YAC-21,YAC-21,ZBO+21,ZBO+21)

GROUP 14. Downstream pressure for PARAB=.TRUE.

GROUP 15. Termination of sweeps

DELCON=0.005

RESREF(P1)=0.5*DELCON*0.5*WIN*3.14159*DIAM*DIAM/4.0

RESREF(W1)=DELCON*WIN*RHO1*0.5*WIN*3.14159*DIAM*DIAM/4.0

RESREF(V1)=5.0*DELCON*WIN*RHO1*0.5*WIN*3.14159*DIAM*DIAM/4.0

RESREF(KE)=1.0E+5*DELCON*TKEIN*RHO1*0.5*WIN*3.14159*DIAM*DIAM/4.0

RESREF(EP)=1.0E+8*DELCON*EPIN*RHO1*0.5*WIN*3.14159*DIAM*DIAM/4.0

LSWEEP=500

NPLT=100

TSTSWP=100

GROUP 16. Termination of iterations

LITER(P1)=10;LITER(V1)=10

LITER(W1)=10;LITER(KE)=10

```

LITER(EP)=10
  GROUP 17. Under-relaxation devices
RELAX(P1,LINRLX,0.1); RELAX(V1,FALSDT,0.01)
RELAX(W1,FALSDT,0.001); RELAX(KE,FALSDT,0.001)
RELAX(EP,FALSDT,0.1)
  GROUP 18. Limits on variables or increments to them
  GROUP 19. Data communicated by satellite to GROUND
RSG1=DCEY;RSG2=GY2;RSG3=LU1;RSG4=LU2;RSG5=DIAM
RSG6=DCEZ;RSG7=GZCE;RSG8=DORT;RSG9=DORR
RSG10=ENUL
ISG1=ZBO;ISG2=YBC
ISG3=YAC;ISG4=ZCE;ISG6=ZOT;ISG7=ZAO
  GROUP 20. Preliminary print-out
ECHO=F
  GROUP 21. Print-out of variables
OUTPUT(P1,Y,N,N,Y,Y,Y)
OUTPUT(V1,Y,N,N,Y,Y,Y)
OUTPUT(W1,Y,N,N,Y,Y,Y)
OUTPUT(KE,Y,N,N,Y,Y,Y)
OUTPUT(EP,Y,N,N,Y,Y,Y)
  GROUP 22. Spot-value print-out
IYMON=NY-1;IZMON=ZAO+1
  GROUP 23. Field print-out and plot control
IYPRF=NY-20; IYPRL=NY
IZPRF=ZBO-30; IZPRL=ZAO+30
ITABL=2; NUMCLS=6
  GROUP 24. Dumps for restarts
  -----
  -----
  -----
STOP

```